

University of California  
Santa Barbara

**Photonic integrated coil resonator stabilized narrow  
linewidth lasers and their applications**

A dissertation submitted in partial satisfaction  
of the requirements for the degree

Doctor of Philosophy  
in  
Electrical and Computer Engineering

by

Kaikai Liu

Committee in charge:

Professor Daniel J. Blumenthal, Chair  
Professor Jonathan Klamkin  
Professor Steven P. DenBaars  
Dr. Nicolas K. Fontaine, Nokia Bell Labs  
Dr. Scott B. Papp, NIST

March 2025

The Dissertation of Kaikai Liu is approved.

---

Professor Jonathan Klamkin

---

Professor Steven P. DenBaars

---

Dr. Nicolas K. Fontaine

---

Dr. Scott B. Papp

---

Professor Daniel J. Blumenthal, Committee Chair

December 2024

Photonic integrated coil resonator stabilized narrow linewidth lasers and their  
applications

Copyright © 2025

by

Kaikai Liu

To my beloved family.

## Acknowledgements

I would like to thank my advisor Daniel Blumenthal for his tremendous support and guidance over the years on research directions and small details, and also thank the Blumenthal group members for all our team work and efforts on various projects. I am deeply grateful for this ride of my life during my graduate school and PhD journal, which would be possible without all of the people that I connected here during this journey, including mentors, classmates, colleagues, collaborators, friends, and close friends.

# Curriculum Vitæ

## Kaikai Liu

### Education

- 2024 Ph.D. in Electrical and Computer Engineering, University of California, Santa Barbara.
- 2020 M.S. in Electrical and Computer Engineering, University of California, Santa Barbara.
- 2018 B.S. in Physics, Huazhong University of Science and Technology

### Journal Publications

- Liu, K., N. Chauhan, M. Song, M. W. Harrington, K. D. Nelson, and D. J. Blumenthal. “Tunable broadband two-point-coupled ultra-high-Q visible and near-infrared photonic integrated resonators.” *Photonics Research* **12.9** (2024): 1890-1898.
- Sun, S., B. Wang, K. Liu, M. W. Harrington, F. Tabatabaei, et al. “Integrated optical frequency division for microwave and mmWave generation.” *Nature* **627.8004** (2024): 540-545.
- Bose, D., M. W. Harrington, A. Isichenko, K. Liu, J. Wang, N. Chauhan, Z. L. Newman, and D. J. Blumenthal. “Anneal-free ultra-low loss silicon nitride integrated photonics.” *Light: Science & Applications* **13.1** (2024): 156.
- Liu, K., J. Wang, N. Chauhan, M. W. Harrington, K. D. Nelson, and D. J. Blumenthal. “Integrated photonic molecule Brillouin laser with a high-power sub-100-mHz fundamental linewidth.” *Optics Letters* **49.1** (2024): 45-48.
- Liu, K., J. H. Dallyn, G. M. Brodnik, A. Isichenko, M. W. Harrington, N. Chauhan, D. Bose, et al. “Photonic circuits for laser stabilization with integrated ultra-high Q and Brillouin laser resonators.” *APL Photonics* **7.9** (2022).
- Liu, K., N. Chauhan, J. Wang, A. Isichenko, G. M. Brodnik, P. A. Morton, R. O. Behunin, S. B. Papp, and D. J. Blumenthal. “36 Hz integral linewidth laser based on a photonic integrated 4.0 m coil resonator.” *Optica* **9.7** (2022): 770-775.
- Liu, K., N. Jin, H. Cheng, N. Chauhan, M. W. Puckett, K. D. Nelson, R. O. Behunin, P. T. Rakich, and D. J. Blumenthal. “Ultralow 0.034 dB/m loss wafer-scale integrated photonics realizing 720 million Q and 380  $\mu$ W threshold Brillouin lasing.” *Optics Letters* **47.7** (2022): 1855-1858.
- Puckett, M. W., K. Liu, N. Chauhan, Q. Zhao, N. Jin, H. Cheng, J. Wu, et al. “422 Million intrinsic quality factor planar integrated all-waveguide resonator with sub-MHz linewidth.” *Nature Communications* **12.1** (2021): 934.

## Conference Proceedings

- Liu, K., M. H. Idjadi, S. Grillanda, K. Kim, C. Bolle, M. Cappuzzo, R. Kopf, N. Fontaine, M. Mazur, R. Ryf, and others, “Common cavity waveguide coil-resonator stabilized hybrid integrated WDM laser with 89 Hz integral linewidth,” in *2024 Optical Fiber Communications Conference and Exhibition (OFC)* (IEEE, 2024), pp. 1–3.
- Liu, K., and D. J. Blumenthal, “Integrated Brillouin laser in 4-meter-coil resonator realizing 40 mW output power and 31 mHz fundamental linewidth,” in *CLEO: Science and Innovations* (Optica Publishing Group, 2024), pp. STh4O-4.
- Liu, K., J. Wang, A. Isichenko, N. Chauhan, and D. J. Blumenthal, “Integrated High-Extinction-Ratio 2.0-Meter Unbalanced MZI for Laser Frequency Noise Measurements,” in *2023 Conference on Lasers and Electro-Optics (CLEO)* (IEEE, 2023), pp. 1–2.
- Liu, K., J. Wang, N. Chauhan, and D. J. Blumenthal, “Circulator-free photonic integrated Brillouin laser,” in *Nonlinear Optics* (Optica Publishing Group, 2023), pp. Tu2A-3.
- Liu, K., M. W. Harrington, J. Wang, A. Isichenko, N. Chauhan, K. D. Nelson, and D. J. Blumenthal, “Integrated tunable two-point-coupled 10-meter 336 million Q coil-resonator for laser stabilization,” in *Frontiers in Optics* (Optica Publishing Group, 2023), pp. FM6D-6.
- Liu, K., M. W. Harrington, J. Wang, K. D. Nelson, and D. J. Blumenthal, “Integrated self-delayed 2-m coil-resonator for high sensitivity optical frequency discrimination and laser linewidth narrowing,” in *Frontiers in Optics* (Optica Publishing Group, 2023), pp. JW4A-22.
- Liu, K., M. W. Harrington, K. D. Nelson, R. O. Behunin, S. B. Papp, and D. J. Blumenthal, “Photonic integrated cascade-inhibited Brillouin laser with sub-100-mHz fundamental linewidth,” in *CLEO: Science and Innovations* (Optica Publishing Group, 2022), pp. SF2K-1.
- Liu, K., N. Chauhan, J. Wang, A. Isichenko, G. M. Brodnik, P. A. Morton, R. Behunin, S. B. Papp, and D. J. Blumenthal, “Semiconductor laser stabilized by a photonic integrated 4 meter coil-waveguide resonator,” in *Optical Fiber Communication Conference* (Optica Publishing Group, 2022), pp. Tu3D-2.
- Liu, K., M. W. Puckett, M. W. Harrington, G. M. Brodnik, Q. Zhao, N. Chauhan, J. Wang, R. O. Behunin, K. D. Nelson, and D. J. Blumenthal, “Milliwatt threshold ultra-Low linewidth photonic integrated Si<sub>3</sub>N<sub>4</sub> Brillouin laser,” in *CLEO: Science and Innovations* (Optica Publishing Group, 2021), pp. SF2O-1.
- Liu, K., N. Jin, H. Cheng, M. W. Puckett, R. O. Behunin, K. D. Nelson, P. T. Rakich, and D. J. Blumenthal, “720 million quality factor integrated all-waveguide photonic resonator,” in *2021 Device Research Conference (DRC)* (IEEE, 2021), pp. 1–2.

- Liu, K., N. Chauhan, J. Wang, P. A. Morton, R. Behunin, and D. J. Blumenthal, “Precision laser stabilization using photonic integrated coil resonator,” in *Frontiers in Optics* (Optica Publishing Group, 2021), pp. FTh2A-1.
- Liu, K., G. M. Brodnik, M. W. Harrington, A. Isichenko, Q. Zhao, J. Dallyn, R. O. Behunin, P. Morton, S. Papp, and D. J. Blumenthal, “Self-Similar Ultra-High Q  $\text{Si}_3\text{N}_4$  Integrated Resonators for Brillouin Laser Linewidth Narrowing and Stabilization,” in *Optical Fiber Communication Conference* (Optica Publishing Group, 2021), pp. Th4B-2.



## Abstract

Photonic integrated coil resonator stabilized narrow linewidth lasers and their applications

by

Kaikai Liu

Silicon nitride has become a widely used material platform for photonic integrated circuits owing to its broad optical transparency window (400 nm – 2.5  $\mu\text{m}$ ), relatively high refractive index, widely accessible growth mechanism in CMOS foundries, and ability to achieve low propagation losses. In this dissertation, we discuss the efforts to achieve high laser spectral purity based on high-Q silicon nitride waveguide resonators, nonlinear Brillouin dynamics, and low-noise coil waveguide reference resonators for laser stabilization. The first part focuses on the design and fabrication of low-confinement silicon nitride waveguide resonators with 200 – 700 million intrinsic Qs. Based on the low-loss waveguides, the Brillouin scattering laser using both the higher-order Stokes suppression approach and large mode volume coil resonator approach achieves fundamental linewidths of 77 mHz and 30 mHz, respectively. Enabled by the low-loss silicon nitride platform and its design and fabrication advantages, we developed a scalable integrated optics solution for optical reference resonators for laser stabilization using 8-inch-CMOS-fabricated and 300-million-intrinsic-Q coil waveguide resonators with low thermal noise limits including 4-m, 10-m, and 17-m long coil waveguide resonators. This dissertation concludes with the development and demonstration of a fully stabilized narrow linewidth Brillouin laser with a Brillouin laser, power splitter, coil resonator resonator on one chip, realizing a Hz-level fundamental linewidth and a 70 Hz integral linewidth. These results show great potential of silicon nitride based integrated optical reference resonator and

laser technology in visible and near-infrared wavelengths for a broad range of applications such as coherence communications, low-noise microwave generation, fiber sensing, quantum photonics and atomic, molecular and optical (AMO) applications.

# Contents

<b>Curriculum Vitae</b>	<b>vi</b>
<b>Abstract</b>	<b>ix</b>
<b>List of Figures</b>	<b>xiii</b>
<b>1 Introduction</b>	<b>1</b>
1.1 Background . . . . .	1
1.2 Accomplishments in this thesis . . . . .	4
1.3 Thesis outline . . . . .	5
<b>2 Ultra-low-loss silicon nitride waveguides</b>	<b>7</b>
2.1 Waveguide resonator linewidth and Q factor . . . . .	9
2.2 High-aspect-ratio silicon nitride waveguides . . . . .	19
2.3 Waveguide loss origin investigation . . . . .	30
2.4 Summary and outlook . . . . .	36
<b>3 Laser frequency noise and linewidth</b>	<b>41</b>
3.1 Fundamental oscillator phase and frequency noise . . . . .	43
3.2 Frequency noise, linewidth and Allan deviation . . . . .	46
3.3 Thermo-refractive noise and photothermal noise . . . . .	50
3.4 Summary and outlook . . . . .	53
<b>4 Narrow linewidth stimulated Brillouin scattering lasers</b>	<b>59</b>
4.1 SBS laser modeling . . . . .	64
4.2 Milliwatt threshold SBS lasers . . . . .	75
4.3 Circulator-free SBS lasers . . . . .	81
4.4 Higher-order-Stokes emission suppression . . . . .	83
4.5 Coil SBS lasers . . . . .	89
4.6 Summary and outlook . . . . .	98

<b>5</b>	<b>Coil waveguide reference resonators for laser stabilization</b>	<b>107</b>
5.1	Basics of Pound-Drever-Hall laser stabilization . . . . .	109
5.2	TM coil waveguide resonators (4 meters) . . . . .	115
5.3	TE coil waveguide resonators (4, 10, 17 meters) . . . . .	124
5.4	Two-point-coupled coil resonators . . . . .	133
5.5	Self-delayed coil resonators . . . . .	140
5.6	Coil waveguide MZIs . . . . .	144
5.7	Summary and outlook . . . . .	151
<b>6</b>	<b>Photonic integrated stabilized SBS lasers</b>	<b>164</b>
<b>7</b>	<b>Future work</b>	<b>173</b>

# List of Figures

2.1	Optical fiber loss evolution over the last fifty years since 1970 has seen great advancement [4]. The propagation loss at 1550 nm in best single mode fibers reaches the material limit around 0.17 dB/m and has only decreased by less than 0.05 dB/m since 1980. © SienceDirect Publishing	8
2.2	Photonic integrated waveguide propagation loss using different material waveguide platforms such as InP [6], AlGaAs [7], 220 nm SOI [8, 9], TFLN [10, 11], thick-core and high-confinement Si <sub>3</sub> N <sub>4</sub> [12, 13], and thin-core and low-confinement Si <sub>3</sub> N <sub>4</sub> [14, 15, 16]	9
2.3	Waveguide ring resonator with the add-through and add-drop configurations (Fig. 4.27 in [21]).	10
2.4	Add-drop ring resonator spectral transmission. (a) shows a curve calculated by Eq. 2.2 or 2.3. (b) shows how (a) can be readily mapped to an actual experimental spectral sweep of an ultra-high-Q ring resonator.	11
2.5	CMT picture of waveguide ring resonators. Add-through and add-drop ring resonator illustration with intrinsic loss rate and external coupling loss rate.	13
2.6	Waveguide ring resonator simulations under different configurations such as (a) add-through, (b) add-drop, (c) add-through with CW-CCW mode coupling and resonance splitting, and (d) add-through with Fano resonance effect.	15
2.7	Waveguide design considerations. (a) Bending loss simulation in a 6 $\mu$ wide silicon nitride waveguide at different thicknesses, from 40 nm to 120 nm. (b) High-aspect-ratio waveguide design illustration with thermal oxide as lower cladding and TEOS-PECVD silicon dioxide as upper cladding. (c) Electric field magnitude for the fundamental TE mode in a 6 $\mu$ m by 80 nm waveguide.	20

2.8	Waveguide design considerations. (a) Fiber-to-waveguide coupling loss between the fundamental TE mode in an 80 nm thick waveguide tapered at different widths and different types of fibers such as SMF-28, UHNA1 (4.8 $\mu\text{m}$ MFD), and UHNA3 (4.1 $\mu\text{m}$ MFD) fibers at the wavelength of 1550 nm. (b) The effective indices of all supported waveguide modes in an 80 nm thick waveguide at different widths. . . . .	21
2.9	Waveguide design considerations. (a) Fiber-to-waveguide coupling loss between the fundamental TE mode in an 80 nm thick waveguide tapered at different widths and different types of fibers such as SMF-28, UHNA1 (4.8 $\mu\text{m}$ MFD), and UHNA3 (4.1 $\mu\text{m}$ MFD) fibers at the wavelength of 1550 nm. (b) The effective indices of all supported waveguide modes in an 80 nm thick waveguide at different widths. . . . .	21
2.10	Fabrication process flow with the redeposition and oxidation steps indicated as step 3 and 4. . . . .	23
2.11	Linewidth, ring-down, and photo-thermal absorption loss measurements of the UHQR and control devices. (a) Spectral scan of the fundamental 1570 nm TE mode for the control and UHQR devices. The total and intrinsic linewidths are extracted from a Lorentzian fit. The yellow signal is the fibre MZI. M, million. (b) UHQR ring-down time measurement at 1570 nm. (c) Total and intrinsic linewidths for the UHQR and control samples from 1550 nm to 1600 nm. (d) Measured intrinsic Qs for UHQR and control resonators. (e) Photo-thermal absorption loss measurement from 1550 nm to 1600 nm for UHQR and control. The highest UHQR 422 million intrinsic Q at 1570 nm and the absorption-limited Q of 3.4 Billion at 1600 nm are indicated. The non-absorption loss is fit to the surface scattering loss model (dash lines). . . . .	24
2.12	Photo-thermal heating and absorption loss measurement. (a) Effective index change with respect to temperature shows no wavelength dependence across the range from 1550 nm to 1600 nm. (b) Photothermal effect is amplified by higher on-chip power and the resonance redshift exhibits a linear relationship with the on-chip power. (c) Normal Lorentzian fitting for the lower power spectral sweeping and skewed Lorentzian fitting for the high-power spectral sweeping extracts the intrinsic loss and absorption loss rates. . . . .	25
2.13	Simulations of the spectral scanning of an optical resonance with various laser scanning speeds that corresponds to $N = 100, 4, 1$ . With $N = 1, 4$ , the ring-down effect emerges as the laser is exiting the resonance. Original figure from [30]. . . . .	26
2.14	A spectral scanning experiment with an estimated $N = 12$ sees the ring-down effect. . . . .	27

2.15	Linewidth measurements of a waveguide ring resonator (radius = 8530 $\mu\text{m}$ , 6 $\mu\text{m}$ by 80 nm waveguide) for (a) the $\text{TE}_0$ mode and (b) the $\text{TM}_0$ mode. (c) shows a comparison between the measured bus-ring coupling and simulated values using an approximated coupling length of $L_x = 0.3$ mm. . . . .	29
2.16	(a) Coupling tree testing technique. (b) The coupling tree measurement on the 3.5- $\mu\text{m}$ testing structure yield a coupling of -13.2 dB for the $\text{TM}_0$ mode. (c) Simulated coupling for both the TE and TM modes at different coupling gaps is compared with experimentally measured values. . . . .	29
2.17	Illustration of ultra-high-Q waveguide ring resonator loss origins, with a picture of the real waveguide ring resonator device. . . . .	31
2.18	The dipole radiation from a roughness particle is simulated in COMSOL for both TE and TM modes on the top surface and sidewall surface, which is fed into the 3d-VCM analytical model to estimate the scattering losses. (a) illustrates the roughnesses on different surfaces. (b) shows the dipole radiation farfield. . . . .	33
2.19	Top surface roughness scattering loss simulation using the 3D-VCM model. (a) Scattering loss for TE in waveguides with different thicknesses of 40 nm, 60 nm and 80 nm. (b) Scattering loss for TE and TM losses in the 80 nm thick waveguide. . . . .	34
2.20	TM mode waveguide resonator linewidth and Q. (a) 200-mm wafer after the fabrication and dicing process. (b) Resonance spectral scan at 1615 nm with the 1.078 MHz FSR MZI. (c) Measured loaded and intrinsic Qs from 1550 nm to 1630 nm. M = million. (d) A ringdown time of 444 ns, corresponding to an intrinsic Q = 775 M is measured at 1615 nm. . . . .	35
3.1	Quartz oscillator and MHM-2020 hydrogen maser phase noise and Allan deviation. . . . .	42
3.2	Frequency noise, phase noise, time-jitter noise, fractional frequency noise in time domain and frequency domain, and the conversions between them. Original figure from [23]. . . . .	47
3.3	Different types of frequency noise processes, and the conversion to Allan deviation. Original figure from [23]. . . . .	49
3.4	2D static thermal simulation with the silicon nitride waveguide core being the heat source in COMSOL. The thermal impedance has a frequency response with 4.98 K/W at low frequencies and roll-off from 1 kHz. . . . .	51
3.5	Photothermal redshift strength is measured to be $\Delta f_{opt}/P_{opt} = 0.647$ MHz/mW. . . . .	53
3.6	Estimated photothermal noise in a Brillouin laser in the ring resonator induced by the pump laser's power intensity fluctuations is compared with the measured Brillouin laser frequency noise spectrum. Details can be found in [33]. . . . .	53

4.1	Cascaded emission of SBS laser and its consequences on Stokes output powers and linewidths. (a) Cascaded emission diagram. (b) Simulated Stokes output powers and (c) fundamental linewidth versus pump power, using the theoretical framework in [36]. . . . .	63
4.2	SBS phase/frequency matching illustration. (a) Optical and acoustic field decay illustration. (b) COMSOL simulated Brillouin gain profile at 1550 nm for the TE <sub>0</sub> mode in 6 μm wide silicon nitride waveguide with different thicknesses. (c) SBS phase/frequency matching at different optical wavelengths. (d) SBS gain perceived in the S1 lasing mode at different wavelengths resembles the SBS gain spectrum in (b) and impacts the S1 optical threshold. . . . .	67
4.3	$N_0$ for acoustic phonons at 11.9 GHz frequency as a function of temperature.	72
4.4	Triangle relationship between $P_{th}$ , $\Delta\nu_{min}$ and $\mu$ (Eq. 4.20 and 4.27). . . .	73
4.5	Calculated S1 threshold power and S1 conversion efficiency $\eta_{S1}$ as its clamping point at different coupling regimes of the SBS resonator. . . . .	75
4.6	TE SBS. (a) SBS laser operation with OSA and OFD measurements. (b) Spectral scan of the SBS resonator at 1550 nm. (c) SBS laser spectrum on the OSA shows cascaded emission at 1550 nm. . . . .	76
4.7	SBS laser Stokes powers and linewidth at 1550 nm. (a) Measured S1 and S3 on-chip powers with the simulated curves with an S1 threshold of 2.4 mW. (c) Pump-S1 beatnote frequency as a function of the on-chip power power shows a linear dependency of 0.15 MHz/mW. With the fluctuation within 1 MHz, the group index can be estimated to be $n_g = 1.486 \pm 0.001$ .	76
4.8	TM SBS at 1570 nm. (a) SBS laser operation diagram. (B) SBS laser spectrum on OSA. (c) Measured S1 and S3 on-chip Stokes powers with an S1 threshold of 0.38 mW. (d) Measured S1 threshold powers at different wavelengths enables calculation of the waveguide Brillouin gain at each wavelength point. . . . .	77
4.9	TM SBS frequency matching, S1 efficiency, and threshold. (a) The SBS gain profile in the 80 nm nitride TM waveguide uses that in the 40 nm nitride TE waveguide. (b) Pump-S1 beatnote on an ESA at different wavelengths. (c) SBS frequency matching versus wavelength. (d) Calculated threshold and conversion efficiency of S1 at its clamping point based on the measured parameters of this SBS device. . . . .	79
4.10	Pump-S1 beatnote and group index versus wavelength. (a) Pump-S1 beatnote at 1570 nm on ESA. (b) Beatnote frequency with a linear fitting from 1550 nm to 1600 nm. (c) Group index calculated from the beatnote frequency from 1550 nm to 1600 nm with a linear fitting, $n_g(\lambda) = 1.4956 \times [1 - 9.33 \times 10^{-4}(\lambda - 1550)/50]$ . . . . .	80



4.11	Circulator-free SBS laser PIC. (a) Optical image of the PIC device. (b) Circulator-free SBS laser operation diagram. (c) Spectral scan of the PIC through 1→2 and 1→3. (d) Zoom-in of the split resonance. (d) SBS resonator Q and linewidth measurement. . . . .	82
4.12	Circulator-free SBS laser threshold and fundamental linewidth measurement. (a) OSA spectrum of the SBS laser dropped by a circulator and the ring filter. (b) S1 on-chip power versus on-chip pump power. (c) Frequency noise at different pump powers. TRN, thermorefractive noise. . . . .	82
4.13	SBS numerical simulation under the conditions of cascaded emission, S2-suppression and S3 suppression. (a) Upper shows the Stokes power of S1 – S4 versus pump power (dash lines) in the cascaded emission and S2-suppressed emission (solid line). The lower shows the fundamental linewidth in cascaded and S2-suppressed emission. (b) Upper shows the power of S1 – S4 versus pump power (dash lines) in the cascaded emission and S3-suppressed emission (solid line). The lower shows the Stokes fundamental linewidth in the cascaded emission and S3-suppressed emission. Differential efficiency $\eta_0 = \gamma_{ex}^2/\gamma^2$ . . . . .	84
4.14	S2-suppressed SBS design. (a) Illustration of coupled-ring resonator with split resonances due to mode splitting for S2 suppression, where the split modes correspond to symmetric $ S\rangle$ and asymmetric $ AS\rangle$ hybrid modes. (b) Normalized transmission shows a split resonance and other non-split resonances near 1570 nm. (c) Zoom-in of the split resonance. (d) Q and linewidth measurement of the high-Q non-split resonance. . . . .	86
4.15	S2-suppressed SBS laser threshold, output power and fundamental linewidth measurement. (a) OFD frequency noise of S1. (b) S1 on-chip power with measured 2.3 mW threshold. (c) Fundamental linewidth versus pump power. (d) S2-suppressed SBS laser on OSA. . . . .	87
4.16	Single sideband phase noise is calculated from the frequency noise at the pump power of 170 mW with the phase noise reaching -155 dBc/Hz at 10 MHz. Above 10 MHz, the measured phase noise is limited by OFD noise floor (NFL). . . . .	88
4.17	Large mode volume SBS laser design and operation principles. . . . .	91
4.18	Coil SBS laser single mode lasing. Pump-S1 beatnote spectrum of the SBS laser at 1570 nm on an ESA in spontaneous emission below threshold (blue trace) and stimulated emission above threshold (green trace) demonstrates 73 dB SMSR. Inset shows the Brillouin grating modes at cavity resonances that overlap Brillouin gain spectrum below-threshold (blue trace) and above-threshold (green trace). . . . .	94

4.19	SBS laser output power, frequency noise, and fundamental linewidth. OFD frequency noise measurements for the SBS laser at different pump powers show the minimum fundamental linewidth of 31 mHz, corresponding to a frequency noise of 10 mHz <sup>2</sup> /Hz. At frequency offset above 10 MHz, the OFD frequency noise measurement is limited by a noise floor from the photodetector. Inset shows the SBS laser on-chip power versus on-chip pump power with a threshold of 72 mW and an output power of 41 mW.	95
4.20	Wide-wavelength-range coil SBS laser in C and L band. (a) The SBS phase matching condition is satisfied every ~6 nm, as the Brillouin shift $\Omega_B$ that is linearly proportional to the optical frequency changes by 50 MHz when the pump wavelength changes by ~6 nm around 1570 nm. (b) S1 emission recorded on the OSA reaches a local minimal threshold every ~6 nm in C and L band. $\Omega_B$ , Brillouin shift frequency.	97
5.1	PDH error frequency discrimination slope depends on the modulation depth and resonator coupling.	112
5.2	Block diagram for the PDH laser frequency lock loop.	113
5.3	A numerical simulation for the PDH laser frequency lock loop. (a) Reference tracking frequency response $H(s)$ . (b) Close-loop laser frequency noise contribution from the intrinsic cavity thermo-refractive noise (TRN) in waveguide ring resonators, in-loop residual noise that consists of the residual laser noise, photodetector noise and shot noise.	115
5.4	4-meter coil TM waveguide resonator design and Qs. Reproduced from [36].	117
5.5	1550 nm integrated coil resonator stabilized laser frequency noise, Allan deviation and beatnote frequency drift. (a) OFD (for above 1 kHz offset) and SRL (for below 1 kHz offset) frequency noise measurements for the free-running and coil stabilized laser. (b) Equivalent phase noise is calculated from the frequency noise shown in (a). (c) Allan deviation is estimated based on the SRL heterodyne beatnote signal's frequency recorded by a frequency counter at above 1 ms averaging time; Allan deviation is calculated from the measured OFD frequency noise at below 1 ms averaging time. (d) Beatnote frequency drift for the free-running and the stabilized laser. Reproduced from [36].	118
5.6	Frequency noise of the SRL laser measured by the fiber MZI OFD.	119
5.7	Frequency noise of the 1319 nm freerunning laser and stabilized laser by the 1319 nm 4-meter-coil resonator, measured by the fiber MZI OFD. Reproduced from [36].	120
5.8	Coupling simulation of the directional coupler for the coil resonator using the TE and TM modes at 1319 nm and 1550 nm compared to measured values.	122
5.9	TM mode Q measurement at C and L bands from 1550 nm to 1630 nm of the 1319 nm TM mode 4-meter-coil resonator.	123

5.10	TE mode linewidth and Q measurement from 1550 nm to 1630 nm of the 1319 nm TM mode 4-meter-coil resonator. . . . .	124
5.11	Coupling design for coil resonators of different coil lengths using the 6 $\mu\text{m}$ by 80 nm TE waveguide at 1550 nm. (a) Coupling values needed for 1 MHz coupling rate for 2-m, 4-m, 10-m, and 16-m coil resonators. Simulated directional coupling coefficient by (b) sweeping the coupler gap with $L_x = 1.0$ mm, (c) sweeping $L_x$ at 2.5 $\mu\text{m}$ gap, (d) sweeping $L_x$ at 2.0 $\mu\text{m}$ gap. . . . .	125
5.12	Broadband waveguide loss spectrum of the 6 $\mu\text{m}$ by 80 nm TE <sub>0</sub> waveguide measured in the 4-meter-coil waveguide resonator from 1250 nm to 1650 nm. . . . .	126
5.13	Secondary ion mass spectroscopy of a 4-meter-coil resonator chip sample shows the hydrogen content in the LPCVD nitride layer. . . . .	127
5.14	Hybrid-integrated laser stabilized to a 4-meter-long coil waveguide resonator. (a) PDH locking circuit setup and laser noise measurements. (b) Measured frequency noise spectrum. TRN, thermo-refractive noise. (c) Allan deviation (ADEV). Reproduced from [55]. . . . .	128
5.15	Open-loop frequency response in the PDH feedback lock system shows a 180°-phase-lag frequency of $\sim 200$ kHz. . . . .	129
5.16	10-meter-coil resonator with PM-SMF28 fibers pig-tailed and packaged in a metal enclosure. . . . .	129
5.17	Waveguide loss spectrum of the 6 $\mu\text{m}$ by 80 nm TE <sub>0</sub> waveguide measured in the 10-meter-coil waveguide resonator from 1450 nm to 1630 nm. . . .	130
5.18	Loaded and intrinsic Q measured from the 10-meter-coil waveguide resonator from 1450 nm to 1630 nm. . . . .	131
5.19	Laser stabilization using the packaged 10-meter-coil resonator achieves an $1/\pi$ integral linewidth of 27 Hz and Allan deviation of $1.4 \times 10^{-13}$ at 5.1 ms. . . . .	131
5.20	17-meter-coil resonator design and testing and laser stabilization results. (a) 17-meter coil resonator on 21.6 mm by 26 mm reticle. (b) 249 million intrinsic Q, 115 million loaded Q, and an FSR of 11.2 MHz measured at 1610 nm. (c) Total, intrinsic and coupling linewidths measured from 1550 nm to 1630 nm. (d) Measured intrinsic and loaded Q from 1550 nm to 1630 nm. (e) Measured frequency noise spectrum for the free-running laser and the stabilized laser locked to the 17-meter-coil resonator, . . . . .	133
5.21	Two-point-coupled ultra-high Q resonators for various applications, such as (a) critical-coupled ultra-high Q reference resonators for PDH lock and laser stabilization, (b) over-coupled resonators for increased feedback and output power in self-injection locked lasers, (c) squeezed light generation in over-coupled resonators, (d) multi-wavelength coupling design for efficient OPO processes, and (e) dual-mode coupling. TE, transverse electric. TM, transverse magnetic. SIL, self-injection lock. PDH, Pound-Drever-Hall. OPO, optical parametric oscillation. Reproduced from [59]. . . . .	134

5.22	Two-point coupling working principle. . . . .	135
5.23	Two-point coupled 10-meter-coil resonator. (a) Measured resonator linewidth from 1550 nm to 1630 nm shows resonator coupling tuning with a tuning period of 5.6 nm, and critical coupling from 1550 nm to 1630 nm. (b) The loaded and intrinsic Qs. (c) The under-coupled, critically coupled, and over-coupled resonances. (d) The spectral scan of the critically coupled resonance at 1630 nm. Reproduced from [59]. . . . .	136
5.24	Laser stabilization and frequency noise reduction at multiple critically-coupled wavelengths in the C and L bands. Reproduced from [59]. . . . .	137
5.25	The maximum coupling of a two-point coupler with a coupling length of $L_x = 1.0$ mm is simulated and plotted versus wavelength from 700 nm to 1600 nm at two different coupling gaps, $2.5 \mu\text{m}$ (blue curve) and $0.8 \mu\text{m}$ (green curve), respectively. . . . .	138
5.26	Upper right is the device that is fiber pig-tailed and has a metal tuner on the two-point-coupling phase section which is wire-bonded. From left to right are the spectral scanning measurements of the resonance linewidths and Qs at 780 nm, 910 nm, 1064 nm, 1260 nm, 1320 nm, 1550 nm, 1610 nm. All the resonances are measured while tuning the two-point coupler with the micro-heater. . . . .	139
5.27	The waveguide propagation loss extracted from the resonator linewidth and Q measurements in Fig. 5.26 is shown with a dashed trend line. The loss measured at 780 nm is likely from a higher-order TE mode rather than the fundamental TE mode, due to the coupling roll-off below 800 nm, shown in Fig. 5.25. . . . .	140
5.28	Laser stabilization at 1550 nm and 1320 nm reaches the resonator TRN limit in a single coil resonator that uses a two point coupler that can provide enough coupling for critical coupling from 900 nm to 1600 nm. . . . .	141
5.29	Self-delayed resonator transmission simulations. . . . .	142
5.30	Self-delayed resonator design and testing. Reproduced from [70]. . . . .	143
5.31	Self-delayed resonator for laser stabilization. Reproduced from [70]. . . . .	144
5.32	Waveguide MZI modeling and simulations . . . . .	145
5.33	4-meter-coil Waveguide MZI spectral sweep and ERs from 1550 nm to 1630 nm. (a) Device picture shows the fiber v-groove pig-tailing in a metal package enclosure. (b) Spectral scanning of S11 and S12 at 1550 nm measures the ERs and the FSR to be around 50 MHz. (c) Measured ERs from 1550 nm to 1630 nm. (d) Extracted $\kappa^2$ and $\alpha$ from the measured ERs. . . . .	147
5.34	Comparison between the measured $\kappa^2$ and the simulated values at different waveguide thicknesses. . . . .	148

5.35	15-meter-coil Waveguide MZI spectral sweep and ERs from 1550 nm to 1630 nm. (a) Device picture shows the fiber v-groove pig-tailing in a metal package enclosure. (b) Spectral scanning of S11 and S12 at 1550 nm measures the ERs and the FSR to be around 13.2 MHz. (c) Measured ERs from 1550 nm to 1630 nm. (d) Extracted $\kappa^2$ and $\alpha$ from the measured ERs. . . . .	149
5.36	Waveguide MZI OFD (chip OFD) and fiber MZI OFD measurements of the ULN, SBS lasers and the SLS laser. . . . .	150
5.37	A comparison between all other work and our work in literature using coil resonator approach for laser stabilization and noise reduction. . . . .	152
6.1	Stabilized Brillouin laser chip design and noise reduction principles. . . .	165
6.2	SBS laser with a filter ring resonator to drop the S1 power and filter out the unwanted back-reflected pump with a 23 dB reduction. . . . .	166
6.3	(a) SBS resonator intrinsic and coupling linewidths. (b) S1 on-chip output power from the filter output increases with the on-chip pump power with a threshold of 6 mW. . . . .	166
6.4	The frequency noise of the SBS laser output is being measured by the OFD frequency noise measurement while the feedback power increases. .	167
6.5	Self-delayed 4-meter-coil resonator and the balanced detection of the outputs shows the PDH error signal while the metal heater changes the MZI phase section. . . . .	168
6.6	VNA S12 frequency response measurement of the SBS intensity modulation.	169
6.7	The frequency noise of the coil resonator stabilized SBS laser is measured using a fiber MZI OFD for frequency offsets above 1 kHz and against the stable reference laser below 1 kHz by measuring the frequency noise of the beatnote between the two lasers. (a) The stabilized frequency noise reaches to the coil resonator TRN from 1 kHz to 100 kHz with a locking bandwidth of 1 MHz and yields an integral linewidth of 72 Hz. (b) The Allan deviation of the beatnote between the stabilized laser and stable reference laser reaches $2.8 \times 10^{-13}$ at 5 ms. . . . .	170

# Chapter 1

## Introduction

### 1.1 Background

Integrated photonics is a rapidly advancing field that merges the principles of optics and microelectronics to create compact, efficient, and scalable photonic devices. By enabling the manipulation of light at microscopic scales, integrated photonics combines the advantages of optical systems, such as high speed and low loss, with the scalability and integration capabilities of modern electronics. This interdisciplinary field has emerged as a critical enabler for next-generation technologies, addressing the increasing demand for high-performance communication, sensing, and computational systems. The rise of integrated photonics has been driven by the convergence of technological trends and market demands. The exponential growth of data traffic, driven by global internet usage and data-intensive applications, is outpacing the capabilities of traditional electronic systems. At the same time, advances in fabrication techniques and material science have made it possible to design photonic devices that are not only efficient but also highly scalable. As a result, integrated photonics has become a cornerstone for fields ranging from high-speed data communication to precision sensing and imaging, as well

as emerging areas such as quantum technologies.

Traditional optical systems, which rely on discrete bulk components such as lenses, mirrors, and beam splitters, face limitations in size, cost, and performance scalability. These systems are often bulky, fragile, and require extensive alignment, preventing them from being widely accessible for many modern applications. The advent of photonic integrated circuit (PIC) technologies has revolutionized optical systems by integrating multiple optical functions into a single, compact chip. Leveraging materials such as silicon, indium phosphide, and silicon nitride, integrated photonics achieves high levels of functionality while maintaining a form factor that is orders of magnitude smaller than traditional optical setups. This miniaturization and integration also results in enhanced reliability and the potential for mass production, further reducing costs and enabling widespread adoption.

The rapid development of integrated photonics has been fueled by advancements in complementary metal-oxide-semiconductor (CMOS) technology, which provides a mature and cost-effective manufacturing framework. CMOS fabrication technology, originally developed for electronic circuits, offers a well-established and highly scalable process for creating photonic devices. Using advanced lithography and deposition techniques, CMOS allows precise patterning and layering of materials at nanometer scales. This precision is critical for defining waveguides, modulators, and other photonic structures with minimal losses. In addition, CMOS technology enables mass production, significantly lowering the cost per device and facilitating the integration of photonics with electronics on the same chip. The compatibility with existing semiconductor foundries further accelerates innovation and deployment in this field. As a result, integrated photonics is increasingly being adopted in diverse applications, including telecommunications, data centers, medical diagnostics, environmental monitoring, and advanced computing.

Silicon nitride has emerged as a highly versatile and widely adopted material platform

for waveguide-based photonic devices, among the various material platforms in integrated photonics. Silicon nitride waveguides are celebrated for their exceptional optical properties, which include a wide transparency window spanning from visible to mid-infrared wavelengths (400 nm to 2500 nm) and a low propagation loss.

There are several key distinct advantages of the silicon nitride photonics platform. First, its compatibility with standard CMOS fabrication processes enables the integration of silicon nitride photonic devices with electronic circuitry, paving the way for complex systems-on-chip. Advances in fabrication techniques, such as low-pressure chemical vapor deposition (LPCVD), have enabled the production of silicon nitride films with excellent uniformity and low stress, ensuring high-quality devices. Second, the high refractive index contrast of silicon nitride allows for tight light confinement, enabling compact and densely packed waveguide structures without significant loss of performance. Third, the thermal and mechanical stability of silicon nitride also contributes to its appeal. Silicon nitride waveguides are highly resistant to thermal fluctuations and can operate reliably in demanding environments, making them suitable for applications in aerospace, industrial sensing, and medical diagnostics. Fourth, silicon nitride waveguide platforms have also found a niche in nonlinear optics due to their high optical damage threshold and nonlinear coefficients. These properties are exploited in applications such as frequency comb generation, supercontinuum generation, and optical parametric oscillation. Fifth, the ultra-low loss and weak mode confinement and non-acoustic guiding properties of the silicon nitride waveguides enable key advantages to robust Brillouin scattering and lasing, and enable Brillouin laser resonator cavities of arbitrary geometry (e.g. coils). Sixth, the large mode volume of long coil silicon nitride waveguide resonators enables high power handling as well as simple bus-to-resonator coupling design and tunability that are difficult to do in strongly confined waveguide platforms. Other advantages of the weak mode confinement are lowered susceptibility to packaging epoxies and techniques



for fiber coupling as well as better mode matching to the fiber mode. As a result, silicon nitride is increasingly recognized as a cornerstone material for the next generation of photonic integrated circuits.

## 1.2 Accomplishments in this thesis

The work in this thesis represents a significant advancement in the state of the art of the silicon nitride photonics platform and also shows what is possible for the field of integrated photonics, with the following accomplishments.

- The lowest waveguide propagation loss has been demonstrated in silicon nitride waveguides to date, 0.034 dB/m loss in C and L band wavelengths, corresponding to 720 million intrinsic waveguide resonator  $Q_s$ , highest  $Q_s$  to date for integrated waveguide resonator devices [1].
- Chip-scale photonic integrated coil waveguide reference resonators with a 2 cm by 2 cm footprint size with a resonator waveguide round-trip length of 17 meters long and 200-300 million intrinsic  $Q_s$  are fabricated on an 8-inch silicon wafer, the longest waveguide resonator ever demonstrated to date.
- Laser stabilization using the silicon nitride waveguide based coil waveguide reference resonators achieves a total integral laser linewidth of 30 Hz, the lowest reported to date [2].
- The stimulated Brillouin scattering laser based on the large mode volume coil waveguide resonator achieves 40 mW output power and 30 mHz fundamental linewidth, the lowest fundamental linewidth to date for all lasers.

## 1.3 Thesis outline

This thesis focuses on the development of low-noise and narrow-linewidth integrated semiconductor lasers based on low-loss silicon nitride waveguide resonator devices.

Chapter 2 describes the low-loss silicon nitride waveguide design, fabrication, and testing, and the design bus-waveguide-coupled waveguide resonators, and exploits the limits from different loss mechanism such as scattering loss and absorption loss by experimentally and quantitatively measuring the absorption loss and rigorously modeling the roughness-induced scattering loss.

Chapter 3 starts with a brief introduction of frequency and time standards and a variety of low-noise and stable microwave and optical oscillators, and then touches on a few fundamental noise and instability processes as consequences of quantum-mechanical and thermal-dynamic fluctuations, and discusses the approaches to mitigate such noise processes and how to reliably measure and characterize the laser frequency noise and linewidth.

Chapter 4 focuses on the narrow fundamental linewidth stimulated Brillouin scattering laser based on the low-loss silicon nitride waveguide resonators from its physics and modeling to design and testing.

Chapter 5 dives into the long coil silicon nitride waveguide resonators as low-noise and high-Q reference resonators for semiconductor lasers to reference to by frequency locking to achieve low frequency and phase noise at low frequency offsets and narrow total integral laser linewidths.

Chapter 6 describes the effort to integrate the narrow fundamental linewidth Brillouin laser and a low-noise high-Q coil waveguide reference resonator on the same chip to realize a chip-scale laser with a narrow fundamental linewidth and narrow integral linewidth.

## Bibliography

- [1] K. Liu, N. Jin, H. Cheng, N. Chauhan, M. W. Puckett, K. D. Nelson, R. O. Behunin, P. T. Rakich, and D. J. Blumenthal, *Ultralow 0.034 dB/m loss wafer-scale integrated photonics realizing 720 million  $Q$  and 380  $\mu$ W threshold Brillouin lasing*, *Optics letters* **47** (2022), no. 7 1855–1858.
- [2] K. Liu, N. Chauhan, J. Wang, A. Isichenko, G. M. Brodnik, P. A. Morton, R. O. Behunin, S. B. Papp, and D. J. Blumenthal, *36 Hz integral linewidth laser based on a photonic integrated 4.0 m coil resonator*, *Optica* **9** (2022), no. 7 770–775.

# Chapter 2

## Ultra-low-loss silicon nitride waveguides

The pursuit of ultra-low light propagation loss in confined optical waveguide structures has started since Charles K. Kao proposed in 1966 that the optical fiber propagation loss can reach below 20 dB/km if the silica material could be further purified when at that time the common loss of optical fibers was on the order of 1,000 dB/km [1] and in 1970 Corning Glass Works first demonstrated a fiber with 20 dB/km [2]. Soon in 1978, NTT reported the optical fiber propagation loss of 0.2 dB/km at 1550 nm, and as of 2024 the lowest propagation loss in Corning-manufactured optical fibers is 0.17 dB/km, which has only been reduced by less than 0.05 dB/km, shown in Fig. 2.1 [3, 4]. Only recently has a hollow core DNANF fiber been reported with a record low 0.08 dB/km propagation loss [5].

Inspired by the ultra-low propagation loss of optical fibers, the pursuit of light propagation loss in nano-fabricated photonic integrated waveguides is never ending, either. The predominant material platforms for photonic integrated waveguides and circuits include indium phosphide (InP) [6], AlGaAs [7], silicon on insulator (SOI) [8, 9], thin-film lithium

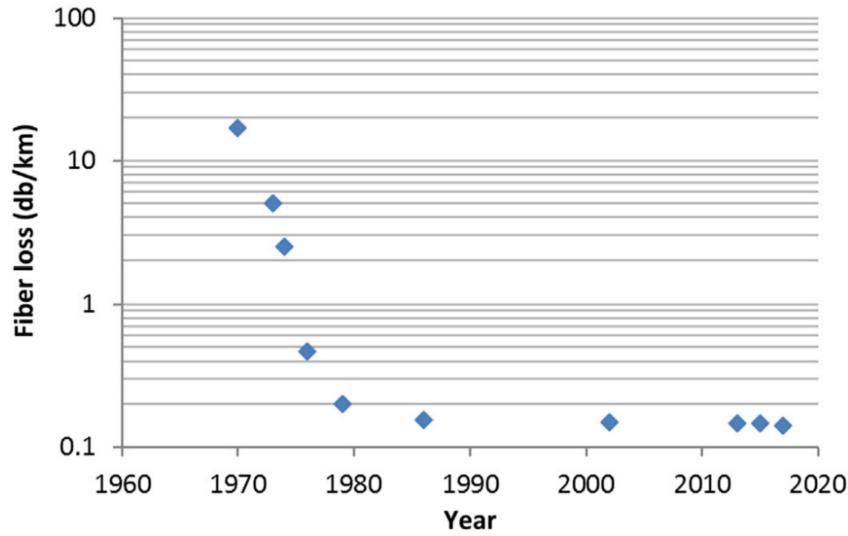


Figure 2.1: Optical fiber loss evolution over the last fifty years since 1970 has seen great advancement [4]. The propagation loss at 1550 nm in best single mode fibers reaches the material limit around 0.17 dB/m and has only decreased by less than 0.05 dB/m since 1980. @ SicenceDirect Publishing

niobate (TFLN) [10, 11], silicon nitride ( $\text{Si}_3\text{N}_4$ ) [12, 13, 14, 15, 16]. There is a general trade-off between the waveguide propagation loss and the waveguide bending radius that holds for almost all different waveguides that a more confined waveguide suffers from larger waveguide surface roughness induced scattering loss but can have a much smaller bending radius due to higher waveguide mode confinement [17, 18]. In thick nitride waveguides, photonic Damascene process that employs a reflow step to reduce roughness at the interface between silicon nitride and lower thermal oxide cladding achieves waveguide loss below 1 dB/m and anomalous group velocity dispersion at the same time [12]. The high-aspect ratio silicon nitride waveguide design with a low-confinement dilute waveguide mode profile reduces the scattering loss from the waveguide surface roughness while compromising the waveguide bending radius which reaches 1~10 mm, achieving 0.034 dB/m waveguide loss in the C and L band and up to 720 million intrinsic Q factors in waveguide ring resonators, shown in Fig. 2.2 [19, 15, 14, 16].

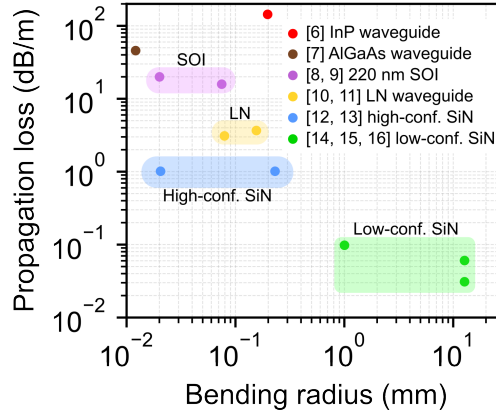


Figure 2.2: Photonic integrated waveguide propagation loss using different material waveguide platforms such as InP [6], AlGaAs [7], 220 nm SOI [8, 9], TFLN [10, 11], thick-core and high-confinement  $\text{Si}_3\text{N}_4$  [12, 13], and thin-core and low-confinement  $\text{Si}_3\text{N}_4$  [14, 15, 16]

## 2.1 Waveguide resonator linewidth and Q factor

### 2.1.1 Resonator-oriented modeling approach

A popular modeling approach that researchers commonly use to model a waveguide microring resonator or a multiple-coupled ring device described in detail in [20, 21] starts from the physical parameters of the device such as the directional coupler's coupling coefficient  $\kappa^2$ , shown in Fig. 2.3, which is referred to as a *primitive parameter modeling approach*. The advantage of this approach is that the ring resonator response is directly linked to its physical parameters, which is also its disadvantage that its analytical expressions are usually complicated and makes it hard for both practical modeling and experimental analysis and physical intuition development. This will become clearer in later discussion sections. One simple example is the through-port response of an add-through ring resonator given by,

$$\frac{E_{thru}}{E_{in}} = \frac{\sqrt{A} - \tau e^{i\phi_{rt}}}{\sqrt{A}\tau - e^{i\phi_{rt}}}, \quad (2.1)$$

where  $\tau$  is the straight-through coupling coefficient of the optical field at the evanescent bus-ring coupler;  $\phi_{rt}$  and  $A = \exp(-\alpha L)$  are the round-trip optical phase and power attenuation, respectively. Here,  $\alpha$  is the propagation loss coefficient in  $[1/m]$  and  $L = 2\pi r$  is the round-trip length of the ring resonator.

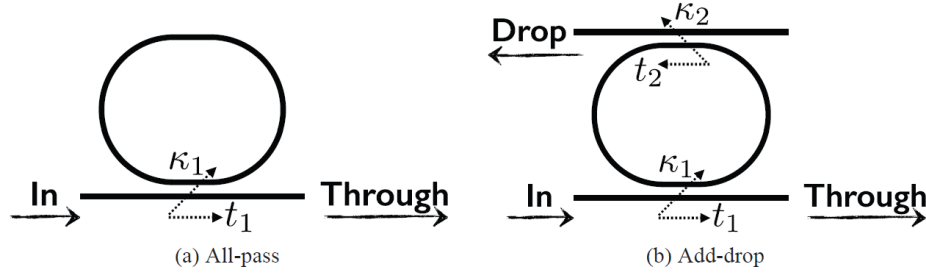


Figure 2.3: Waveguide ring resonator with the add-through and add-drop configurations (Fig. 4.27 in [21]).

In the case of an ultra-high Q ring resonator where the round-trip attenuation is very small and so is required for the bus-ring coupling coefficient  $\kappa^2 = 1 - \tau^2 \ll 1$ , Eq. 2.1 can be simplified to,

$$\frac{E_{thru}}{E_{in}} \simeq \frac{1 - e^{i\phi_{rt}} + \kappa^2/2 - \alpha L/2}{1 - e^{i\phi_{rt}} - \kappa^2/2 - \alpha L/2}. \quad (2.2)$$

Since  $\kappa^2, \alpha L \ll 1$  and the spectral response is of most interests at the slight detuning regime around the resonances, namely,  $\phi_{tr} = 2\pi m + \Delta\phi$ , it can be further simplified to,

$$\frac{E_{thru}}{E_{in}} \simeq \frac{i\Delta\phi + \alpha L/2 - \kappa^2/2}{i\Delta\phi + \kappa^2/2 + \alpha L/2}, \quad (2.3)$$

which is, not surprisingly, a Lorentzian lineshape with a total full-width-half-maximum (FWHM) of  $\Delta\phi_{FWHM} = \kappa^2 + \alpha L$ . Here, Eq. 2.3 reveals intuitive characteristics of a high-Q waveguide ring resonator spectral transmission: (1) Finesse can be expressed as  $\mathcal{F} = 2\pi/(\kappa^2 + \alpha L)$ ; (2) The ring resonator is critically coupled and has maximum contrast at  $\kappa^2 = \alpha L$ ; (3) With the free spectral range (FSR) being expressed as  $\nu_{FSR} = c/n_g L$ , the resonator linewidth in terms of optical frequency can be found as  $\Delta\nu_{FWHM} = \frac{1}{2\pi} \left( \frac{\kappa^2 c}{n_g L} + \right.$

$\frac{\alpha c}{n_g}$ ), where the intrinsic linewidth is  $\Delta\nu_{in} = \frac{1}{2\pi} \frac{\alpha c}{n_g}$  and the external coupling linewidth is  $\Delta\nu_{ex} = \frac{1}{2\pi} \frac{\kappa^2 c}{n_g L}$ . Fig. 2.4 shows a calculated curve using Eq. 2.2 or 2.3 which can be readily mapped to an actual experimental spectral transmission of a high-Q ring resonator.

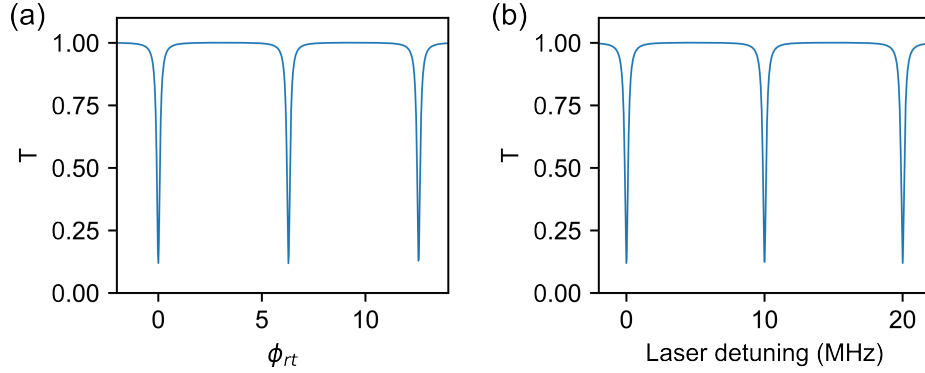


Figure 2.4: Add-drop ring resonator spectral transmission. (a) shows a curve calculated by Eq. 2.2 or 2.3. (b) shows how (a) can be readily mapped to an actual experimental spectral sweep of an ultra-high-Q ring resonator.

As can be seen in the derivations of Eq. 2.1-2.3, instead of treating a waveguide ring resonator as a *ring* structure, treating it and modeling it as a *resonator* (A) simplifies the analytical expression (for example, the Lorentzian lineshape of Eq. 2.3), (B) and provides a straightforward connection between the ring resonator physical parameters such as  $\alpha L$  and  $\kappa^2$  and the spectral characteristics such as  $\mathcal{F}$  and  $\Delta\nu_{FWHM}$ . **For this reason, this dissertation adopts a resonator-oriented modeling approach, rather than the primitive-parameter modeling approach.** One might argue that such an approach seems phenomenological. However, the fact that the *resonator* picture of viewing a single ring resonator and even coupled-ring resonators is so powerful in agreeing with experimental measurements and a ring structure makes an optical resonant structure could indicate that the resonator picture is also quite fundamental. A good example is circuit quantum electrodynamics [22] that models the superconducting transmon qubit circuit which consists of lumped and distributed capacitors and inductors to construct LC microwave resonators as quantum harmonic oscillators, where modeling the electric-magnetic field



in the LC resonators using microwave photon mode in the quantum harmonic oscillator picture is quite powerful and can be more fundamental than an electric-magnetic field picture.

### 2.1.2 Coupled-mode theory (CMT) for add-through ring resonator

The *resonator-oriented modeling approach* focuses on different aspects of the waveguide ring resonator. Such a formalism or approach is widely used in the field of quantum optics that is referred to as the input-output formalism [22, 23, 24], where the central focus is on the quantum bosonic oscillator mode,  $a$ ,

$$\dot{a} = (i\omega - \gamma/2)a + i\sqrt{\gamma_{ex}}s_{in}, \quad (2.4)$$

where  $N = |a|^2$  represents the photon number,  $\omega$  is the oscillator resonant frequency,  $\gamma$  is the oscillator loss rate due to environmental interaction and coupling,  $s_{in}$  is the input field through external channel coupling  $\gamma_{ex}$ . The formalism represented by Eq. 2.4 in waveguide optics is also called coupled-mode theory (CMT) [25, 26], on which much of the details can be found in these references [22, 23, 25, 26, 27].

In a single bus waveguide coupled ring resonator, the bus-ring coupler has a coupling coefficient of  $\kappa^2$ , and the power coupling illustrated in Fig. 2.5 is similar to that of a beamsplitter and describe by,

$$\begin{pmatrix} b_1 \\ b_2 \end{pmatrix} = \begin{pmatrix} \tau & i\kappa \\ i\kappa & \tau \end{pmatrix} \begin{pmatrix} a_1 \\ a_2 \end{pmatrix}, \quad (2.5)$$

where  $\kappa^2 = 1 - \tau^2$  is the coupling coefficient. And the CMT formalism for the add-through

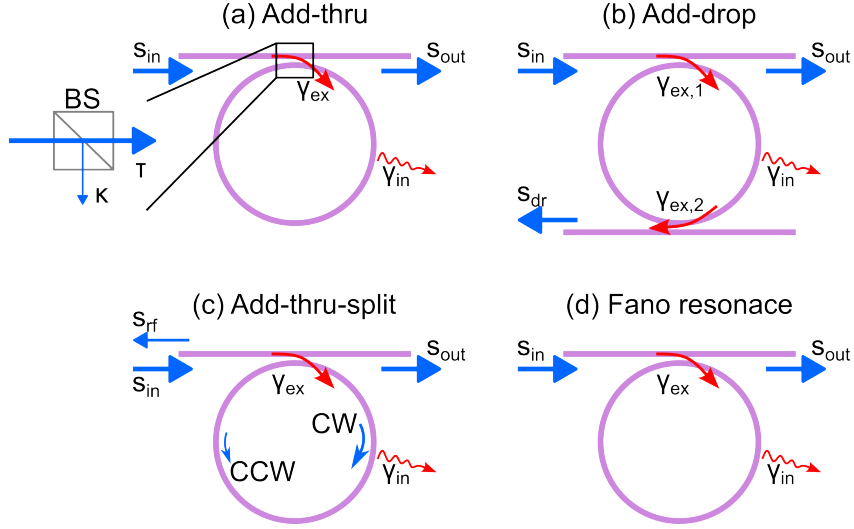


Figure 2.5: CMT picture of waveguide ring resonators. Add-through and add-drop ring resonator illustration with intrinsic loss rate and external coupling loss rate.

single-bus-coupled ring resonator around a resonant mode  $\omega$  is as follows,

$$\dot{a} = (i\omega - \gamma/2)a + i\sqrt{\gamma_{ex}}s_{in}, \quad (2.6)$$

$$s_{out} = \tau s_{in} + i\sqrt{\gamma_{ex}}a, \quad (2.7)$$

where  $a$  is the mode field intensity ( $N = |a|^2$  is the photon number in the optical mode),  $|s_{in}| = \sqrt{P_{opt}/h\nu_{opt}}$  is the optical influx in the bus waveguide in  $[1/\sqrt{Hz}]$ ,  $\gamma_{ex} = c\kappa^2/n_g L$  is the external bus coupling rate,  $\gamma = \gamma_{in} + \gamma_{ex}$  is the total loss rate. In ultra-low-loss waveguide resonators with  $Q$  up to 100 million and ring radii of the order of 1 mm, the bus-ring coupling coefficient is very small,  $\kappa \ll 1$ , or  $\tau \simeq 1$ . For the remainder of the treatment, we assume  $\tau = 1$  for Eq. 2.7 to simplify the analysis and Eq. 2.7 to  $s_{out} = s_{in} + i\sqrt{\gamma_{ex}}a$ . Using rotating wave approximation (RWA) and the replacement of

$s_{in} \rightarrow s_{in}e^{i\omega_{in}t}$   $a \rightarrow ae^{i\omega_{in}t}$ , we find,

$$\dot{a} = (i\Delta\omega - \gamma/2)a + i\sqrt{\gamma_{ex}}s_{in}, \quad (2.8)$$

$$s_{out} = s_{in} + i\sqrt{\gamma_{ex}}a, \quad (2.9)$$

where  $\Delta\omega = \omega - \omega_{in}$  is the input laser detuning from the resonant frequency. The static detuning spectral transmission can be then found by setting  $\dot{a} = 0$ ,

$$T = \left| \frac{s_{out}}{s_{in}} \right|^2 = \left| \frac{i\Delta\omega + (\gamma_{in} - \gamma_{ex})/2}{i\Delta\omega + (\gamma_{in} + \gamma_{ex})/2} \right|^2, \quad (2.10)$$

$$D = \left| \frac{\sqrt{\gamma_{in}}a}{s_{in}} \right|^2 = \frac{\gamma_{in}\gamma_{ex}}{|i\Delta\omega + (\gamma_{in} + \gamma_{ex})/2|^2}, \quad (2.11)$$

where  $T$  is the power-normalized transmission out of the through port of the bus waveguide, and  $D$  is the power-normalized dissipation in the ring resonator due to waveguide propagation loss. It can also be verified that  $T + D = 1$ . Eq. 2.10 is equivalent to Eq. 2.3 and can be converted to it by setting  $\Delta\phi = \Delta\omega/\nu_{FSR}$ . Eq. 2.10 is a Lorentzian lineshape with the FWHM linewidth equal to the resonator total loss rate,  $\Delta\nu_{FWHM} = \gamma$ , and therefore, the external, intrinsic, and loaded Q factors are expressed as,

$$Q_{ex} = \frac{\omega}{\gamma_{ex}}, \quad (2.12)$$

$$Q_{in} = \frac{\omega}{\gamma_{in}}, \quad (2.13)$$

$$Q_L = \frac{\omega}{\Delta\nu_{FWHM}} = \frac{\omega}{\gamma}. \quad (2.14)$$

As an example, the calculated transmission curve using  $\gamma_{in}/2\pi = 2$  MHz and  $\gamma_{ex}/2\pi = 1$  MHz is shown in Fig. 2.6.

Other important and useful formulas include the calculation of the FSR, external

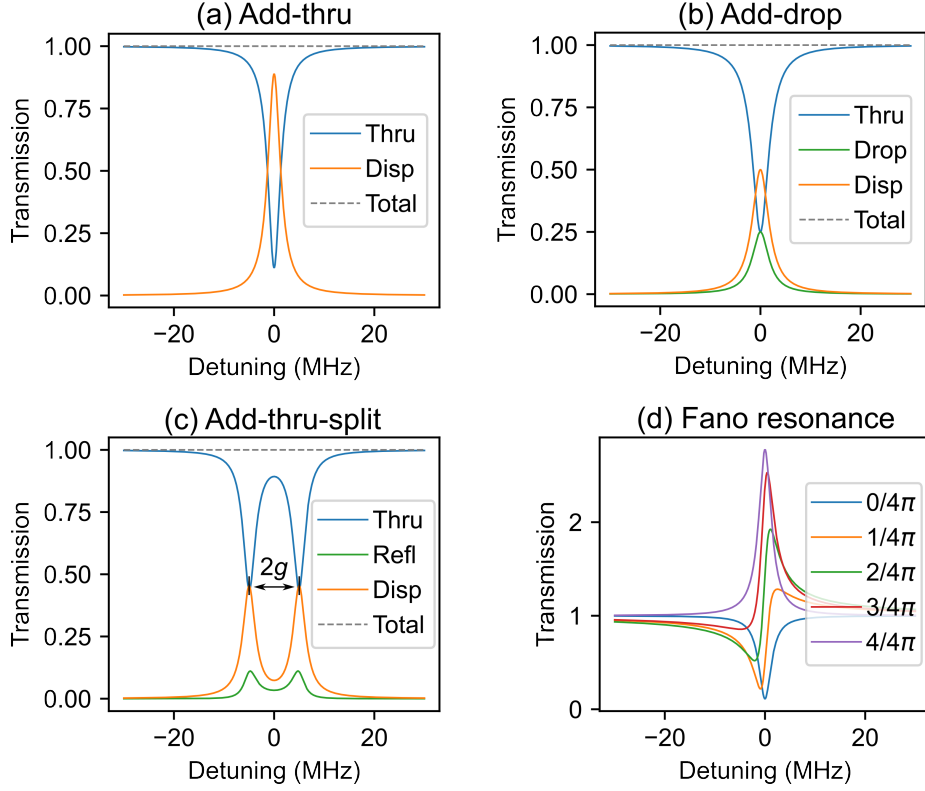


Figure 2.6: Waveguide ring resonator simulations under different configurations such as (a) add-through, (b) add-drop, (c) add-through with CW-CCW mode coupling and resonance splitting, and (d) add-through with Fano resonance effect.

coupling loss rate, and intrinsic loss rate as follows:

$$\nu_{FSR} = \frac{c}{n_g L} = \frac{1}{\tau_{FSR}}, \quad (2.15)$$

$$\gamma_{ex} = \frac{\kappa^2 c}{n_g L} = \frac{\kappa^2}{\tau_{FSR}}, \quad (2.16)$$

$$\gamma_{in} = \frac{\alpha c}{n_g} = \frac{\alpha L}{\tau_{FSR}}. \quad (2.17)$$

Note that  $\gamma_{ex} = \kappa^2 c / n_g L$  is an approximated expression from

$$\gamma_{ex} = \frac{\log(1/\tau^2)c}{n_g L}, \quad (2.18)$$

when  $\kappa^2 \ll 1$ , where  $\alpha_{mir} = \log(1/\tau^2)/L$  is also referred to as *mirror loss*.

The intrinsic Q factor calculation using

$$Q_{in} = \frac{\omega}{\gamma_{in}} = \frac{\omega n_g}{\alpha c} \quad (2.19)$$

is a function of only the waveguide propagation loss  $\alpha$ . The waveguide ring resonator Finesse calculation using

$$\mathcal{F} = \frac{2\pi}{\alpha L + \kappa^2} \quad (2.20)$$

shows that the Finesse  $\mathcal{F}$  is a function of the total round-trip loss in a waveguide ring resonator,  $\alpha L + \kappa^2$ , which corresponds to the total mirror loss in a two-mirror Fabry–Pérot cavity. It is useful to compare the waveguide ring resonator with the Fabry–Pérot cavity, and the difference is subtle but quite clear. In a Fabry–Pérot cavity, mirror loss (or reflectivity) is the fundamental physical parameter that directly determines cavity Finesse  $\mathcal{F}$ , while the cavity linewidth and the Q factor depend on mirror loss and cavity length. In a waveguide ring resonator it is the opposite and the waveguide loss  $\alpha$  is the fundamental parameter that directly determines the ring resonator linewidth and Q factor while the Finesse  $\mathcal{F}$  depend on both the waveguide loss and the ring resonator circumference. Since the waveguide loss and resonator linewidth are the fundamental physical parameters for the waveguide resonator, it is useful to consider the numerical estimation of the resonator intrinsic linewidth,

$$\gamma_{in}/2\pi = 7.32 MHz \frac{\alpha_{dB/m}/[1dB/m]}{n_g/[1.50]}. \quad (2.21)$$

### 2.1.3 Add-drop ring resonator

As illustrated in Fig. 2.5(b), there are two bus coupling channels with two coupling rates,  $\gamma_{ex,1}$  and  $\gamma_{ex,2}$ , and similar to the formulation of Eq. 2.9, the CMT equations for

an add-drop ring resonator can be formulated as follows,

$$\dot{a} = (i\Delta\omega - \gamma/2)a + i\sqrt{\gamma_{ex,1}}s_{in}, \quad (2.22)$$

$$s_{out} = s_{in} + i\sqrt{\gamma_{ex,1}}a, \quad (2.23)$$

$$s_{dr} = i\sqrt{\gamma_{ex,2}}a \quad (2.24)$$

where  $\gamma = \gamma_{in} + \gamma_{ex,1} + \gamma_{ex,2}$ . The static spectral scanning transmission in all the through, drop and intrinsic loss channels can be found,

$$T_{th} = \left| \frac{s_{out}}{s_{in}} \right|^2 = \left| \frac{i\Delta\omega + (\gamma_{in} + \gamma_{ex,2} - \gamma_{ex,1})/2}{i\Delta\omega + \gamma/2} \right|^2, \quad (2.25)$$

$$T_{dr} = \left| \frac{s_{dr}}{s_{in}} \right|^2 = \frac{\gamma_{ex,2}\gamma_{ex,1}}{|i\Delta\omega + \gamma/2|^2}, \quad (2.26)$$

$$D = \left| \frac{\sqrt{\gamma_{in}}a}{s_{in}} \right|^2 = \frac{\gamma_{in}\gamma_{ex,1}}{|i\Delta\omega + \gamma/2|^2}. \quad (2.27)$$

$T_{th} + T_{dr} + D = 1$  can be verified. If the drop port coupling channel is viewed as a loss channel and merged with the intrinsic loss channel,  $\gamma_{ex,2} + \gamma_{in} \rightarrow \gamma_{in}$ , the CMT model of an add-drop ring becomes that of an add-through ring resonator (Eq. 2.9 - 2.11), showing the self-coherence of the CMT modeling approach. As an example, Fig. 2.6(b) shows the calculated transmission of the through and drop ports of an add-drop ring resonator.

#### 2.1.4 CW-CCW coupling and mode splitting

Resonance splitting, or mode splitting, is commonly observed in waveguide ring resonator, which is induced spontaneously by the waveguide surface roughness that couples the light in the forward and backward propagation modes, also referred to as clockwise (CW) and counter-clockwise (CCW) modes, or intentionally by periodic grating struc-

tures along the ring resonator waveguide, shown in Fig. 2.5(c). similar to loss rates, the CW-CCW coupling strength is described by a coupling rate,  $g$ , which is used in the CMT equations as follows,

$$\dot{a}_1 = (i\Delta\omega - \gamma/2)a_1 + iga_2 + i\sqrt{\gamma_{ex}}s_{in}, \quad (2.28)$$

$$\dot{a}_2 = (i\Delta\omega - \gamma/2)a_2 + iga_1, \quad (2.29)$$

$$s_{out} = s_{in} + i\sqrt{\gamma_{ex}}a_1, \quad (2.30)$$

$$s_{rf} = i\sqrt{\gamma_{ex}}a_2, \quad (2.31)$$

where  $a_1$  and  $a_2$  are the CW and CCW modes, respectively. There are a few assumptions here to simplify the modeling process by having fewer number of parameters: The CW and CCW modes are assumed with the same resonance frequency  $\omega$  and the same intrinsic and external loss rates. If necessary, the assumptions can be eliminated by introducing more degrees of freedom such as different resonant frequencies,  $\omega_1$  and  $\omega_2$ . By setting  $\dot{a}_1 = \dot{a}_2 = 0$ , the static spectral transmissions such as the through port transmission  $T_{th} = |s_{out}/s_{in}|^2$ , the add port reflection  $T_{rf} = |s_{rf}/s_{in}|^2$ , and the internal ring dissipation  $D = \gamma_{in}(|a_1|^2 + |a_2|^2)/|s_{in}|^2$ . Calculated from Eq. 2.31, the resonance mode splitting can be found to be  $2g$ . In the case where the resonance splitting is induced by the waveguide surface roughness, the splitting can be buried by the resonance linewidth if  $2g < \gamma$ . Ring resonators with very high Q factors and narrow linewidths on the order of MHz have a greater chance to resolve and observe the resonance splitting in the spectral scanning characterization measurements [15, 14]. An illustrative curve simulated using Eq. 2.31 is shown in Fig. 2.6(c).

### 2.1.5 Fano resonance

Fano resonance occurs in a ring resonator where the input field in the bus waveguide gets a phase shift,  $\phi_{fano}$ , and causes interference in the through port, illustrated in Fig. 2.5(d). The CMT modeling approach makes this easy, as shown below,

$$\dot{a} = (i\Delta\omega - \gamma/2)a + i\sqrt{\gamma_{ex}}s_{in}, \quad (2.32)$$

$$s_{out} = s_{in}e^{i\phi_{fano}} + i\sqrt{\gamma_{ex}}a. \quad (2.33)$$

The transmission can be found,

$$T = \left| \frac{s_{out}}{s_{in}} \right|^2 = \left| e^{i\phi_{fano}} - \frac{\gamma_{ex}}{i\Delta\omega + \gamma/2} \right|^2. \quad (2.34)$$

Note that in Fig. 2.5(d) the maximum exceeds 1 and the model above for Fano resonance can be normalized with respect to the maximum to comply with the law of energy conservation.

## 2.2 High-aspect-ratio silicon nitride waveguides

### 2.2.1 Design considerations: waveguide modes, bending radius, bus-waveguide tapering

Propagation loss is one of the most important metric for photonic integrated waveguide designs, which is described by a distributed and optical power exponential decaying process,

$$P(z) = P_0e^{-\alpha z}, \quad (2.35)$$



where  $\alpha$  is the waveguide propagation loss coefficient in  $m^{-1}$ . It directly determines the intrinsic Q factor of the waveguide ring resonator shown in Eq. 2.14 and 2.17,  $Q_{in} = \omega n_g / \alpha c$ . The propagation loss in dB/m is expressed as,

$$\alpha[dB/m] = 10 \log_{10}(e)\alpha \approx 4.343\alpha[1/m]. \quad (2.36)$$

In addition to propagation loss, there are some other important aspects to take into consideration in waveguide designs including critical or minimal bending radius (Fig. 2.7), how many waveguide modes it supports (single mode vs. multiple mode, Fig. 2.8(a) for 40 nm thick waveguide, 2.9(a) for 80 nm thick waveguide), how well the waveguide at different tapered widths matches the fiber mode for edge coupling (Fig. 2.8(b) for 40 nm thick waveguide, 2.9(b) for 80 nm thick waveguide), etc. Waveguide mode simulations using Lumerical MODE or Tidy3D can yield useful information on the aforementioned aspects. The material refractive indices at 1550 nm are 1.444 for lower cladding thermal oxide, 1.453 for upper cladding TEOS-PECVD oxide, and 1.936 for LPCVD silicon nitride [28].

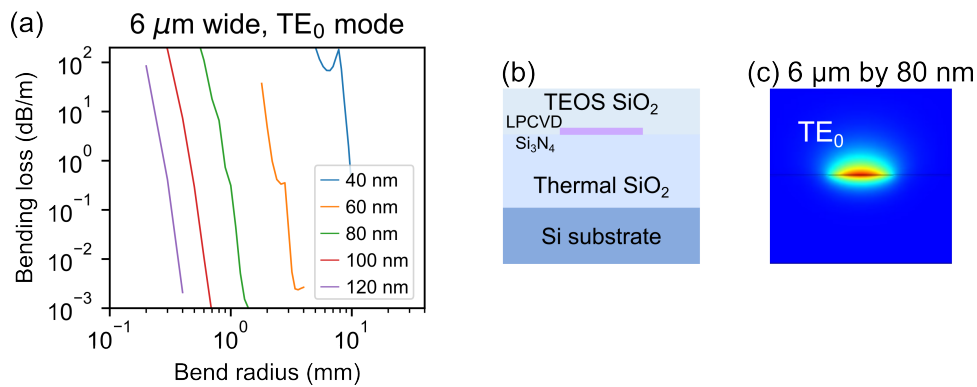


Figure 2.7: Waveguide design considerations. (a) Bending loss simulation in a 6  $\mu$  wide silicon nitride waveguide at different thicknesses, from 40 nm to 120 nm. (b) High-aspect-ratio waveguide design illustration with thermal oxide as lower cladding and TEOS-PECVD silicon dioxide as upper cladding. (c) Electric field magnitude for the fundamental TE mode in a 6  $\mu$  by 80 nm waveguide.

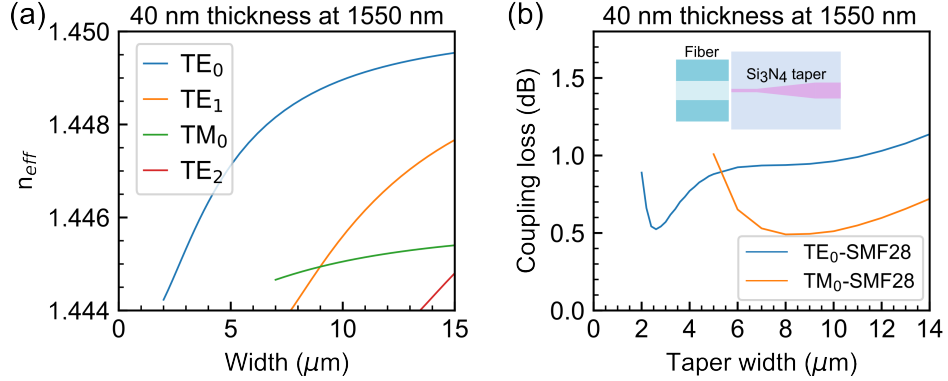


Figure 2.8: Waveguide design considerations. (a) Fiber-to-waveguide coupling loss between the fundamental TE mode in an 80 nm thick waveguide tapered at different widths and different types of fibers such as SMF-28, UHNA1 (4.8  $\mu\text{m}$  MFD), and UHNA3 (4.1  $\mu\text{m}$  MFD) fibers at the wavelength of 1550 nm. (b) The effective indices of all supported waveguide modes in an 80 nm thick waveguide at different widths.

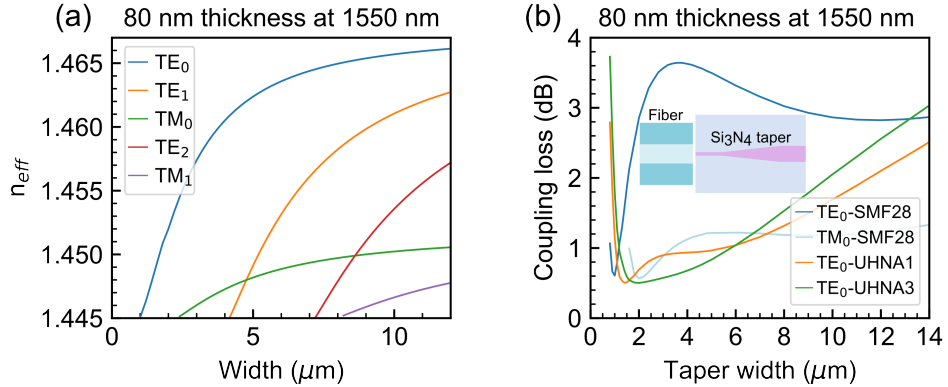


Figure 2.9: Waveguide design considerations. (a) Fiber-to-waveguide coupling loss between the fundamental TE mode in an 80 nm thick waveguide tapered at different widths and different types of fibers such as SMF-28, UHNA1 (4.8  $\mu\text{m}$  MFD), and UHNA3 (4.1  $\mu\text{m}$  MFD) fibers at the wavelength of 1550 nm. (b) The effective indices of all supported waveguide modes in an 80 nm thick waveguide at different widths.

## 2.2.2 TE waveguide resonators: 0.060 dB/m and 422 million Q

Here, we demonstrate a very high-aspect-ratio silicon nitride waveguide design that achieves 0.060 dB/m waveguide loss and 422 million intrinsic Q in C and L band using the fundamental transverse electric ( $\text{TE}_0$ ) mode and 0.034 dB/m waveguide loss and 720 million intrinsic Q in C and L band using transverse magnetic ( $\text{TM}_0$ ) mode. The

waveguide dimension is  $11\ \mu\text{m}$  wide by  $40\ \text{nm}$  thick design for the ultra-high  $Q$  silicon nitride waveguide ring resonator uses a waveguide geometry of  $11\ \mu\text{m}$  by  $40\ \text{nm}$ , a bus-ring coupling gap of  $6.898\ \mu\text{m}$  for slight under-coupling, and a ring radius of  $11.787\ \text{nm}$ . Although such a design is a multimode waveguide, higher order modes have high bending loss, resulting in a quasi-single mode ring resonator [15].

The fabrication process is as follows, illustrated in Fig. 2.10. The substrate and lower cladding consist of a  $15\text{-}\mu\text{m}$ -thick thermal oxide grown on a  $200\text{-mm}$  diameter silicon wafer. The main waveguide layer is a  $40\text{-nm}$ -thick stoichiometric silicon nitride film deposited on the lower cladding thermal oxide using low-pressure chemical vapor deposition (LPCVD). A standard deep ultraviolet (DUV) photoresist layer was spun and then patterned using a DUV stepper. The high-aspect-ratio waveguide core is formed by anisotropically dry etching the silicon nitride film in an inductively coupled plasma etcher using  $\text{CHF}_3/\text{CF}_4/\text{O}_2$  chemistry. Following the etch, the wafer is cleaned using a standard Radio Corporation of America cleaning process. An additional thin layer of silicon nitride was deposited followed by a 30 minute anneal at  $1100\ ^\circ\text{C}$  in an oxygen atmosphere, without additional etching, which is referred to as the redeposition and oxidation (RDO) step. A final  $6\text{-}\mu\text{m}$ -thick silicon dioxide upper cladding layer was deposited in two  $3\text{-}\mu\text{m}$  steps using plasma-enhanced chemical vapour deposition (PECVD) with tetraethoxysilane (TEOS) as a precursor, followed by a final two-step anneal at  $1050\ ^\circ\text{C}$  for 7 hours and  $1150\ ^\circ\text{C}$  for 2 hours. Two wafers of such silicon nitride waveguide ring resonator devices are fabricated with and without the RDO step, respectively, which are termed the ultra-high- $Q$  resonator (UHQR) devices and control devices, respectively.

For the ring resonator  $Q$  and loss measurements, we used the TLB-6730 Velocity™ Widely Tunable Laser in these measurements. An unbalanced fibre-based RF calibrated Mach-Zehnder interferometer (MZI) was used resonator to measure the  $Q$ . To calibrate the MZI FSR, we used a radiofrequency electro-optic phase modulator (EOM) to cre-

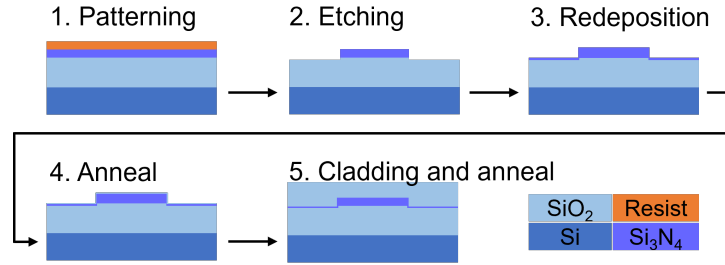


Figure 2.10: Fabrication process flow with the redeposition and oxidation steps indicated as step 3 and 4.

ate two sidebands. During scanning across a resonance, the two sidebands are used to calibrate the MZI FSR. The MZI FSR is measured to be  $5.871 \pm 0.004$  MHz. We simultaneously scan the laser through both the MZI and the UHQR and control devices that produce the calibrated scans reported. A standard cavity ring-down technique [28] was used to confirm the RF calibrated MZI measurements. For this measurement, a fibre laser was frequency swept around a resonator resonance by applying a triangular signal to the laser piezoelectric frequency control. Meanwhile, a 10 kHz square wave was applied to a 10-GHz-bandwidth intensity modulator to serve as the input laser power gate (on-off). A Thorlabs PDB-450C with a 150 MHz bandwidth was used to monitor the optical signal. The laser frequency is ramped slowly enough to allow charge and discharge of the resonator. The ringdown decay time ( $\tau$ ) is measured by fitting the measured exponential decay. The loaded Q factor is evaluated using  $Q_L = \omega\tau$  and the total loss rate is calculated as  $\gamma = 1/\tau$ . From the spectral linewidth and RF calibrated MZI Q measurements, the resonance extinction ratio indicates the ratio between the intrinsic and coupling losses.

It is important to note that the laser spectral scanning Q and linewidth measurement on the ring resonators require the add-through ring resonator model (e.g., Eq. 2.9 developed in the previous section as a fitting model to extract intrinsic loss, external coupling loss, and total loss rates, but the model does not distinguish between  $\gamma_{in}$  and

$\gamma_{ex}$ . This must rely on additional measurements and analysis such as measuring both loss rates in a wavelength range such as from 1550 nm to 1630 nm, where the scattering loss dominated intrinsic loss decreases and the coupling loss rate increases (see Supplementary Information in [15]). Another measurement technique in time domain, similar to the ringdown technique, is shown to be capable of measuring the coupling regime of the resonator coupling: under-coupling, over-coupling, or critical coupling [29].

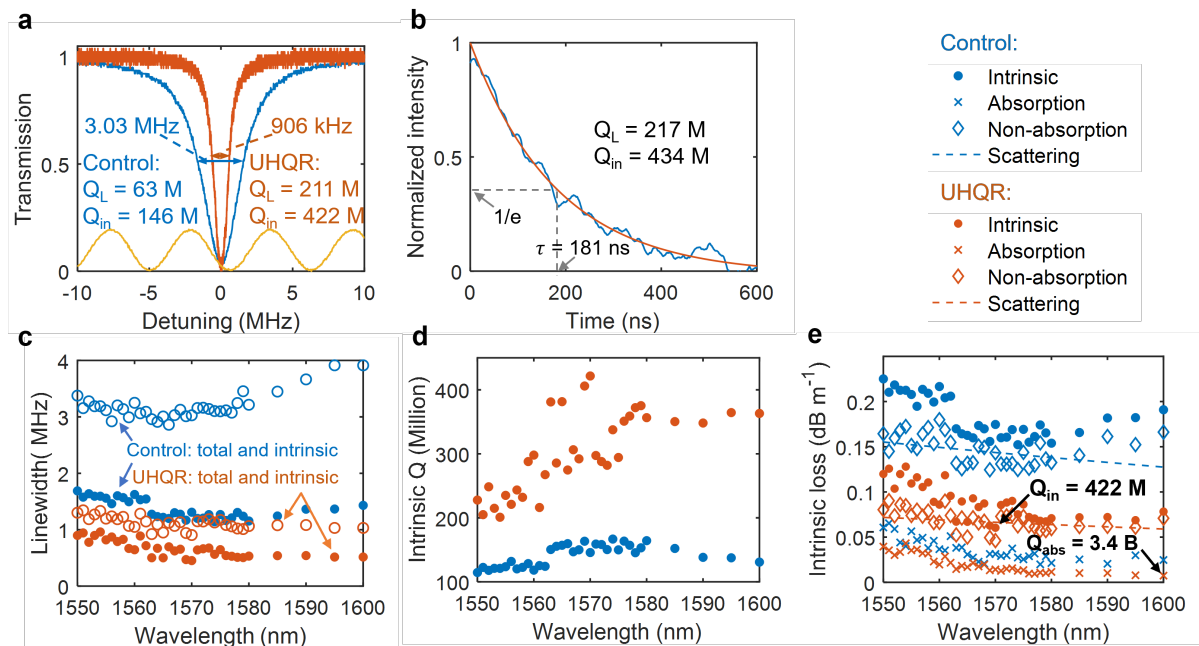


Figure 2.11: Linewidth, ring-down, and photo-thermal absorption loss measurements of the UHQR and control devices. (a) Spectral scan of the fundamental 1570 nm TE mode for the control and UHQR devices. The total and intrinsic linewidths are extracted from a Lorentzian fit. The yellow signal is the fibre MZI. M, million. (b) UHQR ring-down time measurement at 1570 nm. (c) Total and intrinsic linewidths for the UHQR and control samples from 1550 nm to 1600 nm. (d) Measured intrinsic Qs for UHQR and control resonators. (e) Photo-thermal absorption loss measurement from 1550 nm to 1600 nm for UHQR and control. The highest UHQR 422 million intrinsic Q at 1570 nm and the absorption-limited Q of 3.4 Billion at 1600 nm are indicated. The non-absorption loss is fit to the surface scattering loss model (dash lines).

Figure 2.11 summarizes the linewidth, Q and loss of the 11  $\mu$ m wide by 40 nm thick waveguide resonator devices. Compared to the control devices without the nitride RDO

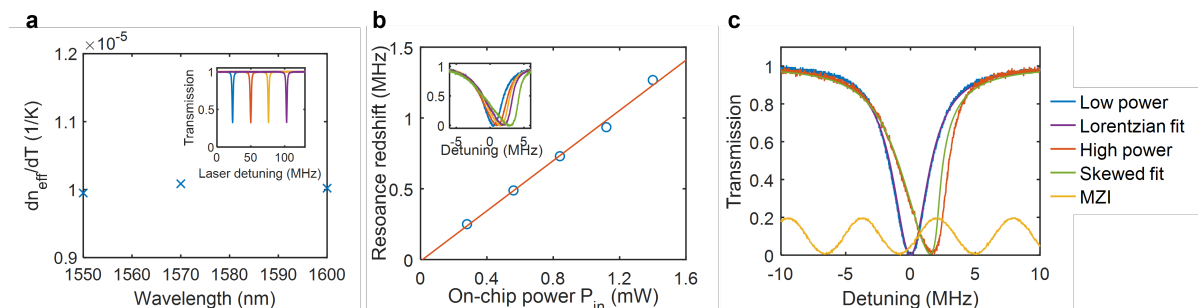


Figure 2.12: Photo-thermal heating and absorption loss measurement. (a) Effective index change with respect to temperature shows no wavelength dependence across the range from 1550 nm to 1600 nm. (b) Photothermal effect is amplified by higher on-chip power and the resonance redshift exhibits a linear relationship with the on-chip power. (c) Normal Lorentzian fitting for the lower power spectral sweeping and skewed Lorentzian fitting for the high-power spectral sweeping extracts the intrinsic loss and absorption loss rates.

process in the fabrication process, the UHQR devices fabricated with the RDO process show reduced intrinsic waveguide losses by reducing both absorption loss and scattering loss. The absorption loss is measured by using a photothermal resonance redshift effect, where the absorbed optical power in the waveguides induces a resonance redshift due to the thermo-optic process comparable to or larger than the resonance linewidth, a result of the on-chip absorption heating, shown in Fig. 2.12. The detailed modeling and analysis details of the absorption loss measurement technique using the photothermal heating effect can be found in [15].

### 2.2.3 Measurements of ultra-high Qs

Measuring the linewidths and Qs of the ultra-high-Q waveguide ring resonators can be a reliable approach of measuring the waveguide propagation loss, especially when the waveguide loss is low and the intrinsic waveguide loss is the only loss mechanism that contributes to the resonator intrinsic loss rate, as there could also exist other loss mechanisms that contributes to the ring resonator intrinsic loss such as the waveguide

bending loss and excess loss from the bus-ring coupler,

$$\gamma_{in} = \frac{c}{n_g} \left( \alpha + \alpha_{bend} + \frac{\xi}{L} \right), \quad (2.37)$$

where  $\alpha$  is the intrinsic waveguide propagation loss,  $\alpha_{bend}$  is the bending loss, and  $\xi$  is the excess coupler power loss per optical roundtrip. When  $\alpha_{bend}$  and  $\frac{\xi}{L}$  are negligible compared to  $\alpha$ , the measurement of the intrinsic linewidth of the ring resonator can reliably estimate the waveguide propagation loss.

The measurement of the waveguide resonator linewidths and Qs does not distinguish between the intrinsic and coupling linewidths, and the modeling and fitting to extract the intrinsic and coupling linewidths using the resonator modeling elaborated in Section 2.1.2 on the bus-coupling add-through ring resonators needs extra information to tell between the intrinsic and coupling linewidth. For example, when the bus-ring coupling is intentionally designed to be small for the resonator to be under-coupled, the larger one in the two measured loss linewidths ( $\gamma_{in}$  and  $\gamma_{ex}$ ) is the intrinsic loss. In the case where it is unknown whether the resonator is under-coupled or over-coupled, measuring the resonator linewidths over a wavelength range can help differentiate one from the other, as the coupling linewidth usually decreases with wavelength.

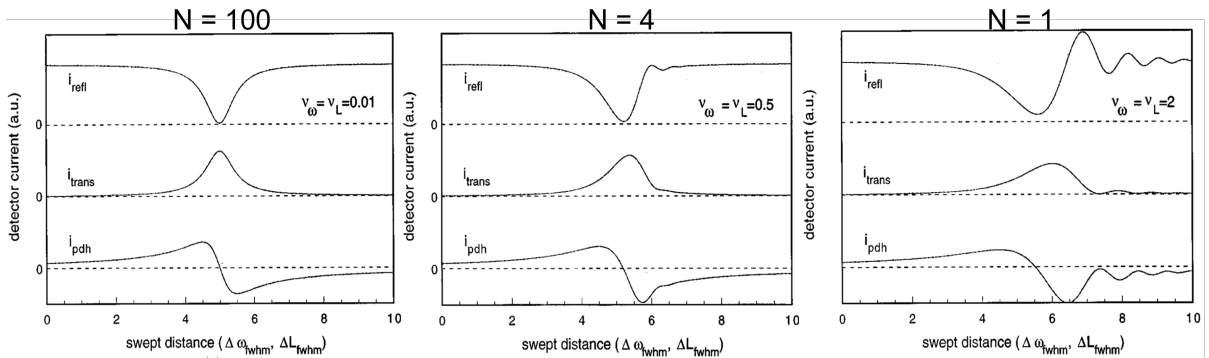


Figure 2.13: Simulations of the spectral scanning of an optical resonance with various laser scanning speeds that corresponds to  $N = 100, 4, 1$ . With  $N = 1, 4$ , the ring-down effect emerges as the laser is exiting the resonance. Original figure from [30].

Another important precaution in the spectral scanning of ultra-high-Q ring resonators in the measurements of linewidths and Qs is the speed of the laser detuning across the resonator resonance, especially for the ring resonators with linewidth below 1 MHz [30]. The figure of merit is the *cross-over time* that the probe laser sweeps across the resonance full-width-half-maximum ( $\Delta\nu_{FWHM}$ ) [30],

$$t_{xo} = \frac{\Delta\nu_{FWHM}}{\dot{f}} = N\tau_{cav}, \quad (2.38)$$

where  $\dot{f}$  is the laser detuning speed in Hz/s or MHz/s,  $\tau_{cav} = 1/(2\pi\Delta\nu_{FWHM})$  is the resonator photon lifetime. Here,  $N = t_{xo}/\tau_{cav}$  characterizes how fast the detuning laser sweeps across the resonance full-width-half-maximum. Figure 2.13 shows some ripples similar to the ring-down effect occurring at fast spectral scans with  $N = 1, 4$ . Therefore, in measuring high-Q resonances, the laser detuning speed cannot be too high to avoid the ring-down effect that can cause inaccuracy in measuring the linewidths and Qs. Such an effect indeed occurs in experiment with an estimated  $N = 12$  in Fig. 2.14.

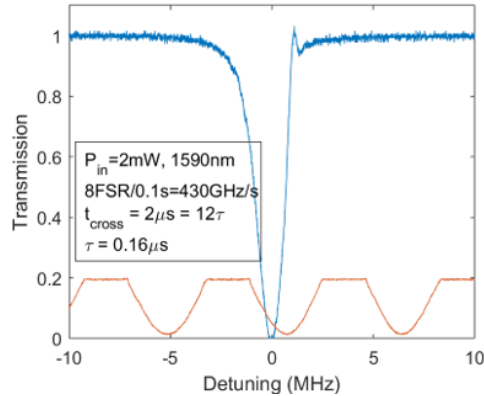


Figure 2.14: A spectral scanning experiment with an estimated  $N = 12$  sees the ring-down effect.



### 2.2.4 Bus-resonator coupling design and simulations

The bus-ring coupling design and simulation are guided by the directional coupling simulation described in detail in Chapter 4 of *Silicon Photonics Design* by Lukas Chrostowski [21]. The cross-section modal simulation of the two waveguides separated by a gap finds a symmetrical mode and an asymmetric mode. When the directional coupler gap is not too small relative to the waveguide width, the waveguide modes in the left and right waveguides can be represented well by a linear combination of the symmetrical and asymmetric modes,

$$\begin{pmatrix} a_L \\ a_R \end{pmatrix} = \frac{1}{\sqrt{2}} \begin{pmatrix} 1 & 1 \\ -1 & 1 \end{pmatrix} \begin{pmatrix} a_S \\ a_{AS} \end{pmatrix}. \quad (2.39)$$

The modal simulations find the index difference,  $\delta n_{eff}$  between the symmetric and asymmetric modes for a specific waveguide mode such as TE<sub>0</sub>, TE<sub>1</sub> or TM<sub>0</sub>, and the index difference causes interference between the symmetrical and asymmetric modes in the input waveguide and results in energy coupling and switching between the left and right waveguides. The power coupling coefficient can be found and expressed,

$$\kappa = \sin \frac{\pi \delta n_{eff} L_x}{\lambda}, \quad (2.40)$$

where  $L_x$  is the coupler length and  $\lambda$  is the wavelength. The resonator coupling rate can be calculated by Eq. 2.18,

$$\gamma_{ex} = \frac{\log(1/\tau^2)c}{n_g L}. \quad (2.41)$$

It is useful to keep in mind the numerical estimation of the resonator linewidth based on  $\gamma_{ex} = c\kappa^2/n_g L$ ,

$$\kappa^2 = 0.0020 \frac{\gamma_{ex}}{[2\pi \times 1\text{MHz}]} \frac{n_g}{[1.50]} \frac{L}{[2\pi \times 1\text{cm}]}, \quad (2.42)$$

where a 1-cm-radius ring resonator only requires a bus-ring coupling of 0.0020 or -27 dB for a 1-MHz bus-ring coupling loss rate.

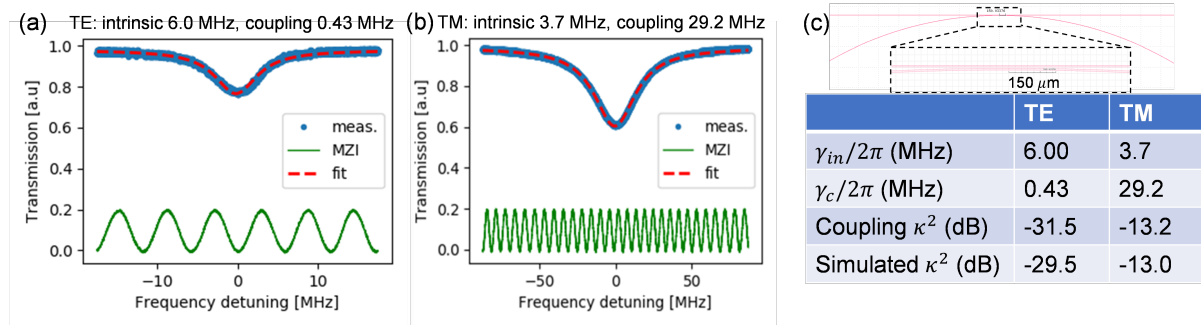


Figure 2.15: Linewidth measurements of a waveguide ring resonator (radius = 8530  $\mu\text{m}$ , 6  $\mu\text{m}$  by 80 nm waveguide) for (a) the TE<sub>0</sub> mode and (b) the TM<sub>0</sub> mode. (c) shows a comparison between the measured bus-ring coupling and simulated values using an approximated coupling length of  $L_x = 0.3$  mm.

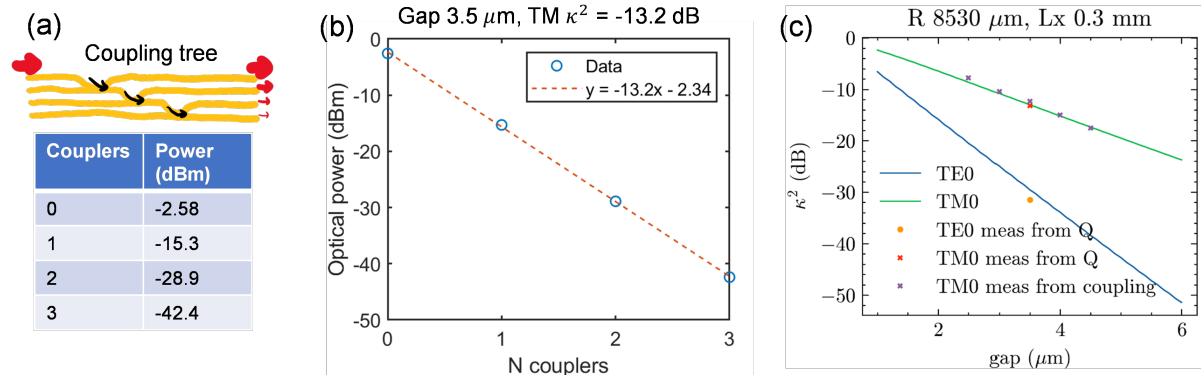


Figure 2.16: (a) Coupling tree testing technique. (b) The coupling tree measurement on the 3.5- $\mu\text{m}$  testing structure yield a coupling of -13.2 dB for the TM<sub>0</sub> mode. (c) Simulated coupling for both the TE and TM modes at different coupling gaps is compared with experimentally measured values.

Although the coupler formed by a waveguide ring resonator and straight bus waveg-

uide is not an ideal directional coupler where the coupling section has a constant gap between the waveguides, a point coupler can be well approximated as a small directional coupler with an approximated coupling length  $L_x$ . An experimental validation example is based on a straight-waveguide-bus-coupled ring resonator with a 8520- $\mu\text{m}$  radius based on the waveguide dimension of 6  $\mu\text{m}$  by 80 nm. Figure 2.15 and 2.16 show the measured bus-ring coupling for such a bus-ring coupler at different coupling gaps and the comparison between the experimentally measured values and the simulated coupling values and curves using the approximate coupling length of  $L_x = 0.3$  mm. The comparison validates that the bus-ring coupling simulation matches very well with the measured values. This coupling simulation approach can be very effective in predicting the coupling not only for different coupling gaps but also for different waveguide modes and at different wavelengths.

## 2.3 Waveguide loss origin investigation

Our ultra-high Q waveguide ring resonator is illustrated in Fig. 2.17(a), and a scanning electron microscopy (SEM) micrograph cross section is shown in Fig. 2.17(b). The roughness of the waveguide surface couples the guided energy into the radiation continuum, resulting in loss of scattering, and bulk material absorption converts the guided modes into heat, as illustrated in Fig. 2.17(c). Point defects on the waveguide surface, created during the material deposition or waveguide etching processes, can introduce coupling between longitudinal modes or the forward and backward propagating modes, causing random resonance splitting as illustrated in Fig. 2.17(d). The material deposition and waveguide etching processes can create reconstructed Si–Si bonds and dangling Si- and N- bonds, which can also become secondary bonds with hydrogen impurities such as Si–H, N–H, and Si–O–H, leading to surface absorption loss. Bus-to-resonator coupling

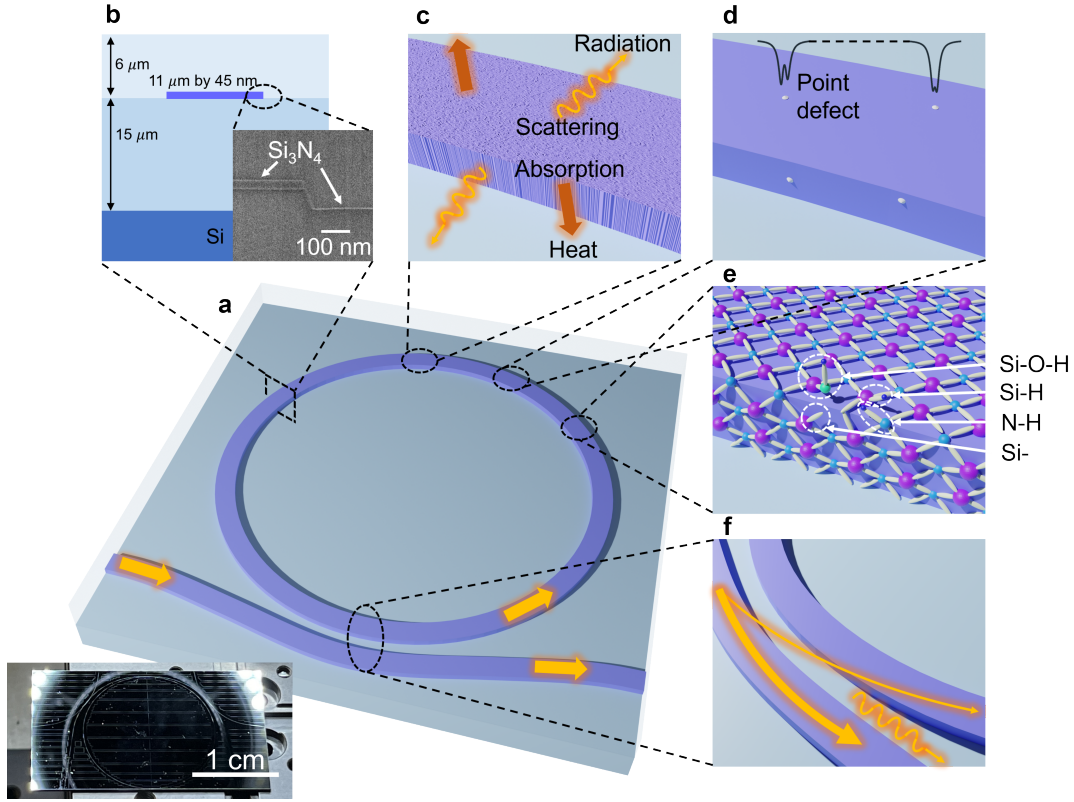


Figure 2.17: Illustration of ultra-high-Q waveguide ring resonator loss origins, with a picture of the real waveguide ring resonator device.

can introduce excess resonator loss in the ultra-high Q regime if there is any. The careful design of the bus-to-resonator coupling is less susceptible to excess loss. The total loss can be decomposed into scattering loss  $\alpha_s$ , absorption loss  $\alpha_{abs}$ , and coupler excess loss  $\alpha_{c,ex}$ ,

$$\alpha_{total} = \alpha_s + \alpha_{abs} + \alpha_{c,ex}. \quad (2.43)$$

### 2.3.1 Absorption loss

The on-resonance drop in transmitted power necessarily means that a resonator is dissipating power:  $P_{disp} = P_{in}(1 - T_{res})$ . Part of the dissipated power is absorbed and converted into heat:  $P_{abs} = \xi P_{disp}$ , where  $\xi$  is the fraction of the absorption loss in

the total measured waveguide propagation (intrinsic) loss, and the absorption loss rate can be expressed as  $\gamma_{abs} = \xi\gamma_{in}$ . Since only the waveguide is heated and the 1 mm thick Si substrate remains mostly undisturbed, the thermo-optic effect dominates, and thermal expansion is negligible. Using the thermo-optic coefficients of SiO<sub>2</sub> ( $0.95 \times 10^{-5}$  1/K) and SiN ( $2.45 \times 10^{-5}$  1/K) at 1550 nm reported in the literature, we perform a COMSOL simulation that simulates the thermal heating due to absorption heating and estimates the redshift given an absorption power:  $\delta f_{res} = \alpha P_{abs}$ , illustrated in the inset of Fig. 2.12(b). The simulation suggests  $R_{th} = 4.98$  K/W,  $\delta f_{res}/\delta T = 1.23$  GHz/K and  $\alpha = \delta f_{res}/P_{abs} = 6.11$  MHz/mW. To confirm the same thermo-optic coefficients at 1550 nm are valid for other wavelengths, we measure the resonance shift with a temperature increase and estimate the effective index change. Fig. 2.12(a) shows that there is no obvious wavelength dependence of the thermo-optic coefficients. A normal Lorentzian fit on the lower power transmission lineshape extracts the linewidths. With the extracted linewidths as the input parameters, we perform another fitting on the high power skewed lineshape with the following equation,

$$T = 1 - \frac{\gamma_{in}\gamma_{ex}}{[\Delta\omega - 2\pi f_D(1 - T)]^2 + (\gamma_{in} + \gamma_{ex})^2/4}, \quad (2.44)$$

where  $f_D = \delta f_{res}/(1 - T) = \xi\alpha P_{in}$  is the only parameter to be extracted allowing  $\xi$  to be determined. Figure 2.12(c) demonstrates the fitting processes using Eq. 2.44. It is important to note that the uncertainty of this absorption fraction measurement technique mainly comes from the simulated value of  $\alpha = 6.11$  MHz/mW and the characterization of on-chip power  $P_{in}$ , as  $\xi = f_D/(\alpha P_{in})$ ,

$$\frac{\delta\xi}{\xi} = \sqrt{\left(\frac{\delta\alpha}{\alpha}\right)^2 + \left(\frac{\delta f_D}{f_D}\right)^2 + \left(\frac{\delta P_{in}}{P_{in}}\right)^2}, \quad (2.45)$$

where  $\alpha = 6.11$  MHz/mW can be reliably simulated and  $f_D$  can be reliably measured and fitted shown in Fig. 2.12(b). However, the characterization of the on-chip power to the resonator ( $P_{in}$ ) depends on a reliable measurement of the fiber-to-chip edge coupling, and a smaller edge coupling loss could reduce the uncertainty of  $P_{in}$ .

### 2.3.2 Scattering loss

The fully three dimensional volume current method [31] (3D-VCM) is employed to rigorously simulate and calculate the waveguide surface roughness scattering loss from both the sidewall roughness and the top and bottom surface roughness, illustrated in Fig. 2.18. The waveguide roughness profiles with the RMS roughness value  $\sigma_{RMS}$  and the correlation length  $L_{cor}$  are assumed for different surfaces:  $\sigma_{side} = 2$  nm,  $L_{side} = 50$  nm,  $\sigma_{side} = 0.3$  nm,  $L_{side} = 10$  nm. Because the waveguide design (11  $\mu\text{m}$  by 40 nm) is in a quite high aspect ratio, the sidewall scattering loss is simulated to be very small and negligible,  $\alpha_{side} \simeq 0.001$  dB/m. Therefore, the scattering simulation focuses on the top and bottom surface roughness scattering loss, shown in Fig. 2.19.

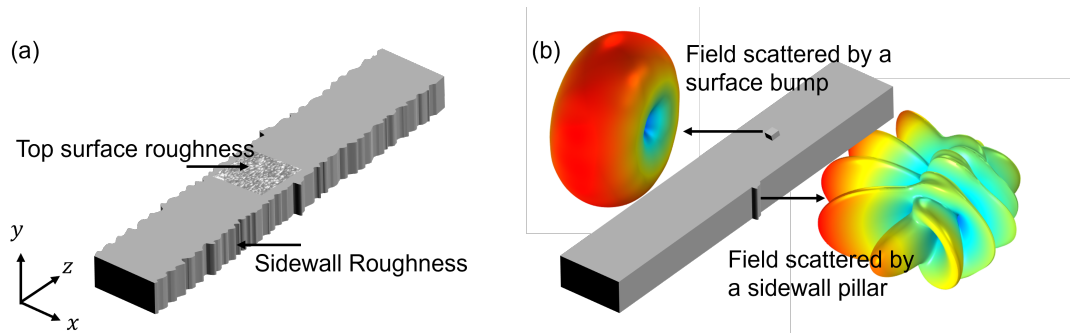


Figure 2.18: The dipole radiation from a roughness particle is simulated in COMSOL for both TE and TM modes on the top surface and sidewall surface, which is fed into the 3d-VCM analytical model to estimate the scattering losses. (a) illustrates the roughnesses on different surfaces. (b) shows the dipole radiation farfield.

For the  $\text{TE}_0$  mode, the scattering loss from the top/bottom surface roughness decreases as the waveguide increases its width and reduces the thickness, which essentially

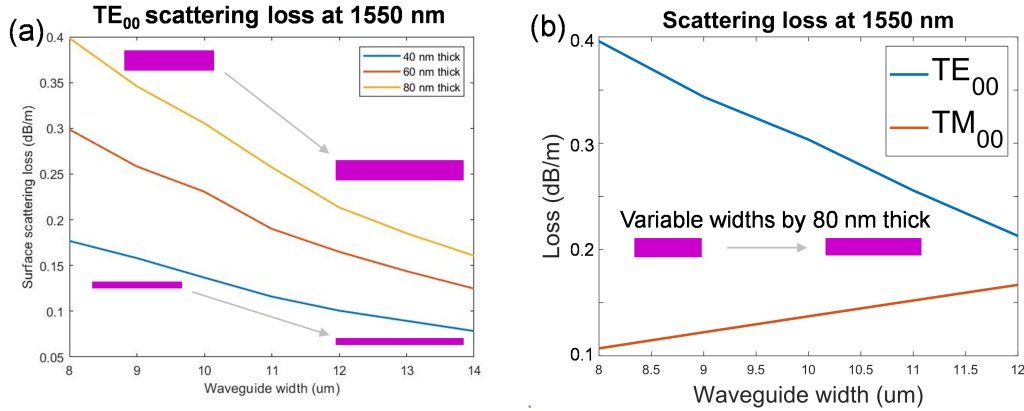


Figure 2.19: Top surface roughness scattering loss simulation using the 3D-VCM model. (a) Scattering loss for TE in waveguides with different thicknesses of 40 nm, 60 nm and 80 nm. (b) Scattering loss for TE and TM losses in the 80 nm thick waveguide.

results in a larger and more-dilute mode profile with a larger critical bending radius, shown in Fig. 2.19(a). However, the TM<sub>0</sub> mode scattering loss increases at wider waveguide widths, and can have much smaller scattering loss from the top/bottom roughness than the TE<sub>0</sub> mode below the waveguide width of 12  $\mu\text{m}$ , shown in 2.19(b).

### 2.3.3 TM waveguide resonators

As discussed in the previous section that the TM mode can have much smaller scattering loss from the top/bottom surface roughness, we use the same waveguide photomask layout to fabricate a new set of waveguide ring resonators with the same fabrication process described in Fig. 2.10, excepted that the nitride thickness is changed from 40 nm to 80 nm to allow the waveguide to support the fundamental TM mode [16]. Although increasing the thickness to 80 nm makes the waveguide to be a multimode waveguide, the coupling for the TE<sub>0</sub> mode reduces by a few orders of magnitude and makes the TE<sub>0</sub> mode very weakly coupled, which is referred to as the *quasi-single-mode* operation.

The loaded and intrinsic Qs are measured from 1550 nm to 1630 nm with a maximum

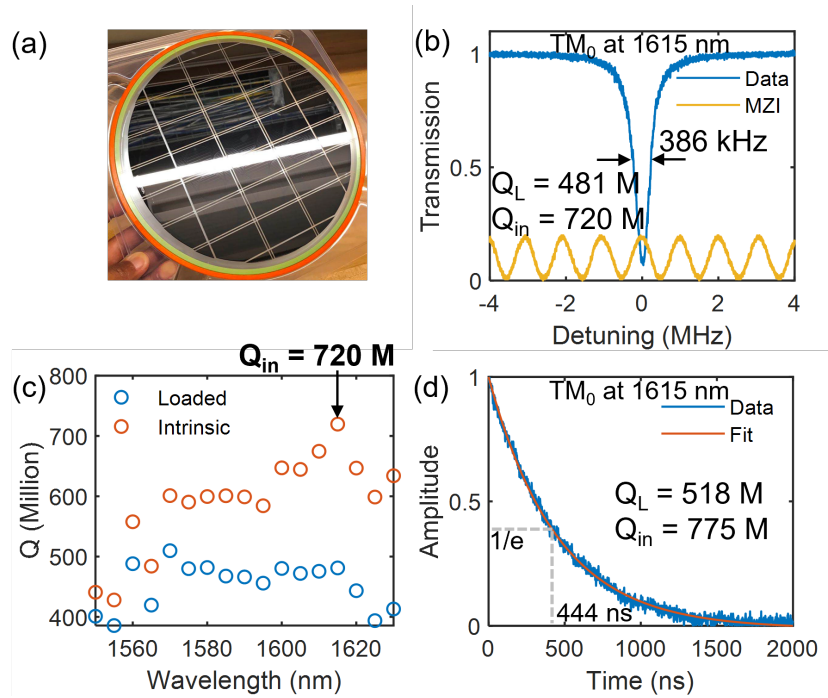


Figure 2.20: TM mode waveguide resonator linewidth and Q. (a) 200-mm wafer after the fabrication and dicing process. (b) Resonance spectral scan at 1615 nm with the 1.078 MHz FSR MZI. (c) Measured loaded and intrinsic Qs from 1550 nm to 1630 nm. M = million. (d) A ringdown time of 444 ns, corresponding to an intrinsic  $Q = 775$  M is measured at 1615 nm.

of 720 million at 1615 nm, corresponding to a propagation loss of 0.034 dB/m. An intrinsic linewidth of 258 kHz, and a loaded linewidth of 386 kHz (Fig. 2.20(b) and (c)) are measured using Mach-Zehnder interferometer (MZI) and ring-down techniques. Ringdown measurements at 1615 nm yield an intrinsic  $775 \pm 8$  million and loaded  $518 \pm 5$  million Q (Fig. 2.20(d)) confirming the MZI measurement within 7%. Measurements at 1615 nm, of all devices fabricated on the same 200 mm wafer, yield a maximum 720 million Q and an average 565 million Q.



## 2.4 Summary and outlook

Propagation loss is one of the most important and fundamental parameters of optical waveguides, which impacts various aspects of the photonic integrated devices based on the waveguide structures. Using the high-aspect-ratio waveguide design and the redeposition and oxidation technique in the fabrication process, we demonstrated the ultra-low propagation loss of 0.05 dB/m in the fundamental TE mode and 0.034 dB/m in the fundamental TM mode in the C and L band, corresponding to 422 million and 720 million intrinsic waveguide resonator Qs. Through the absorption loss measurements and scattering loss modeling, we found that the scattering loss from the top and bottom surface roughness still dominates the waveguide propagation loss outside the hydrogen impurity related absorption losses at 1380 nm and 1520 nm. All these results pave the way for further waveguide loss reduction and possibility of billion Q waveguide resonators.

## Bibliography

- [1] K. C. Kao and G. A. Hockham, *Dielectric-fibre surface waveguides for optical frequencies*, in *Proceedings of the Institution of Electrical Engineers*, vol. 113, pp. 1151–1158, IET, 1966.
- [2] F. P. Kapron, D. B. Keck, and R. D. Maurer, *Radiation losses in glass optical waveguides*, *Applied Physics Letters* **17** (1970), no. 10 423–425.
- [3] J. Hecht, *The breakthrough birth of low-loss fiber optics*, *Optics and Photonics News* **31** (2020), no. 3 26–33.
- [4] M.-J. Li and T. Hayashi, *Advances in low-loss, large-area, and multicore fibers*, in *Optical Fiber Telecommunications VII*, pp. 3–50. Elsevier, 2020.

- [5] Y. Chen, M. N. Petrovich, E. N. Fokoua, A. I. Adamu, M. R. A. Hassan, H. Sakr, R. Slavík, S. B. Gorajooobi, M. Alonso, R. F. Ando, A. Papadimopoulos, T. Varghese, D. Wu, M. F. Ando, K. Wisniowski, S. R. Sandoghchi, G. T. Jasion, D. J. Richardson, and F. Poletti, *Hollow Core DNANF Optical Fiber with  $< 0.11$  dB/km Loss*, in *Optical Fiber Communication Conference*, p. Th4A.8, Optica Publishing Group, 2024.
- [6] S. J. Choi, K. Djordjev, Z. Peng, Q. Yang, S. J. Choi, and P. D. Dapkus, *Laterally coupled buried heterostructure high-Q ring resonators*, *IEEE Photonics Technology Letters* **16** (2004), no. 10 2266–2268.
- [7] L. Chang, W. Xie, H. Shu, Q.-F. Yang, B. Shen, A. Boes, J. D. Peters, W. Jin, C. Xiang, S. Liu, *et. al.*, *Ultra-efficient frequency comb generation in AlGaAs-on-insulator microresonators*, *Nature communications* **11** (2020), no. 1 1331.
- [8] M. A. Tran, D. Huang, T. Komljenovic, J. Peters, A. Malik, and J. E. Bowers, *Ultra-low-loss silicon waveguides for heterogeneously integrated silicon/III-V photonics*, *Applied Sciences* **8** (2018), no. 7 1139.
- [9] Y. Zhang, X. Hu, D. Chen, L. Wang, M. Li, P. Feng, X. Xiao, and S. Yu, *Design and demonstration of ultra-high-Q silicon microring resonator based on a multi-mode ridge waveguide*, *Optics letters* **43** (2018), no. 7 1586–1589.
- [10] M. Zhang, C. Wang, R. Cheng, A. Shams-Ansari, and M. Lončar, *Monolithic ultra-high-Q lithium niobate microring resonator*, *Optica* **4** (2017), no. 12 1536–1537.
- [11] A. Shams-Ansari, G. Huang, L. He, Z. Li, J. Holzgrafe, M. Jankowski, M. Churayev,

- P. Kharel, R. Cheng, D. Zhu, *et. al.*, *Reduced material loss in thin-film lithium niobate waveguides*, *Apl Photonics* **7** (2022), no. 8.
- [12] M. H. Pfeiffer, A. Kordts, V. Brasch, M. Zervas, M. Geiselmann, J. D. Jost, and T. J. Kippenberg, *Photonic Damascene process for integrated high- $Q$  microresonator based nonlinear photonics*, *Optica* **3** (2016), no. 1 20–25.
- [13] J. Liu, G. Huang, R. N. Wang, J. He, A. S. Raja, T. Liu, N. J. Engelsen, and T. J. Kippenberg, *High-yield, wafer-scale fabrication of ultralow-loss, dispersion-engineered silicon nitride photonic circuits*, *Nature communications* **12** (2021), no. 1 2236.
- [14] W. Jin, Q.-F. Yang, L. Chang, B. Shen, H. Wang, M. A. Leal, L. Wu, M. Gao, A. Feshali, M. Paniccia, *et. al.*, *Hertz-linewidth semiconductor lasers using CMOS-ready ultra-high- $Q$  microresonators*, *Nature Photonics* **15** (2021), no. 5 346–353.
- [15] M. W. Puckett, K. Liu, N. Chauhan, Q. Zhao, N. Jin, H. Cheng, J. Wu, R. O. Behunin, P. T. Rakich, K. D. Nelson, *et. al.*, *422 Million intrinsic quality factor planar integrated all-waveguide resonator with sub-MHz linewidth*, *Nature communications* **12** (2021), no. 1 934.
- [16] K. Liu, N. Jin, H. Cheng, N. Chauhan, M. W. Puckett, K. D. Nelson, R. O. Behunin, P. T. Rakich, and D. J. Blumenthal, *Ultralow 0.034 dB/m loss wafer-scale integrated photonics realizing 720 million  $Q$  and 380  $\mu$ W threshold Brillouin lasing*, *Optics letters* **47** (2022), no. 7 1855–1858.
- [17] J. F. Bauters, M. J. Heck, D. D. John, J. S. Barton, C. M. Bruinink, A. Leinse, R. G. Heideman, D. J. Blumenthal, and J. E. Bowers, *Planar waveguides with less*

- than 0.1 dB/m propagation loss fabricated with wafer bonding, *Optics express* **19** (2011), no. 24 24090–24101.
- [18] J. F. Bauters, M. J. Heck, D. John, D. Dai, M.-C. Tien, J. S. Barton, A. Leinse, R. G. Heideman, D. J. Blumenthal, and J. E. Bowers, *Ultra-low-loss high-aspect-ratio  $Si_3N_4$  waveguides*, *Optics express* **19** (2011), no. 4 3163–3174.
- [19] D. T. Spencer, J. F. Bauters, M. J. Heck, and J. E. Bowers, *Integrated waveguide coupled  $Si_3N_4$  resonators in the ultrahigh-Q regime*, *Optica* **1** (2014), no. 3 153–157.
- [20] W. Bogaerts, P. De Heyn, T. Van Vaerenbergh, K. De Vos, S. Kumar Selvaraja, T. Claes, P. Dumon, P. Bienstman, D. Van Thourhout, and R. Baets, *Silicon microring resonators*, *Laser & Photonics Reviews* **6** (2012), no. 1 47–73.
- [21] L. Chrostowski and M. Hochberg, *Silicon photonics design: from devices to systems*. Cambridge University Press, 2015.
- [22] X. Mi, J. Cady, D. Zajac, J. Stehlik, L. Edge, and J. R. Petta, *Circuit quantum electrodynamics architecture for gate-defined quantum dots in silicon*, *Applied Physics Letters* **110** (2017), no. 4.
- [23] C. W. Gardiner and M. J. Collett, *Input and output in damped quantum systems: Quantum stochastic differential equations and the master equation*, *Physical Review A* **31** (1985), no. 6 3761.
- [24] C. Gardiner and P. Zoller, *Quantum noise: a handbook of Markovian and non-Markovian quantum stochastic methods with applications to quantum optics*. Springer Science & Business Media, 2004.
- [25] H. A. Haus and W. Huang, *Coupled-mode theory*, *Proceedings of the IEEE* **79** (1991), no. 10 1505–1518.

- [26] B. E. Little, S. T. Chu, H. A. Haus, J. Foresi, and J.-P. Laine, *Microring resonator channel dropping filters*, *Journal of lightwave technology* **15** (1997), no. 6 998–1005.
- [27] V. Van, *Optical microring resonators: theory, techniques, and applications*. CRC Press, 2016.
- [28] S. Gundavarapu, G. M. Brodnik, M. Puckett, T. Huffman, D. Bose, R. Behunin, J. Wu, T. Qiu, C. Pinho, N. Chauhan, *et. al.*, *Sub-hertz fundamental linewidth photonic integrated Brillouin laser*, *Nature Photonics* **13** (2019), no. 1 60–67.
- [29] C. Cui, L. Zhang, B.-H. Wu, S. Liu, P.-K. Chen, and L. Fan, *Distinguishing under-and over-coupled resonances without prior knowledge*, *Optica* **11** (2024), no. 2 176–177.
- [30] M. Lawrence, B. Willke, M. Husman, E. Gustafson, and R. Byer, *Dynamic response of a Fabry–Perot interferometer*, *JOSA B* **16** (1999), no. 4 523–532.
- [31] C. Ciminelli, F. Dell’Olio, V. M. Passaro, and M. N. Armenise, *Fully three-dimensional accurate modeling of scattering loss in optical waveguides*, *Optical and quantum electronics* **41** (2009) 285–298.

# Chapter 3

## Laser frequency noise and linewidth

### Background of oscillators

Time is a fundamental physics quantity in nature, and timekeeping is inseparable from periodic movements of objects or changes in quantities [1]. The evolution of life has incorporated timekeeping as a basic function of life as various forms of biological clocks that are synchronized to tidal movements, earth rotation, or moon cycles. The history of developing better and better timekeeping devices dates back to ancient human civilizations to regulate human activities within a day, a month, and a year.

Modern timekeeping devices with precision began with the pendulum clock in the 17th century. The 1707 Scilly naval disaster [2] in which four ships were wrecked because of the inability to accurately locate the longitude motivated the British government to offer a huge prize to anyone who could determine the longitude with a 50-km precision, which required a clock for navigation with an instability of less than 6 seconds per day ( $1 \times 10^{-6}$ ). The age of exploration in the 18th century saw the invention of the marine chronometer and the capability for marine fleet to accurately determine the ship longitude to sail across oceans between continents [3]. Here is a great review article on the historical

perspectives of clock inventions as well as on the scientific perspectives [4].

In the 20th century, along with the development of electronic devices, crystal quartz oscillators were invented in Bell Laboratories in 1927, and soon became the most dominant and is still today in micro-electronic microwave oscillators because of its small weight and size and low cost and can be found inside many test and measurement equipment, such as frequency counters, signal generators, and oscilloscopes. The quartz oscillators reaches the uncertainty level of  $1 \times 10^{-10}$ . Soon, atomic resonant frequency were used as references such as the 6.8 GHz  $^{87}\text{Rb}$  resonance ( $1 \times 10^{-12}$ ) and the 9.1 GHz  $^{133}\text{Cs}$  resonance ( $1 \times 10^{-14}$ ) [4].

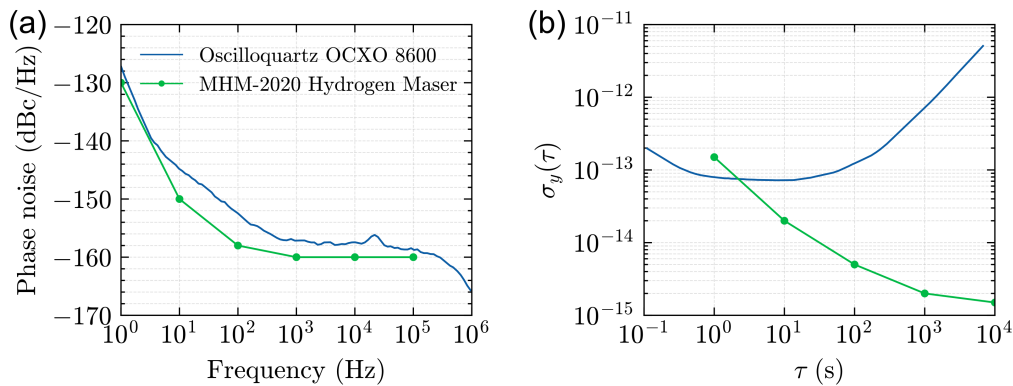


Figure 3.1: Quartz oscillator and MHM-2020 hydrogen maser phase noise and Allan deviation.

State-of-the-art ultra-stable high-precision clock oscillators are mainly divided into two categories: microwave oscillators and optical-atomic oscillators. To date, the best microwave clock oscillator is built of a cryogenic sapphire resonator oscillator, demonstrating  $10^{-16}$  mid-term fractional frequency stability [5]. Ultra-high finesse and low-expansion, single crystal silicon Fabry Perot resonator can achieve an optical stability of  $10^{-16}$  at around 1 s [6, 7]. Referencing to atomic transitions, the optical atomic frequency stability can reach down to  $10^{-18}$  at 1000 seconds [8].

Not only does the long-term stability matter for the frequency standard clock reference

but also the frequency / phase noise and jitter at short time scales, depending on the clock applications. For example, many RF applications require low phase noise at specific frequency offsets such as 10 kHz [9, 10]. Figure 3.1 shows a comparison between the commercially available MHM-202 hydrogen maser and the OCSO8600 quartz oscillator in terms of phase noise and Allan deviation, where both have very comparable phase noise performances from 1 Hz out to 100 kHz, but the long-term stability of the hydrogen maser is much superior to that of the quartz oscillator. Optical frequency division to convert low-phase noise optical frequencies to microwave oscillators has demonstrated the lowest phase noise microwave oscillators [11, 12, 13], owing to the low phase noise lasers and the large frequency division ratio between the optical and microwave frequencies.

In recent years, the field of integrated photonics has seen a lot of efforts towards making miniaturized and integrated optical components for atomic, molecular, and optical experiments and applications such as ultra-stable lasers, magneto-optical traps, optical tweezers, optical-to-microwave frequency division, and etc. To name a few examples, a compact optical atomic clock based on a two-photon transition in Rb demonstrates a  $10^{-15}$  long-term frequency stability [14]. A Rb vapor cell is mounted on a photonic chip with laser stabilization, achieving  $10^{-11}$  long-term stability [15]. Photonic integrated beam delivery chip for a rubidium 3D magneto-optical trap has been demonstrated [16]. Optical frequency division system using all photonic waveguide technologies for low phase noise microwave and mmWave generation has achieved -120 dBc/Hz at 10 kHz phase noise for 100 GHz microwave carrier [9, 10].

### 3.1 Fundamental oscillator phase and frequency noise

Oscillator frequency and phase noise arises not only from the coupling to the environmental disturbance but also intrinsically from the fundamental thermal and quantum-



mechanical fluctuations. The book by Enrico Rubiola, *Phase Noise and Frequency Stability in Oscillators*, is a quite comprehensive review and in-depth discussion on oscillator phase and frequency noise and stability [17]. The fundamental thermal and quantum-mechanical fluctuations originate from the coupling between the oscillator and a heatbath, leading to the Langevin force and the fundamental oscillator linewidth (see Chapter 4 in [18]). Using the laser as an oscillator example, the Hamiltonian of the total system that consists of the single-mode laser, the heatbath, and the coupling between the two reads,

$$H = H_{laser} + H_{bath} + H_{laser-bath}, \quad (3.1)$$

$$H_{laser} = \hbar\omega_0 b^\dagger b, \quad (3.2)$$

$$H_{bath} = \sum_{\omega} \hbar\omega B_{\omega}^{\dagger} B_{\omega}, \quad (3.3)$$

$$H_{laser-bath} = \sum_{\omega} \hbar g_{\omega} B_{\omega} b^{\dagger} + \hbar g_{\omega}^{\dagger} B_{\omega}^{\dagger} b. \quad (3.4)$$

And a set of Langevin equations for the laser optical field operator  $b$  can be derived from the Hamiltonian above,

$$\dot{b} = i\omega_0 b - \gamma b + F, \quad (3.5)$$

$$\dot{b}^{\dagger} = i\omega_0 b^{\dagger} - \gamma b^{\dagger} + F^{\dagger} \quad (3.6)$$

$$\gamma : \int |g_{\omega}|^2 e^{i\omega(t-\tau)} d\omega = 2\gamma\delta(t-\tau), \quad (3.7)$$

$$\langle F^{\dagger}(t)F(t') \rangle = 2\gamma n_{\omega_0}(T)\delta(t-t'), \quad (3.8)$$

$$\langle F(t)F^{\dagger}(t') \rangle = 2\gamma(n_{\omega_0}(T) + 1)\delta(t-t'), \quad (3.9)$$

where  $F = \sum_{\omega} i g_{\omega} B_{\omega} e^{i\omega t}$  is the Langevin force from the coupling to the heatbath,  $\gamma$  is the total loss rate of the oscillator, and  $n_{\omega_0}(T) = 1/[\exp\{(\hbar\omega_0/k_B T)\} - 1]$  is the thermal occupation number of the photon mode at its ambient temperature  $T$  that approximates

to 0 for optical photons ( $\omega_0 = 2\pi \times 10^{14}$  Hz) at room temperature (300 K) when  $\hbar\omega_0 \gg k_B T$ . The fundamental or intrinsic phase noise ( $S_\phi$ ) and frequency noise ( $S_\nu$ ) of the laser photon field operator  $b$  associated with the Langevin forces can be found,

$$S_\phi(f) = \frac{\Delta\nu_0}{2\pi f^2}, \quad (3.10)$$

$$S_\nu(f) = \frac{\Delta\nu_0}{2\pi}, \quad (3.11)$$

where  $\delta\nu_0$  is the fundamental laser linewidth,

$$\Delta\nu_0 = \frac{\gamma(2n_{\omega_0} + 1)}{4\pi|b|^2} \simeq \frac{\gamma}{4\pi|b|^2}. \quad (3.12)$$

Here,  $|b|^2$  can be interpreted as the total photon number in the laser cavity, as  $\langle H_{laser} \rangle = \hbar\omega_0 \langle b^\dagger b \rangle$  represents the total photon energy in the resonant cavity mode. And the term  $(2n_{\omega_0} + 1)$  essentially originates from the summation of the coefficients in the Langevin forces, Eq. 3.9,  $(n_{\omega_0}) + (n_{\omega_0} + 1)$ , and the number  $\mathbf{1}$  in there originates from the non-commutation between  $b$  and  $b^\dagger$ ,  $[b, b^\dagger] = 1$ . In semiconductor lasers [19, 20], due to the coupling between the phase and amplitude, a linewidth enhancement factor can be added to the fundamental laser linewidth equation,  $\Delta\nu_{mod} = \Delta\nu_0(\alpha_H^2 + 1)$ . In the case of stimulated Brillouin scattering (SBS), the linewidth enhancement factor is caused by the phase mismatch between the optical mode and acoustic gain profile [21]. In SBS lasers [22], both the optical photon and acoustic phonon thermal occupation numbers contribute to the Langevin forces, and the fundamental linewidth needs to include both,

$$\Delta\nu_0 = \frac{\gamma(n_\Omega + n_{\omega_0} + 1)}{2\pi|b|^2}. \quad (3.13)$$

Since for the 11-GHz ( $\Omega/2\pi = 11$  GHz) acoustic photon in the material of glass at 300 K,  $n_\Omega \simeq k_B T/\hbar\Omega = 568 \gg 1$ . The fundamental linewidth expression above can be simplified as,

$$\Delta\nu_0 = \frac{\gamma n_\Omega}{2\pi|b|^2}. \quad (3.14)$$

## 3.2 Frequency noise, linewidth and Allan deviation

The subject and content in this section can be found in greater details in [23, 17]. The electric-magnetic oscillating field of lasers can be simply described by a sin wave with amplitude and phase fluctuations,

$$\begin{aligned} E(t) &= (E_0 + \delta E(t)) \sin [2\pi\nu_0 t + \delta\phi(t)], \\ &= (E_0 + \delta E(t)) \sin [2\pi(\nu_0 + \delta\nu(t))t]. \end{aligned}$$

The amplitude noise is characterized by what is referred to as *relative intensity noise* (RIN) in lasers,  $\alpha(t) = 2E_0\delta E(t)/|E_0|^2 = 2\delta E(t)/E_0$ , and the RIN power spectral density  $S_\alpha(f)$  can be measured by directly sampling the fluctuation in the photo-detection current,

$$I(t) = I_0 + \delta I(t), \quad (3.15)$$

$$= \frac{\eta e}{h\nu} [P_0 + \delta P(t)], \quad (3.16)$$

where  $\eta$  is the quantum efficiency of the photodetector, and  $R = \eta e/h\nu$  is the photodetector responsivity, and  $\delta P(t)$  is the optical power fluctuations. In the measurements of laser RIN, it is important to keep in mind two measurement limits - shot noise and photodetector noise, both of which decrease with increasing optical power onto the pho-

todetector,

$$S_{\alpha,sh} = \frac{2h\nu}{\eta P_0}, \tag{3.17}$$

$$S_{\alpha,PD} = \frac{NEP^2}{P_0}, \tag{3.18}$$

where NEP is the noise equivalent power of the photodetector, and  $P_0$  is the optical power onto the photodetector. For example, using the Thorlabs PDB450C photodetector ( $R = 0.9$  A/W,  $\eta = 0.72$ ,  $NEP = 8$  pW/Hz<sup>1/2</sup>, transimpedance gain is 10 kV/A, at the wavelength of 1550 nm) and incident optical power of 1 mW, the shot-noise-limited and photodetector-noise limited RIN can be estimated,  $S_{\alpha,sh} = 3.6 \times 10^{16}$  1/Hz = -155 dBc/Hz,  $S_{\alpha,PD} = 6.4 \times 10^{-17}$  1/Hz = -162 dBc/Hz. In this set of conditions, the laser RIN measurements at high frequency offsets are usually shot-noise-limited, and is dependent on the incident optical power.

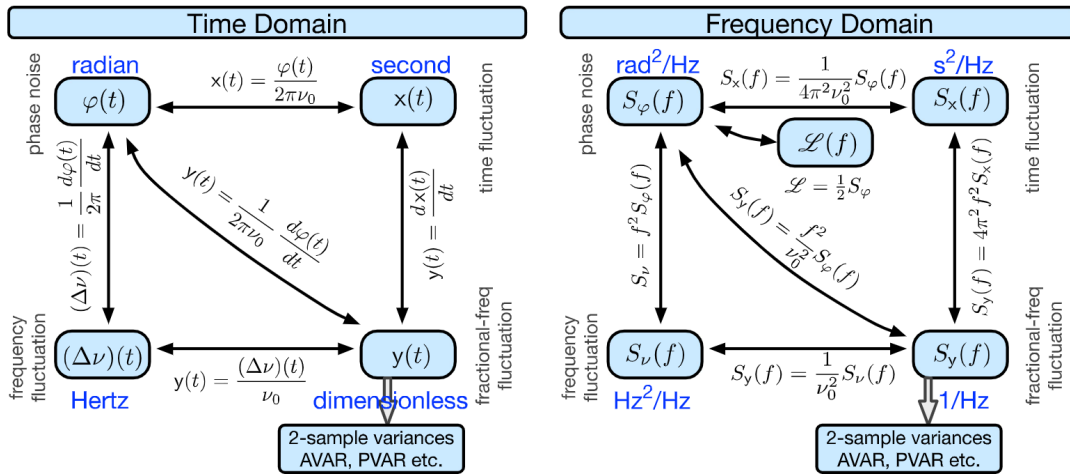


Figure 3.2: Frequency noise, phase noise, time-jitter noise, fractional frequency noise in time domain and frequency domain, and the conversions between them. Original figure from [23].

Since frequency is the derivative of phase,  $\nu(t) = d\phi(t)/dt$  or  $\Delta\nu(t) = d\Delta\phi(t)/dt$ , the power spectral densities of frequency noise  $S_\nu(f)$  and phase noise  $S_\phi(f)$  can be related by

$S_\nu(f) = f^2 S_\phi(f)$ . There is also fractional frequency noise  $S_y(f) = S_\nu(f)/\nu_0^2$ . Discussed in the previous section, the fundamental laser linewidth exhibits a white frequency noise in the frequency noise spectrum,  $S_\nu = \delta\nu_0/\pi$  in  $\text{Hz}^2/\text{Hz}$ , which in turn can also be used to measure the fundamental linewidth from a measured frequency noise spectrum by estimating the white frequency noise floor  $h_0$ ,  $\delta\nu_0 = \pi h_0$ . Due to its coupling to the environmental noise and other noise dynamics in the laser itself at low frequency offsets, the laser frequency noise spectrum can exhibit different noise processes such as random walk frequency noise ( $h_{-2}/f^2$ ) and flicker frequency noise ( $h_{-1}/f$ ), as illustrated in Fig. 3.3, while flicker phase noise ( $h_1 f$ ) and white phase noise ( $h_2 f^2$ ) can show up at much higher frequency offsets. Although there are different variations of Allan deviation [23], the conversion from frequency noise to Allan deviation is illustrated in Fig. 3.3, and by the following equation,

$$\sigma_y^2(\tau) = \int \frac{2 \sin^4(\pi\tau f)}{(\pi\tau f)^2} S_y(f) df. \quad (3.19)$$

A good metric to quantify the frequency noise spectrum at low frequency offsets is what is called  $1/\pi$  *integral linewidth* defined as,

$$\Delta\nu_{1/\pi} : \int_{\infty}^{\Delta\nu_{1/\pi}} S_\phi(f) df = \frac{1}{\pi} \text{rad}^2, \quad (3.20)$$

where the integration over the laser phase noise spectrum from the maximum frequency offset when reaching  $1/\pi \text{ rad}^2$  stops at a frequency offset which defines the  $1/\pi$  integral linewidth. One of the reasons of choosing the integral value to be  $1/\pi$  is that the  $1/\pi$  integral linewidth equals the fundamental linewidth when there is only a white laser frequency noise, as one can verify,

$$\Delta\nu_{1/\pi} = \Delta\nu_0 : \int_{\infty}^{\Delta\nu_0} \frac{\Delta\nu_0}{\pi f^2} df = \frac{1}{\pi} \text{rad}^2. \quad (3.21)$$

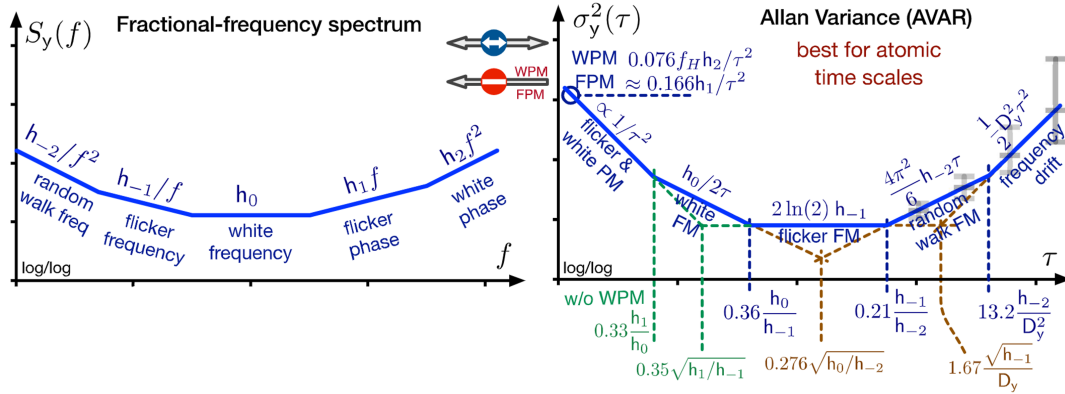


Figure 3.3: Different types of frequency noise processes, and the conversion to Allan deviation. Original figure from [23].

Equally important as the contributions of different noise sources and mechanisms to the laser and reference resonator frequency noise is the measurement of the laser frequency noise. Optical frequency discriminators with high optical frequency and phase discrimination and low intrinsic noise are great tools to reliably measure laser frequency and phase noise at certain frequency offset bands. For any type of laser frequency and phase noise measurements, it is important to bear in mind that the laser noise measurement is always a summation of the laser frequency noise, the intrinsic noise of the optical frequency discriminator with which the laser is measured against, the photodetector noise, shot noise, analog-to-digital data acquisition noise, and other noise contributions.

$$S_{meas}(f) = S_{laser}(f) + S_{OFD}(f) + S_{PD}(f) + S_{sh}(f) + S_{others}(f). \quad (3.22)$$

For example, unbalanced fiber Mach–Zehnder interferometers with long fiber delays with FSRs on the order of MHz or below are great optical frequency discriminators for laser frequency noise and linewidth measurements using delayed self-homodyne laser frequency noise measurement [24].

Therefore, the measured laser noise represents an upper bound of the true laser noise. Thus, it is critical to eliminate or reduce the noises other than the true laser noise so

that the measured frequency and phase noise can represent the true laser noise. For laser frequency noise measurements at low frequencies, the fiber delay line as the optical frequency discriminator can exhibit a significant amount of noise due to its coupling to the environmental noise such as vibrational and acoustic noise, which necessitates a stable low-noise reference laser as an optical frequency discriminator for reliable laser frequency noise measurements [25]. At high frequency offsets, the excess noise of the laser frequency noise measurement usually has contributions from the photodetector or the analog-to-digital data acquisition module, which can be reduced by increasing the optical power onto the photodetector or choosing a low-noise photodetector. This is especially important in measuring the laser fundamental linewidth which is estimated from the laser frequency noise at high frequency offsets where the laser fundamental noise process dominates [26, 27].

### 3.3 Thermo-refractive noise and photothermal noise

The previous section elaborates on the fundamental and intrinsic frequency and phase noise from thermal and quantum-mechanical fluctuations, which exists in all time scales, slow and fast. Apart from intrinsic phase noise, the oscillator phase can also be perturbed by external and environmental forces, such as mechanical vibrations and ambient temperature fluctuations, which perturb the oscillation frequency with changes and movements at certain frequency offsets. In optical resonant cavities for lasers, the optical roundtrip path of the lasing resonant mode is perturbed by the ambient temperature through the thermo-optical effect, and by the mechanical vibrations through opto-elastic effect and etc.

In optical waveguide microring resonators, in addition to environmental disturbances, there are two important noise processes that contribute to the laser phase and frequency

noise spectrum, thermorefractive noise [28], and photothermal noise [29]. The former is due to fundamental thermal fluctuations of matter and can be analyzed using dissipation-fluctuation theorem [30, 31] and simulated in COMSOL [28]. In waveguide resonators, despite its dependence on the geometry of the waveguide cross-section and optical mode profile, the thermorefractive noise simply scales linearly with the ambient temperature  $T$  and inversely with the resonator roundtrip length  $L$ ,  $S_{TRN} \approx T^2/L$ . The frequency noise spectrum of thermorefractive noise has a roll-off towards high frequency offsets, and the roll-off behavior depends on the waveguide design and optical mode profile. Contrast to thermorefractive noise, photothermal noise is an external noise process that is induced by the optical power fluctuations inside the optical resonator and through thermo-optic effect.

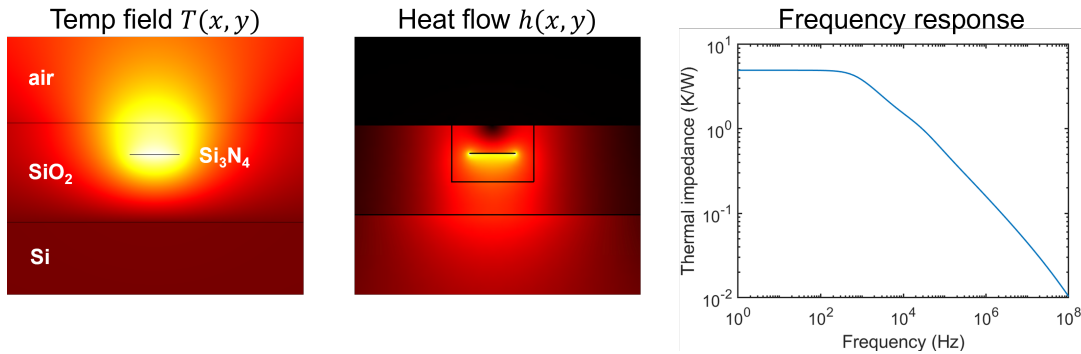


Figure 3.4: 2D static thermal simulation with the silicon nitride waveguide core being the heat source in COMSOL. The thermal impedance has a frequency response with 4.98 K/W at low frequencies and roll-off from 1 kHz.

Here is the procedure for estimating the photothermal noise in a laser cavity or a passive reference resonator, using our high-Q silicon nitride ring resonator that is described in details in Section 2.2.2 and uses the 11  $\mu\text{m}$  wide by 40 nm waveguide geometry and a ring radius of 11.787 mm at the wavelength of 1550 nm. The thermo-optical coefficients of silicon nitride and silica are  $0.95 \times 10^{-5}$  and  $2.45 \times 10^{-5}$  [32], respectively, using which the thermal refractive redshift at 1550 nm in the pure materials of silicon nitride and



silica are,

$$\left. \frac{df_{opt}}{dT} \right|_{SiO_2} = f_{opt} \frac{dn}{ndT} = 1.26 GHz/K, \quad (3.23)$$

$$\left. \frac{df_{opt}}{dT} \right|_{SiN} = f_{opt} \frac{dn}{ndT} = 2.37 GHz/K. \quad (3.24)$$

The thermal impedance can be found in a COMSOL 2D multi-physics simulation including the static thermal simulation with the waveguide core being a heat source and the optical mode profile simulation with the connection from the thermo-optic coefficients. The 2D static thermal simulation is shown in 3.4. The thermal impedance inversely scales with the ring resonator roundtrip length  $L$ , and is simulated to be  $R_{th,0} = 4.98$  K/W and has a frequency response  $R_{th}(f) = R_{th,0}H_{th}(f)$ . The absorption-heating-redshift susceptibility is estimated to be  $\alpha = \Delta f_{res}/P_{abs} = 6.11$  MHz/mW. The fraction of the optical power being absorbed versus the total optical power being dissipated in the ring resonator,  $\xi$ , is needed to estimate the photo-thermal red-shift coefficient  $\Delta f_{res}/P_{opt} = \xi \Delta f_{res}/P_{abs}$ , which is estimated by experimentally measuring the optical power induced red-shift strength  $\Delta f_{res}/P_{opt}$ . Shown in Fig. 3.5 is the experimental measurements of the red-shifted resonances when the probe laser power is being increased. Since the absorption-heating-redshift susceptibility is simulated to be  $\alpha = \Delta f_{res}/P_{abs} = 6.11$  MHz/mW, the absorption loss fraction is  $\xi = 0.647/6.11 = 10.6\%$ . The photothermal effect and the measurement of the absorption loss fraction is also extensively discussed in the previous chapter. The experimentally measured red-shift strength  $\Delta f_{res}/P_{opt} = 0.647$  MHz/mW combined with the simulated thermal frequency response  $H_{th}(f)$  and experimentally measured laser relative intensity noise (RIN) spectrum  $S_{RIN}(f)$  can be used to estimate the photo-thermal frequency noise spectrum induced by the optical power fluctuations in the ring resonators by,

$$S_{PTN}(f) = \left[ \frac{\Delta f_{opt}}{P_{opt}} \right]^2 H_{th}^2(f) P_{opt}^2 S_{RIN}. \quad (3.25)$$

An example of estimating the photothermal noise in a Brillouin laser using the equation shown in Fig. 3.6 above can be found in [33].

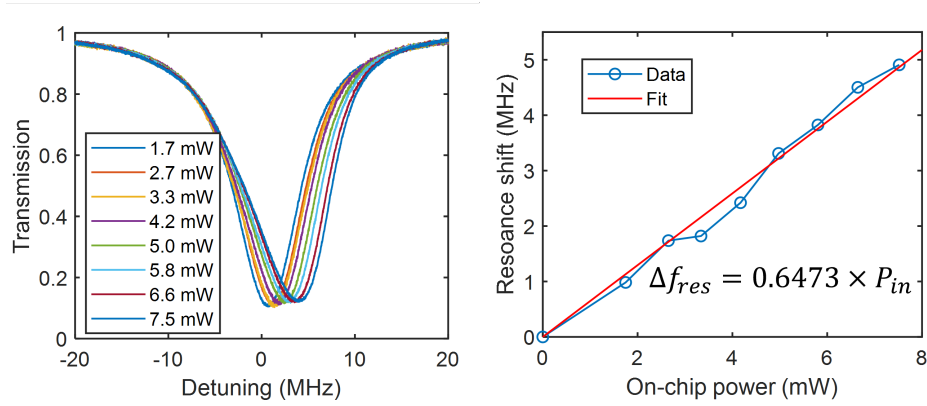


Figure 3.5: Photothermal redshift strength is measured to be  $\Delta f_{opt}/P_{opt} = 0.647$  MHz/mW.

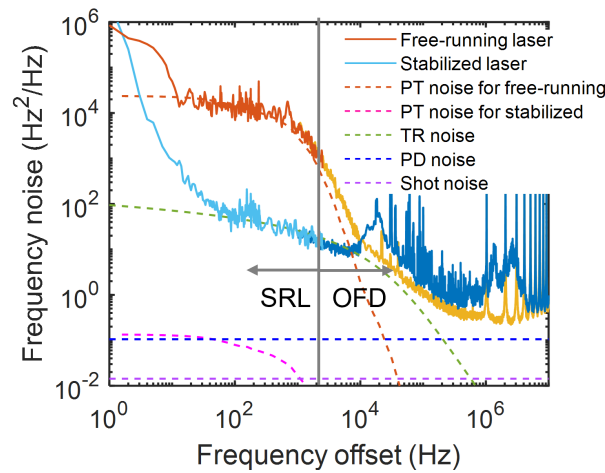


Figure 3.6: Estimated photothermal noise in a Brillouin laser in the ring resonator induced by the pump laser's power intensity fluctuations is compared with the measured Brillouin laser frequency noise spectrum. Details can be found in [33].

### 3.4 Summary and outlook

We introduced the history of the development of timekeeping devices, the modern scientific efforts towards it, and the state-of-the-art modern timekeeping technologies. We

discussed the quantum mechanical origins of laser fundamental phase and frequency noise and the two important laser and resonator noise processes, thermorefractive noise and photothermal noise, and the modeling of each. Finally, we discussed the measurements of laser frequency noise and how to ensure reliable laser frequency noise measurements.

## Bibliography

- [1] “History of timekeeping devices - Wikipedia — en.wikipedia.org.”  
[https://en.wikipedia.org/wiki/History\\_of\\_timekeeping\\_devices](https://en.wikipedia.org/wiki/History_of_timekeeping_devices).
- [2] “Scilly naval disaster of 1707 - Wikipedia — en.wikipedia.org.”  
[https://en.wikipedia.org/wiki/Scilly\\_naval\\_disaster\\_of\\_1707](https://en.wikipedia.org/wiki/Scilly_naval_disaster_of_1707).
- [3] “Marine chronometer - Wikipedia — en.wikipedia.org.”  
[https://en.wikipedia.org/wiki/Marine\\_chronometer](https://en.wikipedia.org/wiki/Marine_chronometer).
- [4] M. A. Lombardi, *Time and Frequency*, in *Encyclopedia of Physical Science and Technology (Third Edition)* (R. A. Meyers, ed.), pp. 783–801. Academic Press, New York, third edition ed., 2003.
- [5] C. Fluhr, B. Dubois, C. E. Calosso, F. Vernotte, E. Rubiola, and V. Giordano, *A cryogenic sapphire resonator oscillator with  $10^{-16}$  mid-term fractional frequency stability*, *Applied Physics Letters* **123** (2023), no. 4.
- [6] T. Kessler, C. Hagemann, C. Grebing, T. Legero, U. Sterr, F. Riehle, M. Martin, L. Chen, and J. Ye, *A sub-40-mHz-linewidth laser based on a silicon single-crystal optical cavity*, *Nature Photonics* **6** (2012), no. 10 687–692.
- [7] D. Matei, T. Legero, S. Häfner, C. Grebing, R. Weyrich, W. Zhang,

- L. Sonderhouse, J. Robinson, J. Ye, F. Riehle, *et. al.*, *1.5  $\mu\text{m}$  lasers with sub-10 mHz linewidth*, *Physical review letters* **118** (2017), no. 26 263202.
- [8] T. L. Nicholson, S. Campbell, R. Hutson, G. E. Marti, B. Bloom, R. L. McNally, W. Zhang, M. Barrett, M. S. Safronova, G. Strouse, *et. al.*, *Systematic evaluation of an atomic clock at  $2 \times 10^{-18}$  total uncertainty*, *Nature communications* **6** (2015), no. 1 1–8.
- [9] S. Sun, B. Wang, K. Liu, M. W. Harrington, F. Tabatabaei, R. Liu, J. Wang, S. Hanifi, J. S. Morgan, M. Jahanbozorgi, *et. al.*, *Integrated optical frequency division for microwave and mmWave generation*, *Nature* (2024) 1–6.
- [10] I. Kudelin, W. Groman, Q.-X. Ji, J. Guo, M. L. Kelleher, D. Lee, T. Nakamura, C. A. McLemore, P. Shirmohammadi, S. Hanifi, *et. al.*, *Photonic chip-based low-noise microwave oscillator*, *Nature* (2024) 1–6.
- [11] A. Hati, C. W. Nelson, C. Barnes, D. Lirette, T. Fortier, F. Quinlan, J. A. DeSalvo, A. Ludlow, S. A. Diddams, and D. A. Howe, *State-of-the-art RF signal generation from optical frequency division*, *IEEE Transactions on Ultrasonics, Ferroelectrics, and Frequency Control* **60** (2013), no. 9 1796–1803.
- [12] T. M. Fortier, M. S. Kirchner, F. Quinlan, J. Taylor, J. Bergquist, T. Rosenband, N. Lemke, A. Ludlow, Y. Jiang, C. Oates, *et. al.*, *Generation of ultrastable microwaves via optical frequency division*, *Nature Photonics* **5** (2011), no. 7 425–429.
- [13] T. Tetsumoto, T. Nagatsuma, M. E. Fermann, G. Navickaite, M. Geiselmann, and A. Rolland, *Optically referenced 300 GHz millimetre-wave oscillator*, *Nature Photonics* **15** (2021), no. 7 516–522.

- [14] B. Stuhl, K. Martin, G. Phelps, and N. Lemke, *A Compact Optical Atomic Clock Based on a Two-Photon Transition in Rubidium*, in *APS Division of Atomic, Molecular and Optical Physics Meeting Abstracts*, vol. 2018, pp. U08–002, 2018.
- [15] M. T. Hummon, S. Kang, D. G. Bopp, Q. Li, D. A. Westly, S. Kim, C. Fredrick, S. A. Diddams, K. Srinivasan, V. Aksyuk, *et. al.*, *Photonic chip for laser stabilization to an atomic vapor with  $10^{-11}$  instability*, *Optica* **5** (2018), no. 4 443–449.
- [16] A. Isichenko, N. Chauhan, D. Bose, J. Wang, P. D. Kunz, and D. J. Blumenthal, *Photonic integrated beam delivery for a rubidium 3D magneto-optical trap*, *Nature communications* **14** (2023), no. 1 3080.
- [17] E. Rubiola, *Phase noise and frequency stability in oscillators*. Cambridge University Press, 2008.
- [18] H. Haken, *Laser theory*, in *Light and Matter Ic/Licht und Materie Ic*, pp. 1–304. Springer, 1984.
- [19] L. A. Coldren, S. W. Corzine, and M. L. Mashanovitch, *Diode lasers and photonic integrated circuits*, vol. 218. John Wiley & Sons, 2012.
- [20] C. Henry, *Theory of the linewidth of semiconductor lasers*, *IEEE Journal of Quantum Electronics* **18** (1982), no. 2 259–264.
- [21] Z. Yuan, H. Wang, L. Wu, M. Gao, and K. Vahala, *Linewidth enhancement factor in a microcavity Brillouin laser*, *Optica* **7** (2020), no. 9 1150–1153.
- [22] R. O. Behunin, N. T. Otterstrom, P. T. Rakich, S. Gundavarapu, and D. J. Blumenthal, *Fundamental noise dynamics in cascaded-order Brillouin lasers*, *Physical Review A* **98** (2018), no. 2 023832.

- [23] E. Rubiola and F. Vernotte, *The companion of Enrico's chart for phase noise and two-sample variances*, *IEEE Transactions on Microwave Theory and Techniques* **71** (2023), no. 7 2996–3025.
- [24] P. Horak and W. H. Loh, *On the delayed self-heterodyne interferometric technique for determining the linewidth of fiber lasers*, *Optics express* **14** (2006), no. 9 3923–3928.
- [25] K. Liu, N. Chauhan, J. Wang, A. Isichenko, G. M. Brodnik, P. A. Morton, R. O. Behunin, S. B. Papp, and D. J. Blumenthal, *36 Hz integral linewidth laser based on a photonic integrated 4.0 m coil resonator*, *Optica* **9** (2022), no. 7 770–775.
- [26] S. Gundavarapu, G. M. Brodnik, M. Puckett, T. Huffman, D. Bose, R. Behunin, J. Wu, T. Qiu, C. Pinho, N. Chauhan, *et. al.*, *Sub-hertz fundamental linewidth photonic integrated Brillouin laser*, *Nature Photonics* **13** (2019), no. 1 60–67.
- [27] K. Liu, J. Wang, N. Chauhan, M. W. Harrington, K. D. Nelson, and D. J. Blumenthal, *Integrated photonic molecule Brillouin laser with a high-power sub-100-mHz fundamental linewidth*, *Optics Letters* **49** (2024), no. 1 45–48.
- [28] G. Huang, E. Lucas, J. Liu, A. S. Raja, G. Lihachev, M. L. Gorodetsky, N. J. Engelsens, and T. J. Kippenberg, *Thermorefractive noise in silicon-nitride microresonators*, *Physical Review A* **99** (2019), no. 6 061801.
- [29] J. H. Dallyn, K. Liu, M. W. Harrington, G. M. Brodnik, P. T. Rakich, D. J. Blumenthal, and R. O. Behunin, *Thermal and driven noise in Brillouin lasers*, *Physical Review A* **105** (2022), no. 4 043506.
- [30] S. Amairi, T. Legero, T. Kessler, U. Sterr, J. B. Wübbena, O. Mandel, and P. O.

- Schmidt, *Reducing the effect of thermal noise in optical cavities*, *Applied Physics B* **113** (2013) 233–242.
- [31] J. Alnis, A. Schliesser, C. Y. Wang, J. Hofer, T. J. Kippenberg, and T. Hänsch, *Thermal-noise-limited crystalline whispering-gallery-mode resonator for laser stabilization*, *Physical Review A* **84** (2011), no. 1 011804.
- [32] A. Arbabi and L. L. Goddard, *Measurements of the refractive indices and thermo-optic coefficients of  $Si_3N_4$  and  $SiO_x$  using microring resonances*, *Optics letters* **38** (2013), no. 19 3878–3881.
- [33] K. Liu, J. H. Dallyn, G. M. Brodnik, A. Isichenko, M. W. Harrington, N. Chauhan, D. Bose, P. A. Morton, S. B. Papp, R. O. Behunin, *et. al.*, *Photonic circuits for laser stabilization with integrated ultra-high  $Q$  and Brillouin laser resonators*, *APL Photonics* **7** (2022), no. 9.

# Chapter 4

## Narrow linewidth stimulated Brillouin scattering lasers

### Brief history and introduction

Photonic integrated ultra-narrow linewidth, ultra-low phase noise lasers, with high output power, have the potential for low cost, size, weight and power solutions for a wide range of precision scientific and commercial applications, including coherent communications [1, 2], fiber-optic sensing [3, 4, 5], atomic and quantum sensing [6], atomic clocks [7, 8], and ultra-low-noise microwave generation[9, 10, 11]. The fundamental linewidth plays a key role in applications that have stringent requirements on the laser frequency noise over several decades offset from carrier from 10 kHz out to multiple MHz. For example, the laser manipulation and interrogation of atom states require ultra-low noise at certain frequency offsets to minimize unwanted interactions with neighboring hyperfine atomic transitions and fast pulse sequencing used in ion and neutral atom manipulation [12]. It is experimentally measured and demonstrated that not only the frequency and phase noise of the master local oscillator laser contributes to the ion qubit's decoherence



through dephasing process but also has a direct impact on the qubit state manipulation fidelity [13, 14]. The phase noise of an ultra-stable laser that is referenced to ultra-stable optical references such as ultra-low-expansion high-finesse single-crystal silicon cavity [15, 16] and ultra-stable atomic optical transitions [17] in optical frequency division can set the performance limit for microwave signal generation [18]. Traditionally, these systems employ costly external cavity lasers and are relegated to costly, table-top systems and utilize frequency doubling of near-infrared (NIR) lasers. In addition to low phase noise and less bulky, other desirable features include high output power, low threshold power, and fabrication in wafer-scale CMOS foundry compatible processes that can be used to integrate other components on chip and allow designs that operate from the visible to NIR such as the ultra-low loss silicon nitride platform [19, 20, 21, 22, 23].

Stimulated Brillouin scattering (SBS) laser process was first discovered bulk media such as solids, liquids and gas along with the observation of hypersonic wave generation [24]. With the development of low-loss optical fibers in the 60s and 70s, SBS was also observed in optical fibers [25]. Later on, the SBS fiber lasers were demonstrated to achieve sub-mW optical pumping threshold [26] and intrinsic linewidths of 30 Hz and 70 Hz [27, 28]. More description of the 100 year history of SBS physics and applications can be found in this excellent review paper [29]. Brillouin scattering process and SBS phenomenon is quite universal and is observed in different materials such as [30], CaF<sub>2</sub> [31], chalcogenide [32], and in different wavelengths such as visible and NIR wavelengths [33, 30, 34].

## SBS laser linewidth narrowing

What makes an SBS laser narrow-linewidth is from its large suppression of the pump-laser-transferred fundamental linewidth due the large ratio between photon lifetime and

phonon lifetime [35, 36],

$$K = 1 + \Gamma_{ac}/\gamma_{opt}, \quad (4.1)$$

where the Brillouin gain bandwidth equals the acoustic phonon decay rate,  $\Gamma_{ac} = 1/\tau_{ac}$ , the inverse of the phonon lifetime, and the optical mode linewidth corresponds to the reverse of the photon lifetime,  $\gamma_{opt} = 1/\tau_{opt}$ . For example, in a low-loss silicon nitride ring resonator, the 0.14 dB/m silicon nitride propagation loss corresponds to a photon lifetime linewidth of 1 MHz, while the phonon-lifetime-related Brillouin gain bandwidth is 100 MHz, resulting in a pump linewidth reduction factor of  $K^2 = 10^4$  and a Stokes linewidth of  $\Delta\nu_s = \Delta\nu_p/K^2$ . After the pump suppression is large enough, the Stokes linewidth enters a "Schawlow-Townes"-like regime and decreases with the increasing photon number in the lasing Stokes mode [36],

$$\Delta\nu_s = \frac{\gamma_{opt}(N_{ac} + n_{opt} + 1)}{4\pi|a_s|^2}, \quad (4.2)$$

where  $\gamma_{opt}$  is the optical mode loss rate,  $|a_s|^2$  is the photon number in the lasing mode,  $N_{ac}$  and  $n_{opt}$  are the thermal occupation numbers of the acoustic and optical modes. There is also a linewidth enhancement factor  $\alpha$  in the Brillouin lasing process that characterizes amplitude-phase coupling of the emission field [37], which in the case of stimulated Brillouin lasing is caused by the phase mismatch between the optical mode and acoustic gain profile [38], yielding a modified linewidth,  $\tilde{\Delta\nu}_s = \Delta\nu_s(1 + \alpha^2)$ .

## Cascaded emission vs cascade-suppressed emission

Cascaded emission happens in SBS lasers because the Brillouin shift is very small compared to optical frequencies and the lasing Stokes can pump the next order Stokes, and the SBS laser can enter the cascaded emission regime after the pump power reaches 4

times the first order Stokes (S1) threshold and the second order Stokes (S2) starts lasing [36, 34], illustrated in Fig. 4.1. The four-times-threshold pump power is called the S1 clamping point, as increasing the pump power passing this point the S1 output power gets clamped. Therefore, SBS lasers usually operate at the S1 clamping power for maximum S1 output power and minimum S1 fundamental linewidth without S2 emission and consequent multimode lasing. Therefore, the cascaded emission characteristic limits the S1 fundamental linewidth and output power. Suppression of the higher order Stokes emissions such as second order Stokes (S2) has been employed in the silicon nitride waveguide SBS lasers through sidewall grating modulation of a silicon nitride ring resonator to split the S2 resonance [39]. In this prior work, the low resonator Q limited the resolution of S2 line splitting and the fundamental linewidth was not characterized [39]. Suppressed S2 in a non-integrated tapered-fiber coupled bulk optic silica microtoroid resonator achieved a fundamental linewidth of 245 mHz at a high output power of 126 mW [40]. However, the limited resonator Q of 31 million resulted in a 49 mW threshold and unwanted output saturation where the laser most likely loses S2-suppression. Although suppressing S2 allows SBS lasers to keep increasing the S1 power at higher pump power and narrowing the S1 fundamental linewidth as a result of the increasing S1 output power, the conversion efficiency drops significantly with increasing pump power, as the S1 output scales with the square root of pump power,  $P_{S1} = \eta\sqrt{P_{in}P_{th}}$ .

## This work

The first few sections describe the results of sub-mW threshold SBS lasers with sub-Hz fundamental linewidths without any spectral resonator designs to suppress S2 using low-loss high-aspect-ratio silicon nitride waveguides described in Chapter 2. Then, the next section describes an S2-suppressed Brillouin laser based on a photonic-molecule integrated

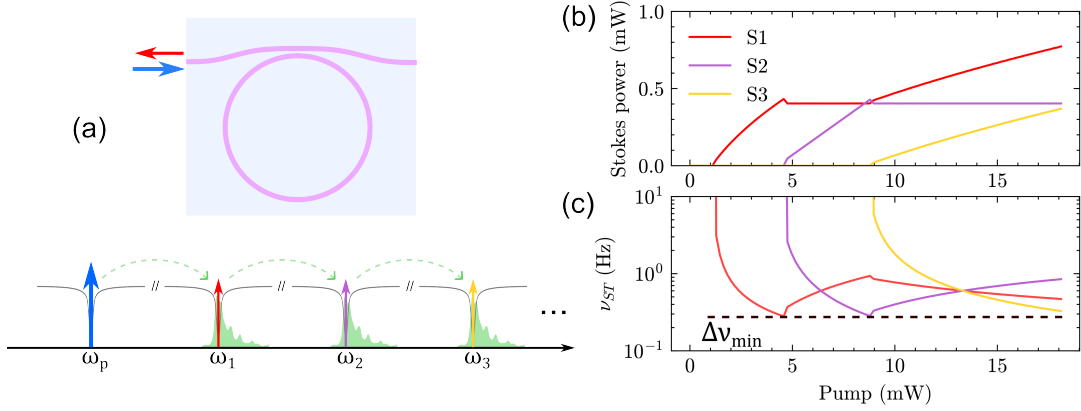


Figure 4.1: Cascaded emission of SBS laser and its consequences on Stokes output powers and linewidths. (a) Cascaded emission diagram. (b) Simulated Stokes output powers and (c) fundamental linewidth versus pump power, using the theoretical framework in [36].

waveguide resonator design that outputs up to 10 mW optical power and achieves a fundamental linewidth of  $71 \pm 18$  mHz, where, however, the 10 mW output power is achieved with a pump power of 170 mW and thus the conversion efficiency is only 6%. Because the S1 output scales with the square root of the pump power,  $P_{S1} = \eta \sqrt{P_{in} P_{th}}$ , the conversion efficiency drops at higher pump power,  $P_{S1}/P_{in} = \eta \sqrt{P_{th}/P_{in}}$ .

In the final section, we propose a simple and novel approach to increase the SBS S1 output power and narrow its fundamental linewidth at the same time by simply increasing the SBS cavity length and reducing the cavity FSR. Integrated SBS lasers based on ultra-low-loss waveguides have been limited to using a microring radius of  $\sim 3.0$  mm or a few times  $\sim 3.0$  mm for one or multiple integers of cavity FSR to match the Brillouin shift frequency, and the cavity Q of up to 100 million in both NIR and visible wavelengths reduces the SBS laser threshold to the sub-milliwatt level [41, 30]. However, a low threshold leads to a low S1 output power, as the SBS lasers without the inhibition of higher order Stokes cascaded emission are pumped at maximum with a pump power that is four times the sub-milliwatt threshold. The SBS theoretical framework [36, 34] suggests that the SBS threshold is proportional to the SBS cavity length and increasing

the SBS threshold using a long SBS cavity can output higher S1 optical power and further reduce the fundamental linewidth. To the best of our knowledge, there is no experimental demonstration to date on exploring the parameter space of increasing the SBS cavity length to meter scale with 100 million cavity Qs and a centimeter footprint, which has been fabricated and used for integrated optical frequency referencing [42, 22]. The coil SBS laser outputs record-high 41 mW optical power into the S1 mode with a record-low 31 mHz fundamental linewidth and single mode operation with a 73 dB side-mode suppression ratio (SMSR). The 4-meter-long coil waveguide resonator enables a decrease in fundamental linewidth through increased total number of photons, reduction in the thermorefractive noise through increased cavity mode volume, and increase in the S1 optical power saturation level through increased optical threshold.

It is interesting to note that in normal SBS lasers without S2 suppression increased cavity Qs result in only reduced S1 threshold and maximum S1 output power consequently but not any change in minimum fundamental linewidths. Therefore, we turned to an approach to design the nested-ring photonic-molecule resonators to suppress S2, where however we found the big drawback that the pump power conversion efficiency drops significantly and the S1 output power is still quite limited. Finally, a simple approach to best tackle this problem is to live with the cascaded emission nature of SBS lasers but to simply increase the SBS cavity length to intentionally increase the S1 threshold and its output power at its clamping point and to decrease the minimum fundamental linewidth.

## 4.1 SBS laser modeling

Much of the following modeling and treatment follows this reference [36]. Because the dilute optical mode energy in the high-aspect-ratio waveguides is mostly in the cladding material of silica, the Brillouin scattering properties in such dilute-mode silicon nitride

waveguides such as the Brillouin shift and gain bandwidth are very similar to those in optical fibers. For example, the Brillouin shift frequency is  $\sim 10.9$  GHz with  $\sim 100$  MHz bandwidth at 1550 nm in standard single mode optical fibers [43]. As the Brillouin scattering process happens in waveguides, the bulk Brillouin gain gets enhanced by the waveguide confinement,

$$G_B = \frac{\rho g_B}{A_{eff}}, \quad (4.3)$$

where  $g_B$  is the bulk Brillouin gain (0.045 m/MW in silica),  $A_{eff}$  is the optical mode area, and  $\rho$  describes the modal overlap between the optical and acoustic modes. In a waveguide ring resonator, the Brillouin gain rate per photon is expressed as,

$$\mu = \frac{h\nu v_g^2 G_B}{2L} = \frac{h\nu v_g^2 g_B \rho}{2V_{eff}}. \quad (4.4)$$

The Brillouin shift frequency is proportional to the optical frequency,

$$\Omega_B = 2 \frac{V_{ac}}{v_{opt}} \omega = \frac{4\pi n_g V_{ac}}{\lambda}. \quad (4.5)$$

## Brillouin frequency matching

**Matching the optical mode FSR with the Brillouin shift frequency** is critical in SBS lasers and can be very challenging due to slight change in material refractive indices and waveguide mode properties from fabrication imperfections. Finding proper ways to mitigate such risks and misalignment in the SBS phase and frequency matching is important, and both experimental measurements and analytical analysis based on the SBS laser modeling are crucial and need to work together coherently, which will be shown and discussed more in later sections. Assuming a perfect Brillouin frequency matching at a particular wavelength  $\lambda$  with  $N$  times the optical mode FSR matching  $\Omega_B$ , as illustrated

in Fig. 4.1(a), we have,

$$\frac{4\pi n_g V_{ac}}{\lambda} = N \times (FSR = \frac{c}{n_g L}) = \frac{Nc}{n_g L}, \quad (4.6)$$

$$\lambda = \frac{4\pi V_{ac} L n_g^2}{Nc}. \quad (4.7)$$

Therefore, the SBS phase and frequency matching wavelength  $\lambda$  can change with a group parameters,

$$\frac{\delta\lambda}{\lambda} = \frac{\delta L}{L} + 2\frac{\delta n_g}{n_g}. \quad (4.8)$$

There are three important notes on such an intricate multi-assumption and multi-parameter analysis. First, since there are parameters that are dependent on each other, it is important to eliminate the dependent parameters down to **only independent parameters or degrees of freedom** so that the parameter redundancy does not get in the way. For example, knowing  $n_g$  is equivalent to knowing  $FSR$ , as  $L = 2\pi r$  is a chosen design parameter. This brings second note: there are two categories of parameters, (A) measurable parameters that can be reliably measured in experiments or predetermined by designers such as phase and frequency matching wavelength  $\lambda$ ,  $n_g$ , and  $L$ , (B) non-measurable parameters that are difficult to measure in experiments or determined in simulations and need to be assumed with some values such as  $V_{ac}$ . Last by not least, assumptions need to be constantly reminded, and carefully and reasonably examined by experimental data if possible, such as the assumptions on  $V_{ac}$  that it is constant with different waveguide designs, and constant at different optical wavelengths, and constant for both the TE and TM modes.

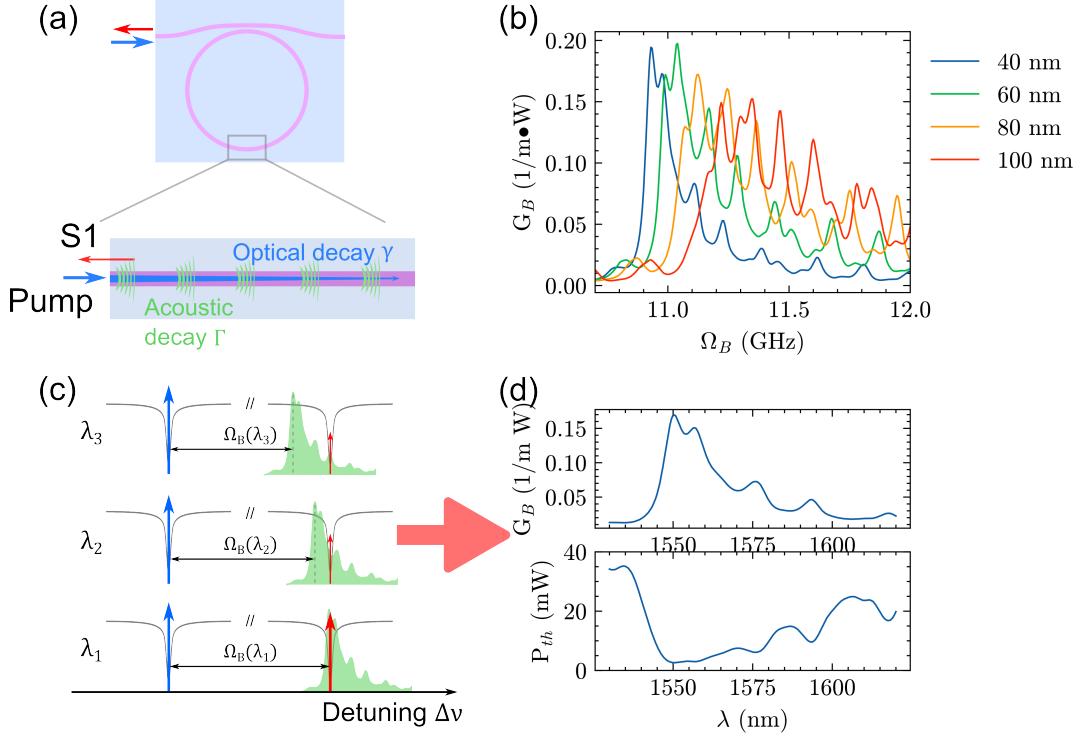


Figure 4.2: SBS phase/frequency matching illustration. (a) Optical and acoustic field decay illustration. (b) COMSOL simulated Brillouin gain profile at 1550 nm for the  $TE_0$  mode in 6  $\mu\text{m}$  wide silicon nitride waveguide with different thicknesses. (c) SBS phase/frequency matching at different optical wavelengths. (d) SBS gain perceived in the S1 lasing mode at different wavelengths resembles the SBS gain spectrum in (b) and impacts the S1 optical threshold.

## Brillouin gain profile

The simplest description for the Brillouin gain profile uses the assumption that the phonon decays exponentially with a phonon lifetime of  $\tau_{ac} = 1/\Gamma$  [44], and the gain profile is similar to the Fourier transform of an exponential delay process that takes the form of a Lorentzian lineshape,

$$G_B(\Omega, \lambda) = G_B(\Omega, \Omega_B(\lambda)) = \frac{G_{B,0}}{1 + i2(\Omega - \Omega_B(\lambda))/\Gamma}, \quad (4.9)$$



where  $\Omega_B(\lambda) \sim 1/\lambda$  is the phonon frequency according to Eq. 4.5, and it is also the peak gain Brillouin frequency, and  $G_{B,0}$  is the peak waveguide Brillouin gain. More practically, such a frequency-dependent Brillouin gain profile in a specific waveguide geometry is simulated in COMSOL. Figure 4.2(b) shows the simulated waveguide Brillouin gain spectra for the fundamental TE mode in the 6  $\mu\text{m}$  wide silicon nitride waveguide (6  $\mu\text{m}$  upper and 15  $\mu\text{m}$  lower cladding) at different thicknesses (40 nm, 60 nm, 80 nm, 100 nm) at the wavelength of 1550 nm. As the Brillouin shift frequency is proportional to the optical frequency and inversely proportional to the wavelength (Eq. 4.5), so is the whole Brillouin gain spectrum, the optical mode for S1 lasing perceives different Brillouin gains accordingly, illustrated in Fig. 4.2(c) and (d). Therefore, the S1 lasing threshold changes accordingly versus wavelength.

Therefore, to achieve an SBS laser at a particular wavelength such as 1550 nm, 1310 nm, or 780 nm needs careful designing on choosing the nitride thickness, precisely determining a ring radius, and etc, where Eq. 4.7 and 4.8 can be very useful in assisting design and testing.

The large Brillouin gain bandwidth  $\Gamma$  due to phonon leaking or no acoustic guiding combined with low waveguid propagation loss and narrow cavity linewidth  $\gamma$  leads to a large pump linewidth suppression [35],

$$\frac{\Delta\nu_s}{\Delta\nu_p} = \frac{1}{(1 + \Gamma/\gamma)^2}. \quad (4.10)$$

## CMT modeling on SBS laser power and linewidth

The SBS laser can be modeled in a fashion similar to the CMT approach in the waveguide resonator modeling presented in Chapter 2, which essentially can be derived from an opto-mechanical-coupled Hamiltonian with the dissipation terms added to both

the optical modes and acoustic modes, described in detail in [36]. The optical modes are denoted in  $a_m$  (e.g.  $a_0$  - pump,  $a_1$  - S1,  $a_2$  - S2, etc.), and the acoustic modes are denoted in  $b_m$  with the opto-mechanical coupling rate being  $\mu$ , which is also referred to as the cavity Brillouin gain rate that can be roughly expressed as Eq. 4.3 and 4.4. The coupled-mode rate equations can be formulated as follows,

$$\dot{a}_m = (i\Delta\omega\delta_{m0} - \gamma/2 + \mu|a_{m-1}|^2 - \mu|a_{m+1}|^2)a_m + i\sqrt{\gamma_{ex}}s_{in}\delta_{m0}, \quad (4.11)$$

$$s_m = F\delta_{m0} + i\sqrt{\gamma_{ex}}a_m, \quad (4.12)$$

where  $\delta_{m0}$  is the delta function,  $\Delta\omega = \omega_0 - \omega_p$  is the pump laser detuning with respect to the pump mode resonant frequency,  $F = \sqrt{P/\hbar\nu}$  is the pump mode photon influx, and  $P_m = \hbar\nu|s_m|^2$  calculates the Stokes powers for the  $m^{\text{th}}$  Stokes. The fundamental/intrinsic linewidth can be expressed by (Eq. (C15) in [36]),

$$\Delta\nu_m = \frac{1}{4\pi|a_m|^2} [\gamma(N_0 + n_0 + 1) + 2\mu|a_m|^2(2n_0 + 1)], \quad (4.13)$$

where  $n_0$  and  $N_0$  are the thermal occupation number of the optical mode and acoustic mode,

$$n_0 = \frac{1}{\exp(\hbar\omega/k_B T) - 1}, \quad (4.14)$$

$$N_0 = \frac{1}{\exp(\hbar\Omega_B/k_B T) - 1}. \quad (4.15)$$

At room temperature 300 K,  $n_0 \sim 0$  for  $\nu = 194$  THz, and  $N_0 \simeq 520$  for  $\Omega_B = 11.9$  GHz. With the  $m^{\text{th}}$  Stokes mode being the highest mode order, Eq. 4.13 can be simplified to,

$$\Delta\nu_m = \frac{\gamma(N_0 + 1)}{4\pi|a_m|^2}. \quad (4.16)$$

Although the cavity Brillouin gain  $\mu$  can depend on the optical mode number  $m$ , it is assumed to be the same for all the Stokes modes.  $\nu$ ,  $\gamma$ , and  $\gamma_{ex}$  are also assumed to be the same for different Stokes modes. So, the analytical model, Eq. 4.12, can be simplified. However, the optical cavity losses do change over a large wavelength range, and need to be retrieved as inputs from actual measured values at different optical wavelengths. Should the optical mode losses be drastically different for different Stokes modes such as S1 and S2, modifications for Eq. 4.12 can be added accordingly. A good example can be the photonic-molecule nested-ring SBS cavity with the S2 lasing mode being a more-lossy and split resonance [45]. A public GitHub repository that has the code for the SBS laser analytical simulations based on the coupled-mode rate equations [36], which is used for all the plots of the simulated Stokes output power and fundamental linewidths such as Fig. 4.1(b) and 4.2(d), can be found online [46].

## First-order-cascaded SBS lasers

Let's start with the simplest case where the pump power is low and only S1 is involved,

$$\dot{a}_0 = (-\gamma/2 - \mu|a_1|^2)a_0 + i\sqrt{\gamma_{ex}}F, \quad (4.17)$$

$$\dot{a}_1 = (-\gamma/2 + \mu|a_0|^2)a_1. \quad (4.18)$$

The S1 threshold condition can be found when the term  $(-\gamma/2 + \mu|a_0|^2)$  reaches 0,

$$a_{0,th}^2 = \frac{\gamma}{2\mu}. \quad (4.19)$$

And the S1 threshold can be expressed by,

$$P_{th} = \frac{\hbar\omega\gamma^3}{8\mu\gamma_{ex}} = \frac{\gamma^3 L}{4\gamma_{ex}v_g^2 G_B} = \frac{\pi^2 n_g^2 Q_{ex} L}{\lambda^2 G_B Q^3}, \quad (4.20)$$

where  $L$  is the SBS cavity length,  $Q$  and  $Q_{ex}$  are the cavity loaded and external coupling Qs. With the pump power above threshold, the S1 output power can be found,

$$P_{S1} = \frac{4\gamma_{ex}^2}{\gamma^2} (\sqrt{PP_{th}} - P_{th}). \quad (4.21)$$

## Second-order-cascaded SBS lasers

The threshold for S2 is the pump power at which the S1 output power is clamped and reaches its maximum with only S1 lasing. The S2 threshold power is also referred to as the S1 clamping point. The CMT rate equations when only S1 and S2 are involved can be expressed as,

$$\dot{a}_0 = (-\gamma/2 - \mu|a_1|^2)a_0 + i\sqrt{\gamma_{ex}}F, \quad (4.22)$$

$$\dot{a}_1 = (-\gamma/2 + \mu|a_0|^2 - \mu|a_2|^2)a_0, \quad (4.23)$$

$$\dot{a}_2 = (-\gamma/2 + \mu|a_1|^2)a_2. \quad (4.24)$$

$$(4.25)$$

At the S2 threshold, similar to the process of finding the S1 threshold, we have  $|a_0|^2 = |a_1| = \gamma/2\mu$  and  $P_{th,S2} = 4P_{th}$ . The S2 output power can also be found,

$$P_{S2} = \frac{\gamma_{ex}^2}{\gamma^2} (P - 4P_{th}). \quad (4.26)$$

## Minimum linewidth in cascaded-emission SBS lasers

At the S2 threshold point or S1 clamp pump power, the S1 reaches minimum fundamental linewidth according to Eq. 4.13 and 4.16,

$$\Delta\nu_{min} = \frac{(N_0 + 1)\mu}{2\pi}. \quad (4.27)$$

This holds for all the Stokes when they reach their first individual clamping points, shown in a simulation of Stokes power output and fundamental linewidth in Fig. 4.1, using Eq. 4.12 and 4.13. Eq. 4.27 suggests two approaches to reduced the minimum Stokes fundamental linewidth  $\Delta\nu_{min}$  by either reducing  $N_0$  or  $\mu$ .  $N_0 = 1/(\exp\{\hbar\Omega_B/h_B T\} - 1)$  approaches to 0 when  $T$  decreases to below  $T = \hbar\Omega_B/k_B = 0.57$  K for  $\Omega_B/2\pi = 11.9$  GHz, meaning  $N_0 + 1 \rightarrow 1$  below 0.57 K, shown in Fig. 4.3. At high temperatures ( $T \gg 0.57$  K),  $N_0 \simeq k_B T/\hbar\Omega_B \simeq T/(0.57K) = 1.8T$ . Theoretically speaking, the minimum Stokes fundamental linewidth reduction can be up to 600 times from 300 K to 1 K. There has been such an attempt to lower down the environmental temperature below 10 K to cool down the phonon to decrease the SBS laser Stokes minimum fundamental linewidth in a cryogenic system[47]. However, there are only three data points at three different temperatures and the linewidth reduction is only 10 times [47].

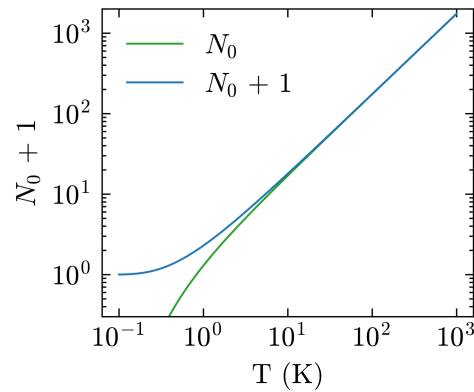


Figure 4.3:  $N_0$  for acoustic phonons at 11.9 GHz frequency as a function of temperature.

The second approach to reduce  $\Delta\nu_{min}$  is by simply increasing the cavity length to reduce  $\mu$ , according to Eq. 4.4. The benefits of this approach are much more pronounced when the waveguide loss is very low and the SBS laser in a single-ring resonator reaches below milli-watt levels. First, the S1 threshold increases linearly with cavity length, thus increasing the S1 output at the clamping power. Second, the minimum fundamental linewidth decreases with increasing cavity length. Third, when the cavity length reaches up to 2 meters and the cavity FSR is reduced to 100 MHz or below, the SBS phase matching is satisfied about every 10 nm, and this relaxes the constraints on the SBS laser cavity length design. This increasing-cavity-length approach is detailed discussed and demonstrated in the last section of this chapter.

### Triangle relationship between $P_{th}$ , $\Delta\nu_{min}$ , and $\mu$

Both Eq. 4.20 on the S1 threshold and Eq. 4.27 on the minimum linewidth depend on the cavity Brillouin gain  $\mu$ , and all other parameters either are constants such as  $\hbar$ ,  $\nu$ , or can be reliably measured values such as  $n_g$ ,  $\gamma_{ex}$  and  $\gamma$ . Therefore, the three unknowns ( $P_{th}$ ,  $\Delta\nu_{min}$ , and  $\mu$ ) with two equations (Eq. 4.20 and 4.27) only need one of them to be measured or known and the other two can be calculated. Such a triangle relationship between the three shown in Fig. 4.4 can be very useful in the modeling, design, testing and analysis of SBS lasers.

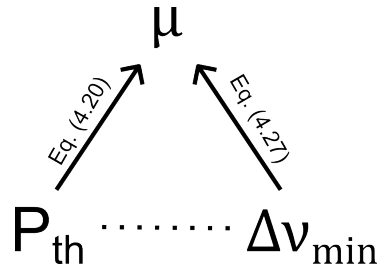


Figure 4.4: Triangle relationship between  $P_{th}$ ,  $\Delta\nu_{min}$  and  $\mu$  (Eq. 4.20 and 4.27).

For example, if  $\mu$  is treated as a model parameter, The experimental measurement of either  $P_{th}$  or  $\Delta\nu_{min}$  yields an estimated  $\mu$  and the other in  $P_{th}$  and  $\Delta\nu_{min}$  can be predicted and verified by its experimental measurement. If  $\mu$  could be simulated and calculated based on multi-physics simulations in COMSOL, both  $P_{th}$  and  $\Delta\nu_{min}$  can be estimated for a particular SBS laser design.

## S1 conversion efficiency

It is worth noting that the S1 and S2 Stokes powers have different dependencies on the pump power and S2 increases linearly with the pump power  $P$  but S1 increases linearly with  $\sqrt{P}$ . The consequences of the square-root power scaling characteristics in S1 will be discussed in more depth in later sections in the case of higher-order-Stokes suppressed SBS lasers.

As the SBS laser is usually pumped at the S1 clamping point,  $P = 4P_{th}$ , the corresponding S1 conversion efficiency can be calculated from Eq. 4.21,

$$\eta_{S1} = \frac{\gamma_{ex}^2}{\gamma^2}. \quad (4.28)$$

Therefore, the S1 conversion efficiency approaches to 1 as the SBS cavity is more and more over-coupled,  $\gamma_{ex} \gg \gamma_{in}$ , but however, over-coupling can significantly increase the S1 threshold, according to Eq. 4.20. This is illustrated in Fig. 4.5.

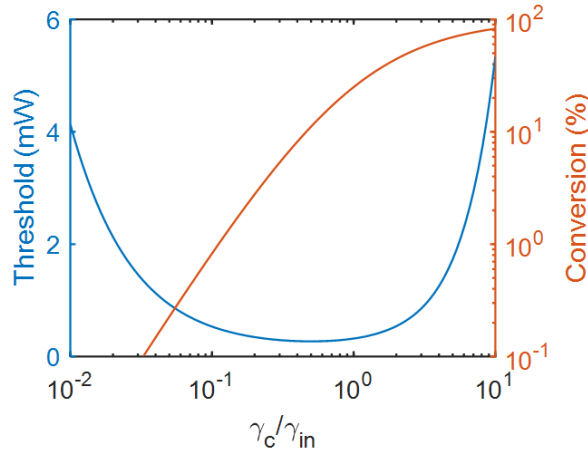


Figure 4.5: Calculated S1 threshold power and S1 conversion efficiency  $\eta_{S1}$  as its clamping point at different coupling regimes of the SBS resonator.

## 4.2 Milliwatt threshold SBS lasers

### 4.2.1 SBS in TE mode 40 nm thick nitride waveguide

The ultra-high Q silicon nitride waveguide ring resonator has a high-aspect ratio waveguide core geometry (11  $\mu\text{m}$  by 40 nm) to mitigate scattering loss and a ring radius of 11.787 mm so that 4 times FSR is aligned to the Brillouin gain frequency shift. The linewidth and Q of the resonator are measured using a 5.871 MHz FSR MZI. The resonator is measured to have a 171 million loaded and 228 million intrinsic Q at 1550 nm, as shown in Fig. 4.6(b), while the maximum intrinsic Q is measured at 1570 nm to be 422 million [20].

The Thorlabs ULN hybrid semiconductor laser is used as the pump laser and is frequency-locked to the resonator for the Brillouin laser operation at 1550 nm. The S1 threshold power is measured to be 2.4 mW, as shown in Fig. 4.7(a), where the Stokes powers are measured on an optical spectral analyzer (OSA). A 1.18 MHz FSR fiber MZI is used as the optical frequency discriminator (OFD) for the laser frequency noise measurements. The fundamental linewidth is the white-frequency-noise floor ( $S_w$ )



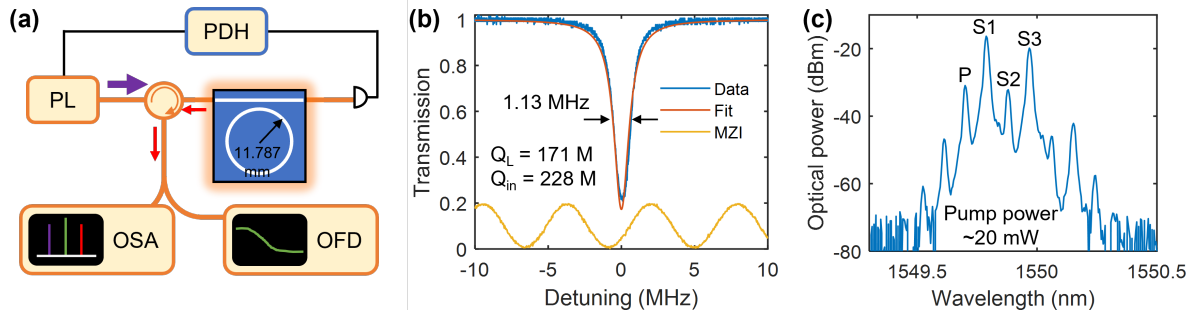


Figure 4.6: TE SBS. (a) SBS laser operation with OSA and OFD measurements. (b) Spectral scan of the SBS resonator at 1550 nm. (c) SBS laser spectrum on the OSA shows cascaded emission at 1550 nm.

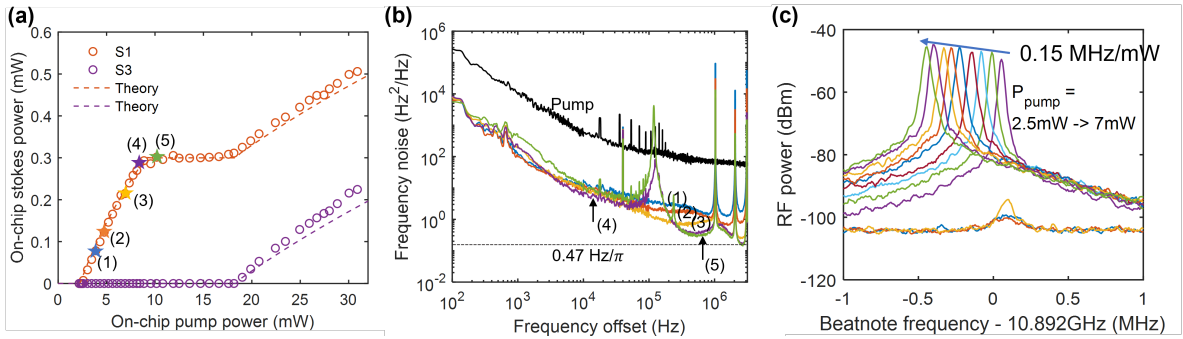


Figure 4.7: SBS laser Stokes powers and linewidth at 1550 nm. (a) Measured S1 and S3 on-chip powers with the simulated curves with an S1 threshold of 2.4 mW. (c) Pump-S1 beatnote frequency as a function of the on-chip power power shows a linear dependency of 0.15 MHz/mW. With the fluctuation within 1 MHz, the group index can be estimated to be  $n_g = 1.486 \pm 0.001$ .

times  $\pi$ . As shown in Fig. 4.7(b), a minimum S1 fundamental linewidth of 0.47 Hz is measured at a 9.5 mW pump power. The pump-S1 beatnote is monitored and measured on an electric spectral analyzer (ESA) while the pump power is being increased, shown in Fig. 4.7(c), and the beatnote changes by less than 1 MHz around 10.892 GHz with the pump power increasing from 2.5 mW to 7 mW. As the S1-pump beatnote frequency is 4 times the FSR, the group index can be accurately calculated based on the measured S1-pump beatnote frequency for the 11  $\mu\text{m}$  by 40 nm silicon nitride waveguide at 1550 nm,  $n_g = 1.4866 \pm 0.0001$ . If the beatnote measurement has an uncertainty level of 10 MHz, that would result in an uncertainty at the fourth significant digit for the group

index measurement,  $n_g = 1.486 \pm 0.001$ .

#### 4.2.2 SBS lasers in TM mode 80 nm thick nitride waveguide

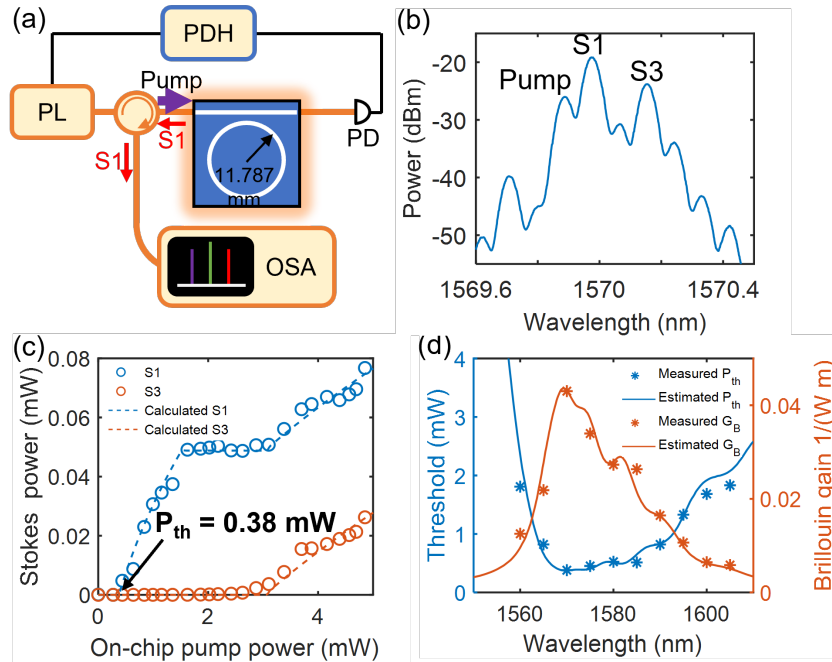


Figure 4.8: TM SBS at 1570 nm. (a) SBS laser operation diagram. (B) SBS laser spectrum on OSA. (c) Measured S1 and S3 on-chip Stokes powers with an S1 threshold of 0.38 mW. (d) Measured S1 threshold powers at different wavelengths enables calculation of the waveguide Brillouin gain at each wavelength point.

Much of the work in this subsection can be found in [41]. The resonator is a bus-coupled  $TM_0$  mode design with an 11  $\mu\text{m}$  wide by 80 nm thick silicon nitride core design located between a 15  $\mu\text{m}$  thick thermal oxide lower cladding and 6  $\mu\text{m}$  thick deposited upper cladding fabricated on a 200 mm wafer-scale process, illustrated in Fig. 2.10. The 11.787  $\mu\text{m}$  resonator radius is the same as the TE waveguide SBS resonator design. The waveguide core thickness is increased from 40 nm to 80 nm to introduce the  $TM_0$  mode besides the TE modes. The 6.898  $\mu\text{m}$  bus-ring coupling gap achieves slight under-coupling of the TM mode and very weak coupling of the TE modes due to much higher

mode confinement compared to the TM mode. Therefore, only the  $TM_0$  mode is properly coupled, and this coupling design makes it a *quasi-single-mode* resonator, although the waveguide by its nature is a multi-mode waveguide.

Next, we demonstrate the SBS laser using the TM mode waveguide resonator by frequency lock a tunable laser (Velocity™ TLB-6700) the resonator. Measurement of S1 on an OSA (Fig. 4.8(b)) as a function of the input pump power at 1570 nm (Fig. 4.8(c)) shows an S1 threshold of 0.38 mW. Similarly, the S1 threshold power is also measured at other wavelengths, shown in Fig. 4.8(d), indicating that the 0.38 mW threshold power at 1570 nm is the minimum threshold and the Brillouin gain at 1570 nm is at its maximum. The low S1 output power makes it difficult to measure the S1 frequency noise and linewidth with a decent signal-to-noise ratio (SNR).

The cavity Brillouin gain is calculated using the S1 threshold equation (Eq. 4.20) shown by the orange stars in Fig. 4.8(d) and is compared with a calculated curve by using the simulated Brillouin gain profile in 40 nm thick nitride TE mode waveguide (blue curve in Fig. 4.2) and the Brillouin gain calculation equation at different acoustic frequencies (Eq. 4.9). Although the calculated curve of the Brillouin gain versus wavelength is fitted with the measured data points, the overall profile resembles very well with the measurements, indicating that the Brillouin gain for the TE mode in the 40 nm waveguide is quite similar to that for the TM mode in the 80 nm waveguide.

The pump-S1 beatnote signal is detected on a 40-GHz bandwidth fast u2t photodetector and measured on an ESA for different wavelengths is shown in Fig. 4.9(b) and 4.10(b), showing that the cavity FSR increases with wavelength, 0.05 MHz/nm, due to the cavity dispersion in the wavelength domain. The linear fitting for the calculated group index yields  $n_g(\lambda) = 1.4956 \times [1 - 9.33 \times 10^{-4}(\lambda - 1550)/50]$ . In the previous subsection of the TE SBS in the 40 nm thick nitride waveguide ring resonator with the same ring radius, the group index at 1550 nm for the  $TE_0$  mode in 40 nm thick waveguide

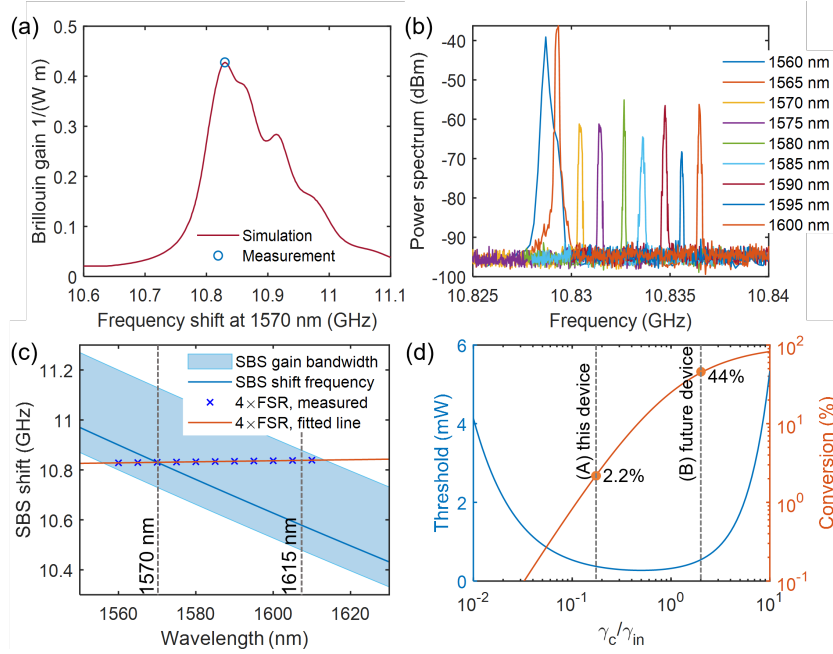


Figure 4.9: TM SBS frequency matching, S1 efficiency, and threshold. (a) The SBS gain profile in the 80 nm nitride TM waveguide uses that in the 40 nm nitride TE waveguide. (b) Pump-S1 beatnote on an ESA at different wavelengths. (c) SBS frequency matching versus wavelength. (d) Calculated threshold and conversion efficiency of S1 at its clamping point based on the measured parameters of this SBS device.

is  $n_g = 1.486 \pm 0.001$ , shown in Fig. 4.7(c). Compared to  $n_g = 1.486 \pm 0.001$ , the group index at 1550 nm for the  $TM_0$  mode in the 80 nm thick waveguide increases by 0.64%, which is very close to the value of 0.4% from the Lumerical MODE simulation on the group index versus waveguide thickness for different waveguide modes.

Using the cascaded Brillouin laser model, we can simulate the S1 and S3 Stokes power (dashed curves in Fig. 4.8(c)) with the measured loaded and intrinsic Q at 1570 nm and an estimated Brillouin gain of  $0.043 (m \bullet W)^{-1}$ . The laser power conversion efficiency for S1 at its first clamping point with the pump power of 1.5 mW is  $\sim 3.1\%$ . The low conversion efficiency is due to the bus-ring under-coupling ( $\gamma_{ex}/\gamma_{in} = \sim 0.17$ ). Designing the bus-ring coupling to have the resonator slightly over-coupled ( $\gamma_{ex}/\gamma_{in} = \sim 2$ ) can significantly increase the conversion efficiency while keeping the threshold still

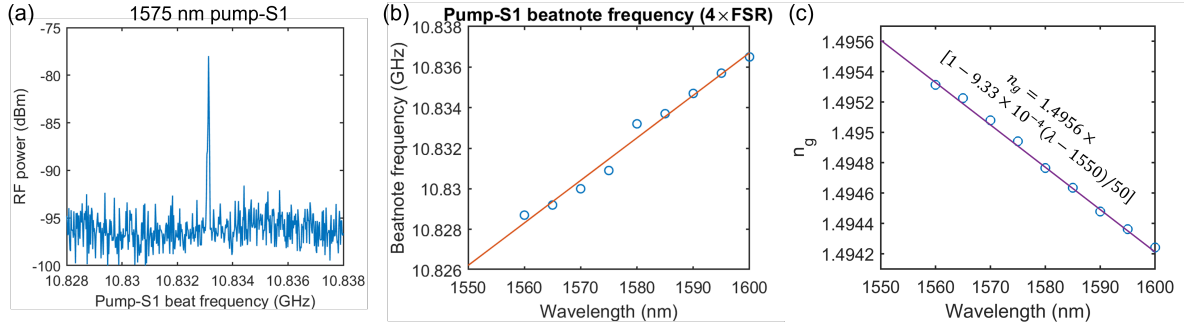


Figure 4.10: Pump-S1 beatnote and group index versus wavelength. (a) Pump-S1 beatnote at 1570 nm on ESA. (b) Beatnote frequency with a linear fitting from 1550 nm to 1600 nm. (c) Group index calculated from the beatnote frequency from 1550 nm to 1600 nm with a linear fitting,  $n_g(\lambda) = 1.4956 \times [1 - 9.33 \times 10^{-4}(\lambda - 1550)/50]$ .

low, shown in Fig. 4.9(d).

### 4.2.3 Photothermal and thermorefractive noise in SBS lasers

Photothermal noise is an important and commonly-seen noise source in SBS lasers due to the high pump circulating power in the SBS ring resonators. Detailed discussion on the characteristics and estimation procedure can be found in Chapter 3. Due to the roll-off of the photothermal response above 1 kHz, the photothermal noise usually dominates at low frequencies below 1 kHz, and can be reduced by increasing SBS resonator Qs and decreasing the laser threshold, or reducing the pump laser intensity noise.

In contrast to the fact that the photothermal noise is induced by the fluctuations in the intra-cavity optical power and is an external noise process, the thermorefractive noise is intrinsic to the SBS resonator and can be carried to and exhibit in the SBS laser frequency noise. The primary factor that can effectively reduce the resonator-intrinsic thermorefractive noise is by increasing the resonator optical mode volume and increasing the waveguide round-trip length. By increasing the SBS resonator mode volume, there are other benefits that go along with the thermorefractive noise reduction such as the increase in the output power and reduction in the fundamental linewidth. This principle

is demonstrated experimentally in the last section of this chapter using a 4-meter-coil resonator for SBS lasing.

### 4.3 Circulator-free SBS lasers

As the S1 in SBS lasers is harnessed from the reflection of a single-bus-coupled ring resonator, an optical circulator is needed to drop the S1 power from the reflection port. Moreover, there is often residual reflection of the pump power at the fiber-to-chip facet coupling, necessitating the need for a very narrow bandwidth filter to filter S1 and reject the reflected pump. The integration of an add-drop ring resonator filter to drop the S1 power and reject any pump power removes the need for an optical fiber circulator. Here, we demonstrate a photonic integrated circuit (PIC) design with a bus-coupled ring resonator for SBS lasing and an add-drop filter for dropping S1 on the same chip. This SBS laser can operate by dropping S1 using the add-drop ring resonator filter without an optical fiber circulator. Such a circulator-free SBS laser outputs the S1 power from the drop bus of the filter resonator and does not need a circulator. This SBS laser measures 11.0 mW threshold, 27% conversion efficiency and 1.3 Hz fundamental linewidth at 42.0 mW pump power, reported in details in [48].

The PIC design is based on the ultra-low-loss silicon nitride waveguide (6  $\mu\text{m}$  by 80 nm). Shown in Fig. 4.11(a) and (b), the SBS ring resonator and the add-drop filter resonator are coupled to the same bus waveguide, while the filter ring has an additional drop bus. The SBS ring radius is 2.693 mm to satisfy the SBS frequency matching condition near 1550 nm,  $\Omega_B = 1 \times FSR$ . The bus-ring coupling gap is 2.5  $\mu\text{m}$ . The filter ring radius is 1.000 mm, and the bus-ring coupling gap is 0.5  $\mu\text{m}$ , so that the filter resonator FSR is about 3 times the SBS resonator FSR and the filtering window is as wide as  $\sim 1$  GHz. Spectral scan (Fig. 4.11(c)) of the PIC through 1 $\rightarrow$ 2 and 1 $\rightarrow$ 3 using a

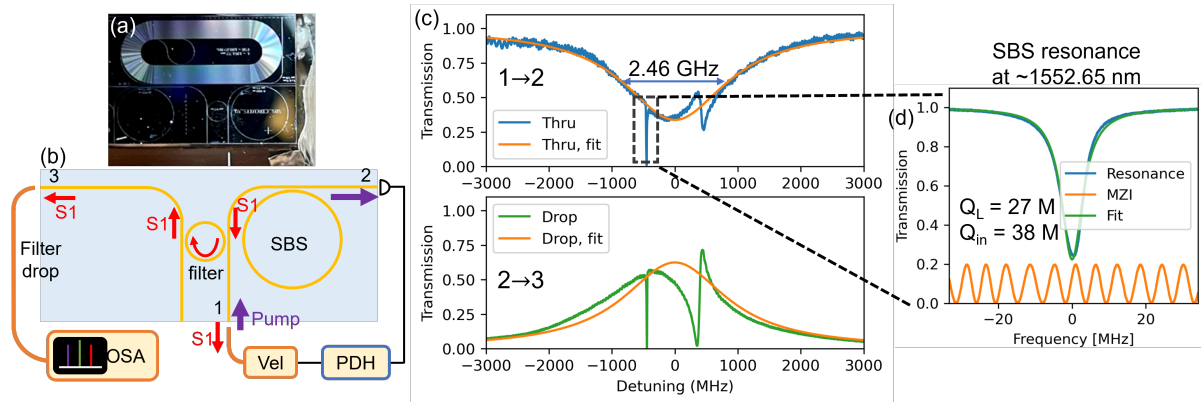


Figure 4.11: Circulator-free SBS laser PIC. (a) Optical image of the PIC device. (b) Circulator-free SBS laser operation diagram. (c) Spectral scan of the PIC through 1→2 and 1→3. (d) Zoom-in of the split resonance. (d) SBS resonator Q and linewidth measurement.

fiber MZI with a 5.87 MHz FSR shows that at 1552.65 nm the SBS resonator resonance is very close to the filter resonance center and the filter resonator has a linewidth and filtering window of 2.46 GHz. This SBS resonator resonance can be used for generating S1, which is then dropped by the add-drop filter. The SBS resonator is measured to have a 27 million loaded and 38 million intrinsic Q (Fig. 4.11(d)).

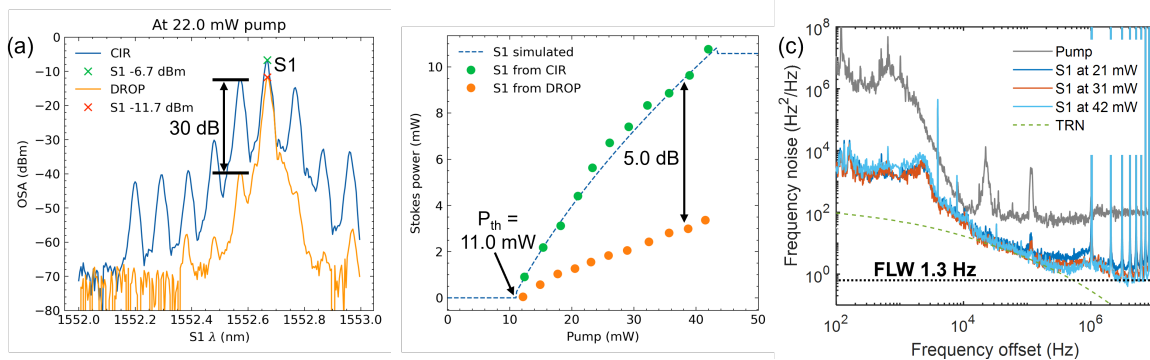


Figure 4.12: Circulator-free SBS laser threshold and fundamental linewidth measurement. (a) OSA spectrum of the SBS laser dropped by a circulator and the ring filter. (b) S1 on-chip power versus on-chip pump power. (c) Frequency noise at different pump powers. TRN, thermorefractive noise.

The PIC device is edge coupled with cleaved fibers and index gel and the coupling loss at each coupling is optimized to be  $\sim 3$  dB, which is used for the on-chip power

calibration. A widely tunable laser (Velocity™ TLB-6700) is used as the pump source and frequency locked to the SBS resonator resonance that is right next to the one at 1552.65 nm so that S1 power can be dropped by the filter. For comparison, the SBS laser is also operated in a nearby wavelength so that S1 cannot be dropped by the filter and needs a circulator. The SBS laser threshold is measured to be 11.0 mW. The S1 power from the reflection port (Fig. 4.12(a)) is observed on an OSA, and the S1 power spectrum dropped by the filter has a 30 dB pump rejection at 22.0 mW pump power. The S1 output dropped by the filter has an excess loss of 5.0 dB compared to being dropped by the circulator. Because of the 3 dB coupling loss at the fiber-chip coupling, the circulator-free SBS laser outputs  $\sim 1$  mW S1 power into the fiber from the filter drop port.

The frequency noise and fundamental linewidth of the circulator-free SBS laser is also measured by the self-delayed homodyne laser noise measurement method, where the fundamental linewidth is calculated by  $\Delta\nu_F = \pi S_w$ . The S1 frequency noise is measured at different pump power and the minimum fundamental linewidth is measured to be 1.3 Hz at 42.0 mW pump power.

## 4.4 Higher-order-Stokes emission suppression

As discussed in the first section of this chapter, the pump power is often set to four times the S1 threshold to avoid the cascaded emission, thus limiting the output power of S1 and linewidth narrowing. Inhibition of the higher order Stokes emission such as S2 has been employed with silicon nitride waveguide SBS cavity design through sidewall grating modulation of the cavity waveguide to split the S2 resonance [39]. Suppressed S2 in a non-integrated tapered-fiber coupled bulk optic silica microtoroid resonator achieved a fundamental linewidth of 0.25 Hz at a high output power of 126 mW with an S1 threshold



of  $\sim 49$  mW [40].

Here, we demonstrate a nested-ring photonic-molecule integrated waveguide resonator with split resonances to suppress the higher-order Stokes emissions. The S2-suppressed SBS laser has a S1 threshold of 2.3 mW and outputs  $\sim 11$  mW with a fundamental linewidth of  $71 \pm 18$  mHz, corresponding to  $23 \pm 6$  mHz<sup>2</sup>/Hz white-frequency noise floor near 1570 nm. The laser phase noise is measured at -155 dBc/Hz at 10 MHz offset. The nested resonator is fabricated in a 200 mm silicon nitride CMOS-foundry compatible wafer-scale platform and has a 184 million intrinsic and 92 million loaded Q, enabling a resonance splitting of 198 MHz. Increasing the pump power from above the threshold to 170 mW ( $\sim 70$  times the 2.3 mW threshold), no higher order Stokes are observed, confirming single mode operation. Details of this demonstration can be found in [45].

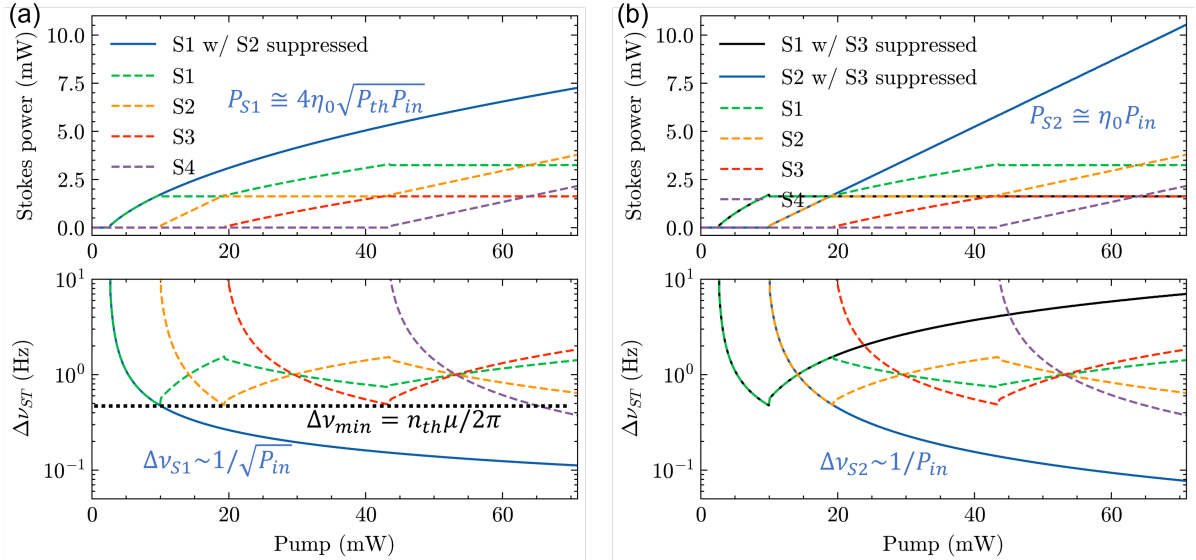


Figure 4.13: SBS numerical simulation under the conditions of cascaded emission, S2-suppression and S3 suppression. (a) Upper shows the Stokes power of S1 – S4 versus pump power (dash lines) in the cascaded emission and S2-suppressed emission (solid line). The lower shows the fundamental linewidth in cascaded and S2-suppressed emission. (b) Upper shows the power of S1 – S4 versus pump power (dash lines) in the cascaded emission and S3-suppressed emission (solid line). The lower shows the Stokes fundamental linewidth in the cascaded emission and S3-suppressed emission. Differential efficiency  $\eta_0 = \gamma_{ex}^2/\gamma^2$ .

Figure 4.13 shows the simulation of the Stokes output powers and linewidths under cascaded emission, S2-suppressed emission and S3-suppressed emission. With S2 suppression, the output of S1 is expressed by Eq. 4.21 and scales with  $\sqrt{P}$ , resulting in significant efficiency drop in conversion efficiency,  $\eta(S1) = 4\gamma_{ex}^2/\gamma^2\sqrt{P_{th}/P}$ . However, with S3 suppression to harness S2 as the SBS laser primary output, the S2 increases linear with the pump power with a different efficiency of  $\eta_0 = \gamma_{ex}^2/\gamma^2$ . By the means of higher-order-Stokes suppression, the Stokes output power breaks the limit of the cascaded emission, allowing the fundamental linewidth to keep narrowing with the increasing Stokes output power  $P_{out}$ ,

$$\Delta\nu = \frac{n_{sp}\hbar\omega\gamma_{ex}\gamma}{4\pi P_{out}} = \frac{n_{sp}\hbar\omega^3}{4\pi Q_{ex}QP_{out}}, \quad (4.29)$$

where the spontaneous emission factor  $n_{sp}$  in SBS lasers is the acoustic phonon thermal occupation number  $N_0$  by Eq. 4.15. If the modification with a linewidth enhancement factor is necessary [38], we have  $\Delta\tilde{\nu} = \Delta\nu(1 + \alpha_H^2)$ .

The photonic molecule resonator is based on a nested double-ring structure shown in Fig. 4.14(a) that couples the two ring resonators to produce the resonance splitting at certain resonances. The resonator uses the 11  $\mu\text{m}$  wide by 80 nm thick waveguide design and the fundamental TM mode. The outer ring has a radius of 11.787 mm to satisfy the Brillouin frequency matching near the wavelength of 1570 nm. The inner ring radius is 10.50 mm. The bus-ring gap of the outer ring is 5.2  $\mu\text{m}$  for critical coupling, and the ring-ring gap is 5.0  $\mu\text{m}$  to introduce coupling between the rings that creates a resonance splitting of  $\sim 100$  MHz. To further increase the suppression of the S2 emission, we add an auxiliary bus waveguide with a bus-ring gap of 2.5  $\mu\text{m}$  to over-couple the inner ring to intentionally add loss to the inner ring resonances, resulting in a decreased loaded Qs at the split resonance, which further increases the suppression of S2.

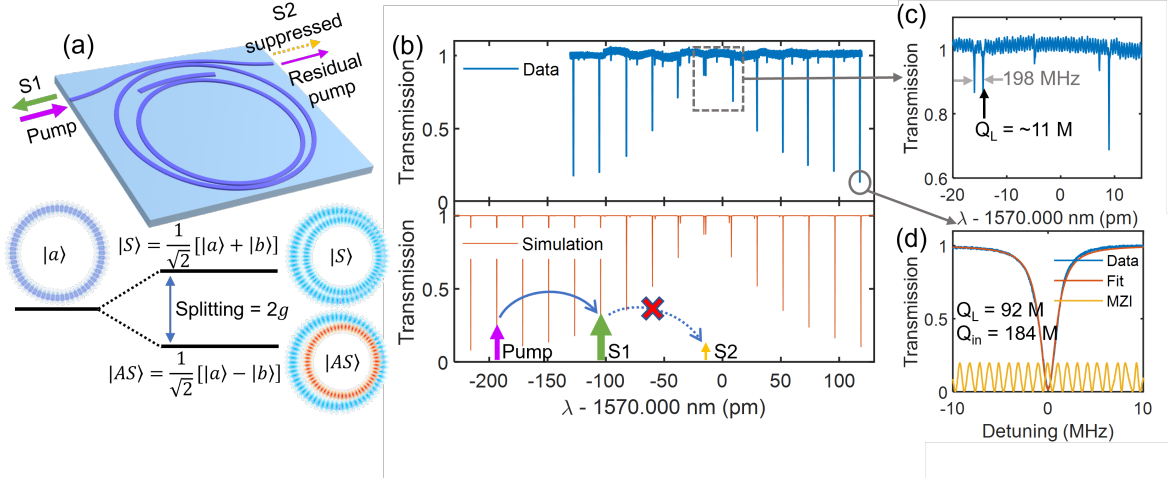


Figure 4.14: S2-suppressed SBS design. (a) Illustration of coupled-ring resonator with split resonances due to mode splitting for S2 suppression, where the split modes correspond to symmetric  $|S\rangle$  and asymmetric  $|AS\rangle$  hybrid modes. (b) Normalized transmission shows a split resonance and other non-split resonances near 1570 nm. (c) Zoom-in of the split resonance. (d) Q and linewidth measurement of the high-Q non-split resonance.

As shown in Fig. 4.14(b), the pump laser is aligned with the non-split resonance that is 8 FSRs away from the split resonance with the intention to suppress S2. The non-split resonance Q is measured to be 184 million intrinsic and 92 million loaded around 1570 nm, while the resonance split at 1569.986 nm is measured to be 198 MHz with a loaded Q of 11 million, shown in Fig. 4.14.

To demonstrate S2 suppression, a widely tunable laser (Velocity™ TLB-6700) is locked to the non-split resonance located 8 FSRs away from the split resonance as the pump and is amplified by an EDFA. The S1 output power is coupled to a fiber circulator at the reflection port and measured on an OSA. The S1 threshold is measured to be 2.3 mW and the pump power is increased up to 170 mW without observation of S2 shown in Fig. 4.15(d).

The frequency noise and fundamental linewidth are measured using a fiber MZI OFD, and the fundamental linewidth  $\Delta\nu_F$  is calculated from the white-frequency-noise floor,

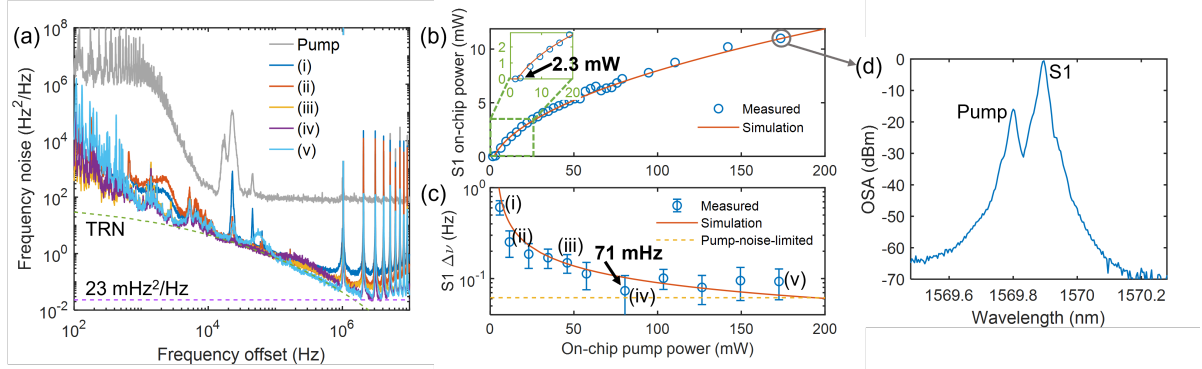


Figure 4.15: S2-suppressed SBS laser threshold, output power and fundamental linewidth measurement. (a) OFD frequency noise of S1. (b) S1 on-chip power with measured 2.3 mW threshold. (c) Fundamental linewidth versus pump power. (d) S2-suppressed SBS laser on OSA.

$\Delta\nu_F = \pi S_w$ . The S1 frequency noise and output power are measured as a function of increased pump power, shown in Fig. 4.15, demonstrating linewidth narrowing. The simulation of S1 output power and linewidth in Fig. 4.15(b) and (c) uses the SBS laser CMT model laid out in previous sections in this chapter and the measured resonator linewidths and S1 threshold as the model input.

The equivalent single-sideband phase noise  $S_\phi(f)$  for the measured frequency noise  $S_\nu(f)$  at on-chip pump power of 170 mW, shown in Fig. 4.16, is calculated by,

$$S_\phi(f) = \frac{S_\nu(f)}{f^2}. \quad (4.30)$$

The OFD laser frequency noise measurement uses the Thorlabs PDB450C with the trans-impedance (TIA) gain set to 10<sup>4</sup> V/A, whose output noise  $S_{pd}(f)$  in V<sup>2</sup>/Hz sets to ultimate measurement noise floor in the OFD measurements. The balanced detection output noise can be sampled on the DAC without light input, and the output noise is then converted to an equivalent frequency noise under the same condition as the laser

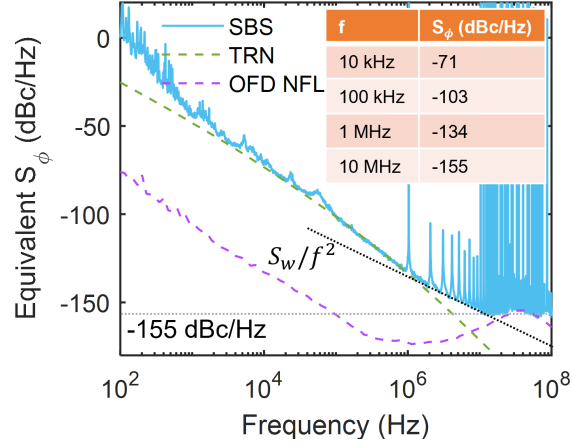


Figure 4.16: Single sideband phase noise is calculated from the frequency noise at the pump power of 170 mW with the phase noise reaching -155 dBc/Hz at 10 MHz. Above 10 MHz, the measured phase noise is limited by OFD noise floor (NFL).

frequency is measured,

$$S_{NFL}(f) = S_{pd}(f) \left( \frac{f}{\sin(\pi f \tau_D) V_{pp}} \right)^2, \quad (4.31)$$

where  $\tau_D$  is the group delay in the fiber MZI and  $V_{pp}$  is the peak-to-peak voltage of the fiber MZI sinusoidal response from the balanced detection output. The characterized photodetector noise is compared with the measured phase noise to show the OFD noise floor above 10 MHz in Fig. 4.16.

To avoid the conversion efficiency drop of S1 at high pump power, the split resonance is also used for S3 suppression to harness S2 as the SBS laser output that grows linearly with the pump, according to Eq. 4.26. However, a four-wave mixing parametric process occurs at the 55-mW pump power and stops the increase of S2 output, unfortunately.

## 4.5 Coil SBS lasers

Large mode volume lasers, such as fiber-based external cavity lasers (ECLs), support the large intra-cavity photon number and high cavity Qs are needed to reduce linewidth and increased output power. Yet, these table-top lasers are highly susceptible to environmental disturbances and require complex cavity stabilization techniques. Moving these systems to the chip-scale is important to improving stability, but most approaches that increase the mode volume lead to a decrease in FSR which drives the laser multimode, requiring the use of optical filters or Vernier cavities at the expense of complexity and reduced reliability and lower output power. Low linewidth integrated designs include ECLs [49, 50, 51], self-injection locking lasers (SIL) [22, 23], and SBS lasers [30, 34, 41, 33, 52]. State of the art integrated ECLs are capable of output powers in the range of 20 mW with the fundamental linewidth on the order of 10 Hz [49, 50]. Integrated SIL and SBS lasers are capable of producing sub-Hz fundamental linewidth, but their output power has been limited to the microwatt to milliwatt regime by output saturation, the onset of higher order modes, and small cavity mode volume [30, 34, 41].

SBS lasers reduce optical frequency noise through nonlinear feedback between photons and phonons. Yet, achieving both high output power and narrow linewidths in SBS laser has been challenging. To date, integrated SBS lasers employed small cavity mode volumes set by the phase matching condition between cavity resonance and the Brillouin frequency shift. The requirement for single mode operation has driven SBS laser cavity designs to support one or more multiple FSR per Stokes frequency shift from the pump where the Brillouin gain bandwidth overlaps with only a single cavity resonance [30, 34, 41, 33, 52]. This also leads to cascaded emission, which limits the output power and linewidth narrowing. Therefore, designs that inhibit the onset of second order Stokes lasing have been employed to decrease the linewidth and increase the single mode output power

[39, 40, 45]. However, in these designs the first-order Stokes (S1) laser emission grows modestly— scaling with the square-root of the pump power —limiting the output power and the linewidth [45, 36]. Additionally, the small mode volume limits the linewidth through thermorefractive noise which scales inversely with the optical mode volume. A typical integrated SBS laser is implemented with a resonator with radius on the order of 3 mm to 10 mm to achieve one or more cavity FSRs to match the Brillouin shift frequency in the range of 10 – 27 GHz for operation in the visible to near-infrared wavelengths. While increasing the resonator Qs of these integrated SBS cavities to 100 – 720 million has enabled reduction of the SBS threshold to the sub-milliwatt level [30, 41], low-threshold designs and the cascaded emission limit the fundamental linewidth and the output power. New solutions are needed for laser design, and in particular SBS lasers, to overcome these limits and allow further reduction in linewidth and increase in optical output power.

Here, we demonstrate the realization of a large mode volume integrated SBS laser that can simultaneously achieve high output power and low fundamental linewidth without the onset of cascaded or multimode lasing. The meter-scale coil waveguide resonator enables a decrease in linewidth through an increased number of photons, a reduction in the TRN floor, and an increase in the S1 optical power saturation level due to an increased optical threshold. The SBS laser is realized in a 4-meter long coil-resonator cavity with 160 million intrinsic Q fabricated in the ultra-low loss silicon nitride platform and outputs 41 mW optical power into the S1 mode with 31 mHz fundamental linewidth and single mode operation. We further demonstrate that this laser can be Vernier tuned across a 22.5 nm range. Remarkably, although the silicon nitride waveguide 4-meter-coil resonator is a multimode cavity with 48.1 MHz FSR that supports 5 longitudinal cavity modes across the Brillouin gain bandwidth, the strong nonlinear Brillouin photon-phonon feedback process demonstrates high selectivity resulting in a 73 dB sidemode suppression ratio (SMSR). Owing to its compact footprint and efficiency, this approach to narrow

linewidth and high-power integrated lasers may enable portable new forms of precision applications spanning from visible to NIR wavelengths.

## Principle of operation

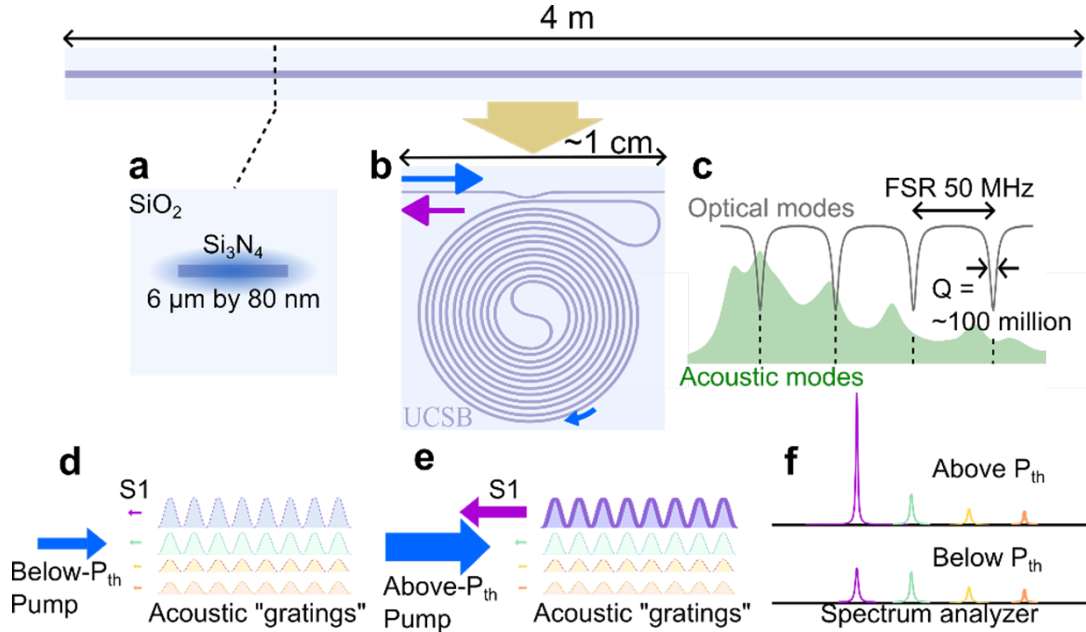


Figure 4.17: Large mode volume SBS laser design and operation principles.

The principle of operation and the large mode volume SBS laser configuration are illustrated in Fig. 4.17. A 4-meter long coil waveguide cavity is implemented as an ultra-low loss silicon nitride ( $\text{Si}_3\text{N}_4$ ) waveguide (Fig. 4.17(a)) coiled into a bus-coupled resonator on a chip smaller than a square centimeter (Fig. 4.17(b)). A critical point is that the Brillouin laser cavity can be implemented in a complex waveguide geometry such as the coil resonator owing to the physics of this type of Brillouin laser, where the photon-phonon scattering interaction occurs over the length of the resonator without using phonon guiding<sup>16,23</sup>. The absence of phonon waveguiding leads to a broad Brillouin gain spectrum of approximately  $250 \text{ MHz}$  at  $1550 \text{ nm}$ , which spans approximately 4 coil cavity FSRs (Fig. 4.17(c)). The physics of this Brillouin laser does not require



acoustic guiding, allowing the resonator design to focus on the waveguide design for low propagation loss. Below threshold, the pump is spontaneously back-scattered by a thermal population of phase-matched phonons into the four optical resonances that lie within the Brillouin gain bandwidth (illustrated by the orange, red, green, and purple acoustic gratings in Fig. 4.17(d)). The scattered power in these four optical modes continues to grow with increasing pump until threshold is met for the mode with the largest optical gain (S1). Above threshold the intracavity pump power is clamped (Fig. 4.17(e)), and only the lasing mode S1 increases with supplied power (purple in middle of Fig. 4.17(f)). Consequently, the other sub-threshold modes within the SBS gain bandwidth that are driven by the pump are clamped, remaining fixed in power (orange, red, green in center of Fig. 4.17(f)). The result is illustrated in Fig. 4.17(d - f) with single mode operation in a large mode volume and traditionally multimode resonator. The nonlinear feedback process of stimulated Brillouin scattering is so dominant, the lasing mode also takes away pump photons from the build-up of spontaneous modes (acoustic gratings or phonons) within the lasing resonance itself, which leads to very strong linewidth narrowing that leads to orders of magnitude smaller laser (S1) linewidth than the cavity resonance.

## Coil SBS laser design

The 4-meter-coil resonator design sets the foundation of SBS laser. For a large mode volume SBS laser, due to the cascaded Stokes emission nature of SBS lasers in general, it is desirable to operate the pump power just below the second-order Stokes (S2) threshold. For the design demonstrated here, the S2 threshold is expected to be 4 times the S1 threshold. Driving the pump up to just below the onset of S2 lasing is the point where the S1 fundamental linewidth reaches a minimum [36]. The cavity external coupling

$Q$  ( $Q_{ex}$ ), loaded  $Q$  ( $Q_L$ ) and the cavity Brillouin gain ( $\mu$ ) determine the S1 threshold, output power, and the minimum fundamental linewidth [36]. The S1 threshold ( $P_{th}$ ) and the S1 output power at its power clamping point are linearly proportional to the cavity length while the corresponding minimal fundamental linewidth ( $\Delta\nu_{min}$ ) reduces linearly with the cavity length ( $L$ ). In this mode of operation, it is desirable to increase the optical mode volume by increasing the cavity length, which in turn increases the S1 output power and reduces the fundamental linewidth. The waveguide loss and coil resonator  $Q$  are important parameters, since SBS threshold is reduced as the cavity  $Q$  increases.

For the coil resonator we employ a silica cladded 6  $\mu\text{m}$  wide by 80 nm thick  $\text{Si}_3\text{N}_4$  waveguide design. This waveguide supports the fundamental transverse-electric ( $\text{TE}_0$ ) mode with moderate waveguide confinement, propagation loss around 0.2 dB/m in C and L band, and a critical bending radius less than 1 mm. By leveraging this tight bending radius, a 4-meter-long waveguide resonator can be realized in a penny-size footprint. The resulting coil resonator has a 48.1 MHz FSR and 160 million intrinsic  $Q$  in the C and L band. Within the coil, neighboring waveguides are spaced by 30  $\mu\text{m}$  and the minimum radius of curvature is  $\sim 1.8$  mm to avoid bending losses. A comprehensive review of the design considerations of coil resonators can be found in the next chapter with details. The  $\text{TE}_0$  mode waveguide losses are measured by spectral scanning the coil resonator with the laser detuning calibrated by a fiber Mach-Zehnder interferometer (MZI). The lowest loss is measured to be  $\sim 0.2$  dB/m from 1550 nm to 1630 nm in L band while below 1550 nm the loss increases due to the N-H absorption at 1520 nm. For better fiber-to-chip coupling, the bus waveguide is tapered from 6  $\mu\text{m}$  to 11  $\mu\text{m}$ . Ultra-high numerical aperture (UHNA) fibers with a mode field diameter of 4.1  $\mu\text{m}$  are used to fiber-pigtail the tapered waveguide facets. The mode-overlapping simulation shows a theoretical coupling loss between the UHNA fiber and the 11  $\mu\text{m}$  tapered waveguide of 1.9 dB per facet and

3.8 dB total. The fiber pigtailed connection results in a total coupling loss of 5.8 dB. More details on the 4-meter-coil waveguide resonator can be found in the next chapter in Section 5.2.1.

### Coil SBS laser characterization: power and linewidth

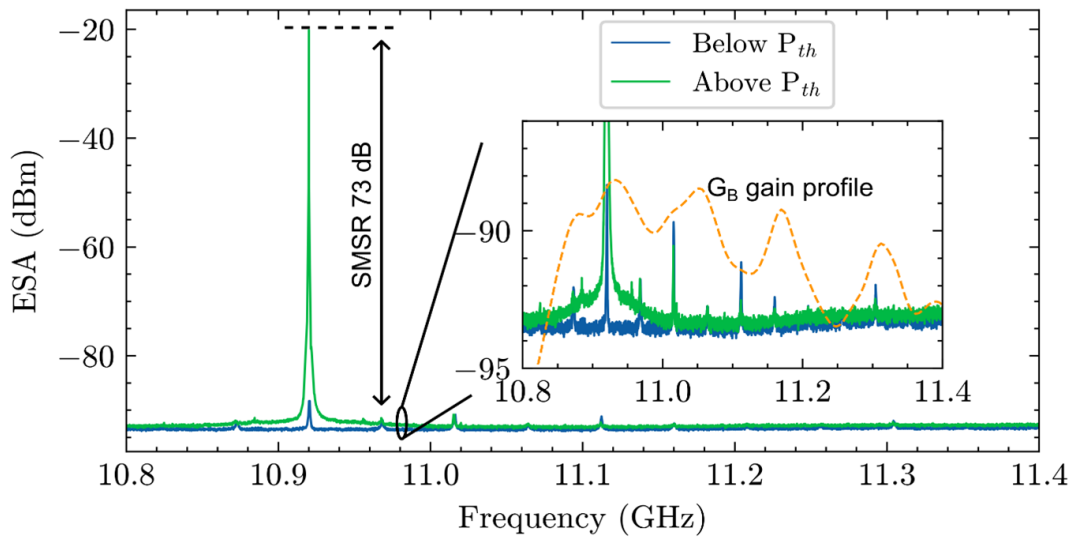


Figure 4.18: Coil SBS laser single mode lasing. Pump-S1 beatnote spectrum of the SBS laser at 1570 nm on an ESA in spontaneous emission below threshold (blue trace) and stimulated emission above threshold (green trace) demonstrates 73 dB SMSR. Inset shows the Brillouin grating modes at cavity resonances that overlap Brillouin gain spectrum below-threshold (blue trace) and above-threshold (green trace).

The SBS laser characterization is featured with the achievement of high output power and narrow fundamental linewidths. The results shown in Fig. 4.18 were obtained using a widely tunable external cavity laser as the SBS pump which is amplified by an EDFA at the resonator, then PDH locked to the coil resonator near 1570 nm. The S1 SBS emission propagating in the opposite direction to the pump is dropped by a fiber circulator located at the chip input. The S1 emission is photo-mixed with the pump on a fast photodetector to generate a beatnote to resolve the S1 power spectrum in the radio-frequency domain

on an ESA. Just below threshold, in the spontaneous Brillouin emission regime, multiple Stokes tones are observed, which resembles the simulated Brillouin gain profile (see the method of the Brillouin gain simulation in Ref. [34]). Above threshold, we observe rapid emergence of the main Stokes lasing mode (S1) with a 73 dB SMSR (Fig. 4.18). Above threshold, all increases in pump energy are directed to the primary lasing mode, enabling this large contrast between the power in the lasing mode and the side modes. Also observed is the further Brillouin linewidth reduction that occurs at the primary cavity mode. After confirming the property of single mode lasing, we increase the pump power to increase the S1 output power, which is measured on an OSA. The on-chip S1 output power is calibrated and plotted versus the pump power (inset in Fig. 4.19). We measure an S1 threshold of 72 mW and generation of 41 mW on-chip S1 power at a 242 mW pump power, which corresponds to an overall 16.5% efficiency. With the 2.9 dB facet fiber coupling loss, there is  $\sim 13$  dBm measured optical output power in the fiber.

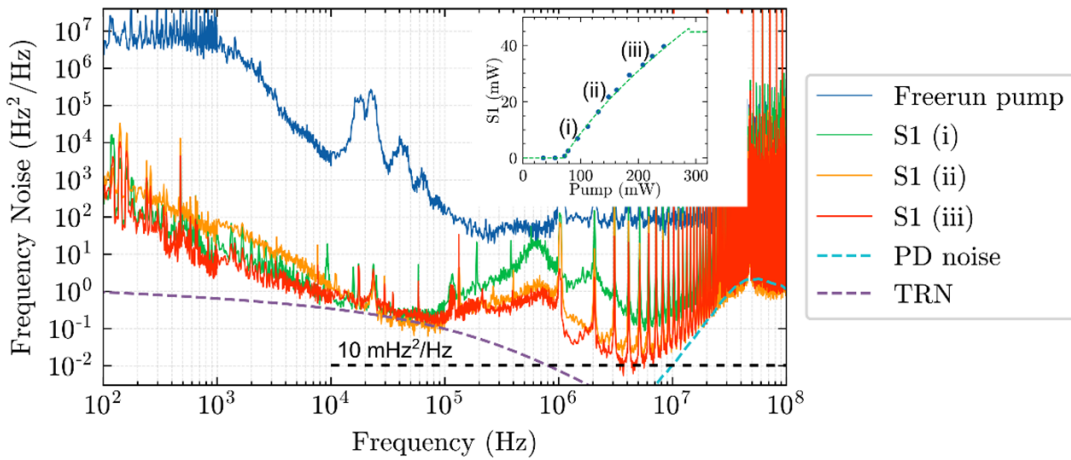


Figure 4.19: SBS laser output power, frequency noise, and fundamental linewidth. OFD frequency noise measurements for the SBS laser at different pump powers show the minimum fundamental linewidth of 31 mHz, corresponding to a frequency noise of  $10 \text{ mHz}^2/\text{Hz}$ . At frequency offset above 10 MHz, the OFD frequency noise measurement is limited by a noise floor from the photodetector. Inset shows the SBS laser on-chip power versus on-chip pump power with a threshold of 72 mW and an output power of 41 mW.

The laser frequency noise and fundamental linewidth are measured using an unbalanced fiber optic MZI with a 1.037 MHz FSR. The fundamental linewidth is calculated from the white-frequency-noise floor of the frequency noise spectrum,  $\Delta\nu_F = \pi S_w$ . To enable measurement of such low frequency noise and fundamental linewidth we characterize the OFD frequency noise floor that starts to emerge above 10 MHz frequency offset and is primarily from the balanced photodetector used in the OFD (light blue dash in Fig. 4.19). The red frequency noise curve in Fig. 4.19 measured  $10 \text{ mHz}^2/\text{Hz}$  frequency noise at high frequency offsets and is used to calculate the fundamental linewidth of 31 mHz.

It is worth noting that the coil SBS laser frequency noise reaches the coil resonator's TRN limit at frequency offsets from 10 kHz to 100 kHz. Below 10 kHz the S1 frequency noise is dominated by environmental noise such as vibrations and acoustic noise, as well as photothermal noise due to the intracavity power fluctuation induced by the pump laser intensity noise. Above 100 kHz and below 1 MHz, there is potentially pump-transferred noise, which prevents resolving the fundamental linewidth below 31 mHz. Although we can measure a fundamental linewidth of 31 mHz, the estimated fundamental linewidth in this 4-meter-coil SBS laser operating at the S1 clamping point is lower than the measured value. In previous work [34], we measured an SBS laser fundamental linewidth of 0.7 Hz at the S1 clamping point in a 11.83-mm-radius ring resonator with a cavity length of 74.3 mm. Here, the 4-meter-coil cavity length is 54 times the ring resonator cavity length, resulting in fundamental linewidth decrease by 54 times to 13 mHz. The ability to measure low magnitude frequency noise and fundamental linewidth at 1 MHz and above is limited by the frequency noise measurement system. Above 10 MHz the OFD frequency noise measurement is limited by the photodetector noise (light blue dashed curve in Fig. 4.19).

## SBS-phase-matched lasing at multiple wavelengths

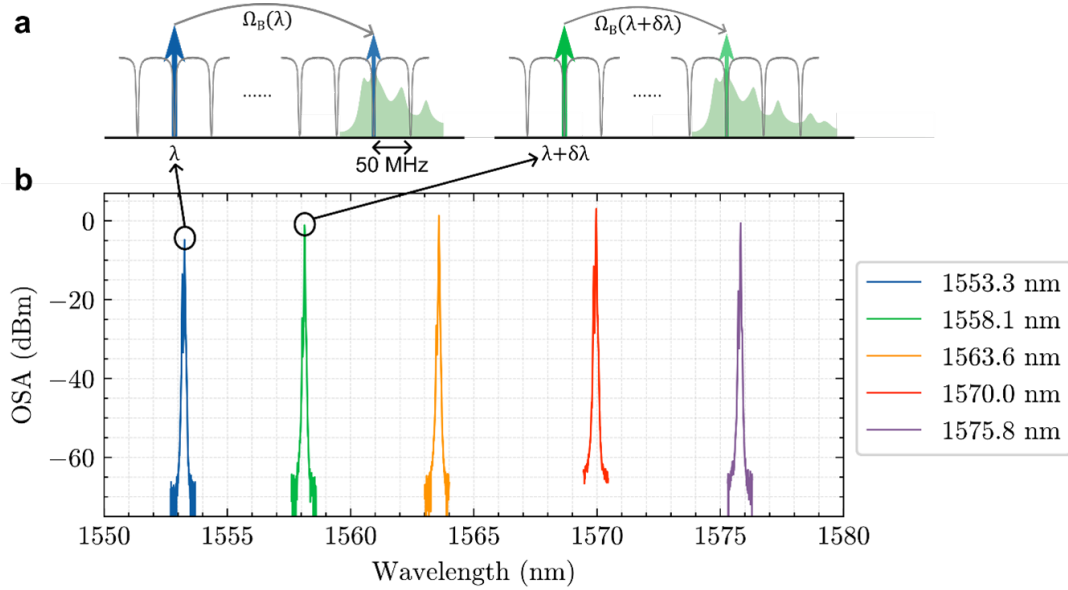


Figure 4.20: Wide-wavelength-range coil SBS laser in C and L band. (a) The SBS phase matching condition is satisfied every  $\sim 6$  nm, as the Brillouin shift  $\Omega_B$  that is linearly proportional to the optical frequency changes by 50 MHz when the pump wavelength changes by  $\sim 6$  nm around 1570 nm. (b) S1 emission recorded on the OSA reaches a local minimal threshold every  $\sim 6$  nm in C and L band.  $\Omega_B$ , Brillouin shift frequency.

We additionally demonstrate that this approach can be used to realize a tunable SBS laser. The SBS laser can tune every 48 MHz on the coil resonator FSR grid and can further tune continuously by adjusting the coil resonator temperature. Moreover, given that every  $\sim 6$  nm a pair of optical modes satisfy the SBS phase matching conditions a Vernier tuning scheme can be realized as illustrated in Fig. 4.20(a). This behavior is enabled by the small optical FSR and is not possible in conventional bus-coupled ring resonators with FSRs on the order of GHz. This form of tuning is primarily due to the Brillouin shift frequency's dependence on the pump mode wavelength, i.e.,  $\Omega_B \propto 1/\lambda$  which enables phase matching to be achieved for pairs of optical modes separated by  $\Omega_B$ . This translates to a Vernier effect where the SBS phase matching wavelength points

every  $\sim 6$  nm near 1570 nm, as expressed by  $\delta\lambda = \lambda \times \nu_{FSR}/\Omega_B$ . The dependence of FSR on wavelength (coil resonator cavity dispersion) is negligible compared to the acoustic frequency dependence on wavelength. The OSA traces of the S1 emission at the on-chip pump power of  $\sim 140$  mW at different wavelengths from 1550 nm to 1580 nm (Fig. 4.20(b)) are recorded when S1 reaches a local minimal threshold or local maximal output power. From 1570 nm to shorter wavelengths, the SBS threshold increases due to increased waveguide losses and decreased cavity Qs. Although above 1570 nm the SBS threshold is estimated to decrease, the C-band EDFA does not provide optical gain and amplification above 1580 nm to pump the SBS laser. With the technique of two-point coupling that provides resonator coupling in large wavelength range, it is possible in the future work to achieve an SBS laser in one single coil waveguide resonator at multiple wavelength bands such as C, L, O bands, and even visible light [33, 52].

## 4.6 Summary and outlook

In this chapter, we first reviewed the underlining nonlinear physics of Brillouin scattering, on which the stimulated Brillouin laser is designed. We demonstrated SBS lasers with ultra-low thresholds due to Qs above 200 million. To suppress higher order Stokes, a nested-ring photonic molecule resonator is designed to employ a split resonance to suppress S2 and such an S2-suppressed SBS laser demonstrates an output power of 10 mW and a fundamental linewidth down to below 100 mHz. To overcome the low-efficiency issue in the S2-suppression approach, a large mode volume coil resonator is used for SBS lasers, achieving both high output power (40 mW) and narrow fundamental linewidth (31 mHz).

For coil-resonator-based SBS lasers, it is feasible to further increase the coil resonator length to further increase the output power and reduce the fundamental linewidth, yet at

a cost of increasing the S1 threshold. With the advancement of the silicon nitride photonic platform and the decreasing propagation loss and increasing waveguide resonator  $Q_s$ , the coil SBS laser threshold can be reduced quadratically with the resonator  $Q_s$ ,  $P_{th} \sim 1/Q^2$ , which will make it feasible to increase the coil SBS resonator length. With the 4-meter-coil resonator and the FSR being 50 MHz, we experimentally demonstrate that the coil SBS laser is highly single-mode, even the Brillouin gain profile has a bandwidth of a few hundred MHz and can provide gain for several optical modes. Increasing the coil length decreases the resonator FSR, which can significantly increase the risk of mode competition and multi-mode lasing. This remains to be an uncharted area.

## Bibliography

- [1] D. J. Blumenthal, H. Ballani, R. O. Behunin, J. E. Bowers, P. Costa, D. Lenoski, P. A. Morton, S. B. Papp, and P. T. Rakich, *Frequency-stabilized links for coherent WDM fiber interconnects in the datacenter*, *Journal of Lightwave Technology* **38** (2020), no. 13 3376–3386.
- [2] G. M. Brodnik, M. W. Harrington, J. H. Dallyn, D. Bose, W. Zhang, L. Stern, P. A. Morton, R. O. Behunin, S. B. Papp, and D. J. Blumenthal, *Optically synchronized fibre links using spectrally pure chip-scale lasers*, *Nature Photonics* **15** (2021), no. 8 588–593.
- [3] E. Ip, J. Fang, Y. Li, Q. Wang, M.-F. Huang, M. Salemi, and Y.-K. Huang, *Distributed fiber sensor network using telecom cables as sensing media: technology advancements and applications*, *Journal of Optical Communications and Networking* **14** (2022), no. 1 A61–A68.
- [4] E. Ip, Y.-K. Huang, G. Wellbrock, T. Xia, M.-F. Huang, T. Wang, and Y. Aono,



- Vibration detection and localization using modified digital coherent telecom transponders, Journal of Lightwave Technology* **40** (2022), no. 5 1472–1482.
- [5] A. Mecozzi, C. Antonelli, M. Mazur, N. Fontaine, H. Chen, L. Dallachiesa, and R. Ryf, *Use of optical coherent detection for environmental sensing, Journal of Lightwave Technology* **41** (2023), no. 11 3350–3357.
- [6] C. Xu, L. Zhang, S. Huang, T. Ma, F. Liu, H. Yonezawa, Y. Zhang, and M. Xiao, *Sensing and tracking enhanced by quantum squeezing, Photonics Research* **7** (2019), no. 6 A14–A26.
- [7] A. D. Ludlow, M. M. Boyd, J. Ye, E. Peik, and P. O. Schmidt, *Optical atomic clocks, Reviews of Modern Physics* **87** (2015), no. 2 637.
- [8] W. Loh, J. Stuart, D. Reens, C. D. Bruzewicz, D. Braje, J. Chiaverini, P. W. Juodawlkis, J. M. Sage, and R. McConnell, *Operation of an optical atomic clock with a Brillouin laser subsystem, Nature* **588** (2020), no. 7837 244–249.
- [9] J. Li, H. Lee, and K. J. Vahala, *Microwave synthesizer using an on-chip Brillouin oscillator, Nature communications* **4** (2013), no. 1 2097.
- [10] S. Sun, B. Wang, K. Liu, M. W. Harrington, F. Tabatabaei, R. Liu, J. Wang, S. Hanifi, J. S. Morgan, M. Jahanbozorgi, *et. al.*, *Integrated optical frequency division for microwave and mmWave generation, Nature* (2024) 1–6.
- [11] I. Kudelin, W. Groman, Q.-X. Ji, J. Guo, M. L. Kelleher, D. Lee, T. Nakamura, C. A. McLemore, P. Shirmohammadi, S. Hanifi, *et. al.*, *Photonic chip-based low-noise microwave oscillator, Nature* (2024) 1–6.
- [12] G. Santarelli, C. Audoin, A. Makdissi, P. Laurent, G. J. Dick, and A. Clairon, *Frequency stability degradation of an oscillator slaved to a periodically interrogated*

- atomic resonator, IEEE transactions on ultrasonics, ferroelectrics, and frequency control* **45** (1998), no. 4 887–894.
- [13] H. Ball, W. Oliver, and M. Biercuk, *The role of master clock stability in quantum information processing. npj Quantum Inf.* **2**, .
- [14] M. L. Day, P. J. Low, B. White, R. Islam, and C. Senko, *Limits on atomic qubit control from laser noise, npj Quantum Information* **8** (2022), no. 1 72.
- [15] T. Kessler, C. Hagemann, C. Grebing, T. Legero, U. Sterr, F. Riehle, M. Martin, L. Chen, and J. Ye, *A sub-40-mHz-linewidth laser based on a silicon single-crystal optical cavity, Nature Photonics* **6** (2012), no. 10 687–692.
- [16] D. Matei, T. Legero, S. Häfner, C. Grebing, R. Weyrich, W. Zhang, L. Sonderhouse, J. Robinson, J. Ye, F. Riehle, *et. al.*, *1.5  $\mu\text{m}$  lasers with sub-10 mHz linewidth, Physical review letters* **118** (2017), no. 26 263202.
- [17] E. Oelker, R. Hutson, C. Kennedy, L. Sonderhouse, T. Bothwell, A. Goban, D. Kedar, C. Sanner, J. Robinson, G. Marti, *et. al.*, *Demonstration of  $4.8 \times 10^{-17}$  stability at 1 s for two independent optical clocks, Nature Photonics* **13** (2019), no. 10 714–719.
- [18] T. M. Fortier, M. S. Kirchner, F. Quinlan, J. Taylor, J. Bergquist, T. Rosenband, N. Lemke, A. Ludlow, Y. Jiang, C. Oates, *et. al.*, *Generation of ultrastable microwaves via optical frequency division, Nature Photonics* **5** (2011), no. 7 425–429.
- [19] D. J. Blumenthal, R. Heideman, D. Geuzebroek, A. Leinse, and C. Roeloffzen, *Silicon nitride in silicon photonics, Proceedings of the IEEE* **106** (2018), no. 12 2209–2231.

- [20] M. W. Puckett, K. Liu, N. Chauhan, Q. Zhao, N. Jin, H. Cheng, J. Wu, R. O. Behunin, P. T. Rakich, K. D. Nelson, *et. al.*, *422 Million intrinsic quality factor planar integrated all-waveguide resonator with sub-MHz linewidth*, *Nature communications* **12** (2021), no. 1 934.
- [21] N. Chauhan, J. Wang, D. Bose, K. Liu, R. Compton, C. Fertig, C. Hoyt, and D. J. Blumenthal, *Ultra-low loss visible light waveguides for integrated atomic, molecular, and quantum photonics*, *Optics express* **30** (2022), no. 5 6960–6969.
- [22] W. Jin, Q.-F. Yang, L. Chang, B. Shen, H. Wang, M. A. Leal, L. Wu, M. Gao, A. Feshali, M. Paniccia, *et. al.*, *Hertz-linewidth semiconductor lasers using CMOS-ready ultra-high-Q microresonators*, *Nature Photonics* **15** (2021), no. 5 346–353.
- [23] C. Xiang, W. Jin, O. Terra, B. Dong, H. Wang, L. Wu, J. Guo, T. J. Morin, E. Hughes, J. Peters, *et. al.*, *3D integration enables ultralow-noise isolator-free lasers in silicon photonics*, *Nature* **620** (2023), no. 7972 78–85.
- [24] R. Chiao, C. H. Townes, and B. Stoicheff, *Stimulated Brillouin scattering and coherent generation of intense hypersonic waves*, *Physical review letters* **12** (1964), no. 21 592.
- [25] E. Ippen and R. Stolen, *Stimulated Brillouin scattering in optical fibers*, *Applied Physics Letters* **21** (1972), no. 11 539–541.
- [26] L. Stokes, M. Chodorow, and H. Shaw, *All-fiber stimulated Brillouin ring laser with submilliwatt pump threshold*, *Optics Letters* **7** (1982), no. 10 509–511.
- [27] S. Smith, F. Zarinetchi, and S. Ezekiel, *Narrow-linewidth stimulated Brillouin fiber laser and applications*, *Optics letters* **16** (1991), no. 6 393–395.

- [28] J. Geng, S. Staines, Z. Wang, J. Zong, M. Blake, and S. Jiang, *Highly stable low-noise Brillouin fiber laser with ultranarrow spectral linewidth*, *IEEE Photonics Technology Letters* **18** (2006), no. 17 1813–1815.
- [29] M. Merklein, I. V. Kabakova, A. Zarifi, and B. J. Eggleton, *100 years of Brillouin scattering: Historical and future perspectives*, *Applied Physics Reviews* **9** (2022), no. 4.
- [30] H. Lee, T. Chen, J. Li, K. Y. Yang, S. Jeon, O. Painter, and K. J. Vahala, *Chemically etched ultrahigh- $Q$  wedge-resonator on a silicon chip*, *Nature Photonics* **6** (2012), no. 6 369–373.
- [31] I. S. Grudinin, A. B. Matsko, and L. Maleki, *Brillouin lasing with a CaF<sub>2</sub> whispering gallery mode resonator*, *Physical review letters* **102** (2009), no. 4 043902.
- [32] I. V. Kabakova, R. Pant, D.-Y. Choi, S. Debbarma, B. Luther-Davies, S. J. Madden, and B. J. Eggleton, *Narrow linewidth Brillouin laser based on chalcogenide photonic chip*, *Optics letters* **38** (2013), no. 17 3208–3211.
- [33] N. Chauhan, A. Isichenko, K. Liu, J. Wang, Q. Zhao, R. O. Behunin, P. T. Rakich, A. M. Jayich, C. Fertig, C. Hoyt, *et. al.*, *Visible light photonic integrated Brillouin laser*, *Nature communications* **12** (2021), no. 1 4685.
- [34] S. Gundavarapu, G. M. Brodник, M. Puckett, T. Huffman, D. Bose, R. Behunin, J. Wu, T. Qiu, C. Pinho, N. Chauhan, *et. al.*, *Sub-hertz fundamental linewidth photonic integrated Brillouin laser*, *Nature Photonics* **13** (2019), no. 1 60–67.
- [35] A. Debut, S. Randoux, and J. Zemmouri, *Linewidth narrowing in Brillouin lasers: Theoretical analysis*, *Physical Review A* **62** (2000), no. 2 023803.

- [36] R. O. Behunin, N. T. Otterstrom, P. T. Rakich, S. Gundavarapu, and D. J. Blumenthal, *Fundamental noise dynamics in cascaded-order Brillouin lasers*, *Physical Review A* **98** (2018), no. 2 023832.
- [37] C. Henry, *Theory of the linewidth of semiconductor lasers*, *IEEE Journal of Quantum Electronics* **18** (1982), no. 2 259–264.
- [38] Z. Yuan, H. Wang, L. Wu, M. Gao, and K. Vahala, *Linewidth enhancement factor in a microcavity Brillouin laser*, *Optica* **7** (2020), no. 9 1150–1153.
- [39] M. Puckett, D. Bose, K. Nelson, and D. J. Blumenthal, *Higher order cascaded SBS suppression using gratings in a photonic integrated ring resonator laser*, in *CLEO: Science and Innovations*, pp. SM4O–1, Optica Publishing Group, 2019.
- [40] Y. Qin, S. Ding, M. Zhang, Y. Wang, Q. Shi, Z. Li, J. Wen, M. Xiao, and X. Jiang, *High-power, low-noise Brillouin laser on a silicon chip*, *Optics letters* **47** (2022), no. 7 1638–1641.
- [41] K. Liu, N. Jin, H. Cheng, N. Chauhan, M. W. Puckett, K. D. Nelson, R. O. Behunin, P. T. Rakich, and D. J. Blumenthal, *Ultralow 0.034 dB/m loss wafer-scale integrated photonics realizing 720 million  $Q$  and 380  $\mu$ W threshold Brillouin lasing*, *Optics letters* **47** (2022), no. 7 1855–1858.
- [42] K. Liu, N. Chauhan, J. Wang, A. Isichenko, G. M. Brodnik, P. A. Morton, R. O. Behunin, S. B. Papp, and D. J. Blumenthal, *36 Hz integral linewidth laser based on a photonic integrated 4.0 m coil resonator*, *Optica* **9** (2022), no. 7 770–775.
- [43] A. Yeniay, J.-M. Delavaux, and J. Toulouse, *Spontaneous and stimulated Brillouin scattering gain spectra in optical fibers*, *Journal of lightwave technology* **20** (2002), no. 8 1425.

- [44] R. W. Boyd, A. L. Gaeta, and E. Giese, *Nonlinear optics*, in *Springer Handbook of Atomic, Molecular, and Optical Physics*, pp. 1097–1110. Springer, 2008.
- [45] K. Liu, J. Wang, N. Chauhan, M. W. Harrington, K. D. Nelson, and D. J. Blumenthal, *Integrated photonic molecule Brillouin laser with a high-power sub-100-mHz fundamental linewidth*, *Optics Letters* **49** (2024), no. 1 45–48.
- [46] “GitHub - kaikai-liu/pyphotonicssims — github.com.”  
<https://github.com/kaikai-liu/pyphotonicssims>. [Accessed 25-12-2024].
- [47] M.-G. Suh, Q.-F. Yang, and K. J. Vahala, *Phonon-limited-linewidth of Brillouin lasers at cryogenic temperatures*, *Physical review letters* **119** (2017), no. 14 143901.
- [48] K. Liu, J. Wang, N. Chauhan, and D. J. Blumenthal, *Circulator-free photonic integrated Brillouin laser*, in *Nonlinear Optics*, pp. Tu2A–3, Optica Publishing Group, 2023.
- [49] Y. Fan, A. van Rees, P. J. Van der Slot, J. Mak, R. M. Oldenbeuving, M. Hoekman, D. Geskus, C. G. Roeloffzen, and K.-J. Boller, *Hybrid integrated InP-Si<sub>3</sub>N<sub>4</sub> diode laser with a 40-Hz intrinsic linewidth*, *Optics express* **28** (2020), no. 15 21713–21728.
- [50] Y. Wu, S. Shao, L. Tang, S. Yang, H. Chen, and M. Chen, *Hybrid integrated tunable external cavity laser with sub-10 Hz intrinsic linewidth*, *APL Photonics* **9** (2024), no. 2.
- [51] S. Grillanda, C. Bolle, M. Cappuzzo, R. Papazian, B. Farah, F. Pardo, P. Iannone, N. Fontaine, M. Mazur, R. Kopf, *et. al.*, *Hybrid-integrated comb source with 16 wavelengths*, *Journal of Lightwave Technology* **40** (2022), no. 21 7129–7135.

- [52] W. Loh, D. Gray, R. Irion, O. May, C. Belanger, J. Plant, P. W. Juodawlkis, and S. Yegnanarayanan, *Ultralow noise microwave synthesis via difference frequency division of a Brillouin resonator*, *Optica* **11** (2024), no. 4 492–497.

# Chapter 5

## Coil waveguide reference resonators for laser stabilization

### Introduction

Frequency and time standard is fundamental in science exploration, technology development, and industrial applications including gravitational wave detection [1, 2, 3, 4], fundamental physics testing [5, 6], optical atomic clocks [7, 8, 9], low-noise microwave generation [10, 11, 12, 13], distributed fiber sensing [14, 15, 16], and coherent LiDAR [17, 18].

Lasers with integral linewidths below 1 Hz and Allan deviations better than  $10^{-16}$  over 1s are realized by ultra-stable and high-finesse, table-top, vacuum-gap Fabry-Perot optical cavities [19, 20]. In compact and portable frequency-reference systems, radio-frequency quartz oscillators have served as the “silver standard” for decades with the fractional frequency instability near  $10^{-11}$  at 1 s [21]. Efforts to develop miniaturized optical reference cavities to translate the performance of the state-of-the-art bulk-optic table-top ultra-stable Fabry-Perot cavities to portable optical references include a centimeter-scale



whispering gallery mode (WGM) resonator with a fractional stability of below  $1 \times 10^{-13}$  at 0.1 s [22, 23], a fused silica microrod Fabry-Perot cavity with a fractional stability of  $1 \times 10^{-13}$  at 20 ms [24], deep-etched silica waveguide spiral resonator reaching  $4 \times 10^{-13}$  at 0.4 ms [25]. Recently, 1 million finesse Fabry-Perot reference cavities constructed with lithographically fabricated micro-mirrors is reported with  $7 \times 10^{-15}$  at 1 s [26, 27, 28].

Photonic integrated mirroring resonators are a good candidate for the search for miniaturized stable and low-noise optical references because of the decreasing optical waveguide loss to the dB-per-meter level or below, such as silicon nitride [29, 30, 31], and lithium niobate [32, 33]. The most dominant intrinsic instability source is thermo-refractive noise (TRN) due to the small ring resonator size and optical mode volume [22, 34, 35]. Waveguide resonator designs leverage the ability to make a long coil waveguide to form a coil cavity with cavity lengths up to a meter long on a footprint of below 1 cm by 1 cm [36, 37, 30]. In addition to TRN, thermoelastic noise can also be a fundamental and intrinsic noise limit in waveguide ring resonators [23], as the thermal expansion coefficient in the silica material of around  $10^{-5}$  1/K is very close to the thermo-optic coefficient of  $10^{-5}$  1/K.

Oscillator stability matters at different time scales depending on applications. For instance, the optical atomic clock application desires good long-term stability that is usually measured by Allan deviation, whereas the microwave oscillators in radar systems benefit from good short-term stability that is often characterized by phase and frequency noise spectrum.

Both long-term and short-term oscillator stability at the same time can be achieved by having a low-phase-noise oscillator to reference and frequency-lock to a high-Q and long-term-stable frequency reference, because a certain-level of short-term stability is required in referencing to a high-Q and long-term-stable reference and frequency stability at different time scales can be provided from separate frequency references. Frequency-

locking a low-phase-noise quartz oscillator to a stable Rb atomic transition to make an excellent microwave oscillator with both short-term and long-term stability is an good example [38]. Start-of-the-art Strontium optical atomic clock uses an ultra-stable-cavity stabilized laser with  $10^{-15}$  stability to interrogate the Strontium 689 nm narrow-linewidth clock transition to achieve the  $10^{-18}$  clock stability [39, 8, 40]. Such a staged approach has also been employed in many recent works in integrated photonic application to demonstrate a low-noise narrow linewidth photonic integrated laser [36, 28] and to generate low-noise microwave and mmWaves [13, 12].

This chapter starts from the design aspects of the waveguide coil resonators including the  $6\ \mu\text{m}$  wide by 80 nm thick waveguide geometry design and coupling design, followed by the demonstration of laser stabilization experiment with an integral linewidth of 36 Hz. Next, we demonstrate a technique of self-delayed coil resonator designs to provide optical frequency discrimination without the need for the sideband modulation on the laser and demodulation of the photo-detected signal in the conventional PDH locking scheme [41]. Then, we show that the design of a waveguide coil MZI with 4 meter and 15 meter delay lengths shows high extinction at the two output ports and the balanced detection of the output ports enables an integrated on-chip high-SNR frequency noise measurement. The final section describes the two-point-coupling waveguide resonator coupling technique that uses an MZI structure to tune the bus-resonator coupling by varying the MZI phase section.

## 5.1 Basics of Pound-Drever-Hall laser stabilization

Waveguide propagation loss and resonator Qs are critical to the relevant application performance. Additionally, bus-resonator coupling to realize the desired resonator coupling regime, namely, under-coupled, critical-coupled, and over-coupled regimes, is

equally important. For example, a single-bus-coupled add-through waveguide resonator for laser stabilization needs critical coupling to maximize SNR in the laser frequency noise discrimination and noise suppression processes [41, 36]. Squeezed light generation requires over-coupling in the squeezing mode, whereas the pump modes are critically coupled [42]. Second-harmonic generation (SHG) and frequency doubling applications require resonators to be critically coupled at both fundamental and second harmonic frequency wavelengths simultaneously [43, 44].

### 5.1.1 Laser frequency discrimination in PDH lock

To show how the coupling of the add-through bus-coupled ring resonator affects the PDH error frequency discrimination slope, we follow the mathematical formulation in [41], where the CW laser light field is modulated by an EOM phase modulator to generate sidebands,

$$E_{in} = E_0 e^{i\Delta\omega + \beta \sin \Omega t} \simeq E_0 e^{i\Delta\omega t} [J_0(\beta) + J_1(\beta) e^{i\Omega t} + J_1(\beta) e^{-i\Omega t}]. \quad (5.1)$$

Here,  $\beta = \pi V_{LO}/V_\pi$  is the phase modulation depth dependent on the LO modulation signal amplitude  $V_{LO}$  and the EOM  $V_\pi$ ,  $\Omega/2\pi$  is the LO modulation frequency,  $J_n(x)$  is the Bessel function with  $\beta$  as the input, and  $\Delta\omega = \omega_L - \omega_{cav}$  is the laser frequency detuning from the cavity resonance frequency. The modulated light signal is then passed through the resonator and applied with a resonator transfer function on the light field dependent on the resonator intrinsic and coupling linewidths ( $\gamma_{in}$  and  $\gamma_{ex}$ ), equivalent to Eq. 2.10,

$$F(\Delta\omega) = \frac{i\Delta\omega + (\gamma_{in} - \gamma_{ex})/2}{i\Delta\omega + (\gamma_{in} + \gamma_{ex})/2}, \quad (5.2)$$

and can be expressed by,

$$E_{sig} = E_0 e^{i\Delta\omega t} [F(\Delta\omega)J_0(\beta) + F(\Delta\omega + \Omega)J_1(\beta)e^{i\Omega t} + F(\Delta\omega - \Omega)J_1(\beta)e^{-i\Omega t}] \quad (5.3)$$

$$= E_0 e^{i\Delta\omega t} [FJ_0 + F_+ J_1 e^{i\Omega t} + F_- J_1 e^{-i\Omega t}]. \quad (5.4)$$

After being detected on the photodetector and expressed in optical powers with only  $\Omega$  terms and removing the DC and  $2\Omega$  terms, we have,

$$P_{sig} = |E_{sig}|^2 \quad (5.5)$$

$$= 2J_0 J_1 P_{in} (Re[FF_+^* - F^*F_-] \cos \Omega t + Im[FF_+^* - F^*F_-] \sin \Omega t) \quad (5.6)$$

$$= 2J_0 J_1 P_{in} |FF_+^* - F^*F_-| (\cos \phi_F \cos \Omega t + \sin \phi_F \sin \Omega t) \quad (5.7)$$

$$= 2J_0 J_1 P_{in} |FF_+^* - F^*F_-| \cos(\Omega t + \phi_F). \quad (5.8)$$

With high modulation frequencies,  $\Omega > \gamma$  ( $\gamma = \gamma_{in} + \gamma_{ex}$ , and near the cavity resonance,  $\Delta\omega < \gamma$ , it leads to  $F(\delta\omega\Omega) \simeq 1$  and,

$$\begin{aligned} FF_+^* - F^*F_- &= 2iIm[F] \\ &= \frac{2\gamma_{ex}\Delta\omega}{|i\Delta\omega + \gamma/2|^2} \\ &\simeq \frac{8\gamma_{ex}\Delta\omega}{\gamma^2}. \end{aligned}$$

After demodulation at the LO frequency  $\Omega/2\pi$ , the PDH error discrimination slope at the cavity resonance ( $\Delta\omega < \gamma$ ) expressed in the optical power domain is,

$$\epsilon = \frac{P_{sig}}{\Delta\omega} = \frac{16J_0 J_1 P_{in} \gamma_{ex}}{(\gamma_{in} + \gamma_{ex})^2}. \quad (5.9)$$

From Eq. 5.9, the frequency discrimination slope  $\epsilon_{PDH}$  maximizes at  $\gamma_{ex} = \gamma_{in}$ , that

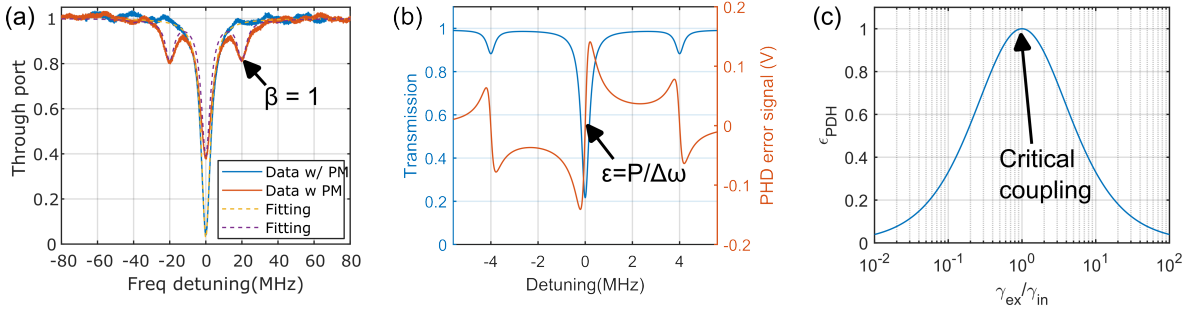


Figure 5.1: PDH error frequency discrimination slope depends on the modulation depth and resonator coupling.

is, critical coupling. This is illustrated in Fig. 5.1(c). At critical coupling, we have,

$$D = \frac{P_{sig}}{\Delta f} = \frac{8J_0J_1P_{in}}{\delta\nu} = \frac{8\sqrt{P_cP_s}}{\delta\nu}. \quad (5.10)$$

Here  $\delta\nu$  is the cavity total linewidth in Hz or MHz,  $\delta f$  is the laser detuning in Hz or MHz, and  $P_c = \sqrt{J_0}P_{in}$  and  $P_s = \sqrt{J_1}P_{in}$  are the carrier optical power and sideband optical power. The optical discrimination slope,  $D$ , increases linearly with  $\sqrt{P_s}$  and  $\sqrt{J_1}$ , when  $\beta \ll 1$  or  $\beta < 1$ .  $\beta \ll 1$  is the condition for the approximation used in Eq. 5.1, and it is important to keep in mind that  $P_cP_s$  reaches a maximum around  $\beta = 1$  and increasing the modulation depth beyond 1 does not significantly increase  $D$ , at which point the frequency discrimination slope is ultimately limited by the cavity linewidth. Fig. 5.1(a) shows the transmission of a high-Q silicon nitride add-through bus-coupled ring resonator with an 8 MHz linewidth and critical bus-resonator coupling probed by a probe laser with a  $\beta = 1$  sideband modulation.

### 5.1.2 Frequency lock loop modeling and noise analysis

The PDH laser frequency lock loop is essentially a phase lock loop, and its frequency response characteristics such as open loop response, close loop response, and noise per-

formance such as total output noise and susceptibility to input noise can be effectively modeled and analyzed using the transfer function approach. This approach can be found being applied in optical communication systems for optical phase lock loops, and here are a few good references [45, 46, 47] and Chapter 8 in *Fundamentals of Communication Systems* by John G. Proakis and Masoud Salehi [48].

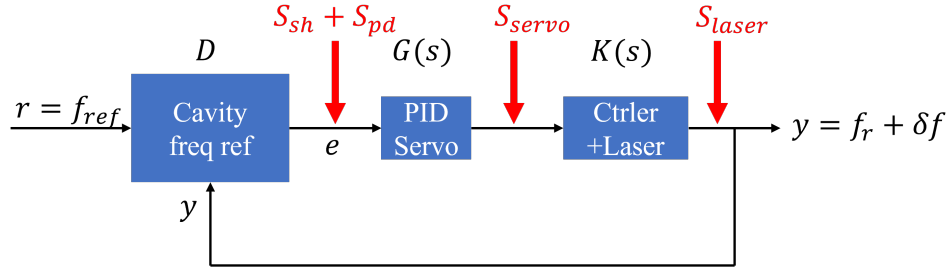


Figure 5.2: Block diagram for the PDH laser frequency lock loop.

Figure 5.2 shows a block diagram of the laser frequency lock loop, where the feedback loop consists of the optical frequency discrimination provided by the optical reference cavity and the photo-detection, the PID feedback servo and the laser and its controller. Each block has its transfer function and input noise. The cavity frequency reference block is a simplified representation of the PDH error signal process and components, which include sideband modulation of laser light before probing the reference cavity and signal demodulation of the photo-detector signal after probing the reference cavity, and is expressed by Eq. 5.10 in the previous subsection. The close loop output signal can be expressed in the small-signal formalism as,

$$y = K\{G[D(r - y) + y_D] + y_G\} + y_K, \quad (5.11)$$

$$y = \frac{KGD}{KGD + 1}r + \frac{KGy_D + Ky_G + y_K}{KGD + 1}, \quad (5.12)$$

where  $r$  is the reference signal (intrinsic cavity noise),  $y_D$  is the added noise in the PDH error signal generation process such as photodetector noise and shot noise,  $y_G$  is the servo

electronic noise, and  $y_K$  is the freerunning laser noise. In Fourier frequency domain it is,

$$y(s) = \frac{K(s)G(s)D(s)}{KGD + 1}r_{cav}(s) + \frac{K(s)G(s)y_D(s) + K(s)y_G(s) + y_K(s)}{KGD + 1}. \quad (5.13)$$

Here the first part is the reference tracking,  $H(s) = K(s)G(s)D(s)/(KGD + 1)$ , which has a limited bandwidth that is determined by the bandwidths of all the loop components and is usually limited by the *slowest* block. The second part is in-loop residual noise that gets suppressed by the close-loop feedback response. The shot noise and photo-detector noise can post a noise limitation in the locked laser frequency noise,

$$S_{y,D} \simeq \frac{S_D}{D^2}. \quad (5.14)$$

And the close-loop laser output frequency noise from the contribution of the shot noise and photo-detector noise can be found by incorporating the expression for  $D$  (Eq. 5.10),

$$S_{y,sh} = \frac{4h\nu P_s}{D^2} = \frac{\delta\nu^2 h\nu}{16P_c}, \quad (5.15)$$

$$S_{y,pd} = \frac{NEP^2}{D^2}. \quad (5.16)$$

Here,  $NEP$  is the noise equivalent power in W/rtHz of the photo-detector. As shown above, the reference cavity linewidth is essential to suppressing the shot noise and photo-detector noise.

Figure 5.3 shows a numerical simulation for Eq. 5.13. The free-running laser frequency noise is from a 1550 nm Thorlabs ULN laser. The simulation is based on a real experimental scenario: The cavity linewidth is 6 MHz; the optical detected on the photo-detector is 0.1 mW; the photo-detector NEP is 4 pW/rtHz; the laser frequency response is assumed to be  $K(s) = K_\nu/[1 + s/(2\pi 10^5)]$ . A public GitHub repository for

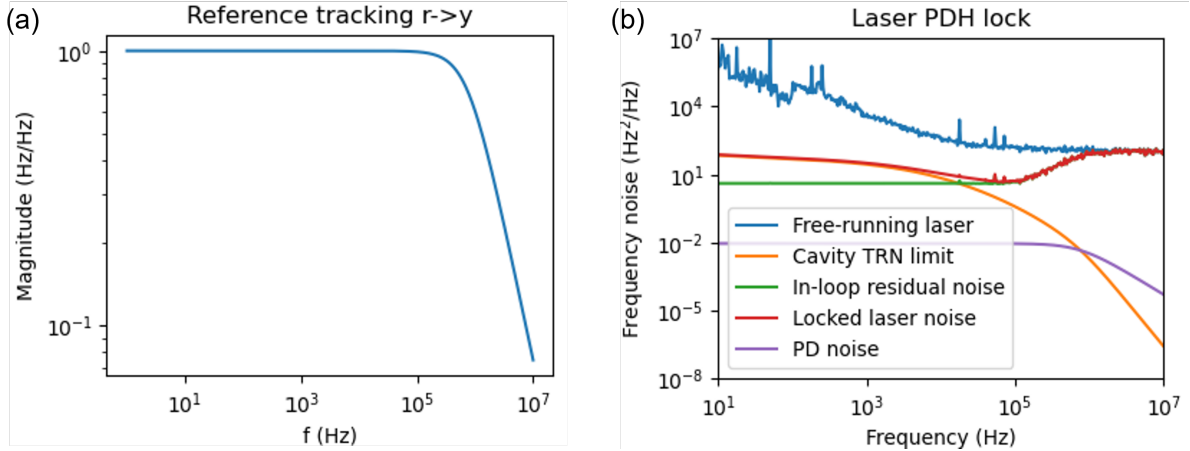


Figure 5.3: A numerical simulation for the PDH laser frequency lock loop. (a) Reference tracking frequency response  $H(s)$ . (b) Close-loop laser frequency noise contribution from the intrinsic cavity thermo-refractive noise (TRN) in waveguide ring resonators, in-loop residual noise that consists of the residual laser noise, photodetector noise and shot noise.

the simulation code can be found online [49].

## 5.2 TM coil waveguide resonators (4 meters)

### 5.2.1 TM 4-meter-coil resonator design and laser stabilization

Here, 4 meter long photonic integrated coil resonators are designed to work in both the C and L bands for photonic integrated laser stabilization, achieving a measured 36 Hz  $1/\pi$ -integral linewidth, an Allan deviation of  $1.8 \times 10^{-13}$  at 10 ms, and 2.3 kHz/s drift. The stabilized laser phase noise at 1550 nm is measured to be  $-30$  dBc/Hz at 100 Hz,  $-64$  dBc/Hz at 1 kHz, and  $-93$  dBc/Hz at 10 kHz, respectively. Both the 1550 and 1319 nm coil resonators employ 4.0 m long coils, significantly lowering the cavity-intrinsic TRN and photothermal noise induced fluctuations. The 1550 nm coil resonator measures a 49.1 MHz FSR, intrinsic 80 million, and loaded 55 million Q; the 1319 nm coil resonator measures a 48.9 MHz FSR, intrinsic 142 million Q, loaded 71 million Q.



We also present numerical modeling of the PDH locking loop noise and the photothermal and thermorefractive noise contributions. It is estimated that if the stabilized laser noise is only limited by the resonator TRN, the performance would reach an 8 Hz integral linewidth and an Allan deviation of  $5 \times 10^{-14}$  at 10 ms, indicating that with mitigation of other noise sources, further performance improvement is possible.

### TM mode 4-meter-coil resonator design and Q

The 4.0-meter coil silicon nitride waveguide resonator employs a high-aspect ratio waveguide core design, 6  $\mu\text{m}$  wide by 80 nm thick, with a 15  $\mu\text{m}$  thick thermally silicon dioxide lower cladding and 6  $\mu\text{m}$  thick oxide upper cladding deposited by tetraethoxysilane pre-cursor plasma-enhanced chemical vapor (TEOS-PECVD). The coil waveguide center-to-center spacing is 40  $\mu\text{m}$ , the minimum bending radius is 9.0 mm, and the S-bend bending radius is 4.5 mm, shown in Fig. 5.4(a), as the bending loss simulation shows the  $\text{TM}_0$  mode bending loss at above 6 mm is below 1 dB/m. This waveguide design supports the  $\text{TM}_0$  mode in order to mitigate sidewall scattering loss [50]. The 1550 nm coil resonator design uses the bus-to-resonator coupler with a 3.5  $\mu\text{m}$  gap and 0.5 mm coupling length, and the 1319 nm coil resonator design aspects are the same as the 1550 nm one except for a different direction coupler design with a 3.5  $\mu\text{m}$  gap and 3.0 mm coupling length. Such a coupler design gives proper coupling for the fundamental TM mode while having the TE modes very weakly coupled.

Spectral scanning of the resonators with a 5.87-MHz-FSR fiber MZI measures the resonator Qs. The 1550 nm resonator is measured to have an intrinsic 80 million and 55 million loaded Q, shown in Fig. 5.4(b), corresponding to a propagation loss of 0.39 dB/m; the 1319 nm resonator is measured to have an intrinsic 142 million and 71 million loaded Q shown in Fig. 5.4(c), corresponding to a propagation loss of 0.16 dB/m. For the coil area and S-bend radius chosen for this design, the 1550 nm bend losses are

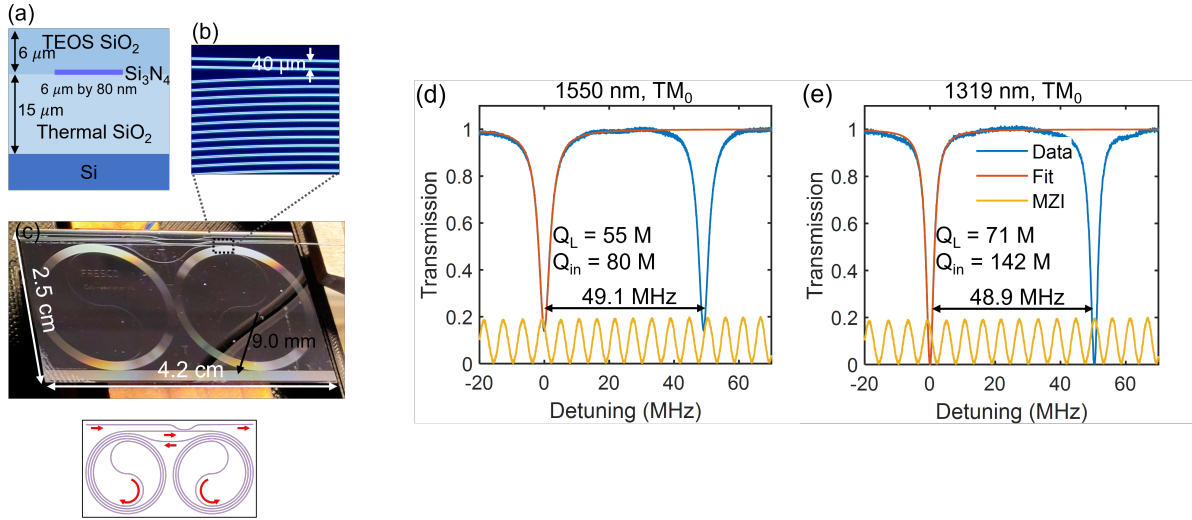


Figure 5.4: 4-meter coil TM waveguide resonator design and  $Q$ s. Reproduced from [36].

higher, whereas the 1319 nm bend loss is further away from the critical bend radius and is scattering loss limited.

### Laser stabilization and frequency noise at 1550 nm

Laser stabilization is demonstrated by PDH locking a Morton Photonics laser [41, 51]. The freerunning and stabilized laser frequency noise above 1 kHz frequency offset is measured by a fiber MZI optical frequency discriminator with a 1.026 MHz FSR using the self-delayed homodyne laser frequency noise measurement technique; below 1 kHz offset, a stable reference laser (SRL), which is a single frequency fiber laser frequency locked to a Stable Laser Systems<sup>TM</sup> (SLS) ultra-low expansion (ULE) cavity, is used as a low-noise local oscillator for generating an heterodyne RF beatnote with the freerunning and stabilized laser on a photodetector, which is measured by a frequency counter. The frequency noise measurements of both the SRL laser and the coil stabilized laser by the fiber MZI OFD, shown in Fig. 5.6, show a common noise source that emerges below 1 kHz that is very likely from the fiber noise in the OFD laser frequency noise measurement

system.

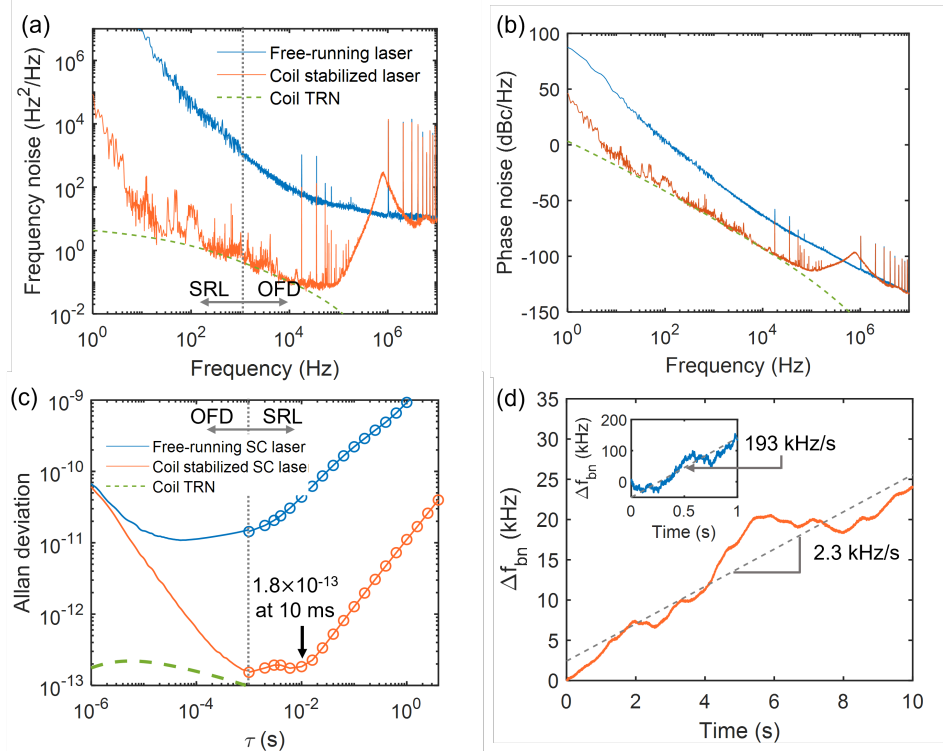


Figure 5.5: 1550 nm integrated coil resonator stabilized laser frequency noise, Allan deviation and beatnote frequency drift. (a) OFD (for above 1 kHz offset) and SRL (for below 1 kHz offset) frequency noise measurements for the free-running and coil stabilized laser. (b) Equivalent phase noise is calculated from the frequency noise shown in (a). (c) Allan deviation is estimated based on the SRL heterodyne beatnote signal’s frequency recorded by a frequency counter at above 1 ms averaging time; Allan deviation is calculated from the measured OFD frequency noise at below 1 ms averaging time. (d) Beatnote frequency drift for the free-running and the stabilized laser. Reproduced from [36].

The frequency noise measurements for the 1550 nm coil-resonator stabilized laser are shown in Fig. 5.5, where the OFD and SRL frequency noise measurements are stitched at the 1 kHz frequency offset for both the free-running and stabilized laser. The  $1/\pi$ -integral linewidths for the free-running and stabilized laser in Fig. 5.5(a) are 1.3 kHz and 36 Hz, respectively. The Allan deviation calculated from the OFD and SRL frequency noise measurements for the stabilized laser reaches a minimum of  $1.8 \times 10^{-13}$  at 10 ms with a linear drift of 2.3 kHz/s. The stabilized laser frequency noise spectrum falls onto

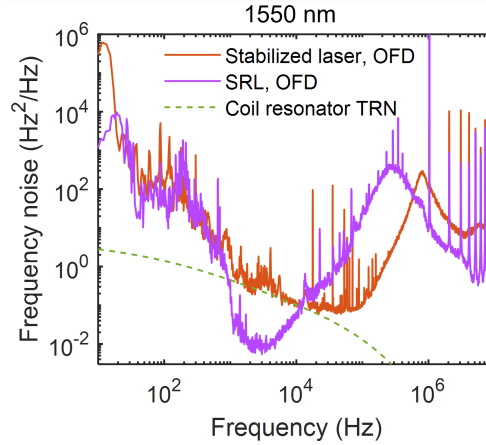


Figure 5.6: Frequency noise of the SRL laser measured by the fiber MZI OFD.

the resonator-intrinsic TRN from 50 kHz down to 20 Hz. The single sideband phase noise is calculated and plotted in Fig. 5.5(b), where the coil resonator stabilized laser phase noise is measured to be -30 dBc/Hz at 100 Hz, -64 dBc/Hz at 1 kHz and -93 dBc/Hz at 10 kHz.

### O-band TM 4-meter-coil resonators for laser stabilization

We also demonstrate this laser stabilization at O band (1319 nm) as shown in Fig. 5.7, where the stabilized laser measured by OFD reaches the TRN limit from 1 kHz to 50 kHz. Below 1 kHz offset, the coil stabilized 1319 nm laser frequency noise couldn't be reliably measured as the SRL laser is at 1550 nm.

## 5.2.2 O & L dual-band 4-meter-coil resonators

### Directional coupler simulations and experimental validations

The analysis of the PDH lock laser frequency discrimination slope in the previous section shows given the resonator intrinsic loss defined by the waveguide propagation loss having the resonator critically coupled maximizes the PDH error frequency discrimination

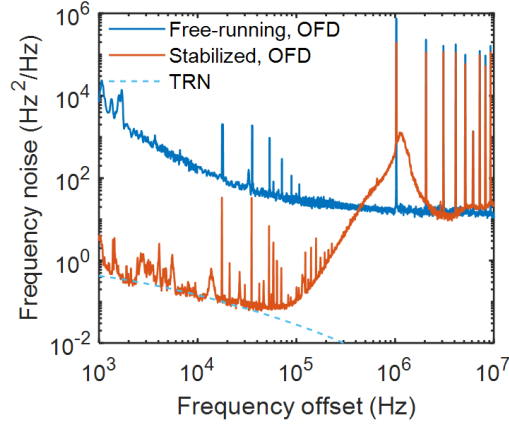


Figure 5.7: Frequency noise of the 1319 nm freerunning laser and stabilized laser by the 1319 nm 4-meter-coil resonator, measured by the fiber MZI OFD. Reproduced from [36].

slope. The resonator coupling design is critical to the SNR in the PDH lock and laser stabilization experiments.

The TM mode 4-meter-coil resonator designed for the wavelength of 1319 nm uses a direction coupling section with a gap of  $3.5 \mu\text{m}$  and length of 3.0 mm, while the TM mode 4-meter-coil resonator at 1550 nm uses a directional coupler with a gap of  $3.5 \mu\text{m}$  and length of 0.5 mm. The coupling designs are guided by the directional coupling simulation laid out in detail in Chapter 4 of *Silicon Photonics Design* by Lukas Chrostowski [52]. The cross-section modal simulation of the two waveguides separated by a gap finds a symmetrical mode and an asymmetric mode. When the directional coupler gap is not too small relative to the waveguide width, the waveguide modes in the left and right waveguides can be represented well by a linear combination of the symmetrical and asymmetric modes,

$$\begin{pmatrix} a_L \\ a_R \end{pmatrix} = \frac{1}{\sqrt{2}} \begin{pmatrix} 1 & 1 \\ -1 & 1 \end{pmatrix} \begin{pmatrix} a_S \\ a_{AS} \end{pmatrix}. \quad (5.17)$$

The modal simulations find the index difference,  $\delta n_{eff}$  between the symmetrical and asymmetric modes for a specific waveguide mode such as  $\text{TE}_0$ ,  $\text{TE}_1$ , or  $\text{TM}_0$ , and the

index difference causes interference between the symmetrical and asymmetric modes in the input waveguide and results in energy coupling and switching between the left and right waveguides. The power coupling coefficient can be found and expressed,

$$\kappa(g, t, \lambda, L_x) = \sin \frac{\pi \delta n_{eff}(g, t, \lambda) L_x}{\lambda}, \quad (5.18)$$

where  $g$  is the coupling gap,  $t$  is the waveguide thickness,  $L_x$  is the coupler length and  $\lambda$  is the wavelength. Since the mode index difference  $\delta n_{eff}(g, t, \lambda)$  is a function of waveguide dimensions, coupling gap  $g$  and wavelength  $\lambda$ , it can be obtained from simulations. And this approach can simulate and perform a numerical sweep of the bus-ring coupling very efficiently versus different variables such as coupling gap, waveguide thickness, wavelength, and coupling length.

The material indices for different materials are important and affect the simulation accuracy to a certain extent. The indices for the lower cladding thermal oxide, upper cladding TEOS-PECVD oxide, and LPCVD silicon nitride can be found in the supplementary information in [53]: thermal oxide - 1.444, TEOS-PECVD oxide - 1.452, LPCVD nitride - 1.936, at 1550 nm. The upper and lower cladding index difference could lead to some asymmetry in the vertical direction of the simulated optical modes, and can cause inconveniences in the modal coupling simulations. Therefore, for all the simulations presented in this thesis, the cladding materials use 1.444 for the refractive index at 1550 nm. At 1319 nm, despite material dispersion, the simulations use the same set of indices: silicon dioxide - 1.444 and silicon nitride - 1.936.

Fig. 5.8(a) shows the simulated power coupling coefficient  $\kappa^2$  of the 3.0-mm-long coupler at different gaps, and the measured power coupling of the TE and TM modes using the testing structures (indicated by circles and crosses) agrees well with the simulated curves. Fig. 5.8(b) shows the comparison between the simulated power coupling coeffi-

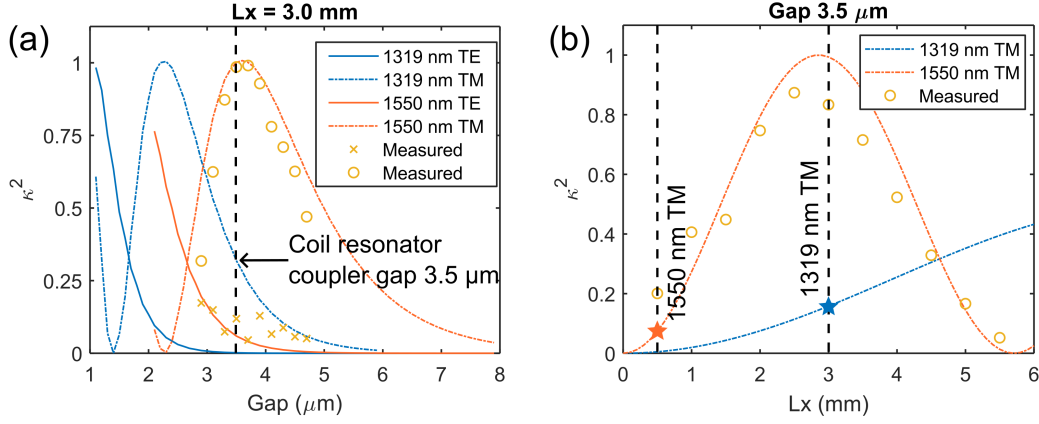


Figure 5.8: Coupling simulation of the directional coupler for the coil resonator using the TE and TM modes at 1319 nm and 1550 nm compared to measured values.

cient of the 3.5- $\mu\text{m}$ -gap coupler at different coupling lengths and the measured values. Both Fig. 5.8(a) and (b) show the sinusoidal oscillation effect, according to Eq. 5.18, through exponentially increasing  $\delta n_{eff}$  at smaller coupling gaps while (b) shows a linear oscillation dependence on the coupling length  $L_x$ . Because  $\delta n_{eff}$  increases exponentially with the decreasing gap, it is beneficial to keep the coupling gap out of the drastic oscillating cycle, and in this case in Fig. 5.8(a) when choosing  $L_x = 3.0$  mm, the gap should not be smaller than 3.0  $\mu\text{m}$ .

Since the TM mode waveguide has an intrinsic loss rate of around 1~3 MHz, achieving 1 MHz coupling rate requires the coupling coefficient to be  $\kappa^2 = 12\%$ , according to Eq. 2.18,

$$\gamma_{ex} = \frac{\log(1/\tau^2)c}{n_g L}. \quad (5.19)$$

The map of the coupling with the coupling gap and length as the input generated from the coupling simulation and validated by experimental measurements guides the coupling design for the desired coupling values needed for different modes and wavelengths. Hence, here, the TM mode 4-meter-coil resonator at 1319 nm uses the a 3.5- $\mu\text{m}$ -gap and 3.0-mm-long direction coupler, while the TM mode 4-meter-coil resonator at 1550 nm uses

a 3.5- $\mu\text{m}$ -gap and 0.5-mm-long direction coupler.

### Near critical coupling at both 1319 nm (TM) and 1630 nm (TE) in one coil resonator

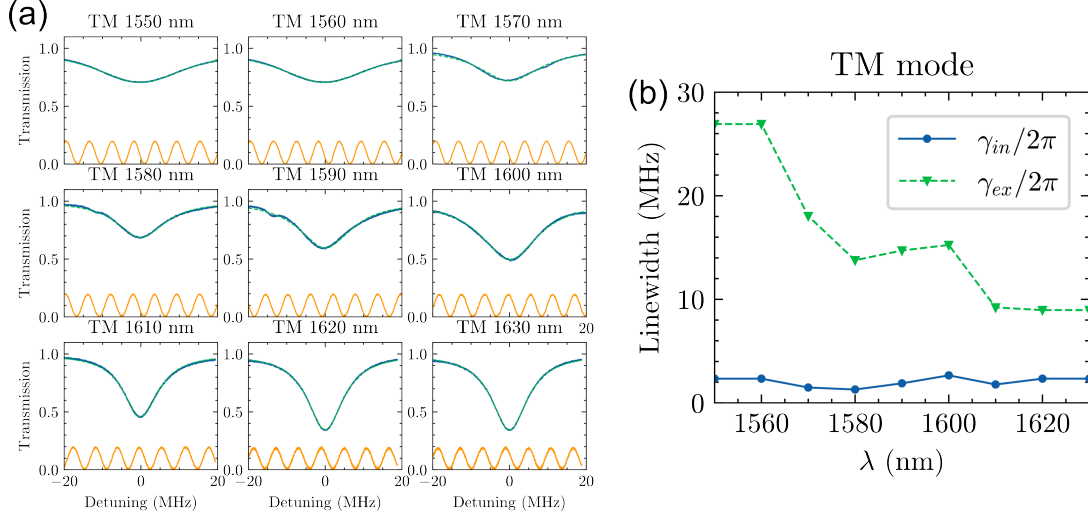


Figure 5.9: TM mode Q measurement at C and L bands from 1550 nm to 1630 nm of the 1319 nm TM mode 4-meter-coil resonator.

Although the coupling design (3.5  $\mu\text{m}$  gap, 3.0 mm length) for the TM mode 4-meter-coil resonator is optimized specifically for the TM mode at 1319 nm. The TM mode in the C and L bands from 1550 nm to 1630 nm is strongly coupled, as shown in Fig. 5.9. Usually, the bus waveguide coupling coefficient increases at longer wavelengths due to decreasing confinement, as  $\kappa = \sin(\pi\delta n_{eff}L_x/\lambda)$  increases with increasing  $\delta n_{eff}$  when  $\pi\delta n_{eff}L_x/\lambda < \pi/2$ . However, it is the opposite in Fig.5.9 and the coupling decreases at longer wavelengths. This is because the coupler (3.5  $\mu\text{m}$  gap, 3.0 mm length) for the TM<sub>0</sub> mode has a nearly 100% coupling coefficient (Fig. 5.8(a)), meaning  $\pi\delta n_{eff}L_x/\lambda \sim \pi/2$  and  $\kappa = \sin(\pi\delta n_{eff}L_x/\lambda) \sim 1$ , and  $\kappa = \sin(\pi\delta n_{eff}L_x/\lambda)$  starts the decreasing cycle with increasing  $\delta n_{eff}$ . However, in contrast to the TM resonances in the C and L band, Fig. 5.10 shows the measured intrinsic and coupling linewidth of the TE mode from



1550 nm to 1630 nm and the TE mode is quite weakly coupled at 1550 nm as confirmed by the coupling simulation for the TE mode at 1550 nm in Fig. 5.8(a). However, because the TE mode at 1550 nm is very weakly coupled and is on the normal side of the coupling oscillation cycle, its coupling increases significantly with wavelength, which is also measured and shown in Fig. 5.10. At 1630 nm, the TE mode is quite close to critical coupling. Therefore, not only is the TM mode 4-meter-coil resonator properly coupled at 1319 nm (shown in Fig. 5.4(c)), which is the initial design intent, but also the TE mode is properly coupled at 1630 nm, in the one single coil waveguide resonator.

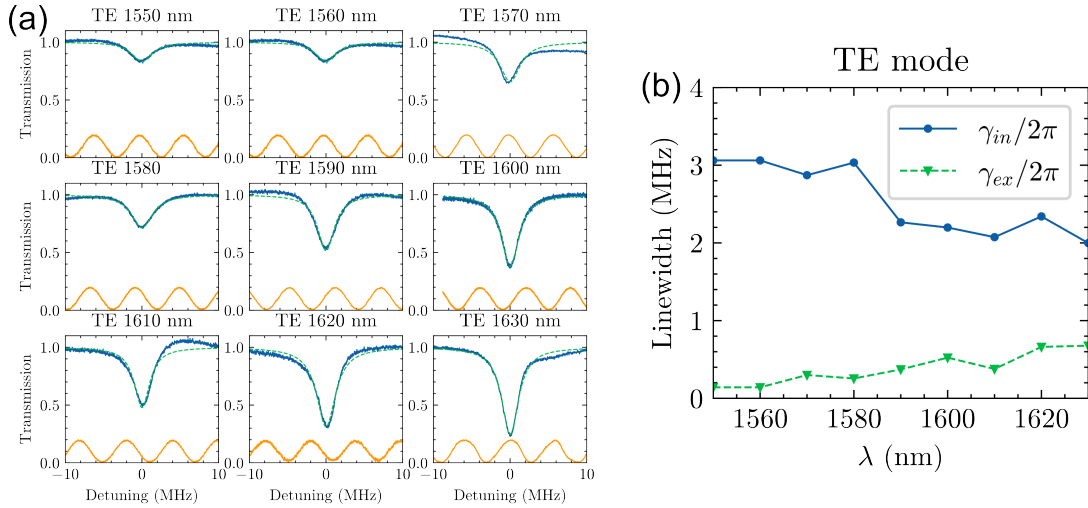


Figure 5.10: TE mode linewidth and Q measurement from 1550 nm to 1630 nm of the 1319 nm TM mode 4-meter-coil resonator.

### 5.3 TE coil waveguide resonators (4, 10, 17 meters)

The TE<sub>0</sub> mode in the 6 μm wide and 80 nm thick waveguide has a critical bending radius below 1 mm, as shown in Fig. 2.7, which enables the making of meter-long spiral waveguides in a center-meter-scale chip size. As such a waveguide design at C and L band has a propagation loss of around 0.2 dB/m and the corresponding waveguide resonator intrinsic loss rate is ~1.4 MHz, to couple the coil resonators of different coil waveguide

lengths with about 1 MHz coupling loss needs the bus-resonator coupling of 6%, 12%, 27%, and 40% for coil lengths of 2 m, 4 m, 10 m, and 16 m, calculated by Eq. 2.18, shown in the table in Fig. 5.11.

(a) Coil length	FSR (MHz)	1 MHz TE $\kappa^2$	$2.5\mu\text{m}$ gap $L_x$	$2.0\mu\text{m}$ gap $L_x$
2.0 m	100 MHz	<b>6.0%</b>	0.8 mm	0.5 mm
4.0 m	50 MHz	<b>12%</b>	1.1 mm	0.7 mm
10.0 m	20 MHz	<b>27%</b>	1.7 mm	1.0 mm
16.0 m	12.5 MHz	<b>40%</b>	2.2 mm	1.2 mm

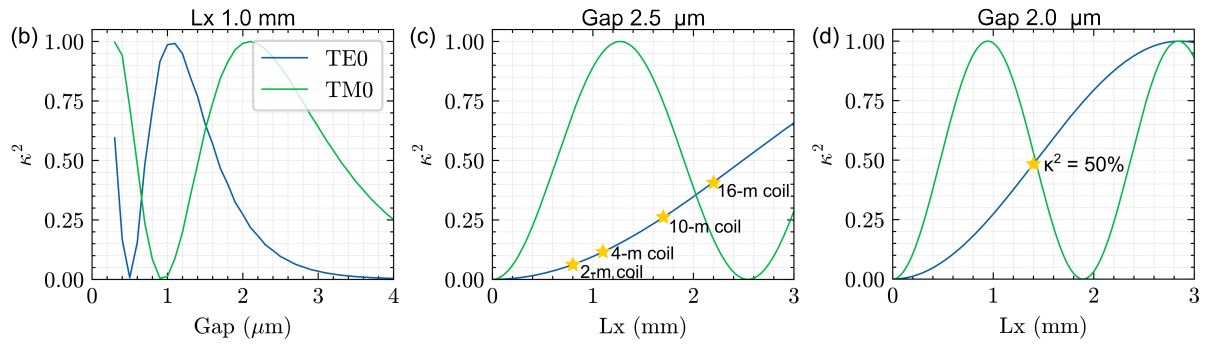


Figure 5.11: Coupling design for coil resonators of different coil lengths using the  $6\mu\text{m}$  by  $80\text{ nm}$  TE waveguide at  $1550\text{ nm}$ . (a) Coupling values needed for 1 MHz coupling rate for 2-m, 4-m, 10-m, and 16-m coil resonators. Simulated directional coupling coefficient by (b) sweeping the coupler gap with  $L_x = 1.0\text{ mm}$ , (c) sweeping  $L_x$  at  $2.5\mu\text{m}$  gap, (d) sweeping  $L_x$  at  $2.0\mu\text{m}$  gap.

The coupling simulation for the coil resonators and the  $6\mu\text{m}$  by  $80\text{ nm}$  TE waveguide employs the same approach described in Section 5.2.2 and Eq. 5.18, and the simulated coupling curves by sweeping the direction coupler gap and coupling length are plotted in Fig. 5.11(b), (c), and (d).

### 5.3.1 TE mode 4-meter-coil resonators

In the design of the 4-meter-coil waveguide resonator, the spiral center-to-center waveguide spacing is reduced from the previous  $40\mu\text{m}$  used in the TM coil resonators to  $30\mu\text{m}$ , because of the TE's larger mode confinement, resulting in a much smaller device

size and making it possible to put two 4-meter-coil resonators on a single die size (21.6 mm by 26 mm). The 4-meter-coil resonator directional coupler uses  $2.5 \mu\text{m}$  gap and 1.0 mm  $L_x$ . The bus waveguide is tapered to  $1.5 \mu\text{m}$  for better fiber-to-chip edge coupling. The S-bend diameter is  $\sim 2.3$  mm.

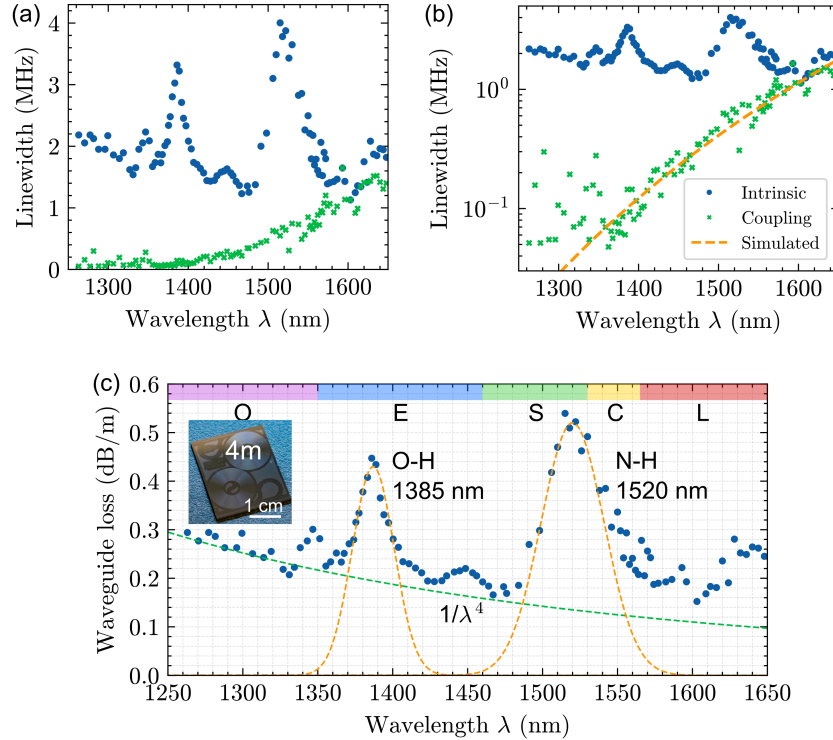


Figure 5.12: Broadband waveguide loss spectrum of the  $6 \mu\text{m}$  by  $80 \text{ nm}$   $\text{TE}_0$  waveguide measured in the 4-meter-coil waveguide resonator from 1250 nm to 1650 nm.

### Waveguide loss spectrum from 1250 nm to 1650 nm

The spectral scanning using several widely tunable lasers measures the coil resonator intrinsic and coupling linewidths from 1250 nm to 1650 nm, covering O, E, S, C and L bands. Two absorption peaks emerge at near 1385 nm and 1520 nm, related to O-H and N-H absorptions in the optical waveguides, shown in Fig. 5.12(a) and (c). The resonator coupling linewidth decreases exponentially towards shorter wavelengths, as confirmed by the simulated dash curve in Fig. 5.12(b).

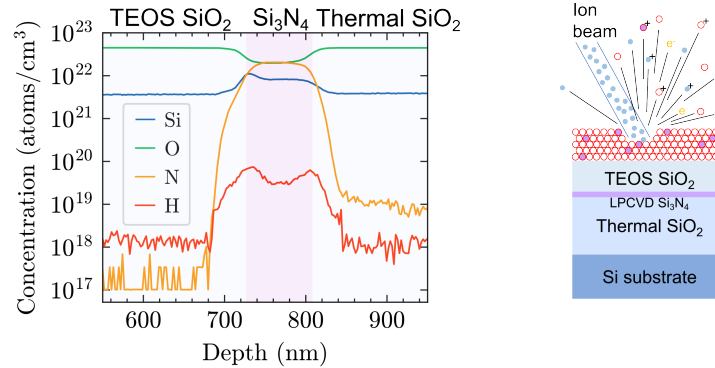


Figure 5.13: Secondary ion mass spectroscopy of a 4-meter-coil resonator chip sample shows the hydrogen content in the LPCVD nitride layer.

By secondary ion mass spectroscopy (SIMS), the atomic content across the waveguide structure depth is sampled on a less than 1-mm-diameter bombarding area on a coil resonator chip after its upper cladding was removed down to less than  $1\ \mu\text{m}$  thick, shown in Fig. 5.13. The hydrogen detection limit in silicon dioxide is about  $10^{18}$  atoms/cm<sup>3</sup>, according to EAG Lab [54]. The bombarding area is a 50% fill pattern on the silicon nitride layer with a 50/50 mixture of silicon dioxide and silicon nitride. As can be seen from Fig. 5.13, the TEOS oxide is as good as the thermal oxide in terms of hydrogen impurity at the SIMS detection limit. The hydrogen impurity content mainly resides in the LPCVD nitride layer. Therefore, further reducing the hydrogen content in the LPCVD nitride is the next step besides further smoothening the waveguide surfaces to further reduce the waveguide loss in the sub-0.1-dB/m loss regime.

### Laser stabilization with hybrid comb laser

To demonstrate the coil resonator as an optical reference, we frequency-lock a hybrid-integrated 16-wavelength-channel comb laser to the coil resonator for laser stabilization and linewidth reduction achieving achieving an 89 Hz integral linewidth and an Allan deviation of  $4.3 \times 10^{-13}$  at 10.5 ms at 1544.4 nm, shown in Fig. 5.14. This is implemented using a Red Pitaya FPGA board (STEMlab 125-14 Low Noise) and pyrpl Python API



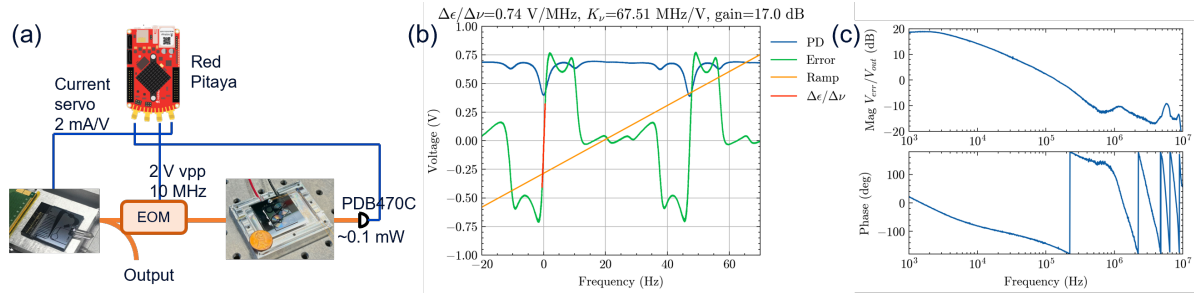


Figure 5.15: Open-loop frequency response in the PDH feedback lock system shows a  $180^\circ$ -phase-lag frequency of  $\sim 200$  kHz.

### 5.3.2 TE mode 10-meter-coil resonators

The 10-meter-coil resonator uses a similar set of design parameters as the 4-meter-coil resonator such as waveguide dimensions, except that the S-bend diameter is  $\sim 3.6$  mm and the coupler length is  $L_x = 1.5$  mm, and the spiral waveguide center-to-center waveguide spacing is reduced to  $25 \mu\text{m}$ . A single 10-meter-coil resonator occupies a single die size (21.6 mm by 26 mm), and Fig. 5.16 shows the fabricated 10-meter-coil resonator device after pig-tailing PM-SMF28 fibers to the bus waveguide facets in a metal packaged.

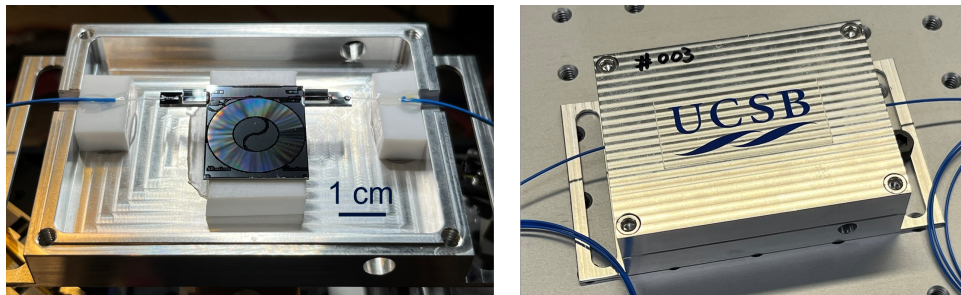


Figure 5.16: 10-meter-coil resonator with PM-SMF28 fibers pig-tailed and packaged in a metal enclosure.

### Waveguide loss spectrum from 1450 nm to 1630 nm

To measure the 10-meter-coil waveguide resonator in a wide wavelength range, we employ two widely tunable lasers, Newport Velocity TLB-6700 laser (1550 nm - 1630 nm) and Keysight/Agilent 81689A tunable laser (1465 nm to 1575 nm). In Fig. 5.17,

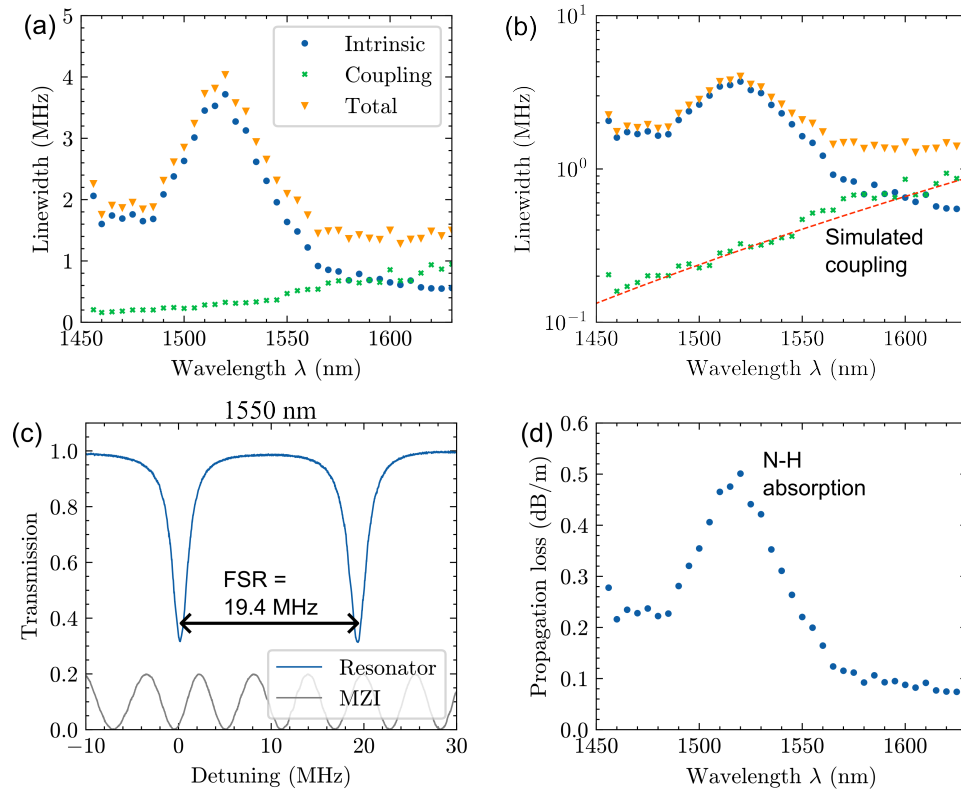


Figure 5.17: Waveguide loss spectrum of the  $6\ \mu\text{m}$  by  $80\ \text{nm}$   $\text{TE}_0$  waveguide measured in the 10-meter-coil waveguide resonator from 1450 nm to 1630 nm.

the N-H absorption peak emerges at 1520 nm with a peak loss of 0.52 dB/m, and above 1600 nm, the waveguide loss falls below 0.1 dB/m.

### Laser stabilization reaching 27 Hz linewidth

A Thorlabs ULN laser is used to frequency lock to the 10-meter-coil resonator that is well packaged as shown in Fig. 5.16 with a layer of acoustic foam wrapped around it for acoustic noise isolation in the 1 to 10 kHz frequency range and put on an optical floating table to isolate ground vibration noise in the 1 to 100 Hz frequency range. The stabilized laser frequency noise and laser stability is measured by a fiber MZI above 1 kHz frequency offset and a ultra-stable laser near 1550 nm below 1 kHz offset, as shown in Fig. 5.19. The stabilized laser frequency noise reaches the 10-meter-coil resonator

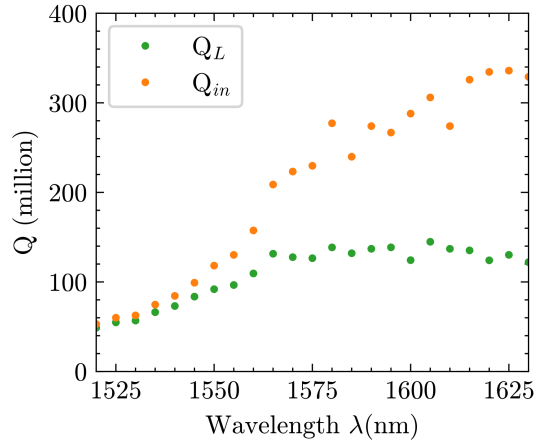


Figure 5.18: Loaded and intrinsic  $Q$  measured from the 10-meter-coil waveguide resonator from 1450 nm to 1630 nm.

TRN limit near frequency offset from 1 kHz to 40 kHz, and is mostly limited by the environmental noise that could not be isolated from the packaged resonator. The  $1/\pi$ -integral linewidth is measured to be 27 Hz and the Allan deviation reaches  $1.4 \times 10^{-13}$  at 5.1 ms, corresponding to the total linewidth of 27 Hz. The  $1/\pi$ -integral linewidth limited by the simulated 10-meter-coil resonator TRN is 2.1 Hz, indicating that the stabilized laser could eventually reach 2.1 Hz with better isolation of the environmental noise from the coil resonator.

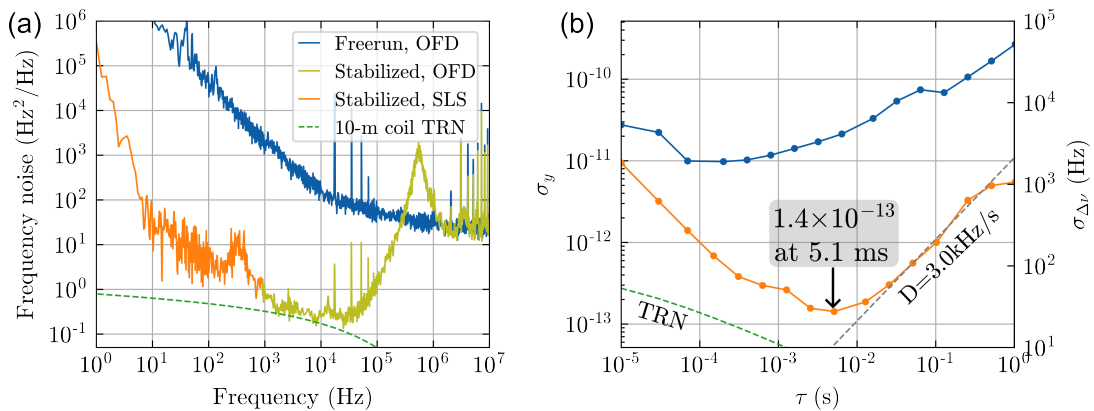


Figure 5.19: Laser stabilization using the packaged 10-meter-coil resonator achieves a  $1/\pi$  integral linewidth of 27 Hz and Allan deviation of  $1.4 \times 10^{-13}$  at 5.1 ms.



### 5.3.3 TE mode 17-meter-coil resonators

In order to pack even longer waveguides into the single die area (21.6 mm by 26 mm), the first redesign is on two S-bend structures used at the center of the coil waveguides and the loop back outside of the coil waveguides, shown in Fig. 5.20(a). All the 4-meter and 10-meter coil resonators in the previous sections use the circular S-bends, which are not the most efficient approach to rerouting the waveguides. Both the coil S-bend and the loop back bending waveguides use the Euler bends with a Euler bend parameter  $p$  and effective bending radius  $R_{eff}$  [58]. Here, the Euler bend parameter  $p$  is the portion of the bend having a linearly increasing curvature. The Euler bend angle  $\alpha$ , the bend parameter  $p$ , and the effective radius  $R_{eff}$  together determine the minimum radius  $R_{min}$ , and a larger  $p$  with fixed  $\alpha$  and  $R_{eff}$  leads to smaller  $R_{min}$ .  $p = 0.1$  can be a quite effective transition for the optical waveguide mode from straight waveguide to circular bend waveguide while maintaining  $R_{min} \simeq 0.90 \sim 0.99R_{eff}$  for  $90^\circ$  to  $180^\circ$  Euler bends. Thus,  $p = 0.1$  is used for all the Euler bends in our layout, where  $R_{min} = 0.93R_{eff}$  with  $\alpha = 90^\circ$ ,  $R_{min} = 0.96R_{eff}$  with  $\alpha = 150^\circ$ , and  $R_{min} = 0.99R_{eff}$  with  $\alpha = 180^\circ$ . Illustrated in Fig. 5.20(a), the coil S-bend structure consists of two  $150^\circ$  Euler bends and a straight waveguide, and the loop back structure outside the coil waveguides consists of a  $180^\circ$  Euler bend and a  $90^\circ$  Euler bend. The second redesign is to decrease the center-to-center waveguide spacing in the coil structure to  $20 \mu\text{m}$ . The bus-resonator coupler has a coupling gap of  $2.0 \mu\text{m}$  and a coupling length of  $1.0 \text{ mm}$  to achieve critical coupling. The bus waveguide is tapered from  $6 \mu\text{m}$  wide down to  $1.5 \mu\text{m}$  for efficient fiber-to-chip edge coupling. Figure 5.20(a) shows a photograph of a 17-meter-coil resonator fabricated on a 200-mm wafer.

The resonator Q factors are measured using a fiber MZI technique and are shown in Fig. 5.20(b) with an FSR of 11.2 MHz, 249 million intrinsic Q, and 115 million loaded Q

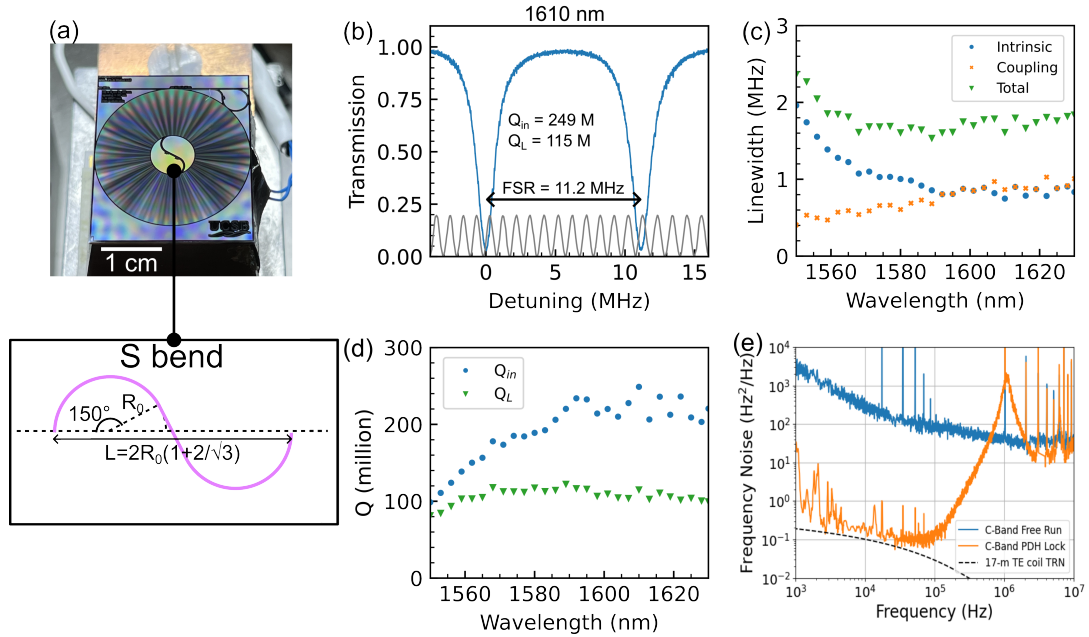


Figure 5.20: 17-meter-coil resonator design and testing and laser stabilization results. (a) 17-meter coil resonator on 21.6 mm by 26 mm reticle. (b) 249 million intrinsic  $Q$ , 115 million loaded  $Q$ , and an FSR of 11.2 MHz measured at 1610 nm. (c) Total, intrinsic and coupling linewidths measured from 1550 nm to 1630 nm. (d) Measured intrinsic and loaded  $Q$  from 1550 nm to 1630 nm. (e) Measured frequency noise spectrum for the free-running laser and the stabilized laser locked to the 17-meter-coil resonator,

measured at 1610 nm. The resonator linewidths and  $Q$ s are measured from 1550 to 1630 nm (Fig. 5.20(c, d)), showing critical coupling from 1590 nm to 1630 nm. To demonstrate the reduced TRN from the 17-meter-long coil resonator, we perform PDH locking with a C-band semiconductor laser [51]. To measure the free-running and stabilized frequency noise, we use a fiber MZI with a 1.026 MHz FSR for laser frequency noise components greater than 1 kHz, shown in Fig. 5.20(e).

## 5.4 Two-point-coupled coil resonators

Waveguide propagation loss and resonator  $Q$ s are critical for the application performance and have made significant progress. Realizing the desired resonator coupling

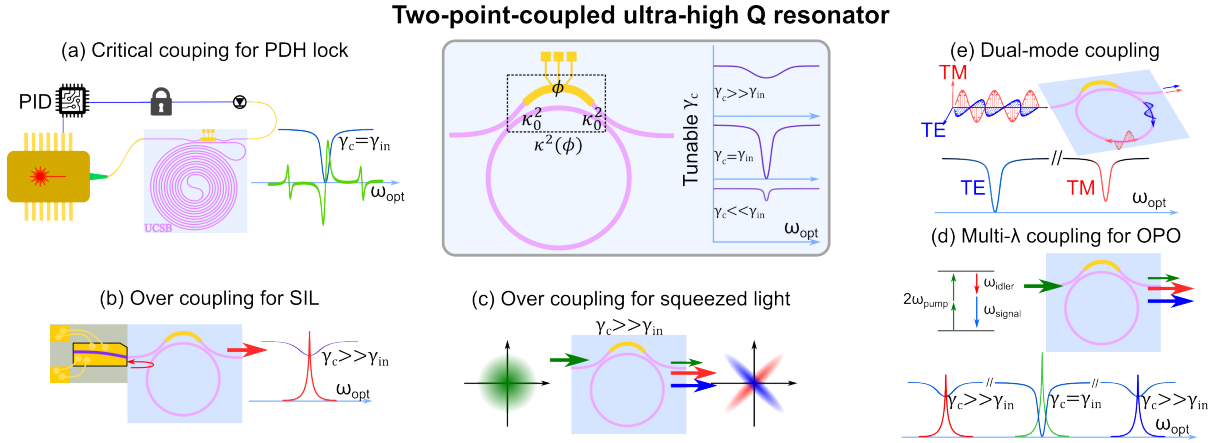


Figure 5.21: Two-point-coupled ultra-high Q resonators for various applications, such as (a) critical-coupled ultra-high Q reference resonators for PDH lock and laser stabilization, (b) over-coupled resonators for increased feedback and output power in self-injection locked lasers, (c) squeezed light generation in over-coupled resonators, (d) multi-wavelength coupling design for efficient OPO processes, and (e) dual-mode coupling. TE, transverse electric. TM, transverse magnetic. SIL, self-injection lock. PDH, Pound-Drever-Hall. OPO, optical parametric oscillation. Reproduced from [59].

regime, i.e. the degree of coupling: under-, over- or critical-coupled is equally important in different applications, as shown in Fig. 5.21. Critical coupling is desirable when the resonance is at its minimum and the extinction ratio is at its maximum for stimulated Brillouin scattering lasers to achieve a low optical threshold, high Brillouin conversion efficiency, high output power, and narrow fundamental linewidth [60, 50, 61, 62]. Low-noise and stable reference resonators for laser stabilization applications require operation at the critical coupling point at the desired stabilized laser wavelength to maximize the SNR in the laser frequency noise discrimination and noise suppression processes, as discussed in Section 5.1.1 [41]. Over-coupled designs in self-injection locked lasers can increase the Rayleigh scattering reflection for nonlinear feedback and the consequent narrowing of the laser linewidth [63, 64]. Squeezed light generation requires over-coupling in the squeezing mode, whereas the pump modes are critically coupled [42]. Applications such as optical parametric oscillation (OPO) processes benefit from critical coupling at two

or more wavelengths simultaneously [44]. Therefore, it is important to have versatility in the resonator coupling design.

An effective approach to make a versatile resonator coupling design is the so-called tunable two-point coupling, which is an unbalanced MZI that can achieve resonator coupling tuning by changing the phase section between zero coupling and its maximum coupling,  $\kappa_{max}^2 = 4\kappa^2(1 - \kappa^2)$ , determined by its single coupler coupling coefficient  $\kappa^2$  [65, 66, 59], and the tunable two-point coupling can be expressed as  $\kappa_t^2 = \kappa_{max}^2 \cos^2(\phi/2)$ . The maximum coupling  $\kappa_{max}^2$  needs to be large enough to provide a wide tuning range, as shown in Fig. 5.22. Here, we employ probe laser wavelength tuning to demonstrate coupling tunability. In wavelength tuning, the tuning period is directly related to the MZI delay ( $\delta L$ ) and corresponds to the MZI FSR, that is,  $\delta\lambda_{2\pi} = \lambda^2/n_g\delta L$ . Similarly, for temperature tuning, a longer MZI delay leads to a shorter temperature tuning period.

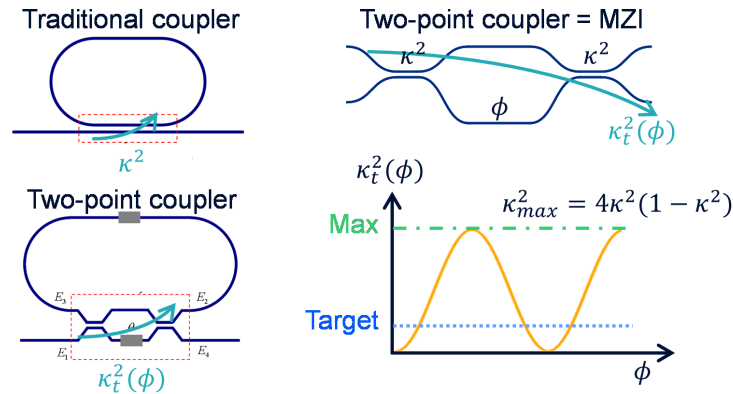


Figure 5.22: Two-point coupling working principle.

### 5.4.1 Two-point-coupled 10-meter-coil resonators

The two-point-coupled 10-meter-coil waveguide resonator has the same set of design parameters as the one-point-coupled 10-meter-coil resonator, except that it has two identical directional couplers (2.5  $\mu\text{m}$  gap and 1.4 mm coupling length) with a 0.28 mm long

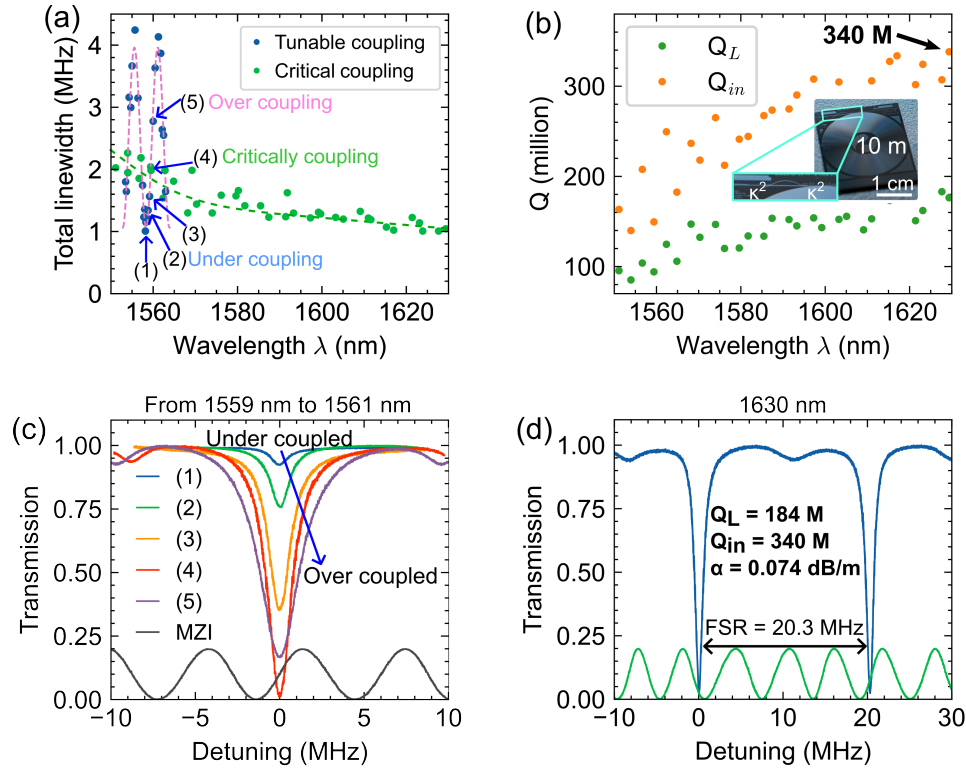


Figure 5.23: Two-point coupled 10-meter-coil resonator. (a) Measured resonator linewidth from 1550 nm to 1630 nm shows resonator coupling tuning with a tuning period of 5.6 nm, and critical coupling from 1550 nm to 1630 nm. (b) The loaded and intrinsic  $Q$ s. (c) The under-coupled, critically coupled, and over-coupled resonances. (d) The spectral scan of the critically coupled resonance at 1630 nm. Reproduced from [59].

phase delay section shown in the picture in Fig. 5.23(b) that corresponds to  $\delta\lambda_{2\pi} = 5.6$  nm at 1550 nm.

The 10-meter-coil resonator linewidth and  $Q$  measurements are shown in Fig. 5.23, where the two-point coupling is measured to have a maximum that is four times the waveguide intrinsic loss with a tuning period of  $\sim 5.6$  nm around 1550 nm. From 1559 nm to 1561 nm, while tuning the coupling from under- through critically- to over-coupled, the coil resonator can be critically coupled twice within each tuning period. Therefore, the coil resonator is critically coupled approximately every  $\sim 2.8$  nm from 1550 nm to 1630 nm. Figure 5.23(b) shows the measured loaded and intrinsic  $Q$ s of the critically

coupled resonances from 1550 nm to 1630 nm, which measures 340 million intrinsic  $Q$  and an equivalent waveguide loss of 0.074 dB/m at 1630 nm (Fig. 5.23(d)).

### Laser stabilization and integral linewidth

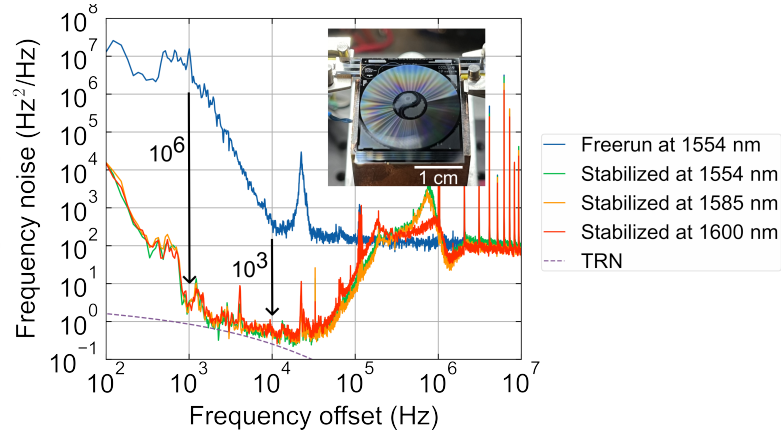


Figure 5.24: Laser stabilization and frequency noise reduction at multiple critically-coupled wavelengths in the C and L bands. Reproduced from [59].

The widely tunable laser (Velocity™ TLB-6700) is used to probe the coil reference resonator and demonstrate the PDH lock at multiple critically coupled wavelengths, 1554 nm, 1585 nm, and 1600 nm, where the free-running and stabilized laser frequency noise is measured with a 1.026 MHz FSR unbalanced fiber MZI. The PDH lock bandwidth reaches  $\sim 1$  MHz and suppresses the laser frequency noise by 6 orders of magnitude at 1 kHz offset and three orders of magnitude at 10 kHz, reducing the integral linewidth to 334 Hz from the 22 kHz free-running integral linewidth, shown in Fig. 5.24. The laser stabilization performances at three different wavelengths are nearly identical, and the stabilized laser frequency noise reaches the TRN from 1 kHz to 40 kHz offset, indicating sufficiently large SNRs in frequency noise discrimination. The measured 334 Hz integral linewidth is limited by the fiber noise in the unbalanced MZI used for measuring the laser frequency noise.

### 5.4.2 Two-point-coupled coil resonators from 900 to 1600 nm

Illustrated in Fig. 5.21, proper coupling in a single resonator at drastically different wavelengths is needed in achieving efficient OPO oscillators and second-harmonic generations, which is very challenging. Using the two-point coupling technique, the previous section has already shown that the two-point-coupled 10-meter-coil resonator can achieve critical coupling from 1550 nm to 1630 nm. Here, we take this step further by significantly increasing the coupling strength at longer wavelengths such as 1550 nm and decreasing the coupler gap, so that the maximum coupling  $\kappa_{max}^2 = 4\kappa^2(1 - \kappa^2)$  also provide sufficient resonator coupling towards shorter wavelengths, which can be simply implemented by decreasing the coupling gap of the directional coupler, illustrated in Fig. 5.25, where the coupling gap is decreased from 2.5  $\mu\text{m}$  to 0.8  $\mu\text{m}$  for a two-point coupler with each directional coupler's coupling length of 1.0 mm, and the maximum coupling is simulated from 700 nm to 1600 nm, compared by the dash line indicating the coupling of 0.12 to yield 1 MHz resonator coupling for a 4-meter-coil resonator.

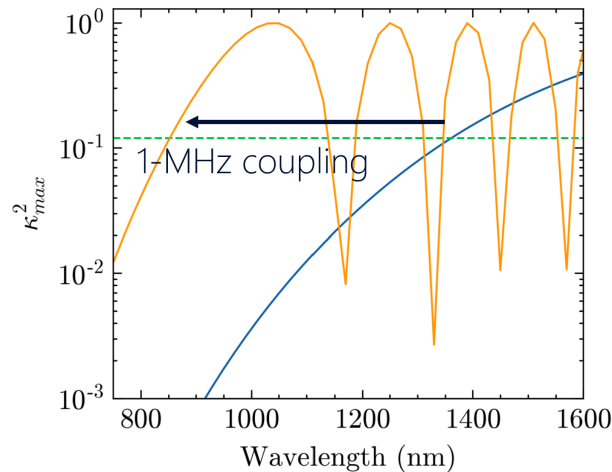


Figure 5.25: The maximum coupling of a two-point coupler with a coupling length of  $L_x = 1.0$  mm is simulated and plotted versus wavelength from 700 nm to 1600 nm at two different coupling gaps, 2.5  $\mu\text{m}$  (blue curve) and 0.8  $\mu\text{m}$  (green curve), respectively.

### Critical coupling achieved from 900 nm to 1600 nm

Figure 5.26 shows the resonator spectral linewidths and  $Q$ s measured at different wavelengths such as 780, 910, 1064, 1260, 1320, 1550, and 1610 nm, where the micro-heater on top of the two-point-coupling phase section tunes the resonator coupling for different wavelengths. The laser sources used at these wavelengths are all single frequency tunable lasers and a few MZIs of different FSRs were used for laser frequency detuning calibration. At all these wavelengths, the resonator can reach critical coupling, except at 780 nm, likely due to the coupler coupling roll-off for the fundamental TE mode below 800 nm shown in Fig. 5.25. The propagation loss for the fundamental TE mode in the 6  $\mu\text{m}$  by 80 nm  $\text{Si}_3\text{N}_4$  waveguide can be estimated and plotted in Fig. 5.27 with the data point of 780 nm being an outlier. In the future designs, the coupler gap can be further decrease from the current 0.8  $\mu\text{m}$  value to increase the evanescent coupling at shorter wavelength to extend the resonator coupling wavelength range.

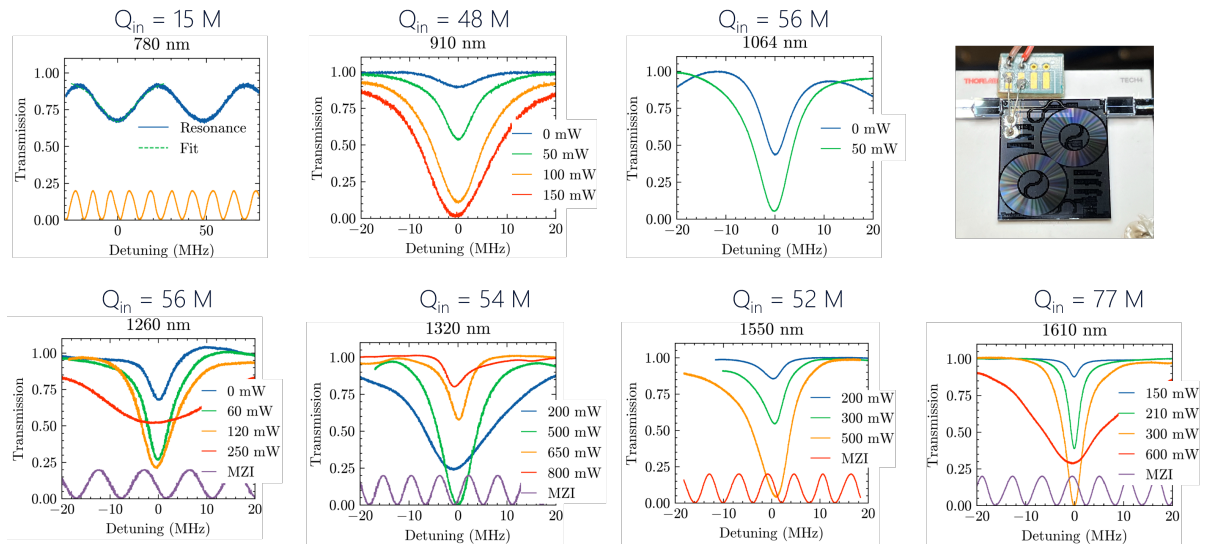


Figure 5.26: Upper right is the device that is fiber pig-tailed and has a metal tuner on the two-point-coupling phase section which is wire-bonded. From left to right are the spectral scanning measurements of the resonance linewidths and  $Q$ s at 780 nm, 910 nm, 1064 nm, 1260 nm, 1320 nm, 1550 nm, 1610 nm. All the resonances are measured while tuning the two-point coupler with the micro-heater.



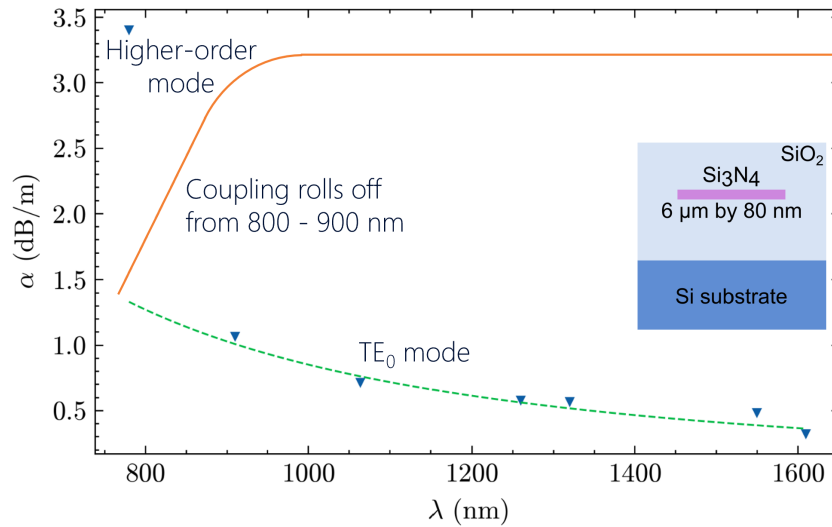


Figure 5.27: The waveguide propagation loss extracted from the resonator linewidth and Q measurements in Fig. 5.26 is shown with a dashed trend line. The loss measured at 780 nm is likely from a higher-order TE mode rather than the fundamental TE mode, due to the coupling roll-off below 800 nm, shown in Fig. 5.25.

### Laser stabilization at 1310 nm and 1550 nm

To demonstrate the utility of the broadband two-point-coupled coil resonator, we use it for laser stabilization at two drastically different wavelengths, 1550 nm and 1320 nm. The freerunning lasers are the Thorlabs Ultra-Low Noise lasers. The resonances at 1550 nm and 1320 nm are near critical coupling for laser locking experiments. The stabilized lasers at both 1550 nm and 1320 nm reaches to the TRN limit of the coil resonator, shown in Fig. 5.28.

## 5.5 Self-delayed coil resonators

Laser stabilization using the PDH locking technique [41] requires sideband modulation and demodulation to avoid photodetector DC noise and the AM-FM noise conversion, which results in residual amplitude noise [67, 68]. In the past, an approach has been demonstrated that generates the PDH lock frequency discrimination error signal without

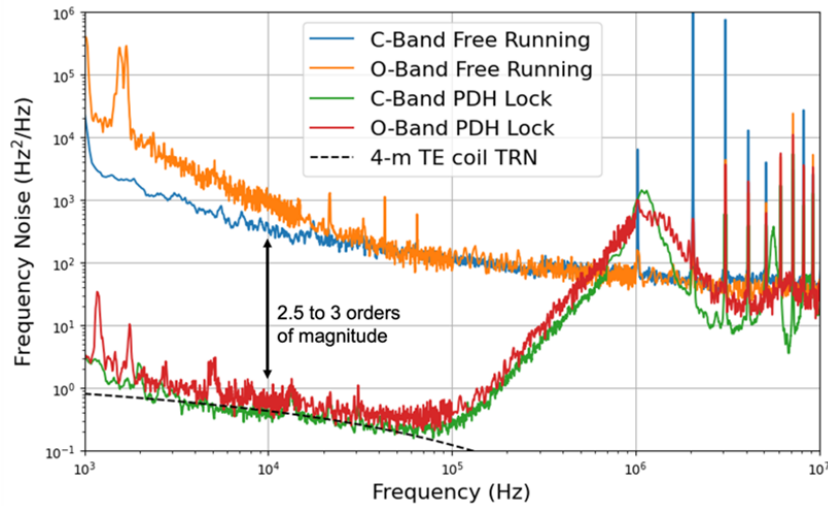


Figure 5.28: Laser stabilization at 1550 nm and 1320 nm reaches the resonator TRN limit in a single coil resonator that uses a two point coupler that can provide enough coupling for critical coupling from 900 nm to 1600 nm.

the use of sideband modulation and demodulation, but instead uses interference from an optical cavity response and delayed laser light and balanced detection of the interference outputs [69].

Here, we demonstrate a self-delayed 2-meter-coil resonator as a reference cavity for laser stabilization without electronic sideband modulation and demodulation that reduces the laser frequency noise by 4 orders of magnitude and achieves an integral linewidth of 212 Hz. The self-delayed coil resonator has 61 million intrinsic  $Q$  and 96.9 MHz FSR [70].

### Working principles of self-delayed resonators

The self-delayed resonator consists of an MZI interferometer and a waveguide resonator that is coupled to one arm of the MZI, illustrated in Fig. 5.29(a). A matrix approach to model this self-delayed resonator can be formulated as

$$\begin{bmatrix} b_1 \\ b_2 \end{bmatrix} = \begin{bmatrix} \tau & i\kappa \\ i\kappa & \tau \end{bmatrix} \begin{bmatrix} F(\Delta\omega) & 0 \\ 0 & e^{i\Delta\phi} \end{bmatrix} \begin{bmatrix} \tau & i\kappa \\ i\kappa & \tau \end{bmatrix} \begin{bmatrix} a_1 \\ a_2 \end{bmatrix}, \quad (5.20)$$

where  $F(\Delta\omega)$  is the add-through bus-coupled waveguide resonator transfer function defined by Eq. 5.2,  $e^{i\Delta\phi}$  is the phase delay in the unbalanced MZI. The two directional couplers are identical with two inputs and outputs and have the same coupling coefficient,  $\kappa^2$ , and can be represented by the 2-by-2 matrix  $\begin{pmatrix} \tau & i\kappa \\ i\kappa & \tau \end{pmatrix}$ .

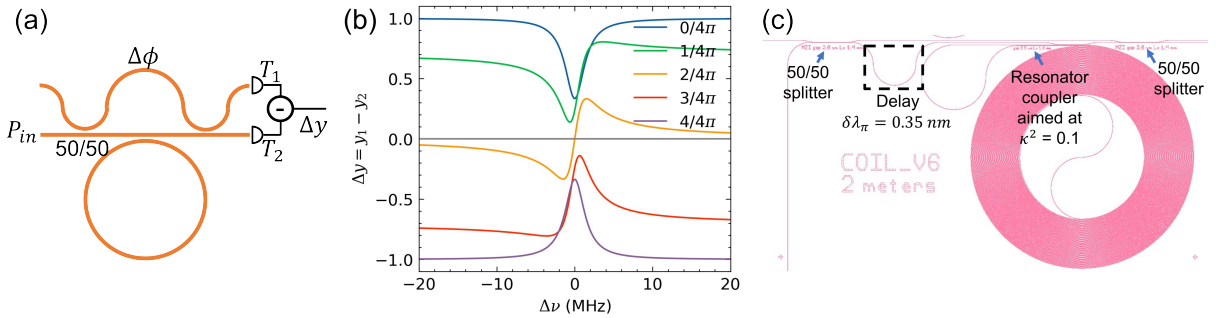


Figure 5.29: Self-delayed resonator transmission simulations.

Fig. 5.29(b) shows the balanced detection as a probe laser sweeps across the resonance, simulated using  $\Delta y = |b_2|^2 - |b_1|^2$  and Eq. 5.20. With the model by Eq. 5.20, one can show that the frequency discrimination slope achieved by the self-delayed resonator approach is identical to that in the normal PDH approach with electronic sideband modulation and demodulation by Eq. 5.10.

### Device design and modulation-free laser stabilization

The self-delayed coil resonator is a 2-meter-long waveguide coil resonator coupled to a waveguide MZI that consists of two 50/50 directional couplers and a waveguide phase delay section, shown in Fig. 5.29(c). The waveguide design is  $6 \mu\text{m}$  by  $80 \text{ nm}$  for the  $\text{TE}_0$  mode to have a waveguide loss below  $0.5 \text{ dB/m}$  and a critical bending radius below

1 mm using the ultra-low-loss silicon nitride fabrication process [29]. The length of the unbalancing delay is  $\Delta L = 2.2$  mm, corresponding to a uMZI FSR of 0.72 nm. The directional coupler is designed for a coupling power of  $\kappa^2 = 50\%$  with a  $2.0 \mu\text{m}$  gap and 1.4 mm coupling length.

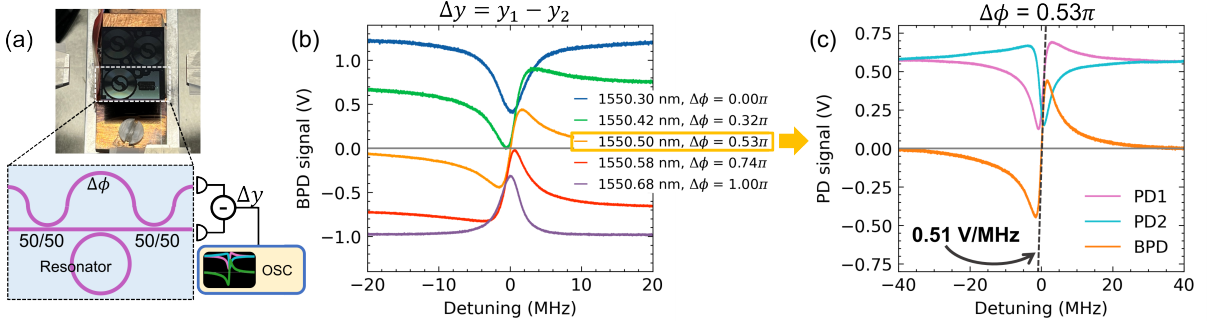


Figure 5.30: Self-delayed resonator design and testing. Reproduced from [70].

To characterize the fabricated device, we use a widely tunable laser (Velocity<sup>TM</sup> TLB-6700) for spectral scanning, a balanced photodetector (Thorlabs PDB470C), and a fiber MZI with a 5.87 MHz FSR for calibration of spectral scanning (Fig. 5.30(a)). At 1550.30 nm and  $\Delta\phi = 0$ , the loaded and intrinsic Qs are measured to be 40 million and 61 million (Fig. 5.30(b)). By changing the laser wavelength from 1550.30 nm to 1550.68 nm, the uMZI phase section delay changes from 0 to  $\pi$ , indicating the uMZI FSR is 0.76 nm (Fig. 5.30(b)). At 1550.50 nm and  $\Delta\phi = 0.53\pi$ , the two outputs are symmetric to each other and the balanced detection of the two yields a PDH-error-signal-like response with a zero-DC quadrature point (Fig. 5.30(c)), where the frequency discrimination slope is measured to be 0.51 V/MHz. Our integrated circuit OFD is compared to a 1-MHz-FSR fiber uMZI OFD. We first measure a free running laser (Velocity<sup>TM</sup> TLB-6700), in Fig. 5.31(a), then frequency-lock the laser to the self-delayed coil resonator, using the frequency discrimination error signal from the balanced detection (Fig. 5.31(b)). We demonstrate over 4 orders of magnitude noise reduction and integral linewidth narrowing

to 212 Hz, representing a  $17\times$  reduction from the free-running 3.7 kHz (Fig. 5.31(b)).

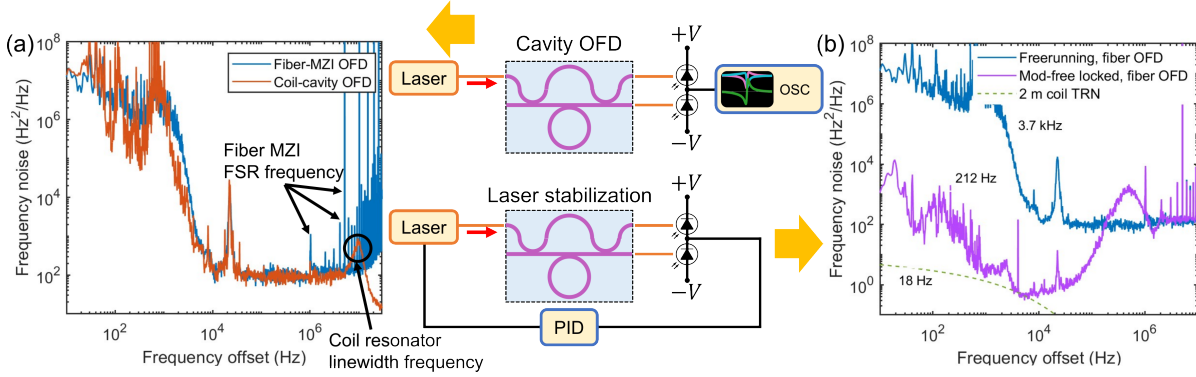


Figure 5.31: Self-delayed resonator for laser stabilization. Reproduced from [70].

## 5.6 Coil waveguide MZIs

Unbalanced fiber optical delay line Mach Zehnder interferometers (MZI) are commonly used as optical frequency discriminators (OFD) in delayed self-homodyne or self-heterodyne laser noise measurements with balanced photo-detection [71], achieving sub-hertz laser integral linewidth [72, 73], where the kilometer-long fiber delay line needs quite sophisticated packaging for vibrational and acoustic noise isolation. Photonic integrated waveguide delay-line MZI devices with ultra-low waveguide losses and up to 10 meter long delay lengths are a great candidate to make integrated versions of such delay-line-interferometer-based laser frequency references for laser stabilization and frequency discriminators for laser frequency noise and linewidth measurements. Packaging of integrated chip devices can be lower costs and more scalable solutions.

### 5.6.1 Modeling of waveguide MZI

To achieve a low noise floor for MZI-OFDs, the delay arm length ( $L$ ) should be as long as possible and the propagation loss ( $\alpha$ ) needs to be as small as possible so that the FSR

can be lowered to below 100 MHz for a high SNR in the frequency discrimination. For example, a 200-meter-long fiber MZI can have a 1 MHz FSR with very little optical loss. In addition, a long fiber delay line reduces the intrinsic thermal noise, such as thermo-refractive and thermo-elastic noise [74, 75, 76]. Making a small foot-print waveguide MZI for a low-noise-floor OFD requires small bending radii and low waveguide loss for the long delay arm, where higher waveguide confinement results in a smaller bending radius without introducing bending loss and thus longer delay ( $L$ ) but this also means more waveguide scattering loss ( $\alpha$ ). This results in a trade-off between how long the waveguide delay ( $L$ ) is designed and how much the delay loss ( $\alpha L$ ) becomes. Since the waveguide has much higher propagation losses than optical fibers and the silicon nitride waveguide loss we can achieve is about 0.2 dB/m, this limits the waveguide delay to 25 meter if the delay loss is kept below 5 dB.

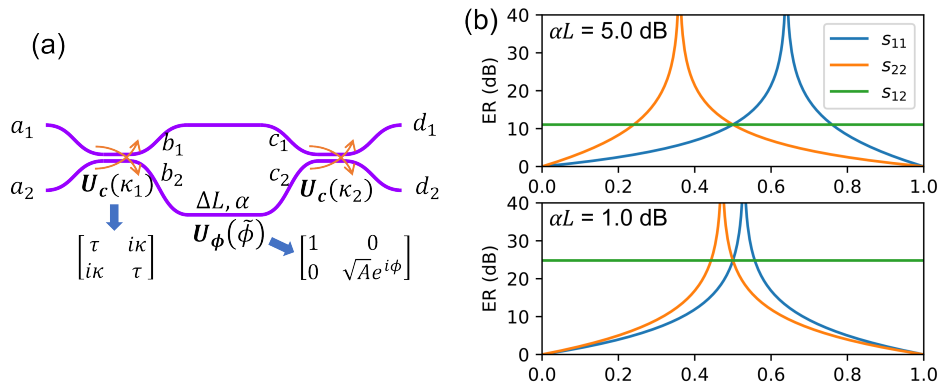


Figure 5.32: Waveguide MZI modeling and simulations

Figure 5.32(a) shows the modeling approach of the waveguide delay-line MZI interferometer, which consists of two directional couplers or splitters and a waveguide delay section and their transfer functions can be represented by matrices. To keep the modeling, design and testing simple, we limit our modeling and design to using identical directional couplers with one coupling coefficient  $\kappa^2$ . The S matrices of the coupler and

waveguide delay sections are expressed by,

$$\mathbf{U}_c(\kappa) = \begin{bmatrix} \tau & i\kappa \\ i\kappa & \tau \end{bmatrix}, \quad (5.21)$$

$$\mathbf{U}_\phi(\alpha, L) = \begin{bmatrix} 1 & 0 \\ 0 & \sqrt{A}e^{i\phi} \end{bmatrix} = \begin{bmatrix} 1 & 0 \\ 0 & e^{i2\pi n_{eff}L/\lambda - \alpha L/2} \end{bmatrix} = \begin{bmatrix} 1 & 0 \\ 0 & e^{i\bar{\phi}} \end{bmatrix} \quad (5.22)$$

Here,  $\bar{\phi} = 2\pi n_{eff}L/\lambda + i\alpha L/2$ . The transfer function of the waveguide MZI interferometer can be the matrix multiplication of each individual component matrix,

$$\mathbf{U}_{MZI} = \mathbf{U}_c \mathbf{U}_\phi \mathbf{U}_c = \begin{bmatrix} u_{11} & u_{12} \\ u_{21} & u_{22} \end{bmatrix} \quad (5.23)$$

$$= \begin{bmatrix} \tau & i\kappa \\ i\kappa & \tau \end{bmatrix} \begin{bmatrix} 1 & 0 \\ 0 & e^{i\bar{\phi}} \end{bmatrix} \begin{bmatrix} \tau & i\kappa \\ i\kappa & \tau \end{bmatrix} \quad (5.24)$$

$$= \begin{bmatrix} \tau^2 - \kappa^2 e^{i\bar{\phi}} & i\kappa\tau(1 + e^{i\bar{\phi}}) \\ i\kappa\tau(1 + e^{i\bar{\phi}}) & \tau^2 e^{i\bar{\phi}} - \kappa^2 \end{bmatrix}. \quad (5.25)$$

The transmission of the MZI outputs can be calculated taking norms of the MZI S-matrix element,  $S_{11} = |u_{11}|^2$ ,  $S_{22} = |u_{22}|^2$ , and  $S_{12} = S_{21} = |u_{12}|^2$ . Therefore, the extinction ratios (ER) of these transmission functions can be calculated,

$$ER(S_{11}) = \frac{\max S_{11}}{\min S_{11}} = \left( \frac{\tau^2 + \sqrt{A}\kappa^2}{\tau^2 - \sqrt{A}\kappa^2} \right)^2, \quad (5.26)$$

$$ER(S_{22}) = \frac{\max S_{22}}{\min S_{22}} = \left( \frac{\sqrt{A}\tau^2 + \kappa^2}{\sqrt{A}\tau^2 - \kappa^2} \right)^2, \quad (5.27)$$

$$ER(S_{12}) = ER(S_{21}) = \frac{\max S_{12}}{\min S_{12}} = \left( \frac{1 + \sqrt{A}}{1 - \sqrt{A}} \right)^2. \quad (5.28)$$

Eq. 5.26-5.28 shows the ERs' dependency on both the delay attenuation  $A$  and the direction coupling coefficient  $\kappa$ . Figure 5.32(b) plots the ERs versus the coupling coefficient while comparing two different scenarios with different delay attenuation. The 50:50 splitting ratio is preferred for the two directional couplers, as the two MZI outputs can have an equally high ER at  $\kappa^2 = 0.5$ . With  $\kappa^2 = 0.5$ , lower waveguide delay line loss yields higher ERs, and the ER is reduced from 25 dB to 11 dB when the waveguide delay-line loss increases from 1.0 dB to 5.0 dB.

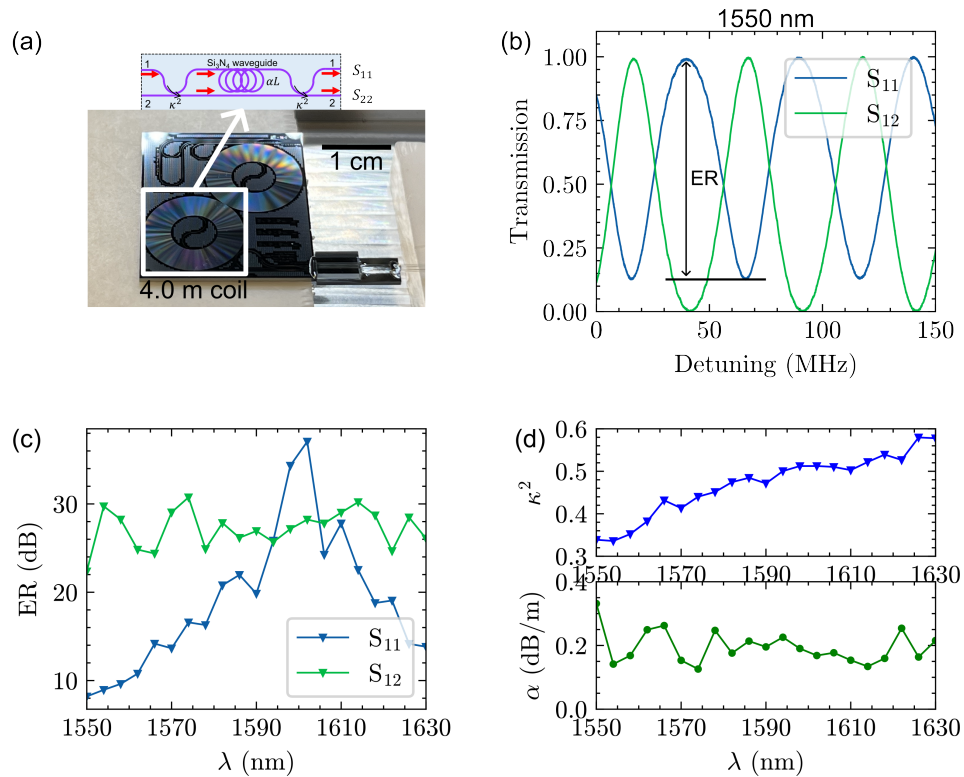


Figure 5.33: 4-meter-coil Waveguide MZI spectral sweep and ERs from 1550 nm to 1630 nm. (a) Device picture shows the fiber v-groove pig-tailing in a metal package enclosure. (b) Spectral scanning of  $S_{11}$  and  $S_{12}$  at 1550 nm measures the ERs and the FSR to be around 50 MHz. (c) Measured ERs from 1550 nm to 1630 nm. (d) Extracted  $\kappa^2$  and  $\alpha$  from the measured ERs.



## 5.6.2 Coil waveguide MZI device design and testing

### 4-meter-coil waveguide MZIs

The 4-meter-coil waveguide MZI uses the same design parameters for the 4-meter-long coil delay in the 4-meter-coil resonator described in Section 5.3.1, such as the center-to-center waveguide spacing of  $30\ \mu\text{m}$ . The two directional couplers for a 50/50 coupling ratio use the  $2.0\ \mu\text{m}$  gap and  $1.4\ \text{mm}$  coupling length, as the coupling estimation shows in Fig. 5.11(d).

Figure 5.33 shows the spectrum scanning results of the 4-meter-coil MZI at different wavelengths from  $1550\ \text{nm}$  to  $1630\ \text{nm}$ , and the ERs of S11 and S12 can be used to estimate the directional coupler coupling and the propagation loss of 4-meter waveguide delay line by using Eq. 5.26 to 5.28. Although the simulated coupling for  $1550\ \text{nm}$  is  $0.5$  for this directional coupler design, the measured value is about  $0.35$  at  $1550\ \text{nm}$  and increases towards longer wavelengths. The extracted waveguide loss is around  $0.2\ \text{dB/m}$ , which is consistent with the waveguide loss measurements in the 4-meter-coil resonators in Fig. 5.12.

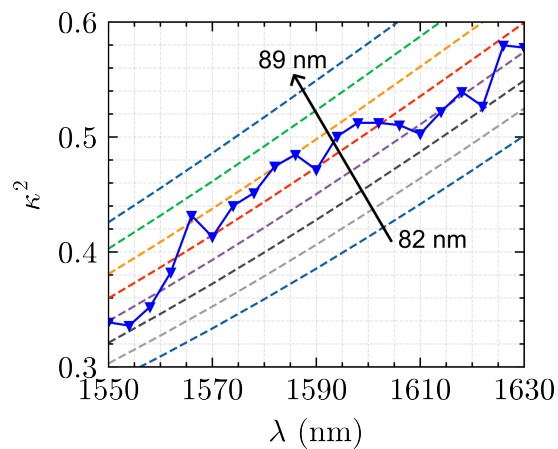


Figure 5.34: Comparison between the measured  $\kappa^2$  and the simulated values at different waveguide thicknesses.

The mismatch between the simulated  $0.50$  coupling and the measured  $0.35$  coupling is

very likely due to the waveguide thickness variations caused by the fabrication processes. By simulating the  $2.0\text{-}\mu\text{m}$ -gap and  $1.4\text{-mm}$ -long directional coupler versus wavelength while sweeping the waveguide thicknesses from  $82\text{ nm}$  to  $90\text{ nm}$ , we compare the simulated coupling curves with different waveguide thicknesses to the measured coupling curve in wavelength in Fig. 5.34, and infer that the actual waveguide thickness could be  $85\text{ nm}$ .

### 15-meter-coil waveguide MZIs

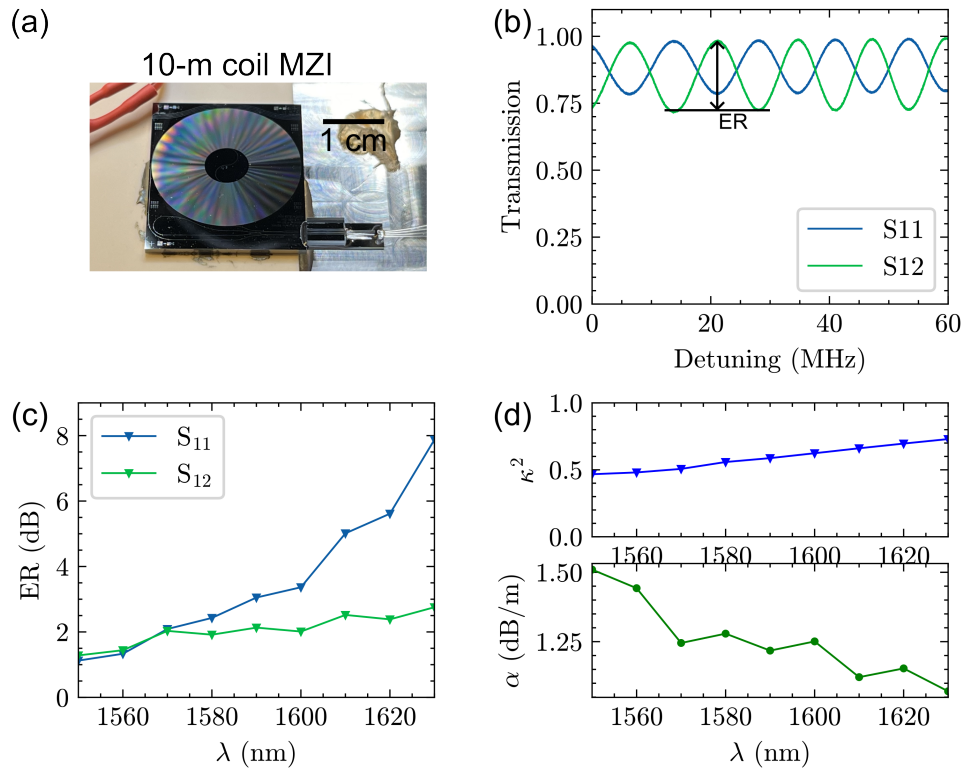


Figure 5.35: 15-meter-coil Waveguide MZI spectral sweep and ERs from  $1550\text{ nm}$  to  $1630\text{ nm}$ . (a) Device picture shows the fiber v-groove pig-tailing in a metal package enclosure. (b) Spectral scanning of  $S_{11}$  and  $S_{12}$  at  $1550\text{ nm}$  measures the ERs and the FSR to be around  $13.2\text{ MHz}$ . (c) Measured ERs from  $1550\text{ nm}$  to  $1630\text{ nm}$ . (d) Extracted  $\kappa^2$  and  $\alpha$  from the measured ERs.

The 15-meter-coil waveguide MZI uses the same directional coupler design parameters as the 4-meter-coil MZI. However, the spiral waveguide center-to-center spacing is

decreased from 30  $\mu\text{m}$  to 20  $\mu\text{m}$ . The ER measurements in Fig. 5.35 significant degradation compared to the 4-meter-coil MZI devices, and the extracted waveguide loss is much higher as a result, which might be due to the reduced waveguide spacing of 20  $\mu\text{m}$  or any fabrication-related issues.

If the 15-meter-coil waveguide delay-line loss were to be limited by the propagation loss measured in the 4-meter-coil MZI devices and 4-meter-coil resonator devices, which is about 0.2 dB/m, the 15-meter-coil waveguide delay-line would have a loss of only 3.0 dB and the ERs of both S11 and S12 would be 15 dB, and 15-dB ERs are sufficient for most of applications related to laser frequency noise measurements.

### 5.6.3 Waveguide MZIs for laser frequency noise measurements

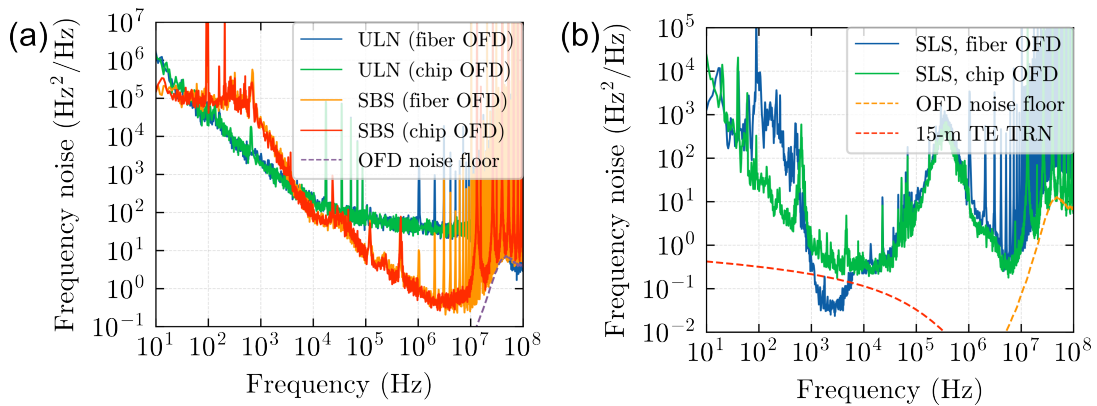


Figure 5.36: Waveguide MZI OFD (chip OFD) and fiber MZI OFD measurements of the ULN, SBS lasers and the SLS laser.

To demonstrate the performance of the waveguide MZI as an OFD to measure the laser frequency noise at both high frequency offsets and low frequency offsets, we use the fiber-pigtailed and packaged 15-meter-coil MZI to measure the frequency noise of different lasers and compare the measurements with a fiber MZI with a 200-meter-long delay-line. The lasers used here include the narrow fundamental linewidth lasers such as the Thorlabs ultra-low-noise (ULN) laser [51], the sub-hertz fundamental linewidth

SBS laser [53], and an ultra-stable laser that is frequency locked to an ultra-stable stable-laser-systems (SLS) Fabry–Pérot cavity and has very low frequency noise at low frequency offsets.

The frequency noise measurements of the ULN and SBS lasers by the 15-meter-coil MZI is referred to as the chip OFD, and agree well with the fiber OFD measurements and have a similar OFD measurement floor as the fiber OFD in Fig. 5.36(a) from the photodetector noise. To test the chip OFD’s measurement limitations at low frequency offsets, the ultra-stable SLS laser is measured by the chip OFD and fiber OFD, shown in Fig. 5.36(b), revealing the environmental noise in both the waveguide and fiber MZIs acting as the predominating measurement noise source at low frequency offsets below 1 kHz.

## 5.7 Summary and outlook

In this chapter, we comprehensively reveal the design details of the 4-meter, 10-meter, and 17-meter long waveguide resonators including the bus-resonator coupling, S-bend loss simulations, fiber-to-chip edge coupling, coil waveguide spacing, and etc. Experimentally, the fabricated coil resonators are tested to achieve above 100 million Qs. Using the coil resonators, the stabilized laser integral linewidth reaches as narrow as 30 Hz. These chip-scale high-Q and low-noise reference coil resonators are used in various demonstrations such as fiber sensing and low-noise microwave generation. Figure 5.37 shows a comparison between all other work [25, 77, 78] and our work [36, 59] in the literature using coil resonator approach for laser stabilization and noise reduction in terms of coil resonator lengths, Qs, stabilized laser integral linewidth, and Allan deviation.

The best performance of the coil resonator stabilized laser with isolation of acoustic noise and vibration noise from 10 Hz to 1 kHz reaches an integral linewidth of around


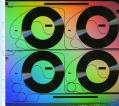
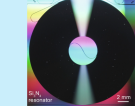



						
Reference	[25]	[77]	[78]	Our work [36]	Our work [66]	Our work
Coil length	1.2 m	1.4 m	14 m	4.0 m	10 m	17 m
$Q_L, Q_{in}$	140 M, 170 M	126 M, 164 M	166 M, 332 M	55 M, 80 M	184 M, 340 M	115 M, 249 M
$\Delta\nu_{1/\pi}$	76 Hz	NA	NA	36 Hz	NA	NA
$\sigma_y(\tau)$	$3.9 \times 10^{-13}$ at 0.4 ms	NA	NA	$1.8 \times 10^{-13}$ at 10 ms	NA	NA
$S_\phi$ at 10 kHz	-83 dBc/Hz	-80 dBc/Hz	-94 dBc/Hz	-90 dBc/Hz	-83 dBc/Hz	-88 dBc/Hz

Figure 5.37: A comparison between all other work and our work in literature using coil resonator approach for laser stabilization and noise reduction.

30 Hz. However, the stabilized laser frequency noise below 10 Hz is not limited by the coil resonator intrinsic TRN. The frequency noise below 10 Hz is likely due to the local temperature fluctuations near or on the coil resonator chip. Therefore, increasing the coil length and reducing the TRN might not help with the reduction of the integral linewidth, and more investigation and understanding is needed to reduce the frequency noise below 10 Hz in the coil resonator laser stabilization experiments, so that the stabilized laser integral linewidth can reach the limit of the TRN, which is around 1~4 Hz for the 10-meter-coil resonators.

The two-point-coupling technique enables the coil resonator to be properly coupled from 900 nm to 1600 nm. It is possible to further increase the bus-resonator coupling strength to increase the coupling wavelength range, so that such a wide-wavelength-range-accessible coil resonator reference can enable potential applications. For example, the low-noise microwave generation uses optical frequency division where the two point locking technique is used, and the two optical frequencies are stabilized to the same optical reference resonator, and the optical frequency division ratio is the ratios between the optical frequency difference between the two optical carriers and the microwave frequency

and can be increased by increasing the separation of the two optical frequencies, which is essentially limited by the working wavelength range of the optical reference resonator. In our recent demonstration [13], the two laser wavelengths are 1550 nm and 1600 nm. Employing a two-point-coupled coil resonator can significantly increase the laser carrier frequency separation, which can further reduce the generated microwave phase noise, assuming that the performance of other parts of the optical frequency division system remains the same.

## Bibliography

- [1] J. M. Hogan and M. A. Kasevich, *Atom-interferometric gravitational-wave detection using heterodyne laser links*, *Physical Review A* **94** (2016), no. 3 033632.
- [2] S. Kolkowitz, I. Pikovski, N. Langellier, M. D. Lukin, R. L. Walsworth, and J. Ye, *Gravitational wave detection with optical lattice atomic clocks*, *Physical Review D* **94** (2016), no. 12 124043.
- [3] B. P. Abbott, R. Abbott, T. D. Abbott, M. R. Abernathy, K. Ackley, C. Adams, P. Addesso, R. X. Adhikari, V. B. Adya, C. Affeldt, *et. al.*, *Exploring the sensitivity of next generation gravitational wave detectors*, *Classical and Quantum Gravity* **34** (2017), no. 4 044001.
- [4] B. P. Abbott, R. Abbott, T. Abbott, M. Abernathy, F. Acernese, K. Ackley, C. Adams, T. Adams, P. Addesso, R. X. Adhikari, *et. al.*, *Observation of gravitational waves from a binary black hole merger*, *Physical review letters* **116** (2016), no. 6 061102.
- [5] Y. Stadnik and V. Flambaum, *Searching for dark matter and variation of*

- fundamental constants with laser and maser interferometry*, *Physical review letters* **114** (2015), no. 16 161301.
- [6] A. Derevianko and M. Pospelov, *Hunting for topological dark matter with atomic clocks*, *Nature Physics* **10** (2014), no. 12 933–936.
- [7] A. D. Ludlow, M. M. Boyd, J. Ye, E. Peik, and P. O. Schmidt, *Optical atomic clocks*, *Reviews of Modern Physics* **87** (2015), no. 2 637.
- [8] E. Oelker, R. Hutson, C. Kennedy, L. Sonderhouse, T. Bothwell, A. Goban, D. Kedar, C. Sanner, J. Robinson, G. Marti, *et. al.*, *Demonstration of  $4.8 \times 10^{-17}$  stability at 1 s for two independent optical clocks*, *Nature Photonics* **13** (2019), no. 10 714–719.
- [9] W. McGrew, X. Zhang, R. Fasano, S. Schäffer, K. Beloy, D. Nicolodi, R. Brown, N. Hinkley, G. Milani, M. Schioppo, *et. al.*, *Atomic clock performance enabling geodesy below the centimetre level*, *Nature* **564** (2018), no. 7734 87–90.
- [10] T. M. Fortier, M. S. Kirchner, F. Quinlan, J. Taylor, J. Bergquist, T. Rosenband, N. Lemke, A. Ludlow, Y. Jiang, C. Oates, *et. al.*, *Generation of ultrastable microwaves via optical frequency division*, *Nature Photonics* **5** (2011), no. 7 425–429.
- [11] X. Xie, R. Bouchand, D. Nicolodi, M. Giunta, W. Hänsel, M. Lezius, A. Joshi, S. Datta, C. Alexandre, M. Lours, *et. al.*, *Photonic microwave signals with zeptosecond-level absolute timing noise*, *nature photonics* **11** (2017), no. 1 44–47.
- [12] I. Kudelin, W. Groman, Q.-X. Ji, J. Guo, M. L. Kelleher, D. Lee, T. Nakamura, C. A. McLemore, P. Shirmohammadi, S. Hanifi, *et. al.*, *Photonic chip-based low-noise microwave oscillator*, *Nature* (2024) 1–6.

- [13] S. Sun, B. Wang, K. Liu, M. W. Harrington, F. Tabatabaei, R. Liu, J. Wang, S. Hanifi, J. S. Morgan, M. Jahanbozorgi, *et. al.*, *Integrated optical frequency division for microwave and mmWave generation*, *Nature* (2024) 1–6.
- [14] P. Lu, N. Lalam, M. Badar, B. Liu, B. T. Chorpeneing, M. P. Buric, and P. R. Ohodnicki, *Distributed optical fiber sensing: Review and perspective*, *Applied Physics Reviews* **6** (2019), no. 4.
- [15] E. Ip, Y.-K. Huang, G. Wellbrock, T. Xia, M.-F. Huang, T. Wang, and Y. Aono, *Vibration detection and localization using modified digital coherent telecom transponders*, *Journal of Lightwave Technology* **40** (2022), no. 5 1472–1482.
- [16] G. Marra, C. Clivati, R. Lockett, A. Tampellini, J. Kronjäger, L. Wright, A. Mura, F. Levi, S. Robinson, A. Xuereb, *et. al.*, *Ultrastable laser interferometry for earthquake detection with terrestrial and submarine cables*, *Science* **361** (2018), no. 6401 486–490.
- [17] G. Lihachev, J. Riemensberger, W. Weng, J. Liu, H. Tian, A. Siddharth, V. Snigirev, V. Shadymov, A. Voloshin, R. N. Wang, *et. al.*, *Low-noise frequency-agile photonic integrated lasers for coherent ranging*, *Nature communications* **13** (2022), no. 1 3522.
- [18] J. Riemensberger, A. Lukashchuk, M. Karpov, W. Weng, E. Lucas, J. Liu, and T. J. Kippenberg, *Massively parallel coherent laser ranging using a soliton microcomb*, *Nature* **581** (2020), no. 7807 164–170.
- [19] T. Kessler, C. Hagemann, C. Grebing, T. Legero, U. Sterr, F. Riehle, M. Martin, L. Chen, and J. Ye, *A sub-40-mHz-linewidth laser based on a silicon single-crystal optical cavity*, *Nature Photonics* **6** (2012), no. 10 687–692.



- [20] D. Matei, T. Legero, S. Häfner, C. Grebing, R. Weyrich, W. Zhang, L. Sonderhouse, J. Robinson, J. Ye, F. Riehle, *et. al.*, *1.5  $\mu\text{m}$  lasers with sub-10 mHz linewidth*, *Physical review letters* **118** (2017), no. 26 263202.
- [21] F. L. Walls and A. E. Wainwright, *Measurement of the short-term stability of quartz crystal resonators and the implications for crystal oscillator design and applications*, *IEEE transactions on instrumentation and measurement* **24** (1975), no. 1 15–20.
- [22] J. Alnis, A. Schliesser, C. Y. Wang, J. Hofer, T. J. Kippenberg, and T. Hänsch, *Thermal-noise-limited crystalline whispering-gallery-mode resonator for laser stabilization*, *Physical Review A* **84** (2011), no. 1 011804.
- [23] J. Lim, A. A. Savchenkov, E. Dale, W. Liang, D. Eliyahu, V. Ilchenko, A. B. Matsko, L. Maleki, and C. W. Wong, *Chasing the thermodynamical noise limit in whispering-gallery-mode resonators for ultrastable laser frequency stabilization*, *Nature communications* **8** (2017), no. 1 8.
- [24] W. Zhang, L. Stern, D. Carlson, D. Bopp, Z. Newman, S. Kang, J. Kitching, and S. B. Papp, *Ultranarrow linewidth photonic-atomic laser*, *Laser & Photonics Reviews* **14** (2020), no. 4 1900293.
- [25] H. Lee, M.-G. Suh, T. Chen, J. Li, S. A. Diddams, and K. J. Vahala, *Spiral resonators for on-chip laser frequency stabilization*, *Nature communications* **4** (2013), no. 1 2468.
- [26] N. Jin, C. A. McLemore, D. Mason, J. P. Hendrie, Y. Luo, M. L. Kelleher, P. Kharel, F. Quinlan, S. A. Diddams, and P. T. Rakich, *Micro-fabricated mirrors with finesse exceeding one million*, *Optica* **9** (2022), no. 9 965–970.

- [27] C. A. McLemore, N. Jin, M. L. Kelleher, J. P. Hendrie, D. Mason, Y. Luo, D. Lee, P. Rakich, S. A. Diddams, and F. Quinlan, *Miniaturizing ultrastable electromagnetic oscillators: Sub- $10^{-14}$  frequency instability from a centimeter-scale Fabry-Perot cavity*, *Physical Review Applied* **18** (2022), no. 5 054054.
- [28] J. Guo, C. A. McLemore, C. Xiang, D. Lee, L. Wu, W. Jin, M. Kelleher, N. Jin, D. Mason, L. Chang, *et. al.*, *Chip-based laser with 1-hertz integrated linewidth*, *Science advances* **8** (2022), no. 43 eabp9006.
- [29] M. W. Puckett, K. Liu, N. Chauhan, Q. Zhao, N. Jin, H. Cheng, J. Wu, R. O. Behunin, P. T. Rakich, K. D. Nelson, *et. al.*, *422 Million intrinsic quality factor planar integrated all-waveguide resonator with sub-MHz linewidth*, *Nature communications* **12** (2021), no. 1 934.
- [30] C. Xiang, W. Jin, O. Terra, B. Dong, H. Wang, L. Wu, J. Guo, T. J. Morin, E. Hughes, J. Peters, *et. al.*, *3D integration enables ultralow-noise isolator-free lasers in silicon photonics*, *Nature* **620** (2023), no. 7972 78–85.
- [31] J. Liu, G. Huang, R. N. Wang, J. He, A. S. Raja, T. Liu, N. J. Engelsen, and T. J. Kippenberg, *High-yield, wafer-scale fabrication of ultralow-loss, dispersion-engineered silicon nitride photonic circuits*, *Nature communications* **12** (2021), no. 1 2236.
- [32] A. Shams-Ansari, G. Huang, L. He, Z. Li, J. Holzgrafe, M. Jankowski, M. Churaev, P. Kharel, R. Cheng, D. Zhu, *et. al.*, *Reduced material loss in thin-film lithium niobate waveguides*, *Apl Photonics* **7** (2022), no. 8.
- [33] M. Zhang, C. Wang, R. Cheng, A. Shams-Ansari, and M. Lončar, *Monolithic ultra-high-Q lithium niobate microring resonator*, *Optica* **4** (2017), no. 12 1536–1537.

- [34] G. Huang, E. Lucas, J. Liu, A. S. Raja, G. Lihachev, M. L. Gorodetsky, N. J. Engelsen, and T. J. Kippenberg, *Thermorefractive noise in silicon-nitride microresonators*, *Physical Review A* **99** (2019), no. 6 061801.
- [35] M. L. Gorodetsky and I. S. Grudinin, *Fundamental thermal fluctuations in microspheres*, *JOSA B* **21** (2004), no. 4 697–705.
- [36] K. Liu, N. Chauhan, J. Wang, A. Isichenko, G. M. Brodnik, P. A. Morton, R. O. Behunin, S. B. Papp, and D. J. Blumenthal, *36 Hz integral linewidth laser based on a photonic integrated 4.0 m coil resonator*, *Optica* **9** (2022), no. 7 770–775.
- [37] W. Jin, Q.-F. Yang, L. Chang, B. Shen, H. Wang, M. A. Leal, L. Wu, M. Gao, A. Feshali, M. Paniccia, *et. al.*, *Hertz-linewidth semiconductor lasers using CMOS-ready ultra-high-Q microresonators*, *Nature Photonics* **15** (2021), no. 5 346–353.
- [38] M. A. Lombardi, *Time and Frequency*, in *Encyclopedia of Physical Science and Technology (Third Edition)* (R. A. Meyers, ed.), pp. 783–801. Academic Press, New York, third edition ed., 2003.
- [39] T. Bothwell, D. Kedar, E. Oelker, J. M. Robinson, S. L. Bromley, W. L. Tew, J. Ye, and C. J. Kennedy, *JILA SrI optical lattice clock with uncertainty of  $2 \times 10^{-18}$* , *Metrologia* **56** (2019), no. 6 065004.
- [40] R. Le Targat, L. Lorini, Y. Le Coq, M. Zawada, J. Guéna, M. Abgrall, M. Gurov, P. Rosenbusch, D. Rovera, B. Nagórny, *et. al.*, *Experimental realization of an optical second with strontium lattice clocks*, *Nature communications* **4** (2013), no. 1 2109.

- [41] E. D. Black, *An introduction to Pound–Drever–Hall laser frequency stabilization*, *American journal of physics* **69** (2001), no. 1 79–87.
- [42] A. Otterpohl, F. Sedlmeir, U. Vogl, T. Dirmeier, G. Shafiee, G. Schunk, D. V. Strekalov, H. G. Schwefel, T. Gehring, U. L. Andersen, *et. al.*, *Squeezed vacuum states from a whispering gallery mode resonator*, *Optica* **6** (2019), no. 11 1375–1380.
- [43] X. Lu, G. Moille, A. Singh, Q. Li, D. A. Westly, A. Rao, S.-P. Yu, T. C. Briles, S. B. Papp, and K. Srinivasan, *Milliwatt-threshold visible–telecom optical parametric oscillation using silicon nanophotonics*, *Optica* **6** (2019), no. 12 1535–1541.
- [44] B. Li, Z. Yuan, W. Jin, L. Wu, J. Guo, Q.-X. Ji, A. Feshali, M. Paniccia, J. E. Bowers, and K. J. Vahala, *High-coherence hybrid-integrated 780 nm source by self-injection-locked second-harmonic generation in a high-Q silicon-nitride resonator*, *Optica* **10** (2023), no. 9 1241–1244.
- [45] L. G. Kazovsky, *Decision-driven phase-locked loop for optical homodyne receivers: Performance analysis and laser linewidth requirements*, *IEEE Transactions on Electron devices* **32** (1985), no. 12 2630–2639.
- [46] J. R. Barry and E. A. Lee, *Performance of coherent optical receivers*, *Proceedings of the IEEE* **78** (1990), no. 8 1369–1394.
- [47] E. Ip, A. P. T. Lau, D. J. Barros, and J. M. Kahn, *Coherent detection in optical fiber systems*, *Optics express* **16** (2008), no. 2 753–791.
- [48] J. G. Proakis and M. Salehi, *Fundamentals of communication systems*. Pearson Education India, 2007.

- [49] “GitHub - kaikai-liu/pyphotonicssims — github.com.”  
<https://github.com/kaikai-liu/pyphotonicssims>. [Accessed 25-12-2024].
- [50] K. Liu, N. Jin, H. Cheng, N. Chauhan, M. W. Puckett, K. D. Nelson, R. O. Behunin, P. T. Rakich, and D. J. Blumenthal, *Ultralow 0.034 dB/m loss wafer-scale integrated photonics realizing 720 million Q and 380  $\mu$ W threshold Brillouin lasing*, *Optics letters* **47** (2022), no. 7 1855–1858.
- [51] P. A. Morton and M. J. Morton, *High-power, ultra-low noise hybrid lasers for microwave photonics and optical sensing*, *Journal of Lightwave Technology* **36** (2018), no. 21 5048–5057.
- [52] L. Chrostowski and M. Hochberg, *Silicon photonics design: from devices to systems*. Cambridge University Press, 2015.
- [53] S. Gundavarapu, G. M. Brodnik, M. Puckett, T. Huffman, D. Bose, R. Behunin, J. Wu, T. Qiu, C. Pinho, N. Chauhan, *et. al.*, *Sub-hertz fundamental linewidth photonic integrated Brillouin laser*, *Nature Photonics* **13** (2019), no. 1 60–67.
- [54] “SIMS — eag.com.” <https://www.eag.com/techniques/mass-spec/secondary-ion-mass-spectrometry-sims/>. [Accessed 27-05-2024].
- [55] K. Liu, M. H. Idjadi, S. Grillanda, K. Kim, C. Bolle, M. Cappuzzo, R. Kopf, N. Fontaine, M. Mazur, R. Ryf, *et. al.*, *Common cavity waveguide coil-resonator stabilized hybrid integrated WDM laser with 89 Hz integral linewidth*, in *2024 Optical Fiber Communications Conference and Exhibition (OFC)*, pp. 1–3, IEEE, 2024.
- [56] “What is PyRPL? &x2014; pyrpl 0.9.4.0 documentation — pyrpl.readthedocs.io.”  
<https://pyrpl.readthedocs.io/en/latest/>. [Accessed 27-05-2024].

- [57] “Bode plot - Wikipedia — en.wikipedia.org.”  
[https://en.wikipedia.org/wiki/Bode\\_plot](https://en.wikipedia.org/wiki/Bode_plot). [Accessed 27-05-2024].
- [58] F. Vogelbacher, S. Nevlacsil, M. Sagmeister, J. Kraft, K. Unterrainer, and R. Hainberger, *Analysis of silicon nitride partial Euler waveguide bends*, *Optics express* **27** (2019), no. 22 31394–31406.
- [59] K. Liu, N. Chauhan, M. Song, M. W. Harrington, K. D. Nelson, and D. J. Blumenthal, *Tunable broadband two-point-coupled ultra-high-Q visible and near-infrared photonic integrated resonators*, *Photonics Research* **12** (2024), no. 9 1890–1898.
- [60] R. O. Behunin, N. T. Otterstrom, P. T. Rakich, S. Gundavarapu, and D. J. Blumenthal, *Fundamental noise dynamics in cascaded-order Brillouin lasers*, *Physical Review A* **98** (2018), no. 2 023832.
- [61] H. Lee, T. Chen, J. Li, K. Y. Yang, S. Jeon, O. Painter, and K. J. Vahala, *Chemically etched ultrahigh-Q wedge-resonator on a silicon chip*, *Nature Photonics* **6** (2012), no. 6 369–373.
- [62] Z. Yuan, H. Wang, L. Wu, M. Gao, and K. Vahala, *Linewidth enhancement factor in a microcavity Brillouin laser*, *Optica* **7** (2020), no. 9 1150–1153.
- [63] C. López-Mercado, V. Spirin, J. B. Escobedo, A. M. Lucero, P. Mégret, I. Zolotovskii, and A. Fotiadi, *Locking of the DFB laser through fiber optic resonator on different coupling regimes*, *Optics Communications* **359** (2016) 195–199.
- [64] R. R. Galiev, N. M. Kondratiev, V. E. Lobanov, A. B. Matsko, and I. A. Bilenko, *Optimization of laser stabilization via self-injection locking to a*

- whispering-gallery-mode microresonator*, *Physical Review Applied* **14** (2020), no. 1 014036.
- [65] X. Han, L. Wang, P. Zou, Y. Wang, S. Zhang, Y. Gu, J. Wang, X. Jian, and M. Zhao, *A tunable optical waveguide ring resonator for microwave photonic filtering*, in *2013 IEEE International Topical Meeting on Microwave Photonics (MWP)*, pp. 88–91, IEEE, 2013.
- [66] H. Shoman, H. Jayatilleka, N. A. Jaeger, S. Shekhar, and L. Chrostowski, *Measuring on-chip waveguide losses using a single, two-point coupled microring resonator*, *Optics Express* **28** (2020), no. 7 10225–10238.
- [67] X. Shi, J. Zhang, X. Zeng, X. Lü, K. Liu, J. Xi, Y. Ye, and Z. Lu, *Suppression of residual amplitude modulation effects in Pound–Drever–Hall locking*, *Applied Physics B* **124** (2018) 1–7.
- [68] H. Shen, L. Li, J. Bi, J. Wang, and L. Chen, *Systematic and quantitative analysis of residual amplitude modulation in Pound-Drever-Hall frequency stabilization*, *Physical Review A* **92** (2015), no. 6 063809.
- [69] C. Wieman and S. Gilbert, *Laser-frequency stabilization using mode interference from a reflecting reference interferometer*, *Optics letters* **7** (1982), no. 10 480–482.
- [70] K. Liu, M. W. Harrington, J. Wang, K. D. Nelson, and D. J. Blumenthal, *Integrated self-delayed 2-m coil-resonator for high sensitivity optical frequency discrimination and laser linewidth narrowing*, in *Frontiers in Optics*, pp. JW4A–22, Optica Publishing Group, 2023.
- [71] P. Horak and W. H. Loh, *On the delayed self-heterodyne interferometric technique*

- for determining the linewidth of fiber lasers, Optics express* **14** (2006), no. 9 3923–3928.
- [72] J. Dong, Y. Hu, J. Huang, M. Ye, Q. Qu, T. Li, and L. Liu, *Subhertz linewidth laser by locking to a fiber delay line, Applied optics* **54** (2015), no. 5 1152–1156.
- [73] F. Kéfélian, H. Jiang, P. Lemonde, and G. Santarelli, *Ultralow-frequency-noise stabilization of a laser by locking to an optical fiber-delay line, Optics letters* **34** (2009), no. 7 914–916.
- [74] R. E. Bartolo, A. B. Tveten, and A. Dandridge, *Thermal phase noise measurements in optical fiber interferometers, IEEE Journal of Quantum Electronics* **48** (2012), no. 5 720–727.
- [75] L. Duan, *General treatment of the thermal noises in optical fibers, Physical Review A* **86** (2012), no. 2 023817.
- [76] J. Dong, J. Huang, T. Li, and L. Liu, *Observation of fundamental thermal noise in optical fibers down to infrasonic frequencies, Applied Physics Letters* **108** (2016), no. 2.
- [77] B. Li, W. Jin, L. Wu, L. Chang, H. Wang, B. Shen, Z. Yuan, A. Feshali, M. Paniccia, K. J. Vahala, *et. al.*, *Reaching fiber-laser coherence in integrated photonics, Optics Letters* **46** (2021), no. 20 5201–5204.
- [78] Y. He, L. Cheng, H. Wang, Y. Zhang, R. Meade, K. Vahala, M. Zhang, and J. Li, *Chip-scale high-performance photonic microwave oscillator, Science Advances* **10** (2024), no. 33 eado9570.



# Chapter 6

## Photonic integrated stabilized SBS lasers

In Chapter 4, we have discussed the design and performances of photonic integrated Brillouin scattering lasers based on ultra-low-loss silicon nitride waveguides that achieve up to 10 mW output optical power and below 0.1 Hz fundamental linewidth using the photonic molecule nested ring resonator configuration and higher-order Stokes suppression approach [1]. The frequency noise performances at low frequency offsets and the total integral linewidth in the Brillouin lasers still need to be reduced and suppressed by laser stabilization and frequency locking to a low-noise optical reference resonator, which is the main focus of Chapter 5, where the large-mode-volume and long-coil-waveguide resonators with a consequently low intrinsic thermo-refractive noise limit and above 100 million Qs can achieve a stabilized laser integral linewidth of 36 Hz or below [2]. In this chapter, we will describe our efforts to combine both aspects onto the same chip design, as illustrated in Fig. 6.1. In this work, we demonstrate a photonic integrated stabilized laser realized with a stimulated Brillouin scattering (SBS) laser, optical filter, 4-meter coil resonator on a single chip. The SBS laser output is filtered by an add-drop resonator

filter with a 9 mW output optical power and 4 Hz fundamental linewidth. Part of the SBS laser output is tapped to probe the 4-meter-coil resonator to be frequency locked to the coil reference resonator, which reduces the output integral linewidth from 1.6 kHz to 72 Hz, reaching an Allan deviation of  $2.8 \times 10^{-13}$  at 5 ms. Figure 6.1(a) shows a picture of the fabricated device and its layout is illustrated in Fig. 6.1(b). The frequency noise and linewidth reduction at high and low frequencies are achieved separately by the SBS laser and the coil resonator, respectively, illustrated in Fig. 6.1(c).

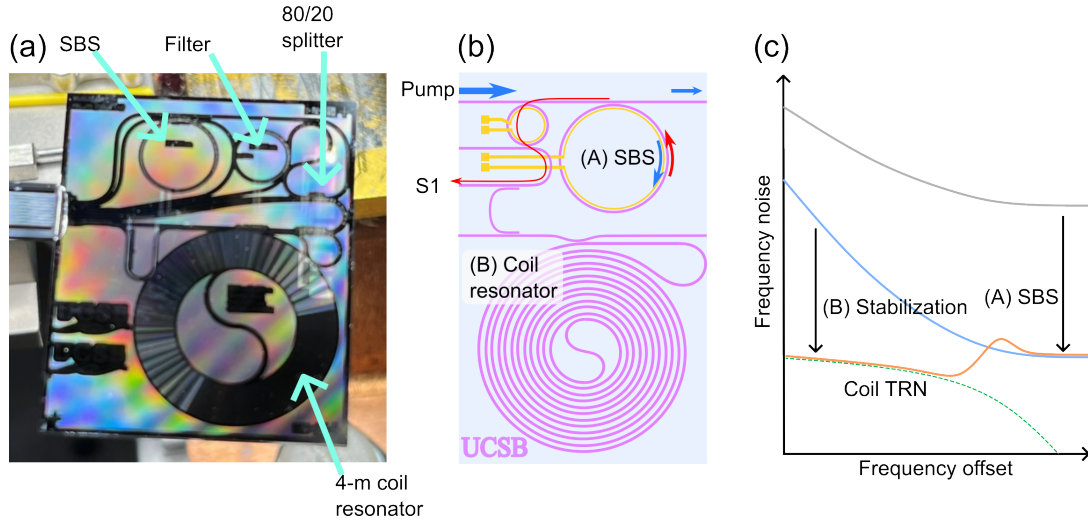


Figure 6.1: Stabilized Brillouin laser chip design and noise reduction principles.

## Isolator-free and circulator-free and SBS lasers

The silicon nitride waveguide design is  $6 \mu\text{m}$  by  $80 \text{ nm}$ , the same as that used in the coil resonators in the previous chapter, which has a good balance between waveguide propagation loss and bending radius. The SBS ring resonator has a radius of  $2.770 \text{ mm}$  and a bus-ring coupling gap of  $2.0 \mu\text{m}$  so that it is slightly over-coupled at  $1550 \text{ nm}$  for better pump-Stokes power conversion efficiency, while the filter ring resonator has a radius of  $2.0 \text{ mm}$  and a bus-ring coupling gap of  $0.5 \mu\text{m}$  so that the add-drop filter

ring resonator is heavily over-coupled and a very minimal add-drop insertion loss. Both of the filter and SBS ring resonators have a micro-heater on top of them to tune the optical resonances thermally. The SBS resonator is measured with a loaded 16.2 million and intrinsic 39.0 million Q at 1550 nm with a total linewidth of 12.0 MHz, while the add-drop filter ring resonator has a total linewidth of 0.7 GHz, as shown in Fig. 6.2. In Fig. 6.3(a), the waveguide loss measured from the SBS ring resonator is 0.7~1.0 dB/m from 1550 to 1630 nm, much higher than previously measured from the coil resonators for the 6  $\mu\text{m}$  by 80 nm silicon nitride waveguide in the previous chapter, which is about 0.2 dB/m.

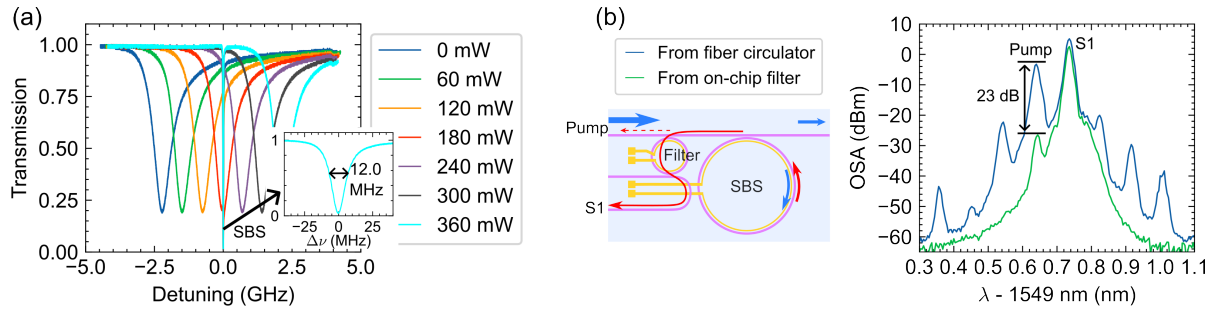


Figure 6.2: SBS laser with a filter ring resonator to drop the S1 power and filter out the unwanted back-reflected pump with a 23 dB reduction.

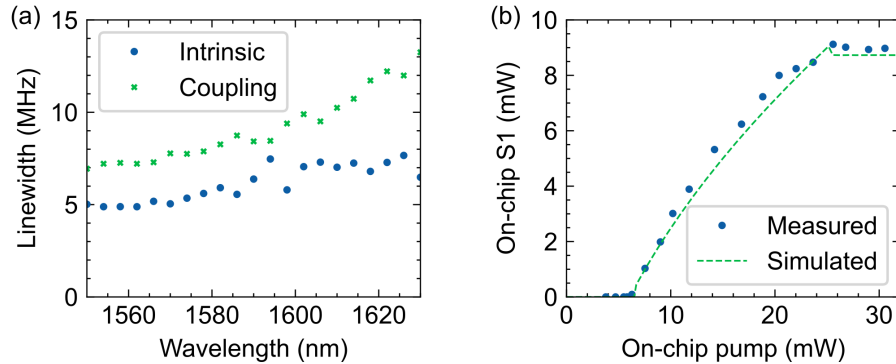


Figure 6.3: (a) SBS resonator intrinsic and coupling linewidths. (b) S1 on-chip output power from the filter output increases with the on-chip pump power with a threshold of 6 mW.

The filter ring resonator can be thermally tuned to align with the SBS resonance so

that the S1 output is dropped by the filter ring resonance to remove the need for a fiber optical circulator and suppress the unwanted back-reflected pump power with a pump reduction of 23 dB, as shown in Fig. 6.2(b). The SBS threshold is measured to be 6 mW, as shown in Fig. 6.3(b).

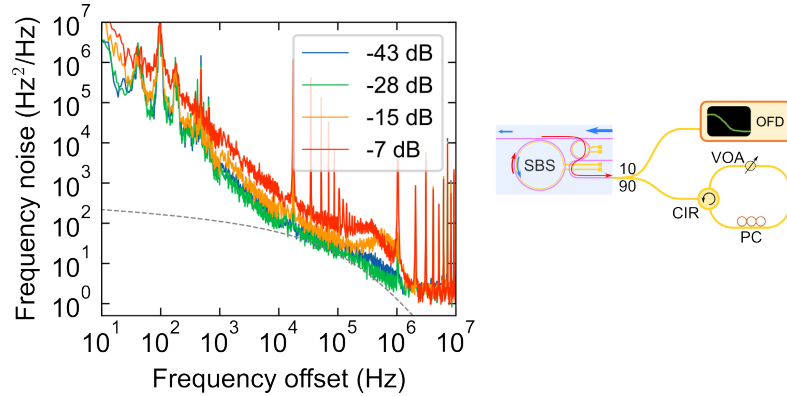


Figure 6.4: The frequency noise of the SBS laser output is being measured by the OFD frequency noise measurement while the feedback power increases.

To test the SBS laser's resilience against any external feedback, we designed an experiment where part of the SBS laser output circulates back into the SBS laser while the frequency noise is being measured by the OFD frequency noise measurement, shown in Fig. 6.4. The feedback ratio is defined as the ratio between the feedback optical power and the total SBS laser output power. As the feedback ratio increases from -43 dB to -7 dB, the fundamental linewidth remains constant at 4 Hz and the frequency noise below 1 MHz slightly increases. Therefore, the SBS laser is robust against any external feedback with up to -7 dB feedback strength.

## Stabilized SBS lasers

Laser stabilization using the reference coil resonators with high Qs and low intrinsic thermo-refractive noise can reduce the frequency noise at low frequencies and the laser integral linewidth, as discussed extensively in the previous chapter. Typically, in the laser

stabilization using the traditional PDH locking technique, the sideband modulation on the laser carrier is required for the error signal generation, which is typically implemented with an EOM. To remove the need of an EOM, we employ the design technique, the self-delayed coil resonator, where the reference coil resonator is nested with a Mach-Zehnder interferometer and the balanced detection of the MZI-nested coil resonator generates the PDH error signal for laser feedback locking. This technique is discussed in detail in Section 5.5 of Chapter 5 and [3].

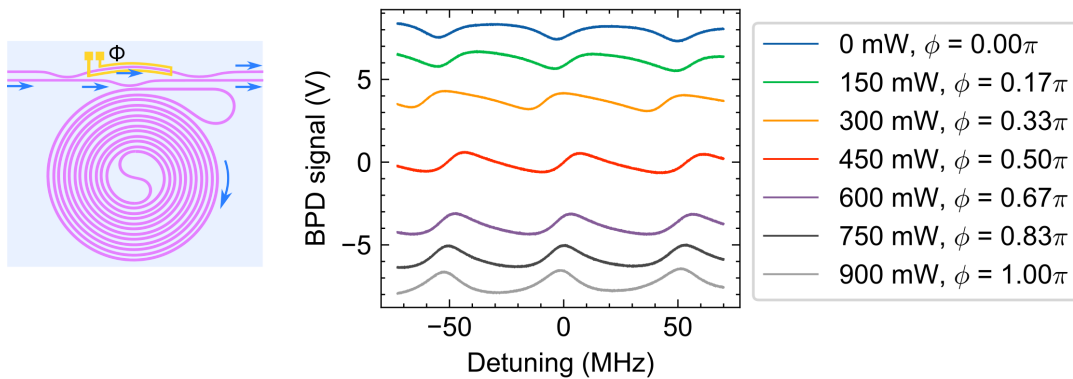


Figure 6.5: Self-delayed 4-meter-coil resonator and the balanced detection of the outputs shows the PDH error signal while the metal heater changes the MZI phase section.

The 4-meter-coil resonator is nested with an unbalanced MZI which consists of two 50/50 splitters (directional coupler of  $2.0 \mu\text{m}$  gap and 1.4 mm length) and a 6.28 mm unbalanced delay section. The directional coupler on one arm of the MZI for the coil resonator has a gap of  $2.0 \mu\text{m}$  and 0.8 mm length, with the intention to achieve critical coupling for the coil resonator. There is a metal heater on the MZI's delay waveguide section to tune the phase of the MZI, as  $\pi/2$  is needed for the PDH error sign from the balanced detection. At  $\phi = 0\pi$ , the balanced detection is simply the typical spectral transmission of the coil resonator, which measures a loaded 16 million and intrinsic 19 million Q near 1550 nm. With the heater power of 450 mW and  $\phi = \pi/2$ , the error signal is used for PDH lock, shown in Fig. 6.5. A widely tunable external cavity diode laser

(Velocity TLB-6730) is used for the spectral scanning of the self-delay coil resonator.

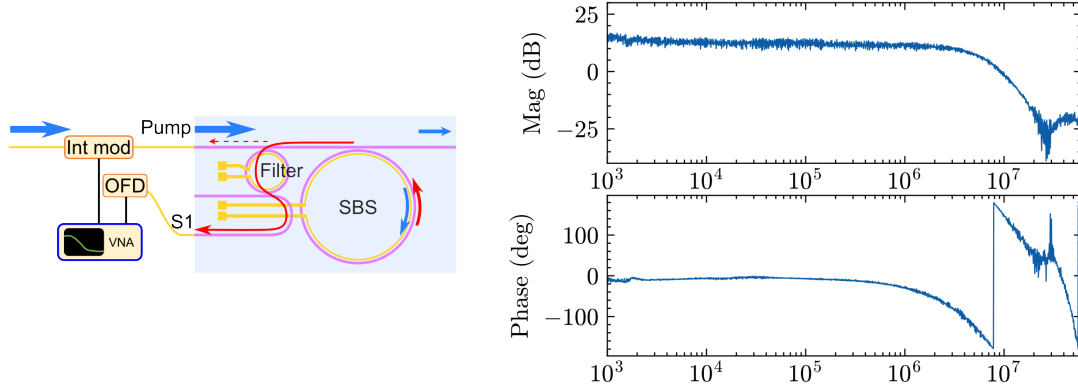


Figure 6.6: VNA S12 frequency response measurement of the SBS intensity modulation.

In typical laser stabilization experiments, an AOM is employed to shift and control the laser carrier optical frequency with the PDH error signal as feedback. Here, in our SBS laser, we modulate the pump laser power using an intensity modulator to shift and control the optical frequency of the SBS laser output for PDH lock and laser stabilization, as illustrated in Fig. 6.6. To test the bandwidth and how fast this modulation mechanism is, we use a vector network analyzer (VNA) that sends the input to the intensity modulator and receives the frequency shift induced by the pump power modulation that is detected using a 50-MHz-FSR fiber MZI as an optical frequency discriminator. Figure 6.6 shows that the 180- $^{\circ}$ C-phase-lag frequency is as high as 7 MHz, which would set the limit of the PDH locking bandwidth.

Figure 6.7 shows the SBS laser frequency noise before and after laser stabilization where the SBS laser feedback is achieved by intensity-modulating the pump laser power and the PDH error signal is generated from the balanced detection of the self-delayed coil resonator outputs. The intensity-modulated optical frequency feedback and stabilization have a bandwidth of 1 MHz. The stabilized SBS laser measures an integral linewidth of 72 Hz, and the Allan deviation from the beatnote between the stabilized SBS laser and

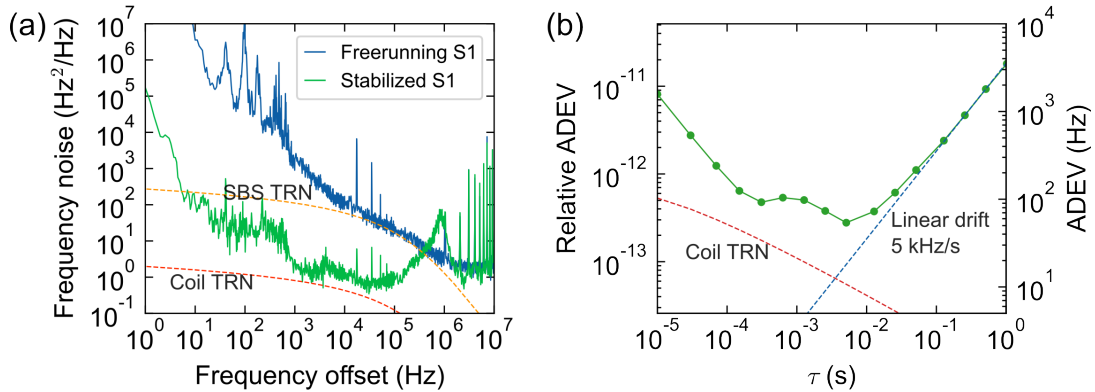


Figure 6.7: The frequency noise of the coil resonator stabilized SBS laser is measured using a fiber MZI OFD for frequency offsets above 1 kHz and against the stable reference laser below 1 kHz by measuring the frequency noise of the beatnote between the two lasers. (a) The stabilized frequency noise reaches to the coil resonator TRN from 1 kHz to 100 kHz with a locking bandwidth of 1 MHz and yields an integral linewidth of 72 Hz. (b) The Allan deviation of the beatnote between the stabilized laser and stable reference laser reaches  $2.8 \times 10^{-13}$  at 5 ms.

ultra-stable reference laser reaches  $2.8 \times 10^{-13}$  at 5 ms.

## Summary and outlook

We demonstrated a photonic integrated stabilized laser realized with a narrow fundamental linewidth SBS laser that uses an on-chip add-drop filter to drop the S1 laser output and filter out the unwanted pump, and a 4-meter coil resonator for laser stabilization on a single chip. The SBS laser output is filtered by an add-drop resonator filter with a 9 mW output optical power and 4 Hz fundamental linewidth. The SBS laser is robust against external feedback with up to -7 dB feedback strength. The coil reference resonator is nested with an MZI for PDH error signal generation without any laser carrier sideband modulation. The SBS laser frequency feedback and locking is achieved by intensity modulation of the pump power with a locking bandwidth of 1 MHz. The laser stabilization reduces the integral linewidth of the SBS laser from 1.6 to 72 Hz, reaching an Allan deviation of  $2.8 \times 10^{-13}$  at 5 ms.

This demonstration shows what is possible with the ultra-low-loss silicon nitride photonic platform for making fully integrated ultra-low-noise and narrow fundamental and narrow integral linewidth lasers. This is the first demonstration to date of the idea of combining a narrow fundamental linewidth laser and a low-noise reference resonator on the same chip, to the best of our knowledge. There are a few improvements for this work in the future. First, the waveguide loss is unusually high, likely due to fabrication, and can be reduced a lot to boost the performance, such as the SBS laser output power and fundamental linewidth and better coil resonator locking loops. Second, the micro-actuators are thermal heaters, which can induce thermal instabilities to the stabilized laser and also has a limited actuation bandwidth. PZT stress-optic actuators that can be deposited and fabricated on top of the optical chip using fully planary processes [4] have nano-watt level power consumption and MHz-level actuation bandwidth, which can significantly increase the robustness and performance of the stabilized laser chip. Lastly, the narrow fundamental linewidth laser can also be replaced by a hybrid integrated external cavity laser, which does not require an external pump laser as does the SBS laser and can achieve a Hertz-level fundamental linewidth [5]. Recently, we also demonstrated the marriage of the coil resonator discussed in this chapter and a hybrid integrated external cavity laser with high-Q silicon nitride waveguide ring resonators providing strong fundamental linewidth narrowing feedback to the active material gain block that is edge coupled to the silicon nitride chip [6], where the external cavity laser and the coil resonator devices are developed separately and are on two different chips. Putting the two together on the same chip will further advance the state of the art for the fully integrated stabilized low-noise narrow-linewidth semiconductor laser.



## Bibliography

- [1] K. Liu, J. H. Dallyn, G. M. Brodnik, A. Isichenko, M. W. Harrington, N. Chauhan, D. Bose, P. A. Morton, S. B. Papp, R. O. Behunin, *et. al.*, *Photonic circuits for laser stabilization with integrated ultra-high Q and Brillouin laser resonators*, *APL Photonics* **7** (2022), no. 9.
- [2] K. Liu, N. Chauhan, J. Wang, A. Isichenko, G. M. Brodnik, P. A. Morton, R. O. Behunin, S. B. Papp, and D. J. Blumenthal, *36 Hz integral linewidth laser based on a photonic integrated 4.0 m coil resonator*, *Optica* **9** (2022), no. 7 770–775.
- [3] K. Liu, M. W. Harrington, J. Wang, K. D. Nelson, and D. J. Blumenthal, *Integrated self-delayed 2-m coil-resonator for high sensitivity optical frequency discrimination and laser linewidth narrowing*, in *Frontiers in Optics*, pp. JW4A–22, Optica Publishing Group, 2023.
- [4] J. Wang, K. Liu, M. W. Harrington, R. Q. Rudy, and D. J. Blumenthal, *Silicon nitride stress-optic microresonator modulator for optical control applications*, *Optics Express* **30** (2022), no. 18 31816–31827.
- [5] Y. Fan, A. van Rees, P. J. Van der Slot, J. Mak, R. M. Oldenbeuving, M. Hoekman, D. Geskus, C. G. Roeloffzen, and K.-J. Boller, *Hybrid integrated InP-Si<sub>3</sub>N<sub>4</sub> diode laser with a 40-Hz intrinsic linewidth*, *Optics express* **28** (2020), no. 15 21713–21728.
- [6] D. A. Heim, D. Bose, K. Liu, A. Isichenko, and D. J. Blumenthal, *Photonic Integrated External Cavity Coil-Resonator Stabilized Laser with Hertz-Level-Fundamental and Sub-250-Hertz Integral Linewidth*, in *2024 Conference on Lasers and Electro-Optics (CLEO)*, pp. 1–2, IEEE, 2024.

# Chapter 7

## Future work

### Extending coil resonators into visible wavelengths

Although most of the work in this dissertation is focused on wavelengths near 1550 nm, they can also be implemented at many other wavelengths that are of interest to different applications, taking advantage of the wide spectral transparency window from 400 nm to 2500 nm of silicon nitride materials and its ultra-low-loss property, as it has been reported that the silicon nitride waveguide losses at visible wavelengths such as 674 nm, 698 nm and 780 nm are below 1 dB/m [1]. At visible wavelengths, stabilized lasers using laser stabilization with photonic integrated coil waveguide resonators with high resonator  $Q$ s, large optical mode volume, and low resonator-intrinsic thermo-refractive noise can benefit many optical-atomic clock applications such as Sr-ion clock that uses a stabilized 674 nm laser [2].

Visible SBS lasers based on ultra-low-loss silicon nitride waveguide resonators have been demonstrated to achieve fundamental linewidths of a few Hz [3]. Extending the waveguide ring resonator to a coil waveguide resonator as the SBS resonator can greatly enhance the output power and reduce the fundamental linewidth of the SBS lasers at

visible wavelengths.

## Multi-wavelength laser stabilization using coil resonators

Multi-wavelength laser stabilization using coil resonators is of interest for the application of low-noise microwave and mmWave generation, where two lasers of different wavelengths are required to stabilize to a single reference resonator and the stabilized optical frequencies are divided down to microwave frequencies using optical frequency division [4, 5, 6]. In our previous work, the two laser wavelengths are 1550 nm and 1600 nm, which is primarily limited by the working wavelength range of the coil waveguide resonator from 1550 nm to 1600 nm. Extending the working wavelength range of the coil resonator using the two-point coupling technique [7] can potentially increase the optical frequency separation of the coil resonator stabilized laser, increasing the optical frequency division ratio and further reducing the phase noise of the generated microwave. It has been demonstrated that two stabilized lasers at the O-band and C-band wavelengths, respectively, are used in an optical frequency division system for low-noise microwave generation [8]. Although the resonator-intrinsic thermo-refractive noise poses a performance limit in each individual laser stabilization, it is reported recently that the differential phase noise of two lasers stabilized to the same reference resonator is measured to be below the phase noise of each individual laser, indicating the multi-wavelength laser stabilization enters into the regime of common-mode noise cancelation [9]. Multi-wavelength stabilization is also of interest for fiber sensing applications using multiple lasers to enhance the detection capabilities and sensitivity [10, 11, 12].

Multi-wavelength stabilization using a single optical reference resonator can also be used for ultra-sensitive optical thermometry and long-term optical frequency drift correction. This has been implemented using dual optical modes in an optical reference

resonator [13, 14, 15]. A dual wavelength approach has also been demonstrated using an NIR-wavelength laser and a visible-wavelength laser stabilized to the optical reference resonator and detecting the resonator temperature drift by measuring the optical frequency difference between the visible laser frequency and the frequency-doubled NIR laser frequency [16, 17, 18]. The two-point-coupling technique for waveguide-based optical reference resonators enables resonator coupling for a wide wavelength range [7], and opens the door for the approach of dual wavelength optical thermometry to be implemented in integrated waveguide resonator devices.

## **Optical-to-microwave link using Brillouin lasers**

Frequency stability transfer from optical frequency to microwave frequency or vice versa is mainly implemented using an optical frequency comb to build a direct radio frequency–optical frequency link [19, 4, 5]. In such systems using optical frequency combs, self-referencing of an octave-spanning frequency comb is required, which significantly increases the system complexity. Microwave synthesis using Brillouin scattering lasers has been demonstrated [20, 21]. A microwave frequency to optical frequency using stimulated Brillouin scattering lasers has never been reported in the literature and is possible by frequency-locking the Brillouin lasing resonator to an ultra-stable laser as a pump laser, instead of frequency-locking the pump laser to the Brillouin resonator.

## **Photonic integration with actives and modulators**

Photonic integration of the ultra-low-loss silicon nitride waveguide platform with other active and modulator devices can enable a fully system-on-chip high-performance devices for high-impact and portable applications such as fiber sensing, optical-atomic clocks, LiDAR systems, and fugitive gas detection applications. Hybrid integrated ex-

ternal cavity lasers based on low-loss silicon nitride waveguide resonators as the laser external cavity and a gain-chip section edge-coupled to the silicon nitride chip have been demonstrated to achieve hertz-level fundamental linewidths [22, 23]. Laser stabilization of silicon nitride external cavity lasers using the silicon nitride coil waveguide resonators has first been demonstrated with a hertz-level fundamental linewidth and a 50 Hz integral linewidth [22]. However, the photodetectors, EOM modulators and feedback PID circuitry for the laser stabilization are off the chip. Integration of photodetectors with the silicon nitride waveguide devices has been demonstrated in the past [24]. Integration of PZT modulators with the silicon nitride waveguide devices has been demonstrated to achieve nano-watt level modulator power consumption and MHz-level modulation bandwidth [25]. A fully integrated system-on-chip stabilized laser enabled by the ultra-low-loss silicon nitride waveguide platform and the integration with the active gain chips and photodetectors and modulators can be realized in the near future.

## Bibliography

- [1] L. Chang, W. Xie, H. Shu, Q.-F. Yang, B. Shen, A. Boes, J. D. Peters, W. Jin, C. Xiang, S. Liu, *et. al.*, *Ultra-efficient frequency comb generation in AlGaAs-on-insulator microresonators*, *Nature communications* **11** (2020), no. 1 1331.
- [2] N. Chauhan, C. Caron, J. Wang, A. Isichenko, N. Helaly, K. Liu, R. J. Niffenegger, and D. J. Blumenthal, *Trapped ion qubit and clock operations with a visible wavelength photonic coil resonator stabilized integrated Brillouin laser*, *arXiv preprint arXiv:2402.16742* (2024).
- [3] N. Chauhan, A. Isichenko, K. Liu, J. Wang, Q. Zhao, R. O. Behunin, P. T. Rakich,

- A. M. Jayich, C. Fertig, C. Hoyt, *et. al.*, *Visible light photonic integrated Brillouin laser*, *Nature communications* **12** (2021), no. 1 4685.
- [4] A. Hati, C. W. Nelson, C. Barnes, D. Lirette, T. Fortier, F. Quinlan, J. A. DeSalvo, A. Ludlow, S. A. Diddams, and D. A. Howe, *State-of-the-art RF signal generation from optical frequency division*, *IEEE Transactions on Ultrasonics, Ferroelectrics, and Frequency Control* **60** (2013), no. 9 1796–1803.
- [5] T. M. Fortier, M. S. Kirchner, F. Quinlan, J. Taylor, J. Bergquist, T. Rosenband, N. Lemke, A. Ludlow, Y. Jiang, C. Oates, *et. al.*, *Generation of ultrastable microwaves via optical frequency division*, *Nature Photonics* **5** (2011), no. 7 425–429.
- [6] T. Tetsumoto, T. Nagatsuma, M. E. Fermann, G. Navickaite, M. Geiselmann, and A. Rolland, *Optically referenced 300 GHz millimetre-wave oscillator*, *Nature Photonics* **15** (2021), no. 7 516–522.
- [7] K. Liu, N. Chauhan, M. Song, M. W. Harrington, K. D. Nelson, and D. J. Blumenthal, *Tunable broadband two-point-coupled ultra-high-Q visible and near-infrared photonic integrated resonators*, *Photonics Research* **12** (2024), no. 9 1890–1898.
- [8] W. Loh, D. Gray, R. Irion, O. May, C. Belanger, J. Plant, P. W. Juodawlkis, and S. Yegnanarayanan, *Ultralow noise microwave synthesis via difference frequency division of a Brillouin resonator*, *Optica* **11** (2024), no. 4 492–497.
- [9] X. Jin, Z. Xie, X. Zhang, H. Hou, F. Zhang, X. Zhang, L. Chang, Q. Gong, and Q.-F. Yang, *Microresonator-referenced soliton microcombs with zeptosecond-level timing noise*, *arXiv preprint arXiv:2401.12760* (2024).

- [10] E. Ip, J. Fang, Y. Li, Q. Wang, M.-F. Huang, M. Salemi, and Y.-K. Huang, *Distributed fiber sensor network using telecom cables as sensing media: technology advancements and applications*, *Journal of Optical Communications and Networking* **14** (2022), no. 1 A61–A68.
- [11] E. Ip, Y.-K. Huang, G. Wellbrock, T. Xia, M.-F. Huang, T. Wang, and Y. Aono, *Vibration detection and localization using modified digital coherent telecom transponders*, *Journal of Lightwave Technology* **40** (2022), no. 5 1472–1482.
- [12] M. H. Idjadi, S. Grillanda, N. Fontaine, M. Mazur, K. Kim, T.-Y. Huang, C. Bolle, R. Kopf, M. Cappuzzo, K. Liu, *et. al.*, *Dual-Wavelength*

\

*phi –OFDRUsingaHybrid –**IntegratedLaserStabilizedtoanIntegratedSiNCoilResonator, arXivpreprintarXiv : 2411.00237*

- [13] W. Loh, A. A. Green, F. N. Baynes, D. C. Cole, F. J. Quinlan, H. Lee, K. J. Vahala, S. B. Papp, and S. A. Diddams, *Dual-microcavity narrow-linewidth Brillouin laser*, *Optica* **2** (2015), no. 3 225–232.
- [14] W. Loh, S. Yegnanarayanan, F. O’Donnell, and P. W. Juodawlkis, *Ultra-narrow linewidth Brillouin laser with nanokelvin temperature self-referencing*, *Optica* **6** (2019), no. 2 152–159.
- [15] Q. Zhao, M. W. Harrington, A. Isichenko, K. Liu, R. O. Behunin, S. B. Papp, P. T. Rakich, C. W. Hoyt, C. Fertig, and D. J. Blumenthal, *Integrated reference cavity with dual-mode optical thermometry for frequency correction*, *Optica* **8** (2021), no. 11 1481–1487.

- [16] I. Fescenko, J. Alnis, A. Schliesser, C. Y. Wang, T. J. Kippenberg, and T. Hänsch, *Dual-mode temperature compensation technique for laser stabilization to a crystalline whispering gallery mode resonator*, *Optics express* **20** (2012), no. 17 19185–19193.
- [17] L. M. Baumgartel, R. J. Thompson, and N. Yu, *Frequency stability of a dual-mode whispering gallery mode optical reference cavity*, *Optics Express* **20** (2012), no. 28 29798–29806.
- [18] W. Weng, J. D. Anstie, T. M. Stace, G. Campbell, F. N. Baynes, and A. N. Luiten, *Nano-Kelvin thermometry and temperature control: beyond the thermal noise limit*, *Physical review letters* **112** (2014), no. 16 160801.
- [19] T. Udem, R. Holzwarth, and T. W. Hänsch, *Optical frequency metrology*, *Nature* **416** (2002), no. 6877 233–237.
- [20] J. Li, H. Lee, and K. J. Vahala, *Microwave synthesizer using an on-chip Brillouin oscillator*, *Nature communications* **4** (2013), no. 1 2097.
- [21] S. Gundavarapu, G. M. Brodnik, M. Puckett, T. Huffman, D. Bose, R. Behunin, J. Wu, T. Qiu, C. Pinho, N. Chauhan, *et. al.*, *Sub-hertz fundamental linewidth photonic integrated Brillouin laser*, *Nature Photonics* **13** (2019), no. 1 60–67.
- [22] D. A. Heim, D. Bose, K. Liu, A. Isichenko, and D. J. Blumenthal, *Photonic Integrated External Cavity Coil-Resonator Stabilized Laser with Hertz-Level-Fundamental and Sub-250-Hertz Integral Linewidth*, in *2024 Conference on Lasers and Electro-Optics (CLEO)*, pp. 1–2, IEEE, 2024.
- [23] Y. Fan, A. van Rees, P. J. Van der Slot, J. Mak, R. M. Oldenbeuving, M. Hoekman, D. Geskus, C. G. Roeloffzen, and K.-J. Boller, *Hybrid integrated*



- InP-Si<sub>3</sub>N<sub>4</sub> diode laser with a 40-Hz intrinsic linewidth*, *Optics express* **28** (2020), no. 15 21713–21728.
- [24] Q. Yu, J. Gao, N. Ye, B. Chen, K. Sun, L. Xie, K. Srinivasan, M. Zervas, G. Navickaite, M. Geiselmann, *et. al.*, *Heterogeneous photodiodes on silicon nitride waveguides*, *Optics Express* **28** (2020), no. 10 14824–14830.
- [25] J. Wang, K. Liu, M. W. Harrington, R. Q. Rudy, and D. J. Blumenthal, *Silicon nitride stress-optic microresonator modulator for optical control applications*, *Optics Express* **30** (2022), no. 18 31816–31827.